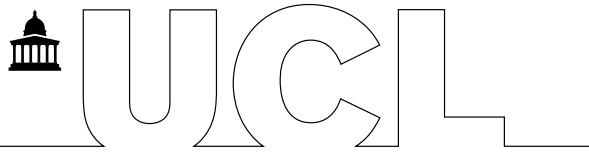

R-matrix Calculations on Molecules of Astrophysical Interest using Quantemol-N

Hemal Naren Varambhia

A thesis submitted to University College London
for the degree of Doctor of Philosophy

Department of Physics and Astronomy
University College London

January 2010

I, Hemal Naren Varambhia, confirm that the work presented in this thesis is my own. Where information has been derived from other sources, I confirm that this has been indicated in the thesis.

Acknowledgements

In accordance with tradition, I must first thank my parents for their constant, loving and encouraging support throughout the period of the Ph.D. The thesis is entirely dedicated to them.

I also thank Prof. Tennyson and Dr. Dan Brown for accepting me as a Ph.D student and as CASE student with Quantemol Ltd. It was an immense pleasure to work with the Company and on Quantemol-N, which, I am certain, will go from strength to strength.

I thank Prof. Tennyson for his support, his patience and time in answering my many questions on the R-matrix method and scattering theory and his allowing me to work independently and collaborate with external research groups.

Formally, I wish to thank Dr. Sumona Gangopadhyay, Harshit Kothari and Prof. Joshipura for providing me with their SiO and CO ionisation cross section data which are presented in this thesis, all his students: Harshad Bhutadia, Dr. Kirtibhai Korot, Foram Shelat, Dr. Bhushit Vaishnav and his colleagues Drs. Chetan Limbachiya and Minaxi Vinodkumar for their friendship, hospitality and care during my time in Ahmedabad and Sardar Patel University, Anand.

A number of the R-matrix studies presented here were part of a collaboration with scientists outside of UCL: the electron scattering study on CS (chapter 8) was carried out with Drs. Tom Field and Karola Graupner of Queen's University Belfast (QUB) and some of the conclusions and observations presented here were theirs. I thank them for allowing me to collaborate with them and to present the work in my thesis; the SiO study (chapter 7) was one carried out with Prof. K. L. Baluja and Dr. Monika Gupta of the University of Delhi (DU); and chapter 10, on the electron-impact rotational excitation of HCN, HNC, DCN and DNC, was carried out with Dr. Alex Faure of the Observatoire de Grenoble, France. Some of the astrophysical conclusions drawn in that chapter are entirely due to his insights.

During the course of the Ph.D, I travelled overseas to Belgrade, Serbia to assist the Institute of Physics at Belgrade in installing Quantemol-N. Accordingly I thank Prof. Zoran Lj. Petrović, Dr. Marija Radmilović-Radjenović and Marija Vranić for their most kind hospitality during the visit, and for the opportunity to discuss my work in the form of a presentation to the various research groups stationed there. I sincerely hope that Quantemol-N continues to be of use to them in their research.

Very special thanks must go to James Munro for helping me develop my JAVA programming skills and my programming skills generally, ones that I value greatly. Indeed I attribute my enthusiasm for computer programming enitirely to James' guidance. Thanks also to Amar Dora, Alex Faure, Jan Franz, Jimena Gorfinkiel, Alex Harvey, Chris Hadley, Chiarra Piccarreta, Bruno Silva and Michal Tarana for very useful discussions and friendship.

I must also thank Prof. and Mrs. Baluja and Jasmeet Rajvanshi for their warm friendship and very kind hospitality during my visit to DU and to their homes. Specifically to Prof. Baluja, I thank him for his kind invitation for me to come to Delhi and many useful discussions on the R-matrix formalism, and thanks also to Dr. Savinder Kaur for her friendship and care during my time in Delhi.

Finally, I also thank Dr. Chirag V. Pandya for kindly inviting me to visit the M. G. Science Institute in Ahmedabad and his family for their hospitality as well.

Abstract

We have carried out a series of *ab initio* R-matrix calculations at the static exchange and close-coupling levels of approximation on molecules of astrophysical interest. These include the polar triatomics HCN and HNC (hydrogen isocyanide) and their isotopologues DCN and DNC, the diatomics CS (carbon monosulphide) and SiO (silicon monoxide), the weakly polar CO molecule and the non-polar CH_4 molecule.

With the exception of CO, all the calculations presented here were carried out using the software 'Quantemol-N' which provides an intuitive user-friendly interface to the UK polyatomic R-matrix codes. A chapter is devoted to the discussion on the software: how to prepare an R-matrix calculation using it, its present capabilities and future development.

The ultimate aim of this thesis is to demonstrate the need to account for electron-induced chemistry in any astrophysical model. We seek to show that in the case of polar molecules, namely, those molecules with large dipole moments, electron collisions are the dominant mechanism of rotational excitation in comets and other astrophysical bodies. Specifically, we will show that electron-impact excitation rate coefficients are several orders of magnitude higher than the corresponding atom-molecule ones.

The thesis concludes with a summary of the key findings and opportunities (and where necessary improvements) that may arise from them.

All the scattering equations presented here used atomic units.

Contents

List of Figures

List of Tables

Chapter 1

Electron-Molecule Scattering and its Applications

1.1 Overview

The electron itself is a fundamental particle in physics, and electron collisions with molecules are not only of great interest from the pure quantum mechanical perspective, but they have a number of applications. They play a vital role in many environments, for example, in plasma etching where ions and radicals may be produced from these collisions (Kimura et al., 2001); in the aurora of the Earth's atmosphere (Meier, 1991) and ionosphere of large planets (Broadfoot et al., 1979, 1981).

In considering the biological effects of ionising radiation, Boudaïffa et al. (2000) found that the majority of energy deposited in cells is channelled into the production of secondary electrons with kinetic energies between 1–20 eV. They showed that the reactions of these electrons induce single- and double-strand breaks in DNA, caused by the rapid decays of transient molecular resonances localised on the DNA's local components.

Low-temperature plasmas are used in the semiconductor industry to etch features, deposit materials and clean reaction chambers. Development of these applications requires a detailed understanding of the physical and chemical processes occurring in the plasmas themselves. Advances in this requires knowledge of the basic processes taking place between species in the plasma. Indeed the most fundamental of the discharge processes are collisions between electrons and atoms, radicals or molecules. Such collisions are precursors of the ions and radicals which drive the etching, cleaning and deposition

processes. Therefore a quantitative understanding of the electron collision processes and rates is important and the availability of accurate data on such observables is key to the success of plasma processing technology (Chistophorou and Olthoff, 2004).

In CO_2 LASERs, electron-impact rotational and vibrational excitation is necessary to provide the energy necessary for population inversion (DeMaria, 1973). Detailed knowledge of electron vibronic cross sections is pivotal in the modelling and performance optimisation of CO_2 LASERs.

Despite the applications of electron-molecule collisions discussed above being important, little is known about their physics and chemistry. In order to fully understand the processes listed above, the scientific community requires detailed knowledge of the electron-molecule interactions underlying these processes. Sparsity of experimental data, and in some cases the inability to carry out scattering experiments on some molecules (e.g. BF_3, Z. Lj. Petrovic, private communication), is a great hindrance to plasma modellers and vice versa.

1.2 Low-Energy Processes

At low energies, defined in this case as all incident electron energies below a molecule's ionisation threshold, the following processes are especially important:

1. *Elastic scattering*

$$AB + e^- \rightarrow AB + e^- \tag{1.1}$$

2. *Inelastic scattering*

   - Rotational excitation:

$$AB(j) + e^- \rightarrow AB(j') + e^- \tag{1.2}$$

   - Vibrational excitation:

$$AB(\nu) + e^- \rightarrow AB(\nu') + e^- \tag{1.3}$$

   - Electronic excitation:

$$AB + e^- \rightarrow AB^* + e^- \tag{1.4}$$

3. *Fragmentation*

   - Dissociative Electron Attachment (DEA):

$$AB + e^- \rightarrow A^- + B \tag{1.5}$$

   - Dissociative recombination:

$$AB^+ + e^- \rightarrow A + B \tag{1.6}$$

   - Electron-impact dissociation

$$AB + e^- \rightarrow A + B + e^- \tag{1.7}$$

At intermediate and higher energies electron-impact ionisation takes place:

$$AB + e^- \rightarrow AB^+ + 2e^- \tag{1.8}$$

1.3 Electron-Molecule Collisions in Astrophysics and Previous Studies

The importance of electron-molecule collisions in astrophysical environments has been a major motivation for a number of studies, including this thesis, on astrophysically important molecules. In this section we shall briefly review the role played by electron collisions in C-type shocks, comets and planetary atmospheres, and some previous work carried out on molecules of astrophysical importance.

Electron-impact excitation plays a significant role in astrophysical environments where the electron fraction is higher than about $\sim 10^{-5}$, e.g. diffuse interstellar media, in shocks and comets. Electrons can dominate the excitation process because the electron-impact excitation rate coefficients can exceed those for neutrals by about five orders of magnitude: modelling of the early stages of C-type shocks predicts that the ion and electron densities are enhanced by the magnetic precursor (Draine, 1980). For molecules like HCO^+, HCN or HNC an electron density enhancement by a factor of about a hundred (e.g. Flower et al. (1996)) would, according to Jimenez-Serra et al. (2006), make electron collisions competitive with excitation by H_2 collisions.

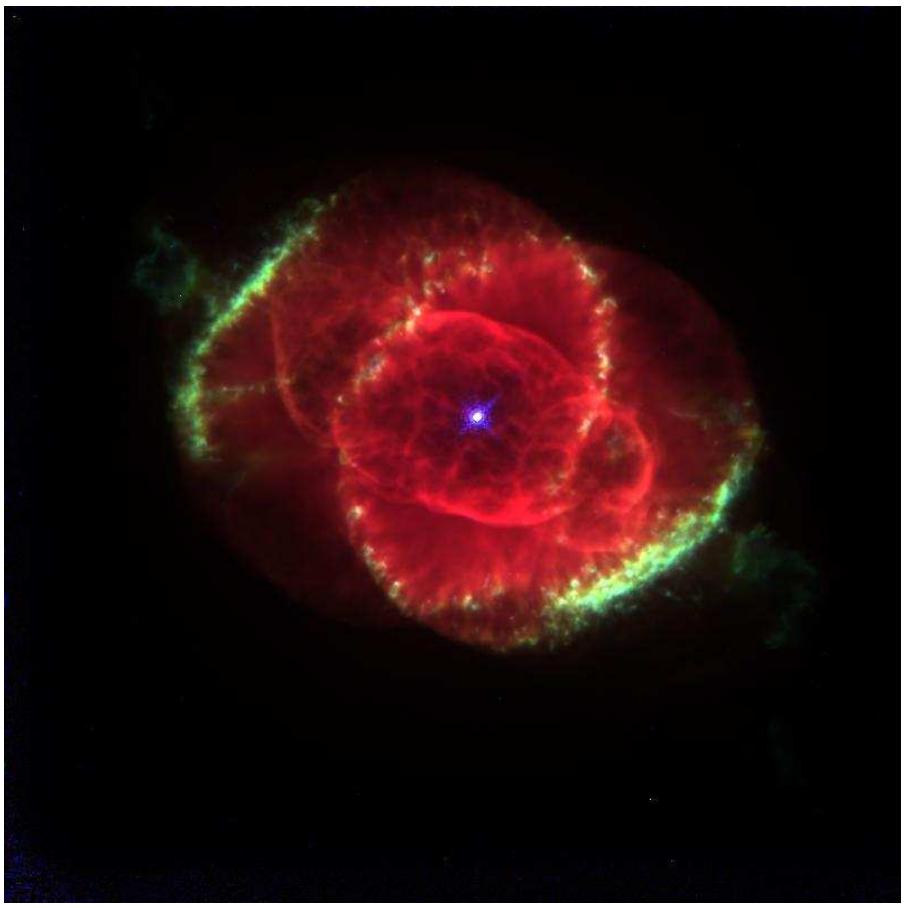

Figure 1.1: Electron induced chemistry plays an important role in planetary nebulae. The image is of the NGC 6543, or 'Cat's Eye' nebula (Credit: J.P. Harrington and K.J. Borkowski (University of Maryland), and NASA)

Electrons are known to have a profound effect in the rotational excitation of the polar water molecule. Xie and Mumma (1992) observed that in the case of the $0_{00} \rightarrow 1_{11}$ rotational transition, the e-H_2O collisional excitation rate exceeds that of neutral-neutral collisions at distances exceeding 3000 km from the cometary nucleus. Their conclusion was that the rotational temperature of water in the intermediate coma may be controlled by collisions with electrons rather than neutrals, and that they may affect the rotational population of the molecule in the intermediate and outer coma of an active comet such as Halley. Similar conclusions were drawn by Lovell et al. (2004) in the case of HCN, which is also very polar ($\sim$ 3 D NIST (2008)). Electron collisions might also contribute to the pumping of H_2O MASERs commonly observed in star forming regions or active galactic nuclei (Strelnitskii, 1984).

Interest in the electron scattering of SO_2 has also been motivated by its detection in

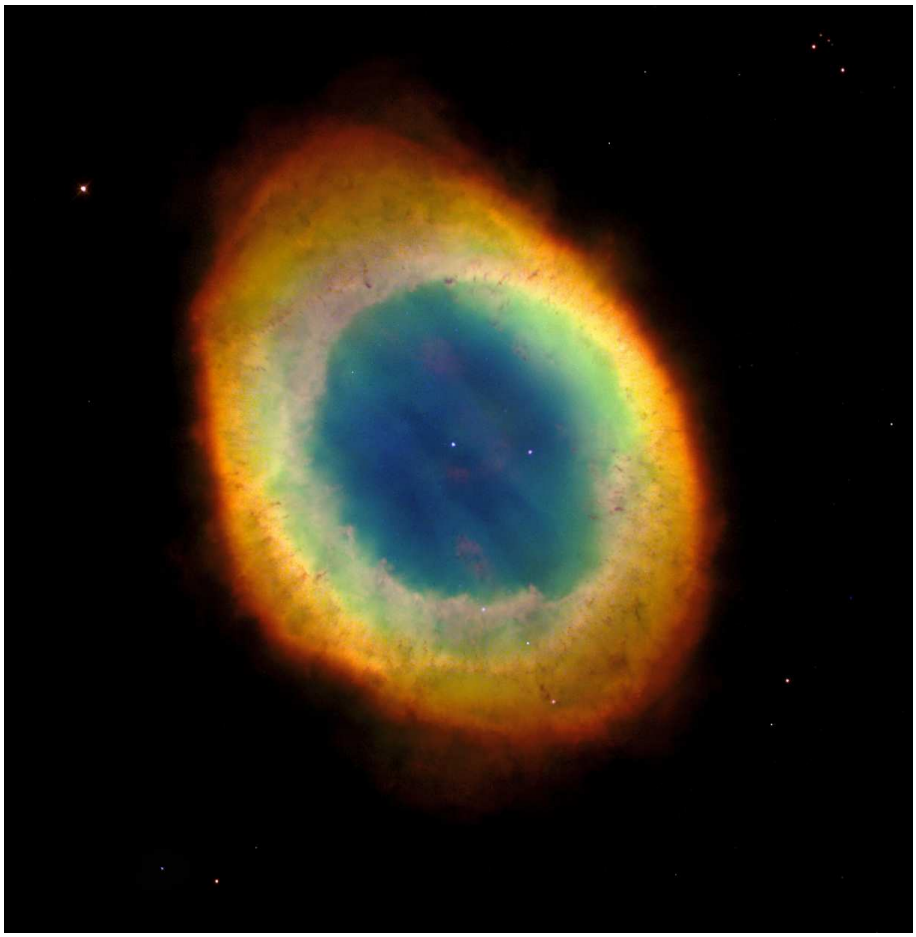

Figure 1.2: Ring Nebula (M57) (Credit: The Hubble Heritage Team (AURA/STScI/NASA))

planetary atmospheres. It is a major constituent (Pearl et al., 1979) of the atmosphere of Io, a satellite of Jupiter, and originates from volcanic eruptions. This SO_2 ends up as ions in the 'plasma torus' following excitation and dissociation by electron and photon impact (Kumar, 1979). A means of modelling such a system requires electron-impact excitation cross sections: this was the motivation for an experimental study by Abuain et al. (1985).

With the second paragraph in mind, we now state the precise aims of this thesis in addressing the role of electron collisions in harsh astrophysical environments.

1.4 Objectives

The objectives of the thesis are as follows:

1. to accurately construct quantum chemistry models for HCN, HNC, CO, SiO, CS

and CH_4 with the aim of obtaining electronic excitation channel thresholds and multipole moments, with special attention paid to the weakly polar CO to reproduce the experimentally observed sign of the dipole moment (polarity C^-O^+- see Harrison (2006)) and its magnitude;

2. using the *ab initio* R-matrix method, construct highly accurate close-coupling scattering models, incorporating many closed excitation channels to model the polarisation interaction and obtain the scattering quantities (R-, K- and T-matrices and multichannel eigenphase sum) and observables (resonances, elastic and inelastic (electronic and rotational) and ionisation cross sections);

3. detect and fit any resonances;

4. using the rotationally inelastic cross sections, compute the rotational excitation rate coefficients and from these the hyperfine excitation ones where it is appropriate. For later use in astrophysical modelling fit the rotational rate coefficients to a functional form;

5. confirm that the role of electron collisions simply cannot be neglected in astrophysical modelling (Lovell et al., 2004) by showing that for polar molecules in particular (SiO, HCN and HNC), the rotational excitation rate coefficients can be several orders of magnitude higher than excitation induced by collisions with neutral projectiles.

1.5 Layout of the Thesis

Chapter 2 begins with a discussion of the electron-molecule scattering problem, the quantum chemistry methods applied to represent the target wavefunctions required in the close-coupling trial wavefunction, the Born-Oppenheimer approximation and the fixed-nuclei (FN) approximation which is applied in all the studies presented in the thesis.

Chapter 3 discusses the scattering method employed to the calculate the scattering quantities and observables, namely, the *ab initio* R-matrix method. Here we shall demonstrate how it is applied to the simple case of scattering by a potential well, whose equations of motion yield analytical solutions. A derivation of the R-matrix in the case of multichannel scattering shall be presented as part of a discussion of the internal region

problem, followed by the equations of motion for the external region and the package structure of the codes utilised.

The R-matrix package is very difficult for non-specialists to use, and takes many months of training to be able to use it proficiently. Even then, the user can often introduce very subtle 'bugs' in the data input stage that could result in the calculated observables being incorrect. Hence Chapter 4 introduces the reader to the new software 'Quantemol-N', which provides a JAVA graphical user-interface to the UK R-matrix codes. The reader is shown how to prepare an ordinary R-matrix calculation by inputting data into a series of wizard panels, how to set up a batch calculation, where the user is able run a queue of R-matrix calculations, and some other facilities to aid new users.

Chapters 5–10 present the models and results obtained during the research. For all the chapters applying the R-matrix method, the close-coupling, or CC level of approximation was used, and each chapter begins with a motivation for studying the molecule in question.

Chapter 5 discusses the application of the R-matrix method to the computation of electron scattering by the polar HCN (hydrogen cyanide) and HNC (hydrogen isocyanide) triatomic molecules.

Chapter 6 discusses the results obtained for the weakly polar CO (carbon monoxide). For this molecule, care was taken to calculate a dipole transition moment with the correct magnitude and sign as observed in experimental studies.

In chapter 7 we present, for the first time, electron scattering by SiO (silicon monoxide), also a polar diatomic. Here we computed, in addition to the quantities usually calculated by the (polyatomic) R-matrix codes, the rotational excitation rate coefficients and rotationally inelastic integral and differential cross sections.

Chapter 8 also presents for the first time a series of R-matrix calculations as a function of bond to probe dissociative electron attachment to CS (carbon monosulphide). This study was the first to be carried out using the Quantemol-N batch job system entirely.

CH_4 is particularly interesting for theoreticians as the electron scattering integral cross sections exhibit very interesting features. In Chapter 9 we discuss the various models tested to reproduce the Ramsauer-Townsend minimum and the cross section maximum at about 8 eV. In addition, to analyse our models deeply, we also computed the rotationally-resolved differential cross sections for some selected energies, comparing them to previous theoretical and experimental data.

Finally, we present in chapter 10 the rotationally resolved differential and integral cross sections, rotational and hyperfine rotational rate coefficients for electron scattering by HCN, HNC and the isotopologues DCN and DNC. These were computed using the fixed-nuclei T-matrices obtained from the best models constructed in chapter 5. These observables may be used in astrophysical modelling.

The thesis concludes with a summary of the results obtained, where appropriate a criticism of them in terms of their quality and any future work that could result from the research that was carried out here.

Chapter 2

Theoretical Pre-requisites

2.1 The Electron-Molecule Scattering Problem

Whereas in electron-atom scattering there are only three outgoing channels:

1. *elastic scattering*

$$e^- + A \rightarrow e^- + A \tag{2.1}$$

2. *inelastic scattering*

$$e^- + A \rightarrow e^- + A^* \tag{2.2}$$

3. *electron-impact ionisation*

$$e^- + A \rightarrow e^- + A^+ \tag{2.3}$$

as shown in chapter 1 the electron-molecule scattering problem is much more complicated because there can be excitation of the nuclear rotational and vibrational degrees of freedom with very little electron energy. The electron-molecule interaction is multi-centred which leads to coupling between states, and there are many fragmentation channels (dissociation, dissociative electron attachment and dissociative ionisation).

The equation of motion for the scattering process is the Schrödinger equation, but due to the size of the system often involved, it cannot be solved analytically– even electron scattering by H_2 must be treated numerically. There are different models that

may be used to solve the electron-molecule scattering problem as accurately as possible. In treating electronically elastic scattering we will consider some of the models:

1. *static*: at this level the scattering electron is deemed to be a separate entity from the target molecule. The exchange is neglected and it is assumed that the target remains unperturbed by the approaching electron, i.e. the polarization is also neglected. Treating the problem at this level has the advantage that the equations are easily solved, but it has the disadvantage that the answers may be quantitatively and qualitatively incorrect, particularly at low collision energies;

2. *static exchange* (SE): here the exchange interaction is included implicitly or explicitly. Again, the target is not allowed to be perturbed i.e. the polarisation is neglected. This and the static approximation are useful for high-energy calculations;

3. *static exchange plus polarisation* (SEP): with the inclusion of the exchange, the target is now allowed to be perturbed by the polarisation and correlation interactions;

4. *close-coupling* (CC): the scattering wavefunction is expanded in terms of a complete set of unperturbed eigenstates of the isolated molecule ψ_i (Lane, 1980):

$$\Psi_\varepsilon = \hat{A} \sum_i F_i(\mathbf{r}_{N+1}) \psi_i \tag{2.4}$$

where $\hat{A}$ is the antisymmetrisation operator and $\mathbf{r}_{N+1}$ is the scattering. electron position vector. In principle the summation in equation (2.4) can include the continuum states of the molecule as well. The one-electron scattering function $F_i(\mathbf{r}_{N+1})$ satisfies the set of coupled equations

$$\left[\nabla^2_{N+1} + k_n^2\right] F_i(\mathbf{r}_{N+1}) = \sum_j [V_{ij} + W_{ij}] F_j(\mathbf{r}_{N+1}) \tag{2.5}$$

where k_n is the channel linear momentum and $nabla^2_{N+1}$ is the Laplacian operator for the scattering electron. $F_i(\mathbf{r}_{N+1})$ corresponding to a target state i depend on the initial target state specified in the asymptotic boundary conditions

$$\lim_{r \to \infty} \Psi_\varepsilon \sim \Psi_{inc} + \Psi_{scat} \tag{2.6}$$

where for some initial target state ψ_0 and wave vector $\mathbf{k}_0$

$$\Psi_{inc} = e^{i\langle \mathbf{k}_0, \mathbf{r} \rangle} \psi_0 \tag{2.7}$$

and

$$\Psi_{scat} = \frac{1}{r} \sum_j e^{i\mathbf{k}_j \cdot \mathbf{r}} f_{j0}(\mathbf{k}_j, \mathbf{k}_0) \psi_j \tag{2.8}$$

$f_{j0}(\mathbf{k}_j, \mathbf{k}_0)$ is the scattering amplitude for a transition $0 \rightarrow j$. V_{ij} is the electron-molecule scattering potential and W_{ij} is the exchange matrix. In this thesis, in outer region, the exchange is considered negligible so the antisymmetrisation operator $\hat{A}$ is omitted and $W_{ij} = 0$ (see chapter 3).

$F_i(\mathbf{r}_{N+1})$ may be expanded in terms of spherical harmonics $Y_l^m(\theta, \phi)$. Equation (2.5) is then reduced to a set of coupled second order ordinary differential equations which has to be truncated in order to be soluble.

The method is used in all the chapters presented here to account for electronic excitation channels, but it can also be used to account for the rotational and vibrational excitation channels.

5. *dipole Born approximation*: when a potential contains a long-range dipole potential the number of partial waves required to converge the total cross section can become very large. Such systems can treated using the Born approximation (e.g. Chu and Dalgarno (1974), Altshuler (1957)). Higher partial waves, those above a certain minimum l_0 say, are only weakly scattered and certainly can be treated using the Born approximation (Chu and Dalgarno, 1974). Those partial waves below l_0 can be treated using a scattering theory which models the short-range interactions more accurately. A Born *correction* accounting for the higher partial waves ($l > l_0$) is calculated by computing first the Born cross section for *all* partial waves and for the partial waves $l \leq l_0$:

$$\delta\sigma(E) = \sigma_B(E) - \sigma_{B,l \leq l_0}(E) \tag{2.9}$$

for some incident energy E and then is added to the cross sections for $l \leq l_0$.

We applied the Born approximation and correction to electron-impact rotational excitation of HCN, HNC, DCN and DNC (chapter 10) and SiO (chapter 7). In

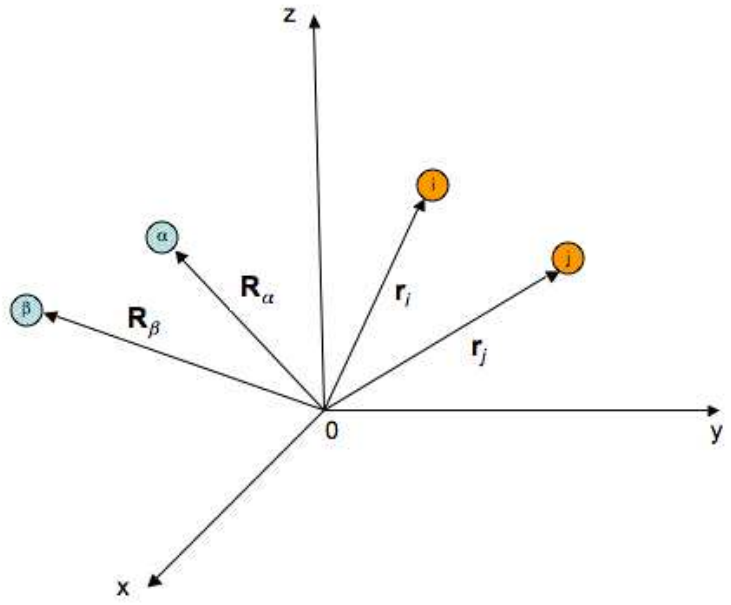

Figure 2.1: A molecular coordinate system: i, j correspond to electrons and α, β to nuclei (Szabo and Ostlund, 1996).

both of these calculations we took $l_0 = 4$.

2.2 Born-Oppenheimer Approximation

Consider a molecule with N_n nuclei and N_e electrons. Then the non-relativistic Hamiltonian in atomic units is

$$\hat{H}_t = -\sum_{A=1} \frac{1}{2M_A}\nabla_A^2 - \sum_{i=1} \frac{1}{2}\nabla_i^2 - \sum_{A,i} \frac{Z_A}{|\mathbf{r}_i - \mathbf{R}_A|} + \sum_{A>B} \frac{Z_A Z_B}{|\mathbf{R}_A - \mathbf{R}_B|} + \sum_{i>j} \frac{1}{|\mathbf{r}_i - \mathbf{r}_j|} \quad (2.10)$$

It is clear that the attractive electron-nucleus coulomb potential prevents one from separating the electronic and nuclear parts of the motion and using the separation of variables method, which would allow one to write the total molecular wavefunction $\Psi(\{\mathbf{r}_i\}_{i=1}^{N_e}, \{\mathbf{R}_A\}_{A=1}^{N_n})$ as a product of nuclear and electronic terms $\psi_e(\{\mathbf{r}_i\}_{i=1}^{N_e})\Phi_n(\{\mathbf{R}_A\}_{A=1}^{N_n})$. The key idea behind the Born-Oppenheimer approximation is that since the constituent nuclei are much heavier than the electrons, they move much more slowly. So to a good approximation, one may consider the electrons in a molecule to be moving in the Coulomb field of the nuclei. Within this approximation the nuclear kinetic energy term in (2.10)

may be neglected and the nuclear repulsion term may be considered a constant with no effect upon the eigenkets, since the addition of a constant operator ($C\hat{I}$ say, where C is a constant) only affects the operator eigenvalues. The resulting Hamiltonian is called the electronic Hamiltonian $\hat{H}_e$ describing the motion of N_e electrons in the Coulomb field of N_n nuclei:

$$\hat{H}_e = -\sum_{i=1} \frac{1}{2}\nabla_i^2 - \sum_{A,i} \frac{Z_A}{|\mathbf{r}_i - \mathbf{R}_A|} + \sum_{A>B} \frac{Z_A Z_B}{|\mathbf{R}_A - \mathbf{R}_B|} + \sum_{i>j} \frac{1}{|\mathbf{r}_i - \mathbf{r}_j|} \tag{2.11}$$

So the Schrödinger equation for the electronic motion is then

$$\hat{H}_e \psi_e(\{\mathbf{r}_i\}_{i=1}^{N_e}; \{\mathbf{R}_A\}_{A=1}^{N_n}) = E_e(\{\mathbf{R}_A\}_{A=1}^{N_n}) \psi_e(\{\mathbf{r}_i\}_{i=1}^{N_e}; \{\mathbf{R}_A\}_{A=1}^{N_n}) \tag{2.12}$$

Its solutions depend explicitly on $\{\mathbf{r}_i\}_{i=1}^{N_e}$ and parametrically on $\{\mathbf{R}_A\}_{A=1}^{N_n}$, the nuclear co-ordinates, as does the electronic energy eigenvalue $E_e(\{\mathbf{R}_A\}_{A=1}^{N_n})$ of course. Parametric dependence means that for a given nuclear geometry, the electronic wavefunction ψ_e is a different function of the electronic co-ordinates. Equation (2.12) is initially solved excluding the nuclear repulsion term. The electronic energy eigenvalue $\varepsilon_e(\{\mathbf{R}_A\}_{A=1}^{N_n})$ is then modified by adding the nuclear repulsion to it to obtain the Hamiltonian eigenvalue E_e

$$E_e(\{\mathbf{R}_A\}_{A=1}^{N_n}) = \varepsilon_e(\{\mathbf{R}_A\}_{A=1}^{N_n}) + \sum_{A>B} \frac{Z_A Z_B}{|\mathbf{R}_A - \mathbf{R}_B|} \tag{2.13}$$

In summary equations (2.11) and (2.13) describe the electronic motion entirely.

Having solved for the electronic part of the molecular motion, the nuclear motion can be solved under the same assumptions as in the electronic one: since the electron move much faster than the nuclei, to a reasonable approximation, the electronic co-ordinates of equation (2.10) can be replaced by their averaged values, averaged over the electronic wavefunctions. Therefore the Hamiltonian operator for the nuclear motion in the averaged field of the electrons is

$$\begin{aligned}\hat{H}_n &= -\sum_{A=1}\frac{1}{2M_A}\nabla_A^2 + \left\langle -\sum_{i=1}\frac{1}{2}\nabla_i^2 - \sum_{A,i}\frac{Z_A}{|\mathbf{r}_i-\mathbf{R}_A|} + \sum_{i>j}\frac{1}{|\mathbf{r}_i-\mathbf{r}_j|}\right\rangle \\ &\quad + \sum_{A>B}\frac{Z_A Z_B}{|\mathbf{R}_A-\mathbf{R}_B|} \qquad (2.14)\\ &= -\sum_{A=1}\frac{1}{2M_A}\nabla_A^2 + \varepsilon_e(\{\mathbf{R}_A\}_{A=1}^{N_n}) + \sum_{A>B}\frac{Z_A Z_B}{|\mathbf{R}_A-\mathbf{R}_B|} \qquad (2.15)\\ &= -\sum_{A=1}\frac{1}{2M_A}\nabla_A^2 + E_e(\{\mathbf{R}_A\}_{A=1}^{N_n}) \qquad (2.16)\end{aligned}$$

$E_e(\{\mathbf{R}_A\}_{A=1}^{N_n})$ is commonly referred to as a molecule's potential energy surface (PES) and provides a potential for the nuclear motion. Thus in the Born-Oppenheimer approximation the nuclei move on a PES obtained by solving the electronic problem first.

Solutions to a nuclear Schrödinger equation

$$\hat{H}_n\Phi_n(\{\mathbf{R}_A\}_{A=1}^{N_n}) = \varepsilon_n\Phi_n(\{\mathbf{R}_A\}_{A=1}^{N_n}) \qquad (2.17)$$

describe the vibration, rotation and translation of a molecule, where ε_n is the Born-Oppenheimer approximation to the total energy, including the electronic, vibrational, rotational and translation energy. The total wavefunction solution of equation (2.10) is then

$$\Phi(\{\mathbf{r}_i\}_{i=1}^{N_e};\{\mathbf{R}_A\}_{A=1}^{N_n}) = \psi_e(\{\mathbf{r}_i\}_{i=1}^{N_e};\{\mathbf{R}_A\}_{A=1}^{N_n})\Phi_n(\{\mathbf{R}_A\}_{A=1}^{N_n}) \qquad (2.18)$$

An example of the above is given in chapter 8, where we applied the Born-Oppenheimer approximation to compute the PES for some of the low-lying electronic states of the diatomic CS.

2.3 Hartree-Fock Approximation

The Hartree-Fock approximation is a simple but powerful approximation in quantum chemistry, providing an important foundation for much more accurate techniques which incorporate the effects of correlation.

One can equate Hartree-Fock theory to single determinant theory (Szabo and Ostlund, 1996). Thus one seeks to obtain a set of spin-orbitals χ_a such that the single determinant formed from these:

$$|\Psi_0\rangle = |\chi_1\chi_2\cdots\chi_a\chi_b\cdots\chi_{N_e}\rangle \qquad (2.19)$$

is the best possible representation for the ground state of an N_e-electron system described by an electronic Hamiltonian. By the variational principle, the best spin-orbital set is that which minimises the electronic energy functional

$$E_0(\Psi_0) = \langle \Psi_0 | \hat{H}_{elec} | \Psi_0 \rangle = \sum_a \langle a | \hat{h} | a \rangle + \frac{1}{2} \sum_{ab} \langle aa | bb \rangle - \langle ab | ba \rangle \tag{2.20}$$

where

$$\langle ij | kl \rangle = \int d\tau_1 d\tau_2 \chi_i^*(\mathbf{x}_1) \chi_j(\mathbf{x}_1) r_{12}^{-1} \chi_k^*(\mathbf{x}_2) \chi_l(\mathbf{x}_2) \tag{2.21}$$

and the one-particle Hamiltonian is

$$\hat{h}(1) = -\frac{1}{2}\nabla_1^2 - \sum_A \frac{Z_A}{r_{1A}} \tag{2.22}$$

with the constraint that the spin-orbitals be orthogonal:

$$\langle \chi_i | \chi_j \rangle = \delta_{ij} \tag{2.23}$$

The spin-orbitals are then varied until E_0 is minimised. The equation for obtaining the best possible spin-orbitals set is the Hartree-Fock eigenvalue equation:

$$\left[\hat{h}(1) + \sum_{b \neq a} \mathcal{J}_b(1) - \sum_{b \neq a} \mathcal{K}_b(1) \right] \chi_a(1) = \varepsilon_a \chi_a(1) \tag{2.24}$$

and where the exchange and Coulomb operator are defined such that

$$\mathcal{K}_b(1)\chi_a(1) = \left[\int d\tau_2 \chi_b(2)^* \frac{1}{r_{12}} \chi_a(2) \right] \chi_b(1) \tag{2.25}$$

$$\mathcal{J}_b(1)\chi_a(1) = \left[\int d\tau_2 \chi_b(2)^* \frac{1}{r_{12}} \chi_b(2) \right] \chi_a(1) \tag{2.26}$$

respectively. From the restricted summation, the operator in the square brackets is different for every spin-orbital χ_a. However, if one lets $b = a$ it is clear, from equations (2.25) and (2.26), that $[\mathcal{J}_b(1) - \mathcal{K}_b(1)]\chi_a(1) = 0$ and therefore it is quite possible to add this term to equation (2.24) with no major effect on the spin-orbitals. Now, we define a Fock operator $\hat{f}$

$$\hat{f}(1) = \hat{h}(1) + \sum_b \mathcal{J}_b(1) - \mathcal{K}_b(1) \tag{2.27}$$

The Hartree-Fock equation is simplified to

$$\hat{f}|\chi_a\rangle = \varepsilon_a|\chi_a\rangle \tag{2.28}$$

A full derivation of the Hartree-Fock (HF) equations is presented in Szabo and Ostlund (1996). Normally, to solve these, basis functions are introduced in the expansion of the spin-orbitals and one then proceeds to solve a set of matrix equations.

2.3.1 Introduction of a Basis: The Roothan Equations

Spin-orbitals are of course represented by a spatial and spin component:

$$\chi_i(\mathbf{x}) = \begin{cases} \psi_i(\mathbf{r})|\alpha\rangle, \\ \psi_i(\mathbf{r})|\beta\rangle \end{cases} \tag{2.29}$$

By eliminating spin, the calculation of the molecular orbitals is equivalent to solving the

$$\hat{f}(\mathbf{r}_i)\psi_i(\mathbf{r}_i) = \varepsilon_i\psi_i(\mathbf{r}_i) \tag{2.30}$$

eigenvalue equation (Szabo and Ostlund, 1996). By introducing a known spatial basis set (Roothan, 1951) the equations (2.30) may be transformed to a set of algebraic equations which may be solved by techniques of linear algebra.

In solving for the spatial part of the spin-orbitals one expands the molecular orbitals as a linear combination of known (atomic) ones:

$$\psi_i = \sum_{j=1} C_{ij}\phi_j \tag{2.31}$$

If the basis set were complete then one would have the exact solution to the Fock eigenvalue equation, but this is not possible for computational reasons and one is restricted to a finite set with B basis function elements.

From equation (2.31) the problem of calculating the HF molecular orbitals reduces to the problem of solving for the expansion coefficients C_{ij}. By substituting equation (2.31) into (2.30) one obtains the Roothan equations

$$\mathbf{FC} = \mathbf{SC}\varepsilon \tag{2.32}$$

where $\mathbf{F}$ is the Hermitian Fock matrix,

$$F_{ij} = H_{ij} + \sum_{a=1}^{N_e/2} \sum_{kl} C_{ka} C_{la}^* [2\langle ij|kl\rangle - \langle ik|lj\rangle] \tag{2.33}$$

$$= H_{ij} + \sum_{kl} P_{kl} \left[\langle ij|kl\rangle - \frac{1}{2}\langle ik|lj\rangle \right] \tag{2.34}$$

where $\mathbf{C}$ is an $B \times B$ matrix of the expansion coefficients in equation (2.31) and $\mathbf{S}$ is a Hermitian overlap matrix with elements

$$S_{ij} = \int d\tau_1 \phi_i^* \phi_j \tag{2.35}$$

$$P_{ij} = 2 \sum_{a=1}^{N_e/2} C_{ia} C_{ja} \tag{2.36}$$

The matrix representations presented here are in the basis of atomic functions. The basis functions are not in general orthogonal so S_{ij} will have small non-diagonal elements. But since it is Hermitian it is possible via a unitary transformation to obtain a diagonal representation of the same.

2.3.2 The Self-Consistent Field Optimisation

The procedure is as follows (Szabo and Ostlund, 1996). A simplified flow diagram is shown in figure 2.2:

1. specify a molecule (nuclear co-ordinates, proton numbers and electrons)and a basis set $\{\phi_i\}_{i=1}^B$;

2. compute the required molecular integrals S_{ij}, H_{ij} and $\langle ij|kl\rangle$;

3. diagonalise the overlap matrix and obtain the transition matrix $\mathbf{X}$ such that

$$\varphi_i = \sum_j X_{ij} \phi_j \tag{2.37}$$

   where $\{\varphi_i\}_{i=1}^B$ is an orthonormal basis set;

4. obtain a guess for $\mathbf{P}$, the matrix with elements as given in equation (2.36);

5. obtain the second summation term of equation (2.34) using the two-electron integrals and the P-matrix;

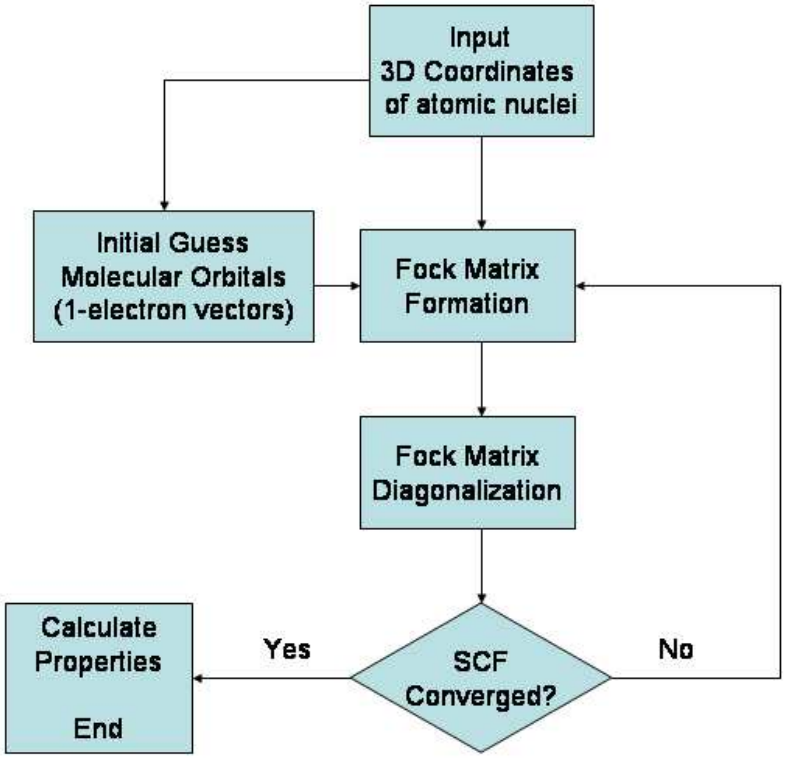

Figure 2.2: Simplified flow diagram for the SCF optimisation procedure (image URL: http://en.wikipedia.org/wiki/File:Hartree-Fock.png)

6. evaluate the Fock matrix;
7. calculate the transformed Fock matrix $\mathbf{F}' = \mathbf{X}^{\dagger}\mathbf{F}\mathbf{X}$;
8. diagonalise $\mathbf{F}'$ to obtain $\mathbf{C}'$ and ε;
9. using the transition matrix $\mathbf{X}$ obtain $\mathbf{C}$;
10. using $\mathbf{C}$ calculate the new density matrix $\mathbf{P}$;
11. confirm whether the procedure has yielded convergence, namely, whether the new density matrix is the same as that in step 4 within a threshold. If not, then return to step 5 using the new density matrix;
12. if it has converged then this orbital set may be used elsewhere.

2.3.3 Basis Sets

In representing these basis sets $\{\phi_i\}_{i=1}^{B}$ there are two particular types of interest: Slater-type orbitals (STOs) (Slater, 1960)

$$\phi_{nlm}^{s} = \sqrt{\frac{(2\zeta)^{2n+1}}{(2n)!}} r_{\alpha}^{n-1} e^{-\zeta r_{\alpha}} Y_l^m(\theta_{\alpha}, \phi_{\alpha}) \tag{2.38}$$

with ζ a constant; and Gaussian-type orbitals (GTOs) (Boys, 1950)

$$\phi_{nlm}^{g} = N r_{\alpha}^{n-1} e^{-\zeta r_{\alpha}^2} Y_l^m(\theta_{\alpha}, \phi_{\alpha}) \tag{2.39}$$

where r_α is the distance of the electron from a nuclear centre α, ζ is again a constant and N is a normalisation constant.

Although with Slater-type orbitals one can obtain the best possible representation of the molecular orbitals ψ_i with the least number of expansion terms, Gaussian-type orbitals have the advantage that two-electron integrals can be evaluated very fast and very accurately. By using *contracted* Gaussian functions one gets the best of both worlds. A contraction has the form

$$\phi_i^{cg}(r_{\alpha}) = \sum_{p=1}^{L} d_{pi} g_p(\alpha_{pi}, r_p) \tag{2.40}$$

where α_{pi} and d_{pi} are the contraction exponents and coefficients and L is the length of the contraction. Integrals involving such basis functions reduce to sums of integrals involving the primitive Gaussian functions g_p. Although there may be many primitive integrals to be evaluated for each basis function, the basis function integrals will be rapidly calculated provided the method of computing primitive integrals is very fast (Szabo and Ostlund, 1996). A library of contracted GTO basis sets may be found in *EMSL Gaussian Basis Set Order Form* (2009).

2.4 Configuration Interaction Method

Although the HF approximation has been remarkably successful, it does have limitations. For example the dipole moment is often inaccurate but most importantly the HF approximation neglects the short-range correlation interaction: it assumes that each electron interacts with an averaged charge distribution due to the other electrons.

A much more accurate means of modelling the correlation is the Configuration Interaction (CI) method which employs the HF spin-orbitals discussed earlier as its foundation. The underlying principle is to obtain a diagonalised representation of the N_e-electron Hamiltonian operator in the basis of N_e-electron functions or Slater determinants. We wish to express the exact wavefunction as a linear combination of N_e-electron trial Slater determinants (more commonly referred to as configuration state functions or CSFs) by appealing to the principle of variation.

In principle, the CI method can yield an exact solution to the N_e-electron problem but in practice one can only handle a finite set of N_e-electron trial functions so the method only provides upper bounds on the exact eigenenergies.

Having determined the Hartree-Fock spin-orbitals from the SCF optimisation procedure the determinant $|\Psi_0\rangle$ of the N_e lowest energy spin orbitals is easily formed. In addition, a large number of other N_e-electron determinants may also be formed from all the orbitals, occupied and unoccupied. In describing these other N_e-electron determinants it is convenient to compare how they differ from $|\Psi_0\rangle$, the reference determinant. Thus in addition to $|\Psi_0\rangle$ we have singly excited determinants, $|\Psi_a^r\rangle$, which differ by having spin orbital χ_a being replaced by χ_r, doubly excited determinants $|\Psi_{ab}^{rs}\rangle$ which differ from $|\Psi_0\rangle$ in that orbitals χ_a and χ_b are replaced by χ_r and χ_s etc. up to and including n-tuply excited determinants. These determinants or CSFs may be used as a basis for the expansion of the exact wavefunction $|\Phi_0\rangle$ say:

$$|\Phi_0\rangle = |\Psi_0\rangle + \sum_{ar} c_a^r |\Psi_a^r\rangle + \frac{1}{2!} \sum_{a<b,r<s} c_{ab}^{rs} |\Psi_{ab}^{rs}\rangle + \cdots \tag{2.41}$$

and similarly for electronically excited state wavefunctions. c_a^r and c_{ab}^{rs} are variationally determined coefficients, and the summation pre-factor ensures that an excitation is counted only once. Hence equation (2.41) is the form of the full CI (FCI) wavefunction, which provides the exact solution to the N_e-electron Hamiltonian eigenvalue problem. But the size of the Hamiltonian matrix expands with the number of determinants and the FCI method is only feasible for small molecules e.g. H_2 and H_2^+.

By restricting the summation in equation (2.41) to include only singly and doubly excited CSFs, this elaborate method may be made feasible.

Another possibility is to employ the complete active space CI (CASCI) method, as has been applied in this thesis, where the spin-orbitals may be divided into a core, active and virtual orbitals space. The lowest energy core orbitals are fully occupied in

all orbitals configurations, the highest-lying virtual orbitals remain unoccupied and the active orbitals vary in occupancy (Shimamura, 1998).

2.4.1 Natural Orbitals

Using Hartree-Fock spin-orbitals in the CI method results in the corresponding expansion being slowly convergent. Since any one-electron basis may be used to construct the N_e-electron configurations (Szabo and Ostlund, 1996), one might seek to obtain some one-electron basis for which a CI expansion is more rapidly convergent than HF orbitals: the set of natural orbitals, introduced by Löwdin (1955), is one such basis.

In order to define these natural orbitals consider the first-order reduced density matrix of an N_e-electron system

$$\rho(\mathbf{x}_1, \mathbf{x}_1') = N \int \prod_{i=2}^{N_e} d\tau_i \Phi(\mathbf{x}_1, \mathbf{x}_2, \ldots, \mathbf{x}_{N_e}) \Phi^*(\mathbf{x}_1', \mathbf{x}_2, \ldots, \mathbf{x}_{N_e}) \tag{2.42}$$

The same may be expanded in the orthonormal basis of Hartree-Fock spin orbitals:

$$\rho(\mathbf{x}_1, \mathbf{x}_1') = \sum_{i,j} \chi_i(\mathbf{x}_1) \gamma_{ij} \chi_j(\mathbf{x}_1')^* \tag{2.43}$$

When Φ is the Hartree-Fock ground state wavefunction Ψ_0, it can be shown that (Szabo and Ostlund, 1996)

$$\gamma(\mathbf{x}_1, \mathbf{x}_1') = \sum_{i} \chi_i(\mathbf{x}_1) \chi_i(\mathbf{x}_1')^* \tag{2.44}$$

If this is not the case, the matrix representation of the first-order reduced density matrix is not diagonal in the basis of the HF spin-orbitals. γ is Hermitian so it is possible to define an orthonormal basis $\{u_i\}$ say, related by a unitary transformation to the HF spin-orbitals, such that γ is diagonalised. The elements u_i are called natural spin-orbitals. The new matrix is then expressed as

$$\gamma_{diag} = \sum_{i} \lambda_i u_i(\mathbf{x}_1) u_i(\mathbf{x}_1')^* \tag{2.45}$$

where λ_i is the occupation number of u_i. Those configurations constructed from natural orbitals with large occupation numbers make the significant contribution to the eigenenergy; those natural spin-orbitals with negligible occupation number may be safely omitted without affecting the accuracy of the calculation.

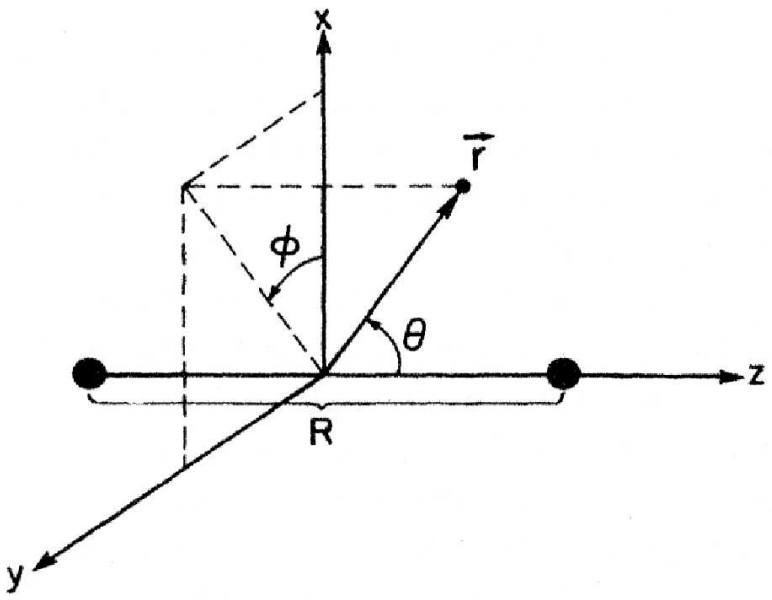

Figure 2.3: BODY co-ordinate frame in the fixed-nuclei formulation (Lane, 1980)

The natural orbitals employed in this thesis (chapter 5) were computed from approximate wavefunctions hence termed 'pseudo natural orbitals'. They were generated using all possible single and double excitations into the high lying virtual orbitals discussed earlier in this chapter. The pseudo natural orbitals can be averaged by giving different weightings to target states used in a natural orbitals calculation to give state-averaged natural orbitals.

2.5 The Fixed-Nuclei Formulation

Suppose the nuclei of a molecule are held fixed in space. Then one need only solve for the eigenvalues and corresponding eigenvectors of the electronic Hamiltonian (Lane, 1980). An appropriate co-ordinate frame may simplify the equations describing the collision process. Hence define two reference frames: the body (BODY) frame of reference (figure 2.3) and the laboratory (LAB) frame (figure 2.4) (Lane, 1980). Here the BODY co-ordinate frame is defined such that the z-axis lies along the vector direction of the dipole moment while in the laboratory frame it lies along the momentum vector of the incident electron. In both the origin coincides with the centre of mass of the molecule.

Define $\{\mathbf{r}_i\}_{i=1}^{N_e}$ and $\{\mathbf{R}_A\}_{i=1}^{N_n}$ to be the position vectors of the electrons and nuclei of the molecule respectively and $\mathbf{r}_{N+1}$ the co-ordinates of the projectile electron in the

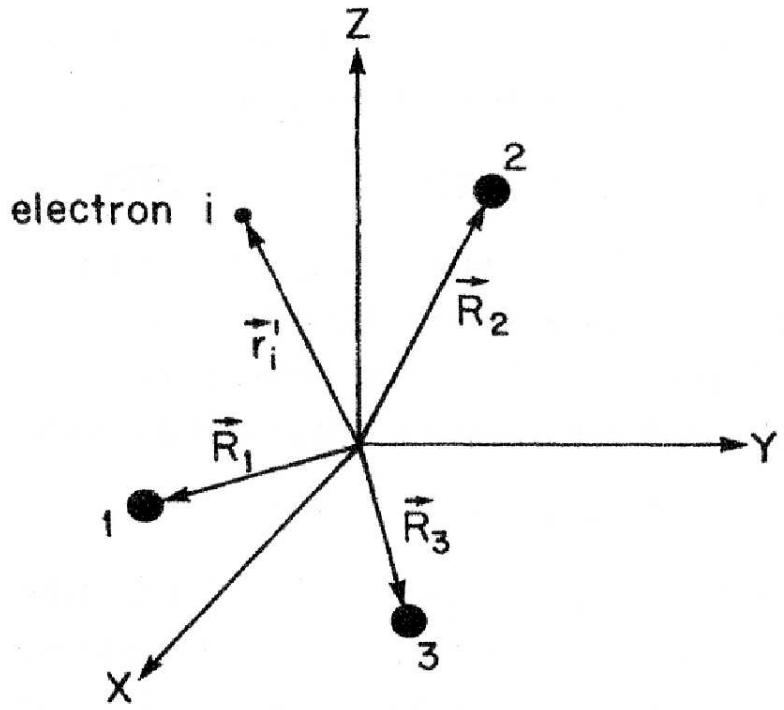

Figure 2.4: LAB co-ordinate frame in the fixed-nuclei formulation: i indicates an electron and the integers 1, 2 and 3 indicate the nuclei (Lane, 1980)

BODY co-ordinate frame. The primed version of these are defined relative to the LAB frame. Hence the electron-molecule Hamiltonian operator is

$$\hat{H}_{N+1,elec} = -\frac{1}{2}\nabla^2_{N+1} + \hat{H}_{N,elec} + \hat{V}_{e-mol} \tag{2.46}$$

where ∇^2_{N+1} is the electron kinetic energy operator appropriate for the body frame, $\hat{H}_{N,elec}$ is the electronic target Hamiltonian and $\hat{V}_{e-mol}$ is the electron-molecule interaction potential operator. For a molecule with N_e electrons and N_n electrons these may be written as

$$\hat{H}_{N,elec} = -\sum_{j=1}^{N_e}\frac{1}{2}\nabla^2_j - \sum_{i}^{N_e}\sum_{A=1}^{N_n}\frac{Z_A}{|\mathbf{r}'_i - \mathbf{R}_A|} + \sum_{i=1}^{N_e}\sum_{j>i}^{N_e}\frac{1}{|\mathbf{r}'_i - \mathbf{r}'_j|} \tag{2.47}$$

$$\hat{V}_{e-mol} = -\sum_{A=1}^{N_n}\frac{Z_A}{|\mathbf{r}'_{N+1} - \mathbf{R}_A|} + \sum_{j=1}^{N_e}\frac{1}{|\mathbf{r}'_{N+1} - \mathbf{r}'_j|} \tag{2.48}$$

The fixed-nuclei (FN) approximation is only valid when the collision time is very much shorter than the time of nuclear rotation or vibration and corresponds to a 'fast' collision.

It is not however applicable to systems where scattering is dominated by a strong long-range interaction, such as electron scattering by a polar molecule, or when the incident electron energy is close to a narrow, long-lived resonance, where the collision time is long.

The fixed-nuclei approximation may be combined with other methods to obtain reliable cross sections (Lane, 1980). In the frame-transformation procedure (Fano, 1970; Chang and Fano, 1972) the FN approximation is only appropriate in the region close to the nuclei, where the BODY co-ordinate frame is used. Then, a boundary is chosen such that the nuclear Hamiltonian can be ignored, and where the exchange and electron-electron correlation interactions are dominant but can be ignored in the outer region. At this boundary the solutions are transformed to the LAB frame, the nuclear Hamiltonian is introduced and the new set of equations solved in the asymptotic region. The frame-transformation approach underlies the R-matrix method used here and which is described in the next chapter.

2.6 Adiabatic Nuclei Approximation

In some cases the inner region employed in the frame-transformation approach may be extended to infinity and the entire problem solved in this region. The actual frame transformation is carried out at the end of the calculation when the scattering quantities (T-matrix etc.) have been computed. It is valid under the following conditions– that the incident electron energy is away from threshold, there are no resonances and absence of any significant long range interactions.

2.7 Other Methods

All the results presented in this thesis applied the R-matrix method, but there are two other *ab initio* variational methods and they are briefly discussed below.

2.7.1 Complex Kohn Variational Method

The complex Kohn variation method (Schneider and Rescigno, 1988) employs a trial wavefunction of the form

$$\psi_{\Gamma^1} = \sum_{\Gamma} \hat{A}(\chi_{\Gamma} F_{\Gamma\Gamma^1}) + \sum_{\mu} d_{\mu}^{\Gamma^1} \Phi_{\mu} \tag{2.49}$$

where the first summation runs over the energetically open N-electron target states χ_Γ and Φ_μ are an orthonormal set of antisymmetric, square-integrable $(N+1)$-electron functions used to represent polarisation and correlation effects not included in the summation. Γ represents the complete set of commuting observables required to represent the scattering state.

In addition in the formulation developed by Schneider and Rescigno (1988) the channel continuum functions $F_{\Gamma\Gamma^1}$ are expanded as

$$rF_{\Gamma\Gamma^1} = \sum_{l,m} \left[{f_l}^\Gamma(r)\delta_{ll^1}\delta_{mm^1}\delta_{\Gamma\Gamma^1} + T^{\Gamma\Gamma^1}_{ll^1,mm^1} g_l^\Gamma(r) \right] Y_l^m(\hat{\mathbf{r}}) + \sum_k c_k^{\Gamma\Gamma^1} \phi_k^\Gamma(\mathbf{r}) \tag{2.50}$$

where $f_l^\Gamma(r)$ and g_l^Γ are linearly independent continuum orbitals that are regular at the origin.

The variation formulation involves obtaining $T^{\Gamma\Gamma^1}_{ll^1mm^1}$, $c_k^{\Gamma\Gamma^1}$ and $d_\mu^{\Gamma^1}$ are determined from a stationary principle.

The Kohn variational principle (Kohn, 1948) is invoked to characterise the T-matrix as the stationary value of the functional

$$\left[T^{\Gamma\Gamma^1}\right] = T^{\Gamma\Gamma^1} - 2\langle \Psi_\Gamma | \hat{H} - E\hat{1} | \Psi_{\Gamma^1} \rangle \tag{2.51}$$

The method has been successfully applied to calculate electron scattering by NF_3 (Rescigno, 1995), NH_3 (Rescigno et al., 1992) and methanoic acid (Trevisan et al., 2006). In the case of methane (chapter 9) we compare our results with those obtained applying this principle (Gil et al., 1994).

2.7.2 Schwinger Multichannel Method

The Schwinger multichannel (SMC) method (Takatsuka and McKoy, 1981, 1984) employs a variational approach to obtaining the multichannel scattering amplitude (equation (2.12) of Takatsuka and McKoy (1984)). Its computation requires knowledge of the Green's function matrix elements and the electron-molecule interaction method itself. Winstead and McKoy (2000) have said that computation of the Green's function matrix elements are the most difficult and computationally-intensive part of the calculation; the advantage of the method is that all matrix elements, including those of the Green's function, involve the electron-molecule interaction which vanishes at large radial distances. In contrast in the complex Kohn variation and R-matrix method no boundary

conditions have to be satisfied by a trial wavefunction since this is the purpose of the Green's function.

The SMC method has also been successfully applied to a number of molecules including a study of the water molecule (Khakoo et al., 2008, 2009), pryazine (Winstead and McKoy, 2007) and uracil (Winstead and McKoy, 2006). Details of their theoretical models may be found in the literature.

Chapter 3

The *ab initio* R-matrix method

3.1 Introduction

The R-matrix method was first introduced by Wigner (1946) and Wigner and Eisenbud (1947) to study nuclear reactions dominated by the formation of a compound state. The method involves the division of configuration space into two distinct regions: the internal region contains the compound nucleus and the external region corresponds to the various possible reactions (or channels) prior to and after the reaction. In the early 1970s the method was extended to treat a number of atomic processes including electron-atom scattering by Burke et al. (1971), Robb (1972) and Burke (1973) and electron-molecule scattering by Schneider (1975) and Schneider and Hay (1976). Their ideas were developed further by Burke et al. (1977) to treat electron-diatomic scattering and by Morgan et al. (1997) to treat scattering by polyatomic systems. Comprehensive review articles on the theory were published by Lane and Thomas (1958) for nuclear reaction theory, and recently by Burke and Tennyson (2005) for electron-molecule scattering and Burke et al. (2007) for atomic, molecular and optical processes.

The UK R-matrix package has been widely applied to calculate electron scattering for a number of species, charged and neutral. They include the close-coupling (CC) studies of ozone O_3 (Gupta and Baluja, 2005), F_2O (Gupta and Baluja, 2006) and NH_3 (Munjal and Baluja, 2006), the static-exchange-plus-polarisation (SEP) study of HBr (Fandreyer et al., 1993), and the cations H_3^+ and H_3O^+ (Faure and Tennyson, 2002) also at the close-coupling level. Recently the package was extended to treat water dimer scattering (Bouchiha et al., 2008; Caprasecca et al., 2009), much larger systems (uracil, Dora et al. (2009)), intermediate-energy scattering using pseudo states (MRMPS) (Gorfinkiel

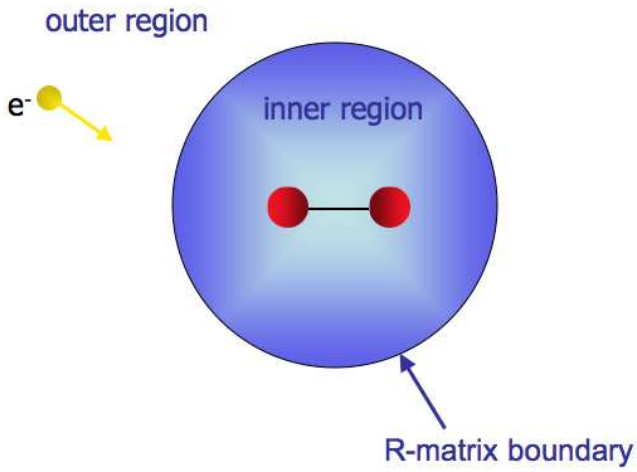

Figure 3.1: Partition of configuration space in fixed-nuclei R-matrix theory

et al., 2005) and positron scattering (Tennyson, 1986; Baluja et al., 2007).

As well as from the Schrödinger equation, the R-matrix has been derived for the relativistic case from the Dirac equation, modified using a Bloch operator, by Halderson (1988).

Adiabatic R-matrix theory is based on the partition of coordinate space into an internal region and an external region separated by a spherical boundary of radius a. In the internal region, the short-range electron exchange and electron-electron correlation effects between the scattering electron and the N target electrons are dominant and the $(N + 1)$-collision complex behaves in a similar way to a bound state. Hence a configuration interaction expansion similar to molecular quantum chemistry calculations is used to determine the $(N + 1)$-inner region scattering eigenkets. In the outer region the electron is assumed to propagate in the multipole potential of the target and the short-range forces so dominant in the inner region are assumed to be negligible, and a single-centre expansion of the scattering wavefunction is employed. Thus it is possible to reduce the scattering problem to a set of coupled ordinary differential equations which are much easier to solve.

In the discussion that follows the fixed-nuclei approximation is employed, with the origin coincides with the molecule's centre of mass.

3.2 Scattering By a Potential Well

We begin by demonstrating a simple application of the R-matrix method to scattering of a particle by a potential well (Lane and Thomas, 1958):

$$V(r) = \begin{cases} V_0, & r \leq a \\ 0, & r > a \end{cases} \tag{3.1}$$

with $V_0 < 0$ and imposing the zero logarithmic boundary condition on the radial part of the total wavefunction

$$\frac{a}{f_l(a)} f_l'(a) = 0 \tag{3.2}$$

The problem will be solved using spherical polar co-ordinates.

3.2.1 The Inner Region

The time-independent Schrödinger equation for the inner region is

$$-\frac{1}{2}\nabla^2\psi + V_0\psi = E\psi \tag{3.3}$$

Let $\psi = \frac{f_l(r)}{r} Y_l^m(\theta, \phi)$. Substitution into equation (3.3) yields:

$$-\frac{1}{2}\left\{\frac{1}{r^2}\left(\frac{d}{dr} r^2 \frac{d(r^{-1}f_l)}{dr}\right) Y_l^m - \frac{l(l+1)}{r^2}\frac{f_l}{r} Y_l^m\right\} - (E - V_0)\frac{f_l}{r} Y_l^m = 0 \tag{3.4}$$

since $\nabla^2 Y_l^m = -l(l+1)Y_l^m$. Then multiplying on the right by Y_l^{m*} and integrating both sides with respect to Ω ($d\Omega = \sin\theta d\theta d\phi$) gives

$$-\frac{1}{2}\left[\frac{1}{r^2}\left(\frac{d}{dr} r^2 \frac{d(r^{-1}f_l)}{dr}\right) - \frac{l(l+1)}{r^2}\frac{f_l}{r}\right] - (E - V_0)\frac{f_l}{r} = 0 \tag{3.5}$$

Then multiplying by $-2r^3$ and evaluating the derivative term yields

$$r^2 f_l'' - l(l+1)f_l + (Kr)^2 f_l = 0 \tag{3.6}$$

where $K^2 = 2(E - V_0)$. Let $u = Kr$. After some algebra it may be shown that

$$u^2 \frac{d^2 f_l}{du^2} + [u^2 - l(l+1)]f_l = 0 \tag{3.7}$$

the solution to which is the spherical Riccati-Bessel function $\hat{j}_l(Kr)$.

Appealing to the standard definition, the R-matrix for the l^{th} partial wave and arbitrary logarithmic boundary condition b

$$R_l = \frac{f_l(a)}{a[f_l'(a) - ba^{-1}f_l(a)]} \tag{3.8}$$

$$= \frac{\hat{j}_l(Ka)}{a[K\hat{j}_l'(Ka) - ba^{-1}\hat{j}_l(Ka)]} \tag{3.9}$$

3.2.2 The External Region

By matching to the asymptotic boundary condition

$$f_l(r) \sim \hat{h}_l^-(kr) - s_l(k)\hat{h}_l^+(kr) \tag{3.10}$$

using

$$\frac{f_l'(a)}{f_l(a)} = \frac{1 + bR_l}{aR_l} \tag{3.11}$$

where $\hat{h}_l^{\pm}$ are out-going and incoming Riccati-Hankel functions respectively, the S-matrix can be shown to be

$$s_l(k) = \frac{\hat{h}_l^-(ka) + bR_l\hat{h}_l^-(ka) - kaR_l\hat{h}_l^{-\prime}(ka)}{\hat{h}_l^+(ka) + bR_l\hat{h}_l^+(ka) - kaR_l\hat{h}_l^{+\prime}(ka)} \tag{3.12}$$

- $l = 0$ and $b = 0$:

  Using

  $$\hat{j}_0(z) = \sin z \tag{3.13}$$

  $$\frac{d\hat{j}_0(z)}{dz} = \cos z. \tag{3.14}$$

  substitution into the equation (3.9) for R_l yields

  $$R_0 = \frac{\tan Ka}{Ka} \tag{3.15}$$

  Here the poles of this matrix E_n are easily determined by imposing the zero-logarithmic (or zero-derivative) boundary condition (3.2)

  $$af_l'(a) = 0 \tag{3.16}$$

  $$Ka\cos Ka = 0, \tag{3.17}$$

which implies that

$$\cos Ka = 0 \Rightarrow Ka = \left(n - \frac{1}{2}\right)\pi \tag{3.18}$$

squaring both sides:

$$(Ka)^2 = \left[\left(n - \frac{1}{2}\right)\pi\right]^2 \tag{3.19}$$

$$K^2 = 2(E - V_0) = \left[\left(n - \frac{1}{2}\right)\frac{\pi}{a}\right]^2 \tag{3.20}$$

and therefore

$$E_n = \tfrac{1}{2}\left[\tfrac{\pi}{a}\left(n - \tfrac{1}{2}\right)\right]^2 + V_0 \quad n > 0 \tag{3.21}$$

In solving for the S-matrix we take the Ricatti-Hankel functions to be

$$\hat{h}_0^{\pm}(z) = e^{\pm iz} \tag{3.22}$$

Then, using equation (3.12)

$$s_0(k) = \exp\left[2i\left(\arctan\left[\frac{k}{K}\tan Ka\right] - ka\right)\right] \tag{3.23}$$

and by comparing to the standard definition

$$s_l(k) = e^{2i\delta_l(k)} \tag{3.24}$$

the s-wave phase shift is found to be

$$\delta_0 = \arctan\left(\frac{k}{K}\tan Ka\right) - ka \tag{3.25}$$

- $l = 1$ and $b = 0$:

  Here we take

$$\hat{j}_1(z) = \frac{\sin z}{z} - \cos z \tag{3.26}$$

$$\frac{d\hat{j}_1(z)}{dz} = \frac{z\cos z - \sin z}{z^2} + \sin z \tag{3.27}$$

to obtain

$$R_1 = \frac{\sin Ka - Ka\cos Ka}{(Ka)^2 \sin Ka + Ka\cos Ka - \sin Ka} \tag{3.28}$$

For the Riccati-Hankel functions

$$\hat{h}_1^{\pm}(z) = \left(1 \pm \frac{i}{z}\right) e^{\pm i\left(z - \frac{\pi}{2}\right)} \tag{3.29}$$

substitution of this and its derivative into equation (3.12) yields

$$s_1 = \exp\left\{2i\left[\arctan\left(\frac{(ka)^2 R_1 - R_1 - 1}{ka(1+R_1)}\right) - ka + \frac{\pi}{2}\right]\right\} \tag{3.30}$$

3.3 The Internal Region for Multichannel Electron-Molecule Scattering

The scattering process is described by the time-independent Schrödinger equation

$$\hat{H}_{N+1}|\Psi\rangle = E|\Psi\rangle \tag{3.31}$$

where $\hat{H}_{N+1}$ is the molecular Hamiltonian operator:

$$\hat{H}_{N+1} = \sum_{i=1}^{N+1}\left(-\frac{1}{2}\nabla_i^2 - \sum_A \frac{Z_A}{r_{iA}}\right) + \sum_{i>j=1}^{N+1}\frac{1}{r_{ij}} + \sum_{A>B}\frac{Z_A Z_B}{|\vec{r_A} - \vec{r_B}|} \tag{3.32}$$

The solution to equation (3.31) in the internal region is of the form:

$$|\Psi\rangle = \sum_k A_{Ek}|\psi_k\rangle \tag{3.33}$$

where $|\psi_k\rangle$ are energy-independent complete basis kets. Since a finite volume is being considered non-Hermitian surface terms (due to the kinetic energy operator) appear at the interaction radius (see appendix A). There are two ways of regaining Hermicity– one is to impose boundary conditions upon each eigenfunction or to modify the Hamiltonian operator. For the latter option, a Bloch operator is introduced (appendix A):

$$\hat{L}_{N+1} = \sum_{i=1}^{N+1}\delta(r_i - a)\left(\frac{d}{dr_i} - \frac{b}{r_i}\right) \tag{3.34}$$

The spherical boundary a is chosen so as to fully contain the electron charge cloud of the molecule. The eigenbases $|\psi_k^{\Delta}\rangle$ are now such that:

$$\langle\psi_k^\Delta|\hat{H}_{N+1}+\hat{L}_{N+1}|\psi_{k'}^\Delta\rangle = E_k\delta_{kk'} \tag{3.35}$$

where Δ represents the constants of the motion which correspond to the irreducible representation of the point group of the molecule.

We are now in a position to derive the multi-channel R-matrix R_{ij}^Δ. The procedure adopted here is the derivation of the appropriate Green's theorem as described by Lane and Thomas (1958).

3.3.1 Derivation of the R-matrix

Equation (3.31) is solved for a fixed geometry and for each scattering symmetry by re-writing as follows

$$(\hat{H}_{N+1}+\hat{L}_{N+1}-E\hat{1})|\Psi^\Delta\rangle = \hat{L}_{N+1}|\Psi^\Delta\rangle \tag{3.36}$$

which has a formal solution

$$|\Psi^\Delta\rangle = (\hat{H}_{N+1}+\hat{L}_{N+1}-E\hat{1})^{-1}\hat{L}_{N+1}|\Psi^\Delta\rangle \tag{3.37}$$

Appealing to the eigenket completeness theorem:

$$\sum_k |\psi_k^\Delta\rangle\langle\psi_k^\Delta| = \hat{1} \tag{3.38}$$

$$|\Psi^\Delta\rangle = \sum_{k,k'} |\psi_k^\Delta\rangle\langle\psi_k^\Delta|(\hat{H}_{N+1}+\hat{L}_{N+1}-E\hat{1})^{-1}|\psi_{k'}^\Delta\rangle\langle\psi_{k'}^\Delta|\hat{L}_{N+1}|\Psi^\Delta\rangle \tag{3.39}$$

$$= \sum_{k,k'} \frac{|\psi_k^\Delta\rangle\langle\psi_{k'}^\Delta|\hat{L}_{N+1}|\Psi^\Delta\rangle}{E_k-E}\delta_{kk'} \tag{3.40}$$

$$= \sum_k \frac{|\psi_k^\Delta\rangle\langle\psi_k^\Delta|\hat{L}_{N+1}|\Psi^\Delta\rangle}{E_k-E} \tag{3.41}$$

Comparing equation (3.41) to equation (3.33) it is clear that

$$A_{Ek} = \frac{\langle\psi_k^\Delta|\hat{L}_{N+1}|\Psi^\Delta\rangle}{E_k-E} \tag{3.42}$$

The channel basis functions $|\psi_i^N Y_{l_i}^{m_i}\rangle$ constitute a complete basis set and the Bloch operator may therefore be expanded in terms of these:

$$\frac{1}{2}\sum_{i=1}^{N+1}\sum_{j=1}|\psi_j^N Y_{l_j}^{m_j}\rangle\delta(r_i-a)\left(\frac{d}{dr_i}-\frac{b}{r_i}\right)\langle\psi_j^N Y_{l_j}^{m_j}| \tag{3.43}$$

Now let us define the reduced radial function

$$F_j(a)=\langle\psi_j^N Y_{l_j}^{m_j}|\Psi^\Delta\rangle, \tag{3.44}$$

the (energy-independent) surface amplitudes

$$w_{jk}^\Delta(a)=\langle\psi_j^N Y_{l_j}^{m_j}|\psi_k^\Delta\rangle \tag{3.45}$$

and

$$w_{jk}^\Delta(a)^\dagger=\langle\psi_k^\Delta|\psi_j^N Y_{l_j}^{m_j}\rangle \tag{3.46}$$

Substituting (3.43) into (3.42) one obtains

$$A_{Ek}=\frac{1}{2}\sum_{j=1}\frac{(w_{jk}^\Delta(a))^\dagger\left(F_j'(a)-ba^{-1}F_j(a)\right)}{E_k-E} \tag{3.47}$$

The integrations represented by the Dirac bra-ket notation are carried out over all $N+1$ electronic spin-space co-ordinates in the internal region except the radial co-ordinate of the scattered electron.

Hence the total wavefunction Ψ^Δ can be simplified to

$$\Psi^\Delta=\frac{1}{2}\sum_{k,j}\frac{w_{jk}^\Delta(a)^\dagger\left(F_j'(a)-ba^{-1}F_j(a)\right)}{E_k-E}\psi_k^\Delta \tag{3.48}$$

Projecting (3.48) onto the channel ket $|\psi_i^N Y_{l_i}^{m_i}\rangle$ and evaluating the bra-ket at the boundary of the internal region $r=a$, the R-matrix may then be determined:

$$R_{ij}^\Delta(E)=\frac{1}{2a}\sum_k\frac{w_{ik}^\Delta(a)(w_{jk}^\Delta(a))^\dagger}{E_k-E} \tag{3.49}$$

The R-matrix essentially contains information on the surface value and derivative matching boundary condition to be satisfied by the scattering wavefunction. It provides the boundary condition for the Schrödinger equation appropriate for the outer region. The precise structure of the trial wavefunction employed by the UK R-matrix package (Morgan et al., 1998) to represent $|\psi_k^\Delta\rangle$ is discussed below.

3.3.2 The Trial Inner Region Scattering Wavefunction

The following close-coupling trial wavefunction is implemented in the inner region

$$\psi_k^{\Delta}(\mathbf{X}_{N+1};R) = \hat{A}\sum_{i=1}\sum_{j=1} a_{ijk}^{\Delta}\Phi_i^{\Delta}(\mathbf{X}_N;\hat{\mathbf{r}}_{N+1}\sigma_{N+1})\eta_{ij}^0(\mathbf{x}_{N+1}) + \sum_{l=1}\chi_l^{\Delta}(\mathbf{X}_{N+1})b_{lk}^{\Delta} \quad (3.50)$$

where $\mathbf{X}_{N+1} = \{\mathbf{x}_i\}_{i=1}^{N+1}$ and $\mathbf{x}_i = \mathbf{r}_i\sigma_i$ is the spin-space co-ordinate of the i^{th} electron. The channel wavefunctions Φ_i^{Δ}, the continuum orbitals η_{ij}^0 and square integrable functions χ_i^{Δ} depend parametrically on the geometry R, and $\hat{A}$ is the antisymmetrisation operation which is applied to ensure that the wavefunction is antisymmetric with respect to interchange of any two electrons.

Φ_i^{Δ} are formed from fixed-nuclei electronic target states spin-coupled to the angular and spin functions of the scattering electron (see above). In the polyatomic suite these channel functions and the quadratically integrable functions χ_i^{Δ} are constructed from GTOs (Gaussian-type orbitals) centred on the nuclei. The target electronic wavefunctions can be represented using the elaborate CI expansion technique or the basic Hartree-Fock method.

The first summation runs over the electronic target states. It represents a situation where one electron exists in the continuum states, with the remaining N electrons remaining in the target state, and is known as a 'target+continuum' configuration.

The continuum orbitals are constructed from continuum basis functions, which take the form $f_{il_i}(\mathbf{r}) = \frac{1}{r}u_{il}(r)Y_{l_i}^{m_i}(\theta,\phi)$, and target molecular virtual orbitals. Initially, the radial wavefunction u_{il} is numerically generated as a solution of a second order ordinary differential equation:

$$\left[\frac{d^2}{dr^2} - \frac{l(l+1)}{r^2} + 2V_0(r) + k_i^2\right] u_{il}(r) = 0 \quad (3.51)$$

u_{il} is based on expansions of GTOs (Faure et al., 2002; Morgan et al., 1997) and subject to boundary conditions at $r = 0$ and $r = a$:

$$u_{ij}(0) = 0 \quad (3.52)$$

$$\frac{a}{u_{ij}(a)}u'_{ij}(a) = b \quad (3.53)$$

Then, in order to obtain $\eta_{il_i}^0(\mathbf{r}_{N+1})$, the functions $\{f_{il}\}$ are first orthogonalised to the target molecular orbitals using Schmidt orthogonalisation and then amongst themselves us-

ing Löwdin orthogonalisation to remove linearly dependent functions (Tennyson, 2010).

In the polyatomic R-matrix package the above logarithmic boundary condition is *not* imposed; instead, as discussed above, the second option of modifying the operator is adopted. The logarithmic boundary condition is, however, imposed in the diatomic R-matrix package and results in slow convergence of the R-matrix expansion (equation (3.49)). The diatomic code thus adds a 'Buttle' correction (Buttle, 1967) to the diagonal elements of the R-matrix. There is no such problem or implementation in the polyatomic suite.

The second summation in equation (3.50) runs over the χ_i^Δ configurations where all the electrons occupy the target molecular orbitals. Since the molecular orbitals are mutually orthogonal, these L^2 functions are required to guarantee that important regions of configuration space are included. These configurations also account for correlation effects including virtual excitation to higher electronic states excluded from the first summation.

Finally, the coefficients a_{ijk}^Δ and b_{lk}^Δ in equation (3.50) are obtained by diagonalising the operator $\hat{H}_{N+1} + \hat{L}_{N+1}$ in the basis of the internal region $|\psi_k^\Delta\rangle$ (equation (3.35)).

It can be shown that the operator $\hat{H}_{N+1}+\hat{L}_{N+1}$ is Hermitian in the basis of quadratically integrable functions satisfying arbitrary boundary conditions at $r = a$. The Hamiltonian matrix elements in equation (3.35) can be evaluated using standard molecular quantum chemistry packages modified to carry out the radial integrals over a finite range and to treat continuum orbitals in addition to GTOs and STOs. However, it is possible to exploit the structure of the trial wavefunction given by equation (3.50) to enhance the efficiency of the scattering calculation (Tennyson, 1996*a*).

In the polyatomic code the continuum orbitals are employed to calculate the R-matrix surface amplitudes of equation (3.45):

$$w_{ik}^\Delta(a) = \sum_{j=1} \eta_{ij}^0(a) a_{ijk}^\Delta \tag{3.54}$$

3.4 The Outer Region for Multichannel Electron-Molecule Scattering

3.4.1 Equations of motion

In the external region the interaction radius is chosen so that the short-range electron exchange and electron-electron correlation effects between the scattered electron and the target electrons vanish. The outer region wavefunction is expanded in the basis of the channel functions $\psi_i^N Y_{l_i}^{m_i}$, which are eigenfunctions of the Hamiltonian describing the projectile and scatterer when they are not interacting:

$$\Psi^{\Delta}(\mathbf{X}_{N+1}) = \sum_{i=1} \psi_i^N Y_{l_i}^{m_i} \frac{F_i^{\Delta}(r_{N+1})}{r_{N+1}} \tag{3.55}$$

The wavefunctions ψ_i^N are formed by coupling the scattered electron spin σ_{N+1} to a fixed-nuclei target state Φ_i^N. Since the scattered electron and target electrons occupy two distinct regions the antisymmetrisation operator is omitted and the L^2 or quadratically integrable functions χ_i^{Δ} vanish in the outer region. The scattered electron may then be represented by single-centre reduced radial wavefunctions $F_i^{\Delta}(r_{N+1})$. Substitution into equation (3.31) and projecting both sides onto the channel basis leads to a set of coupled second order ordinary differential equations that are satisfied by the reduced radial wavefunctions (appendix B):

$$F_{\lambda}^{\Delta\prime\prime} - \frac{l_\lambda(l_\lambda+1)}{r_{N+1}^2} F_\lambda^{\Delta} + 2(E-E_\lambda)F_\lambda^{\Delta} = 2\sum_{\lambda'} V_{\lambda\lambda'} F_{\lambda'}^{\Delta} \tag{3.56}$$

The radial wavefunctions are then matched to the asymptotic boundary condition, via the R-matrix, to yield the S-matrix from which the other important scattering quantities and observables may be determined. In order to fully specify the S- (K- or T-) matrix one requires all linearly independent reduced radial wavefunctions (Burke et al., 1971).

The system of equations (3.56) are solved over the range $[a, a_p]$ where the boundary $r = a_p$ interfaces the external and asymptotic regions. The differential equations are subject to the boundary conditions at the interaction radius a,

$$F_i^{\Delta}(a) = \sum_j R_{ij}^{\Delta} \left(a F_j'(a) - b F_j(a) \right) \tag{3.57}$$

and equation (3.49) (Burke et al., 2007). This may be done using a number of standard methods (e.g. Burke and Seaton (1971)). In R-matrix propagation techniques, the R-

matrix calculated at $r = a$ may be propagated from there by subdividing the external region into p sub-regions. Within each sub-region $[a_{i-1}, a_i]$, the reduced radial wavefunction is expanded in a basis of shifted Legendre polynomials (Baluja et al., 1982). Applying this method, the R-matrix is determined on the boundary of the external region, at a_p. Having determined the R-matrix on the subregion boundaries a_i, the reduced radial wavefunction may be obtained across each sector. The boundary a_p is chosen to be large enough that the solution to the coupled differential equations may be accurately represented by the asymptotic boundary condition for open channels

$$F_{ij}^{\Delta} \sim \frac{1}{\sqrt{k_i}} \left[\sin\left(k_i r - \frac{l_i \pi}{2}\right) \delta_{ij} + \cos\left(k_i r - \frac{l_i \pi}{2}\right) K_{ij}^{\Delta} \right] \tag{3.58}$$

for in-channel i and out-channel j and

$$F_{ij}^{\Delta} \sim e^{-|k_i| r} \tag{3.59}$$

for closed ones. The $n_o \times n_o$ K-matrix may then be determined by matching to the open channel asymptotic boundary condition, where n_o is the number of open channels at each incident energy inside the range being considered. The multichannel S- and T-matrices are defined:

$$\mathbf{S}^{\Delta} = (1 + i\mathbf{K}^{\Delta})(1 - i\mathbf{K}^{\Delta})^{-1} \tag{3.60}$$

$$\mathbf{T}^{\Delta} = \mathbf{S}^{\Delta} - \mathbf{1} = (2i\mathbf{K}^{\Delta})(1 - i\mathbf{K}^{\Delta})^{-1} \tag{3.61}$$

From the T-matrix the excitation cross section for electronic transition $i \rightarrow i'$ is written as

$$\sigma(i \rightarrow i') = \frac{\pi}{k_i^2} \sum_{\Delta} \frac{2S+1}{2(2S_i+1)} \sum_{l_\lambda m_\lambda l_{\lambda'} m_{\lambda'}} |T_{\lambda\lambda'}^{\Delta}|^2 \tag{3.62}$$

The importance of the K-matrix in multichannel scattering is its connection to the eigenphase sum, which can provide information on resonance phenomena and Ramsauer-Townsend minima. The K-matrix is initially diagonalised to yield a new matrix $\mathrm{diag}(K_1^{\Delta}, K_2^{\Delta}, \ldots, K_{n_o}^{\Delta})$. The arctangent of the diagonal elements are summed over the channels retained in the outer region to yield a quantity analogous to the phase shift of potential scattering, the multichannel eigenphase sum:

$$\eta^{\Delta}(E) = \sum_i \arctan K_i^{\Delta} \tag{3.63}$$

3.4.2 Electron Scattering by Polar Molecules

For very polar molecules (large dipole moment μ) the $\frac{\mu P_1(\cos\theta)}{r_{N+1}^2}$ term decays very slowly. Consequently additional partial waves (here $l > 4$) must be retained in order to converge the integral cross sections. The dipole potential may be treated, for large radial distance, using first-order Born correction (Clark, 1977) (at the T-matrix, cross section or scattering amplitude level) for high l-scattering, with the lower partial waves included via some accurate scattering theory (R-matrix) since the approximation does not fully account for short-range interactions between the electron and the scatterer. For shorter distances one has to transform to the laboratory frame as the potential transfers angular momentum outside the validity of the Born-Oppenheimer approximation, so the body-fixed frame is no longer appropriate (Clark, 1977).

The theoretical treatment of electron scattering by polar molecules is particularly interesting and has been studied by a number of workers including Altshuler (1957) and Mittleman and von Holdt (1965), by Garrett (1972), Rudge et al. (1976), Dickinson and Richards (1975), Collins and Norcross (1978) and Fabrikant (1980). A comprehensive review article on the subject was published by Itikawa (1978).

The basic model initially considered scattering by a stationary dipole. A major finding for scattering using this model was made by Turner and Fox (1966), who observed the existence of a minimum dipole moment (0.6393 a.u.) required for electron binding. Their model represented a dipole by charges $\pm q$ separated by a distance R, namely the finite dipole model. This minimum was also independently observed by Mittleman and Myerscough (1966), Lévy-Leblond (1967), Crawford and Dalgarno (1967) and Coulson and Walmsley (1967). But, Garrett (1970) and Garrett (1971) stated that any realistic model of electron scattering by a polar molecule should include the molecular rotational motion (in the laboratory co-ordinate frame). He showed that if it is indeed taken into account, a finite number of stable bound states are still possible, whereas there are infinitely many bound states in the case of a fixed dipole, that the critical dipole is sensitive to the molecule's moment of inertia I and total angular momentum J, and the charge separation. Indeed, as the moment of inertia tends to infinity, Garrett (1970) and Garrett (1971) demonstrated that this dipole moment for the rotating system converges, slowly, to the corresponding value for the fixed dipole.

Studies of electron-impact rotational excitation by the polar molecules HCl and CN were carried out by Itikawa and Takayanagi (1969) using the close-coupling (CC) method.

In addition, as a test, they compared the CC dipole-allowed rotational excitation cross section $\sigma(0 \rightarrow 1)$ to that obtained using the Born approximation: the latter was found to be as reliable in producing rotation cross sections for polar systems (see figures 3 and 6 of their paper). We carried a similar exercise for the $J = 0 - 1$ and $J = 1 - 2$ transitions in chapter 7 and came to the same conclusion. However, Itikawa and Takayanagi (1969) mentioned that for large dipole moments, the coupling between the molecular rotation and the projectile electron is strong, so for close encounters the Born correction is not necessarily reliable.

Similar studies on linear cations (CH^+) were carried out by Chu and Dalgarno (1974) who also included the rotational motion of the molecule.

Finally, an entirely different semi-classical perturbation approach was taken by Dickinson and Richards (1975) and Dickinson (1977) to calculate rotational excitation integral and differential cross sections for the polar CsF, CsCl and KI molecules. They reported good agreement with beam experiments on these diatomics at higher electron energies and with the close-coupling and Glauber calculations.

In terms of interesting phenomena Bottcher (1970), Bottcher (1971) and Itikawa (1978) have predicted and commented on the appearance of resonance phenomena respectively. A much more detailed study on rotational Feshbach resonances was carried out by Garrett (1975), who considered the problem of electron scattering by a dipolar system below the first rotational excitation threshold, using the finite dipole model mentioned above with $R = 0.667\ a_0$. In this energy region he suggested that they must be Feshbach-type (Feshbach, 1962) rotational resonances, or shape resonances. According to Garrett (1975) the existence of a Feshbach resonance is guaranteed for certain choices of the moment of inertia, dipole strength and electron energy. His model study also found that, associated with a given critical moment, a rotational Feshbach resonance can occur in a system whose dipole moment lies with a certain range of the critical value. Experimentally, Rohr and Linder (1976) confirmed the existence of threshold resonances in the vibrational excitation of the polar molecules HCl, HF and H_2O which have dipole moments comparable to or larger than the above-mentioned critical value. They commented that these threshold resonances seem to be characteristic of polar molecules. The experimental data of Frey et al. (1995) suggested that resonances associated with dipole-supported states can be important in electron-polar molecule scattering at ultra-low energies.

Research in this area still continues (Thummel et al., 1992; Gómez-Camacho et al., 1998).

3.4.3 Multichannel Resonances

Resonances are particularly interesting features in scattering theory generally. In their most basic form they appear as 'bumps' in the cross sections, and are characterised by a position E_r and a width Γ_r, the latter of which arises from the Heisenberg Uncertainty Principle.

Resonances correspond, under certain conditions, to poles of the S-matrix in the unphysical sheet. A detailed discussion of this (and multichannel bound states) may be found in Taylor (2006) and Mosinsky (1953). In the vicinity of this pole the eigenphase sum η^{Δ} undergoes a rapid increase by π radians. The parameters of a resonance can be obtained by fitting to the Breit-Wigner formula (Breit and Wigner, 1936)

$$\eta^{\Delta}(E) = \eta^{\Delta}_{bg} + \eta^{\Delta}_{res} \tag{3.64}$$

$$= \eta^{\Delta}_{bg}(E) + \arctan \frac{\Gamma_r}{E_r - E} \tag{3.65}$$

where $\eta_{bg}(E)$ is the background phase.

In terms of classification, there are three resonance types: *shape*, *core-excited* and *nuclear-excited* resonances. Shape and core-excited resonances are observed in electron-atom and electron-molecule scattering; nuclear-excited resonances are only observed in electron-molecule scattering.

Shape resonances have the molecular electronic ground state as their parents. They occur when the electron is trapped by the centrifugal barrier and the attractive polarisation of the molecule. The latter influences the width (life-time) of the resonance which is usually large (short). Shape resonances cannot occur therefore for s-wave scattering. As molecular bond lengths are increased the shape resonance can become bound as the position decreases and moves to the negative real axis of the energy complex plane, and the width decreases to zero. In the R-matrix theory a bound state is usually indicated by an R-matrix pole E^{Δ}_k that is slightly lower than the ground state energy. A clear demonstration of this phenomenon is given in chapters 7 and 8 for SiO and CS respectively.

Core-excited resonances (Feshbach, 1958, 1962) in contrast have (electronically) excited target states as their parents, consisting of a hole in a normally occupied orbital and

two electrons in normally unoccupied (virtual) orbitals. Depending upon whether they lie below or above their parent states they may be classified as Feshbach or core-excited shape resonances respectively.

Feshbach or closed-channel resonances are associated with parent states that exhibit a positive electron affinity. They are normally found below the excitation threshold of their parent state and so decay to lower-lying excited states. Such resonances are usually very narrow or, equivalently, have a long life-time. Fraser and Burley (1982) developed an analytical model, aimed at students of scattering theory, involving scattering by a Dirac delta potential to re-produce a Feshbach resonance. An important feature of this problem is the discontinuity in the radial wavefunction at the boundary. Nevertheless they were able to obtain the S-matrix and phase shifts from which they probed the important features.

A core-excited shape resonance, associated with parents of negative electron affinity, is found lying above its parent state and can therefore decay back to its parent state or lower-lying ones.

Finally, a nuclear-excited resonance occurs only for molecules. Narrow and with a very low resonance energy, they occur when the $N+1$-complex has a weakly bound state. In this case the nuclear excitation is vibrational excitation or nuclear motion rather than the excitation of a nucleus. Such resonances appear when the scatterer is a cation and can only be examined by going beyond the Born-Oppenheimer approximation.

In the UK molecular R-matrix codes RESON (Tennyson and Noble, 1984) is employed to first detect and then fit those resonances. It does give good results for isolated resonances that are away from channel thresholds. However, detection and fitting becomes more complicated for closely-spaced resonances. As the size of the energy interval being fitted increases the assumptions to be made concerning the variation of the background eigenphase polynomial with respect to energy introduce uncertainties. A general approach is complicated by the fact that the polynomial representation is not applicable near excitation thresholds (Noble et al., 1993). Instead, Noble et al. (1993) considered multichannel resonances in complex energy R-matrix theory, where the R-matrix is allowed to take complex energy values, and then determined the zeroes of a descrepancy function $d(E)$ (equation 22 of their paper) to extract the resonances and bound states i.e. the S-matrix poles. Their approach yielded many more narrow resonances than methods using a fitting procedure. Overlapping resonances and double poles can also

Λ_0	m_{l_i}	Λ_s
	0	$^2\Sigma^+$
$^2A_1$	2	$^2\Delta$
	4	$^2\Gamma$
	1	$^2\Pi$
$^2B_1$		
	3	$^2\Phi$

Table 3.1: Rule for transforming a C_{2v} T-matrix of symmetry Λ_0 to a $C_{\infty v}$ one with symmetry Λ_s

be detected; this approach is not used in the UK molecular R-matrix codes.

3.4.4 T-matrix transformations

In this thesis electron scattering calculations for linear systems with an X $^1\Sigma^+$ ground state were carried out in C_{2v}– the highest Abelian sub-group of the natural group $C_{\infty v}$. In the course of this study, we sought to compute the rotationally-resolved differential cross sections and rotationally inelastic integral cross sections for electronically elastic scattering in the natural symmetry.

Initially the fixed-nuclei (FN) C_{2v} T-matrices had to be transformed to $C_{\infty v}$. Since the Hamiltonian for linear molecules has $C_{\infty v}$ symmetry, the group elements g commute with the Hamiltonian:

$$g\hat{H}\tilde{g} = \hat{H} \quad \forall g \in C_{\infty v} \tag{3.66}$$

Specifically, the group element corresponding to infinitesimal rotation about the z axis commutes with $\hat{H}$ hence the z-projection of the angular momentum $\Lambda_{t,s}$ is a constant of the motion for both the N- and $N+1$-molecular Hamiltonian respectively. Therefore in order to obtain a T-matrix in the $C_{\infty v}$ representation from the C_{2v} one merely extracts those T-matrix elements with $m_{l_i} = \Lambda_s$ ($\Lambda_t = 0$ for Σ^+ ground state targets). The rule for the transformation is given in table 3.1.

3.5 Additional Scattering Quantities Required in Astrophysics

In chapters 6, 7 and 10 of this thesis rotational integral cross sections were computed in order to obtain rotational and hyperfine (de)-excitation rate coefficients, so the underlying theory is discussed. As tests to confirm the accuracy of the theoretical models, we also computed the rotationally resolved differential cross sections.

3.5.1 Rotational Cross sections

Electron scattering calculations considered here invoked the fixed-nuclei (FN) approximation (Lane, 1980). In this approach, the cross sections are expressed as a partial-wave expansion within the ANR (adiabatic-nuclei-rotation) approximation, which assumes that the initial and final rotational states are degenerate. For low partial waves (here taken to be $l \leq 4$) the cross section is computed from the FN T-matrices yielded from the R-matrix method. For the dipole-forbidden transitions (those with $\Delta J > 1$), cross sections are expected to converge rapidly and can be evaluated using the FN T-matrices alone. For dipole-allowed transitions ($\Delta J = 1$) however, the partial-wave expansion does not converge due to the long-range nature of the dipole moment. To circumvent this problem, the standard procedure is to use the dipole Born correction to account for contributions due to the higher partial waves otherwise not included in the FN T-matrices (Crawford and Dalgarno, 1971). The final cross section is calculated as the sum of two contributions and may be regarded as a 'short-range' correction to the Born approximation.

The known unphysical behaviour of the FN cross sections near rotational thresholds, inherent in the ANR approximation, is corrected using a simple kinematic ratio (Chang and Temkin, 1970) which forces the excitation cross sections to zero at threshold. In the case of e-H_2 collisions, this procedure has been shown to be accurate down to a collision energy of $E \sim 2 \times \Delta E$ where ΔE is the rotational threshold (Morrison, 1988). Recently, experimental data for the scattering of cold electrons by water also confirmed the validity of the adiabatic 'threshold-corrected' approximation to very low incident electron energies (Faure et al., 2004*b*). Rotational threshold effects are formally incorporated in a full rotational close-coupling calculation, which would be impractical for the collision energies considered in this thesis.

In order to make comparisons with available experimental data, differential cross sections were computed using the Born-closure approach for the multichannel scattering amplitude (Itikawa, 2000) to remedy the slow convergence of the partial-wave expansion. In addition to the formula for rotational excitation Itikawa (2000) also presented formulae for vibrational excitation. Practical calculations applying their formalism include CO_2 (Takekawa and Itikawa, 1998), HCl (Shimoi and Itikawa, 1999) and this thesis (HCN, CO and SiO). In this approach the high partial-waves due to quadrupole and induced-dipole interactions were also included.

3.5.2 Hyperfine Rate Coefficients

The hyperfine interaction arises due to the very weak coupling of the nuclear spin to the molecular rotation, which to an excellent approximation does not affect the overall scattering dynamics. In the laboratory, Ahrens et al. (2002) measured ground state rotational transitions of HCN using sub-Doppler saturation spectroscopy in the THz region. This technique enables features such as hyperfine structures to be revealed, which within Doppler limits, would remain hidden. Nine consecutive rotational transitions with their associated hyperfine structures have been partly resolved. Additional studies include that of Turner (2001): here the transitions $J = 1 \rightarrow 0$ and $2 \rightarrow 1$ were observed for the deuterated molecules N_2D^+, DCN and DNC, from which molecular constants including the nuclear quadrupole hyperfine splitting were derived for these species, which are essential to determine accurate abundances. More recently, the nuclear quadrupole hyperfine structure of HNC was resolved in the laboratory for the first time using millimetre-wave spectroscopy (Bechtel et al., 2006). New rest frequencies for the $J = 1 \rightarrow 0$, $J = 2 \rightarrow 1$ and $J = 3 \rightarrow 2$ rotation transitions of the vibrational ground state were determined. It was found that the hyperfine structure of HNC is dominated by the interaction of the valence shell electrons with the nuclear spin of the nitrogen atom; the hyperfine structure of DNC however, was much more complicated due to the additional coupling of the deuterium nucleus ($I = 1$). This coupling gave rise to a septet in the $J = 1 \rightarrow 0$ transition.

As the hyperfine structure is resolved in some of the astronomical spectra, it is crucial to know the hyperfine excitation rate coefficients among these energy levels. At high resolution it is possible to resolve the hyperfine components arising from the nitrogen ^{14}N nuclear spin from transitions arising from low-lying rotational levels. In this thesis,

for HCN, HNC and their isotopologues, only the nuclear spin I of ^{14}N was considered as the effects of the spins of the H and D atoms on the collision were assumed negligible, although they do affect the energy levels of course. The hyperfine states are labelled by J and F, which is the total angular momentum obtained by coupling J to I ($I = 1$ for ^{14}N) in the usual way. If one assumes the hyperfine levels to be degenerate, then it is possible to considerably simplify the scattering problem (Corey and McCourt, 1983). Within the ANR or IOS (infinite order sudden) approximation (Secrest, 1975; Hunter, 1975) which both ignore the rotational spacings, the scattering equations of motion are simplified further and the rate coefficients among the rotational and hyperfine levels can be calculated simply in terms of 'fundamental' rotational rate coefficients $k^{IOS}(L \to 0)$:

$$k^{IOS}(J \to J') = [J'] \sum_L [L] \begin{pmatrix} J & J' & L \\ 0 & 0 & 0 \end{pmatrix}^2 k^{IOS}(L \to 0) \tag{3.67}$$

$$k^{IOS}(J\ F \to J'\ F') = [J][J'][F'] \sum_L [L] \begin{pmatrix} J & J' & L \\ 0 & 0 & 0 \end{pmatrix}^2 \begin{Bmatrix} L & F & F' \\ I & J' & J \end{Bmatrix} k^{IOS}(L \to 0) \tag{3.68}$$

where $[x] = 2x + 1$ and

$$\begin{pmatrix} a & b & c \\ \alpha & \beta & \gamma \end{pmatrix} \tag{3.69}$$

and

$$\begin{Bmatrix} a & b & c \\ d & e & f \end{Bmatrix} \tag{3.70}$$

are Wigner-3j and Wigner-6j symbols respectively. However, as the ANR rotational cross sections are corrected for threshold effects (see above) equations (3.67) and (3.68) are only moderately accurate for the actual rate coefficients. Therefore we implemented the 'scaling' method proposed by Neufeld and Green (1994) in which the hyperfine rate coefficients are obtained as a scaling of the rotational ones:

$$k(J\ F \to J'\ F') = \frac{k^{IOS}(J\ F \to J'\ F')}{k^{IOS}(J \to J')} k(J \to J') \tag{3.71}$$

using the actual rate coefficients $k(L \to 0)$ for the corresponding IOS fundamental coefficients. For quasi-elastic transitions, that is, $J\ F \to J'\ F'$ with $F \neq F'$, equation (3.68) was applied directly. In our study fundamental rate coefficients for *downward*

transitions were employed because they yielded better results in the case of He-HCN scattering for which accurate close-coupling hyperfine collisional rate coefficients are available (Monteiro and Stustzki, 1986).

Finally, it should be noted that within the IOS approximation, the allowed transitions or selection rules are determined by the Wigner-6j symbol. The same selection rules were obtained by Chu (1976) from multipole expansion approaches. Radiative (dipolar) selection rules are also determined by the Wigner-6j symbol with $L = 1$.

3.6 UK R-matrix Package Structure and the Computational Implementation of the Theory

Here the modules constituting the polyatomic R-matrix code (Morgan et al., 1998) are listed. The package makes use of the Sweden-Molecule suite of quantum chemistry codes developed by Almlof and Taylor (1984) in order to generate target molecular orbitals and transformed integrals. Except those otherwise referenced the outer region modules were programmed by Morgan, who organised this module structure from an earlier, less-structured, version. The flow charts for running a typical target, inner region scattering and outer region calculation are given in figures 3.2, 3.3 and 3.4 respectively.

3.6.1 Inner Region

- **SWMOL3**: generates one and two-electron integrals from the given GTO basis set;
- **GAUSTAIL**: evaluates the contribution to each integral from outside the R-matrix sphere and adds matrix elements of the Bloch operator to the Hamiltonian ones (Morgan et al., 1997);
- **SWORD**: orders the atomic integrals evaluated by SWMOL3;
- **SWFJK**: forms combinations of Coulomb and exchange integrals for the Fock matrix;
- **SWSCF**: performs the Hartree-Fock self consistent field (HF-SCF) optimisation to generate the target molecular orbitals from linear combinations of atomic ones. Here it employs the integrals obtained from the SWFJK code;

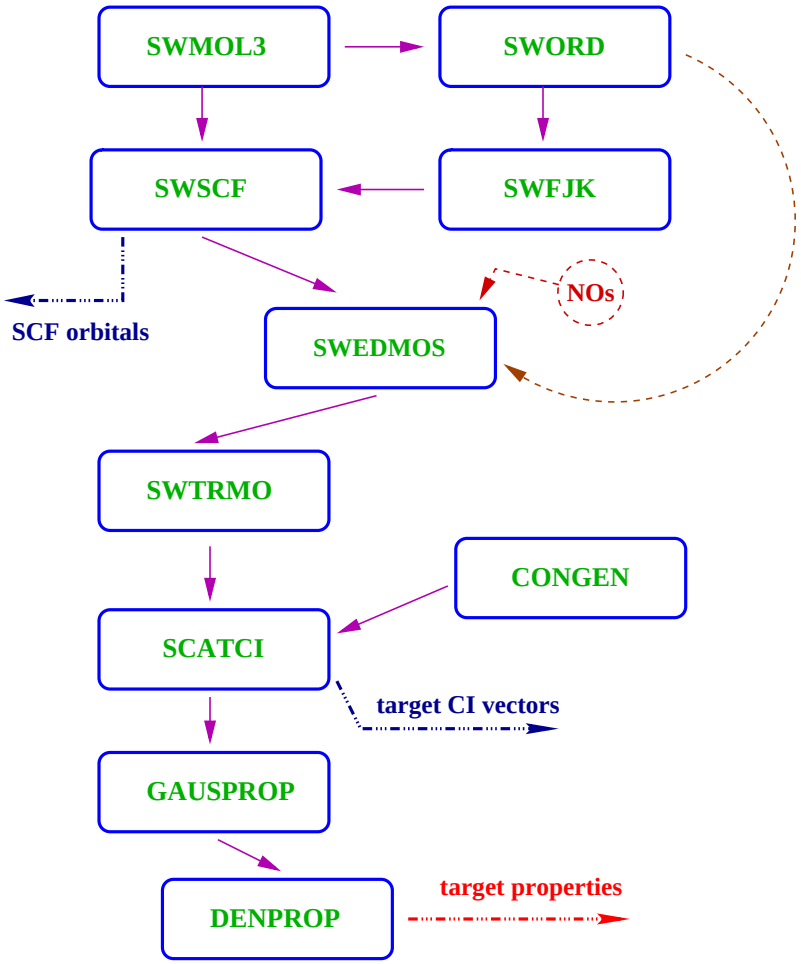

Figure 3.2: R-matrix inner region flow diagram for the target calculation

- **SWEDMOS**: constructs molecular orbitals and boundary amplitudes for the continuum and Gaussian-type orbital (GTO) target wavefunction. It applies Schmidt orthogonalisation to orthogonalise each continuum orbital to all the target ones and symmetric orthogonalisation to orthogonalise the continuum orbitals among themselves. A threshold (typically of order 10^{-7}) is employed for orbital deletion. Those continuum orbitals with overlap matrix eigenvalues less than this threshold are deleted;

- **SWTRMO**: carries out the four-index transformation from atomic orbital to molecular orbital representation of the ordered integrals obtained from SWMOL3;

- **CONGEN**: generates the necessary configuration state functions with appropriate spin and symmetry couplings for performing a configuration interaction (CI) calculation. It generates prototype CSFs for the target molecule and for the $(N+1)$-

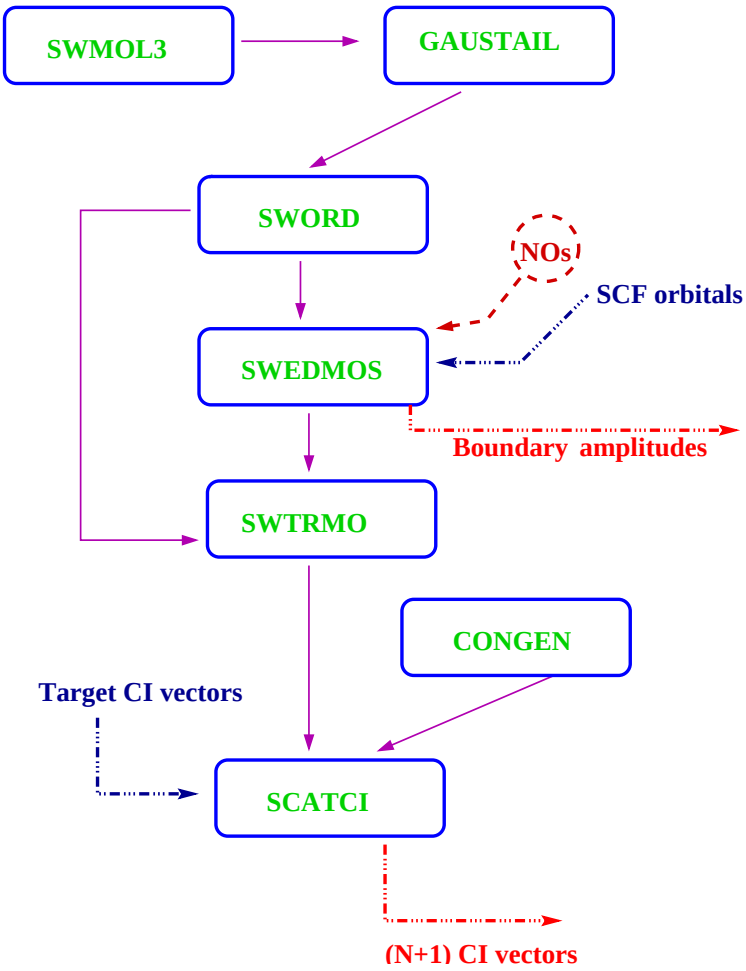

Figure 3.3: R-matrix inner region flow diagram for the calculation of the $(N+1)$ scattering eigenket $|\psi_k^{\Delta}\rangle$ (equation (3.50))

electron system. CONGEN also solves phase factor problems that arise from the use of CI expansions (Tennyson, 1997);

- **SCATCI**: performs a CI calculation of the target molecular and the $(N+1)$-complex wavefunctions (Tennyson, 1996*a*). It employs the CSFs generated earlier by the CONGEN module. The Hamiltonian is diagonalised to obtain the CI expansion coefficients (eigenkets) and the corresponding eigenvalues. In the case of the $(N+1)$-complex these are the R-matrix poles of equation (3.49);

- **GAUSPROP**: generates the property integrals required by DENPROP;

- **DENPROP**: constructs the transition density matrix from the target eigenvectors obtained from the CI calculation. From this it then calculates the multipole transition moments $M_l^m(\lambda \rightarrow \lambda')$ (appendix B) required for solving the outer region

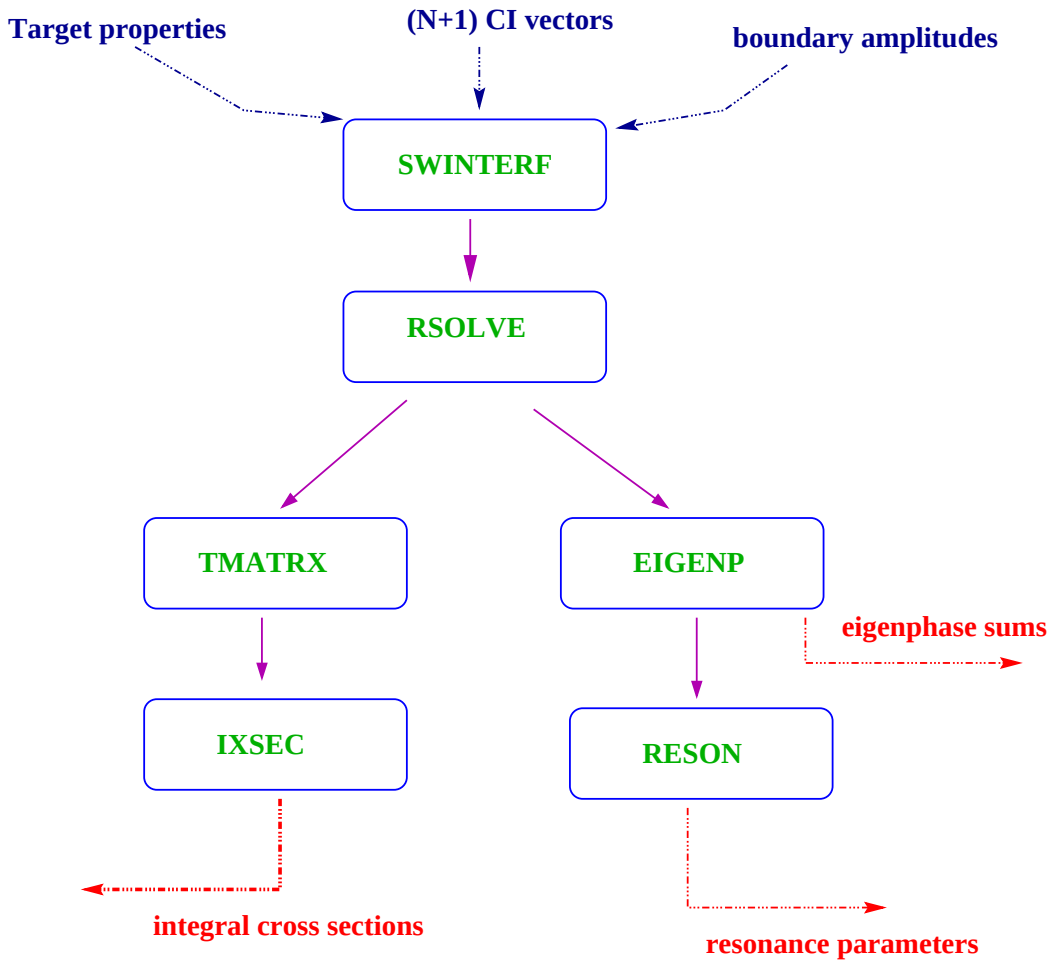

Figure 3.4: R-matrix outer region flow diagram

coupled equations (3.56), the dipole spherical polarisability α_0, and where possible the diagonalised tensor components α_{xx}, α_{yy} and α_{zz}. These are computed using second-order perturbation theory and the property integrals evaluated by GAUSPROP. Only multipole moments up to and including $l = 2$ are computed, and together with the target Hamiltonian eigenvalues (figure 3.2), they are saved to unit 24 (fort.24) for later use in SWINTERF (figure 3.4);

- **PSN**: generates the pseudo-natural orbitals by diagonalising the density matrices computed by DENPROP. It can generate state-averaged NOs by introducing different weightings for the target states being considered through the namelist parameter WGT.

3.6.2 Outer region

- **SWINTERF**: interfaces the internal and outer regions. It requires the boundary amplitudes from SWEDMOS, the $N+1$-system eigenvectors and their corresponding eigenvalues and the molecule's multipole moments (figure 3.4). Its output provides for the target properties and other data necessary to rapidly construct the R-matrix initially at the interaction radius as a function of energy;

- **RSOLVE**: constructs the R-matrix at the interaction radius and uses RPROP (Morgan, 1984) to propagate this R-matrix to the asymptotic region for matching to the boundary condition there (equation (3.58)) by solving the coupled ordinary differential equations (3.56) in an outer region which is divided into sectors. It then constructs the fixed-nuclei K-matrices using CFASYM (Noble and Nesbet, 1984). The output of SWINTERF is used as input;

- **EIGENP**: calculates the multichannel eigenphase sum in the manner discussed earlier, namely, by diagonalising the K-matrix and summing over channels (equation (3.63));

- **TMATRX**: calculates the T-matrix from the K-matrix using equation (3.61). It uses the channel data in unit LUCHAN ('fort.10') and K-matrices in unit LUKMT ('fort.19');

- **IXSEC**: computes the integral cross sections from the T-matrices (unit LUTMT or 'fort.10');

- **RESON**: detects resonances and performs a least squares fit of the eigenphase sums to a Breit-Wigner profile (Tennyson and Noble, 1984);

- **TMATSUB**: transforms the C_{2v} FN T-matrices to $C_{\infty v}$ ones using the algorithm in table 3.1. The $^2A_1$ T-matrix is used to obtain the $^2\Sigma^+$, $^2\Delta$ and $^2\Gamma$ matrices, while the $^2B_1$ T-matrix yields the $^2\Pi$ and $^2\Phi$ ones. This module is intended to be run independently of the outer region suite of codes;

- **ROTLIN**: using the ANR approximation it computes, from the $C_{\infty v}$ T-matrices, the rotationally resolved integral cross sections. It computes and includes the Born correction for $|\Delta J| = 1$. It was adapted from the existing ROTIONS code (Rabadán and Tennyson, 1998), which computes the same for cations, and

invokes the Coulomb-Born approximation. Like TMATSUB, this module is also intended to be run independently of the outer region codes;

- **DCS**: an implementation of the Born completion formalism of Itikawa (2000), this suite of codes is designed to treat linear molecules. It calculates the differential cross sections (DCSs) using fixed-nuclei $C_{\infty v}$ T-matrices (calculated by TMATSUB for example). Additional information required includes the dipole and quadrupole moment, the rotational constant, spherical and non-spherical polarisabilities, the angular grid, J-transition and incident electron energy. This suite is entirely independent of the R-matrix codes.

  DCS was developed by Thierry Stoeklin of the Institut des Sciences Moléculaires, Talence in France;

- **POLYDCS**: the suite calculates the rotationally elastic and inelastic DCSs for electron (and positron) scattering by neutral polyatomic molecules of various symmetries (including C_{2v}, C_{3v}, T_d and $C_{\infty v}$) be they polar, weakly polar or non-polar. POLYDCS takes a number of inputs including the K-matrices, polarisabilities, dipole and quadrupole moments, incident electron energies and the desired rotational transition. It also contains 4 examples of DCS calculations– O_3, CO, CH_4 and NH_3. This module is also independent of the R-matrix codes.

  The code documentation may be found in Sanna and Gianturco (1998).

3.7 Contributions to the R-matrix package

I have made three contributions to the UK R-matrix package which are listed below. The first two are both solutions to long-standing computer bugs with some improvements to how the results (polarisability) are presented. Correct irreducible representation labels for groups with the same 'nsym' were added. Finally I re-wrote an existing FORTRAN code for the computation of hyperfine transition rate coefficients for linear molecules in another language, PYTHON, and extended this new version to treat half-integer as well as integer angular momenta.

3.7.1 SWMOL3

It was found that running the methane molecule in C_{2v} (natural point group T_d), after appropriate spatial transformation, caused the code to fail, with the code stating that the

symmetrically redundant hydrogen atom was too close to (lying on top of) the original symmetrically non-redundant one. This occurred for atoms lying on the x-z plane, and it could be a reason why water calculations were carried out with the plane of the molecule lying on the σ_{yz} mirror plane rather than the σ_{xz} one.

SWMOL3 applies a particular symmetry operation depending on the value of the integer 'MULK' the symmetrically non-redundant atom has. The value of MULK that such an atom has depends upon the plane than it lies on and the number of symmetry operations the point group of the molecule has. Here the error was due to the symmetrically non-redundant hydrogen atom having an incorrect value of MULK that resulted in its symmetric equivalent partner lying directly on top of the original. That portion of code has now been re-written so that the correct MULK value is yielded, with care taken to distinguish between point groups with the same number of generating symmetry operations– C_s and C_2 (one generating symmetry operation) and C_{2v}, C_{2h}, D_2 (two generating symmetry operations).

3.7.2 DENPROP

It has been known for some time that the dipole polarisability for water was much too low (J. Gorfinkiel, private communication) and that there were problems in other cases with permanent dipoles of A_1 symmetry. Here I used the methane molecule as a test case because $\alpha_{xx} = \alpha_{yy} = \alpha_{zz}$ and $\mu_{A_1 \rightarrow T_2} \rightarrow \mu_{A_1 \rightarrow A_1}, \mu_{A_1 \rightarrow B_1}, \mu_{A_1 \rightarrow B_2}$, in accordance with the correlation table for T_d to C_{2v}. It was found that the $A_1 \rightarrow A_1^*$ dipole transition moment was much too low (the asterisk implies electronic excitation).

The density matrix is computed for a particular electronic excitation as follows (McWeeny, 1989):

$$\rho_{\Gamma \rightarrow \Gamma'} = |\Psi_\Gamma\rangle\langle\Psi_{\Gamma'}| \tag{3.72}$$

$$= \sum_{i,j} C_i^\Gamma \bar{D}_j^{\Gamma'} |\Phi_i^\Gamma\rangle\langle\Phi_j^{\Gamma'}| \tag{3.73}$$

where $|\Phi_i^\Gamma\rangle$ is the i^{th} configuration state function (CSF) term for target state Γ and C_i^Γ is the corresponding CI expansion coefficient.

For transitions from an electronic state Γ to itself, for purposes of optimisation one is justified in computing only the upper-half of the density matrix ρ since it is symmetric. However a problem arises where one wishes to consider the transition from a state (say

the ground state) to an *electronically excited* state of the same irreducible representation (IR) and spin multiplicity, where the upper triangular and lower triangular half of the density matrix are distinct and therefore must be calculated. Here the lower half was never computed because DENPROP incorrectly presumed that wavefunctions with the same spin multiplicity and IR were identical, resulting in the corresponding dipole transition moment being too low because the contribution from the lower half of ρ was neglected. Hence a line was added to check whether two wavefunctions of the same spin multiplicity and IR are indeed the same by comparing CI expansion coefficients; if they are not then the lower-half of the density matrix is also calculated.

DENPROP produces a properties file ('fort.24') with the target Hamiltonian eigenstate labels and eigenvalues, the dipole and quadrupole transition moments. It was not able to distinguish between point groups with the same number of IRs i.e. C_2 and C_s, and C_{2v}, D_2 and C_{2h} and so used incorrect IR labels when assigning target states. It used a parameter 'nsym', which is the number of IRs the point group has, as the filter. This is clearly insufficient since, for example, the point groups C_{2v}, D_2 and C_{2h} have the same number of IRs (4). This problem was solved by simply adding an extra distinguishing namelist integer parameter to INPUT called 'ksym', the assignments of which are given in table 3.2. The point group filtering takes place in function 'CMAKSTN'. Now, in addition to filtering by nsym, ksym is used to distinguish between point groups with the same number of IRs. The IRs, ksym and nsym for the listed and missing Abelian point groups were of course added. As a test we calculated the vertical excitation energies of C_2H_6 (ethane) in C_{2h} symmetry (natural symmetry D_{3d}). This was the very first study to use that Abelian point group. We checked them against the *ab initio* results of Buenker and Peyerimhoff (1975*a*) and our energy ordering and spectroscopic assignments of the target states were the same. But our data were consistently much higher than theirs owing to the fact that our quantum chemistry model did not account for the Rydberg-like nature of the excited states.

Finally, although the capacity for DENPROP to compute the dipole polarisability has always existed via subroutine 'GETPOL', the components α_{xx}, α_{yy} and α_{zz} of the (2nd rank diagonalised) polarisability tensor for transitions from the ground state were never written to file in a simple way. This has now been rectified. In addition, GETPOL now computes the spherical polarisability α_0. For some point group symmetries however, e.g. C_s, the tensor cannot be diagonalised so the only the spherical compo-

Point group	ksym	nsym
D_{2h}	1	8
C_s	1	2
C_2	2	2
C_i	3	2
C_{2v}	1	4
C_{2h}	2	4
D_2	3	4

Table 3.2: ksym namelist parameter assignments in DENPROP (see also Rmat documentation)

nent is written to file. α_0 is particularly important in the SCOP high-energy scattering formalism (Joshipura, Gangopadhyay and Vaishnav, 2007).

3.8 PythonHyperfines

Originally, a FORTRAN code was written to compute the hyperfine transitions for linear systems as discussed above, but at present it is restricted to integer nuclear spins (A. Faure, private communication). I re-wrote the code in the PYTHON scripting language (platform 2.5.2) so that it could handle half-integer nuclear spins as well (K. L. Baluja and S. Kaur, private communication) and read input data (molecular formula, rotational constant, temperature, pure close-coupling rotational rate coefficients) from a text file rather than the user having to directly edit the source code as is the case with the FORTRAN version. The code requires the PYTHON scientific libraries 'numpy' (1.3.0) and 'scipy' (0.7.0) which are freely available from the web (http://www.scipy.org/). PythonHyperfines is cross-platform and so can be used on either WINDOWS or LINUX machines. The structure of the application is as follows:

- io:

  'UnixScript.py': contains a number of python translations of UNIX commands;

  'RatesDataIO.py': reads the necessary data– molecular formula, temperate, rotational constant and pure rotational rate coefficients;

- util:

  'FormulaException.py': exception handling for when a molecular formula is incor-

rect;

'Util.py': contains a range method where the intervals can be varied;

'HyperfineExcitationThread.py': thread of execution for computing the hyperfine rate coefficients from the rotational excitation ones;

'HyperfineDeexcitationThread.py': this is the same as HyperfineExcitationThread.py except it uses the rotational de-excitation rate coefficients;

- science:

  'Wigner.py': computes the Wigner-3j, Wigner-6j, Clebsch-Gordan coefficients and Wigner D rotational matrices- here the scipy gamma function is used to compute the factorial;

  'ExcitationHyperfine.py': computes the hyperfine rate coefficients from the rotational excitation rate coefficients, as discussed above;

  'DeexcitationHyperfine.py': computes the hyperfine rate coefficients from the rotational de-excitation rate coefficients, as discussed above;

- Chemistry:

  'Elements.py': 'JAVA enum-like' objects representing the chemical elements;

  'ChemFormula.py': checks that the chemical formula string conforms to the standard nomenclature;

- test: this is a comprehensive test suite that checks the code carries out calculations correctly. It reproduces some of the hyperfine collisional rate coefficients presented in chapter 10;

  'TestWigner.py': computes Wigner-3j and 6j coefficients for various arguments (including non half-integers and complex numbers). Correct answers are given as comments and were obtained from an online Wigner coefficients analytical calculator (Stone, 2009). Of course the code confirms a failed result for non half-integer and complex number arguments;

  'TestChemFormula.py': checks that some sample chemical formulae valid and that incorrect ones fail;

  'TestDeexcitationHyperfine.py': a test script that reproduces the hyperfine rate

coefficients presented in chapter 10;

3.9 New Developments

Electron-molecule re-collisions take place when a molecule is exposed to a strong LASER field and consequently ionised. The ionised electron then re-scatters off the resulting cation. In these experiments it is usual to use aligned molecules. A new module, ALIGN, has been developed for the R-matrix package by Harvey and Tennyson (2009) to compute the scattering observables for neutral and charged molecules. The re-scattering process is especially important in attosecond molecular imaging.

Finally, a new JAVA-based software, Quantemol-N, has been developed to make the UK polyatomic molecular R-matrix package accessible to non-specialists: this is discussed in the next chapter.

Chapter 4

Quantemol-N: An Expert System for the Calculation of Electron-Molecule Scattering using the R-matrix Method

4.1 Introduction

For many electron-molecule scattering problems it is difficult to make the relevant measurements in the laboratory. Thus there is an increasing demand for computational procedures to obtain reliable estimated cross sections and rates for key processes, or to aid in the interpretation of observations. At present there are three accurate *ab initio* methods for treating low-energy electron-molecule scattering including electronic excitation channels, including the Complex Kohn variational method, the Schwinger multi-channel method and the R-matrix method. Of these the R-matrix is widely used (Kolorenc et al., 2005; Izmaylov et al., 2004; Bezzaouia et al., 2004; Huo and Brown, 1999; Pfingst et al., 1994; Abdolsalami et al., 1994).

The most advanced and widely used R-matrix codes are the UK molecular R-matrix codes (Morgan et al., 1998), which have been developed over a period of about 30 years by a number of scientists based at Queen's University Belfast, Daresbury Laboratory, Royal Holloway College and University College London. This project has been extensively supported by the UK Collaborative Computational Project 2 (CCP2) on the continuum states of atoms and molecules.

The UK R-matrix codes are very flexible. Besides the computation of the basic scattering quantities and observables, the package has been adapted to locate (diffuse) bound

states (Rabadán and Tennyson, 1996; Sarpal, Branchett, Tennyson and Morgan, 1991), compute differential and momentum transfer cross sections (Faure et al. (2004*b*) for example), treat rotational (Faure and Tennyson, 2001; Rabadán and Tennyson, 1998; Faure et al., 2006) and vibrational (Sarpal, Tennyson and Morgan, 1991; Rabadán and Tennyson, 1999) excitation, obtain resonance parameters, quantum defects and branching ratios (Tennyson et al., 1984; Tennyson and Noble, 1984), treat dissociative recombination both using a complete non-adiabatic method (Sarpal et al., 1994) and in tandem with multichannel quantum defect theory (Schneider et al., 2000) and study photoionisation (Tennyson et al., 1986; Tennyson, 1987). The R-matrix package has been extended to treat intermediate energies– above the ionisation threshold by Gorfinkiel and Tennyson (2004) and calculate positron collisions (Tennyson, 1986; Danby and Tennyson, 1988). The package is available freely from http://www.tampa.phys.ucl.ac.uk/rmat/, but can only be used by experienced scientists. Hence the Quantemol-N software system was developed to especially address this problem: it provides a JAVA swing interface for the non-specialist to perform *ab initio* electron-molecule scattering calculations and also provides training for those wishing to learn about such calculations. We used the JAVA Development Kit 1.6.0 (JDK 1.6.0).

4.2 The Quantemol-N Approach

4.2.1 Ordinary Calculation Setup

In the practical implementation of the R-matrix method, the user has to make a large number of choices covering issues such as the implementation of symmetry rules, target basis set, continuum basis set, the R-matrix interaction radius, type and number of target orbitals to retain in both the configuration interaction (CI) and as virtual orbitals, target CI representation, CI model for the inner region scattering problem, reference configurations for each of these CI expansions, the deletion threshold for the continuum orbitals, the scattering energy grid, the R-matrix propagation distance, resonance fitting etc. Combined with an old-fashioned user interface, the package is technically demanding to use. It is for this reason that the expert system Quantemol-N was developed (Tennyson et al., 2007), which provides both a friendly and intuitive graphical user interface (GUI), and a package of classes which takes decisions on the issues listed above or provides a limited menu of choices for the user. The principal aim of Quantemol-N is to make *ab*

initio scattering calculations accessible to the non-specialists, but we have discovered by experience that Quantemol-N makes it much easier and quicker for specialists to perform such calculations too.

Quantemol-N is menu driven. Figures 4.1–4.7 show a series of screen panels the user must complete to initialise and perform the calculation, and at runtime each panel checks that the inputs are valid, preventing the user from progressing if the inputs are indeed invalid. The panels also incorporate help buttons if the user is unsure of how to proceed. The first panel, figure 4.1, is for specifying the molecule's chemical formula. The panel checks that the formula is in accordance with the standard way of writing chemical formulae.

The second panel is shown in figure 4.2 and it deals with the target geometry. The Cartesian position vectors of the constituent atoms are entered into the table in Angstroms. This panel checks that the distance between any two atoms is greater than 0.2 Å. The geometry can be obtained from a number of sources: our tutorial provides a link to the NIST Computational Chemistry Comparison and Benchmark Database (CCCBDB) (NIST, 2008).

Using the specified the geometry Quantemol-N employs the molecule visualisation application Jmol (*Jmol: an open-source Java viewer for chemical structures in 3D*, 2009) to display the molecule in 3D (figure 4.3). By clicking on the point group menu, the point group symmetry operations are imposed on the molecule. In the figure the well-known H_2O molecule is displayed and the C_{2v} point group operations σ_{xz}, σ_{yz} imposed. Of course the constraint on the point group options available is the same as for the R-matrix package, namely, the Abelian D_{2h}, D_2, C_{2v}, C_{2h}, C_s, C_2 and C_i symmetries and no symmetry. The symmetrically equivalent atoms must be selected in order to proceed. Here the tutorial furnishes the user with a number of interactive Jmol examples of how to do this.

The fourth and fifth panels, figures 4.4 and 4.5, deal with the assumptions of the quantum chemistry method used to represent the target wavefunctions and, hence, the scattering calculation. The user can supply the ground state configuration of the molecule, or if it is not known, an initial guess can be generated which the software optimises using the Hartree-Fock self consistent field (HF-SCF) method to yield the occupied and virtual molecular orbitals. These are then employed in the target and scattering calculations. In the fifth panel one is required to choose the quantum chemistry method (hence the

scattering method to be employed), between using a HF representation (static exchange) or complete active space configuration interaction (CASCI) (close-coupled method). Although the number of target states to be computed in a CI calculation may also be varied, only those states with channel thresholds below (or equal to) the user specified cut-off are retained in the inner region CC calculation and for the construction of the R-matrix. The CASCI space is generated automatically by Quantemol-N and may be varied in size by changing the 'Number of virtual orbitals' option in the penultimate screen.

The target (GTO) basis is selected, usually from the library supplied with the software. The current version (3.5.2) library contains 6–31G, 6–31G*, 6–311G, 6–311G*, DZP, TZ and cc-pVTZ. A user is not necessarily limited to these and an option is available to import other basis sets from *EMSL Gaussian Basis Set Order Form* (2009), the link to which is given in the panel's tutorial page. The continuum basis set used to represent the scattering electron (Faure et al., 2002) is automatically chosen according to whether the species is (positively) charged or neutral and according to the interaction radius chosen.

The penultimate screen deals with the set up of the outer region calculation, namely the number of target states per symmetry to be included (default set to one for a CI target representation), the R-matrix interaction radius, default 10 a_0, and the energy grid, default setting 0.1 eV to 10 eV in steps of 0.02 eV, all of which may be set. This panel contains an animation of the molecule inside the sphere to give a feel for the dimensions of the molecule in relation to the size of the R-matrix sphere. The last panel, figure 4.7, gives the calculation parameters that were chosen by the user in the previous six panels, which must be saved in order to proceed with the R-matrix calculation.

4.2.2 Batch Calculations

This new feature enables the user to prepare and run a queue of R-matrix calculations, be it one consisting of several different molecules, or calculations on the same molecule as a function of geometry, say.

An R-matrix calculation can be added to the summary table simply by pressing the 'Import a job...' button and the user can select one from the examples directory. In order to edit the calculation, or job parameters one must select/click on the job in the table and then the 'Edit selected job' button, as shown in figure 4.10. The point

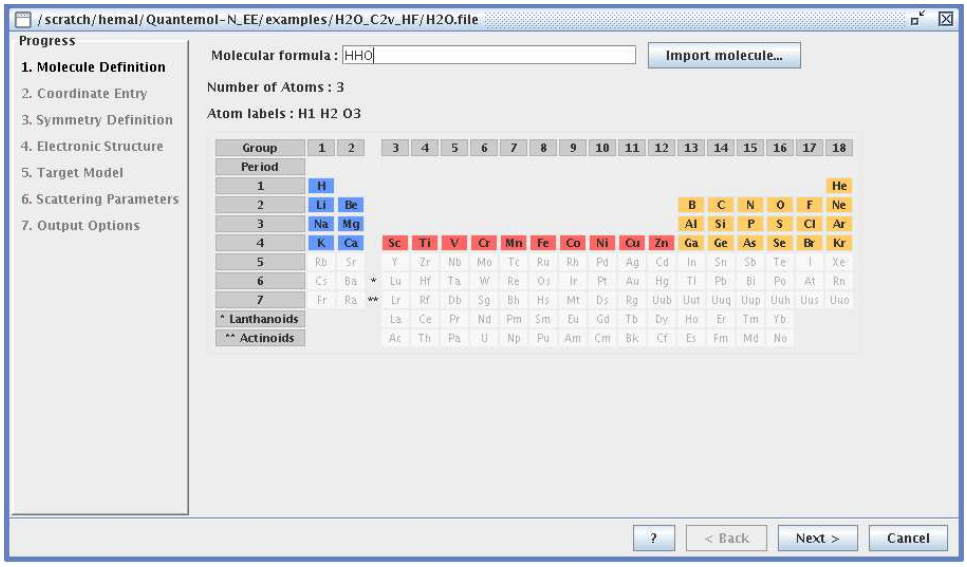

Figure 4.1: Wizard panel 1: molecular chemical formula

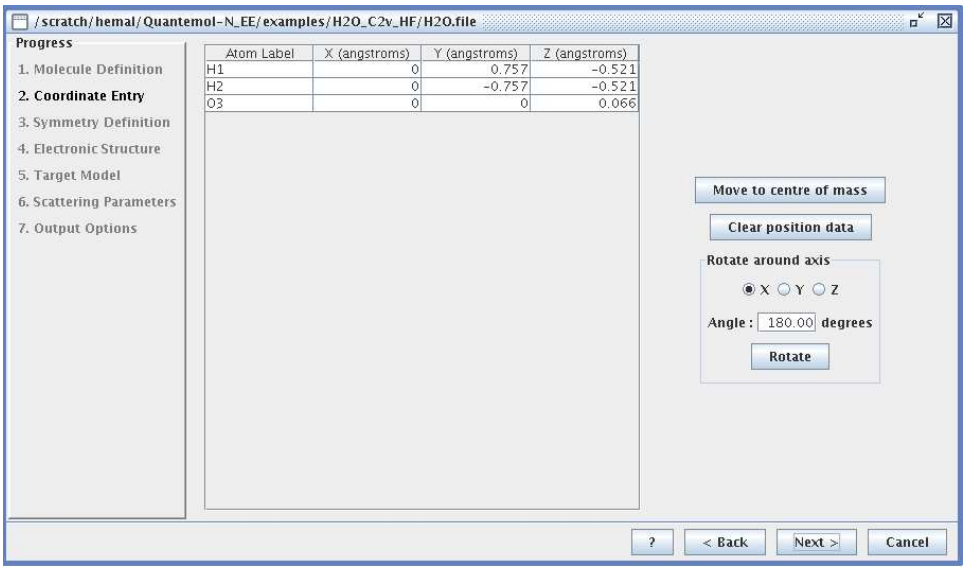

Figure 4.2: Wizard panel 2: molecular geometry

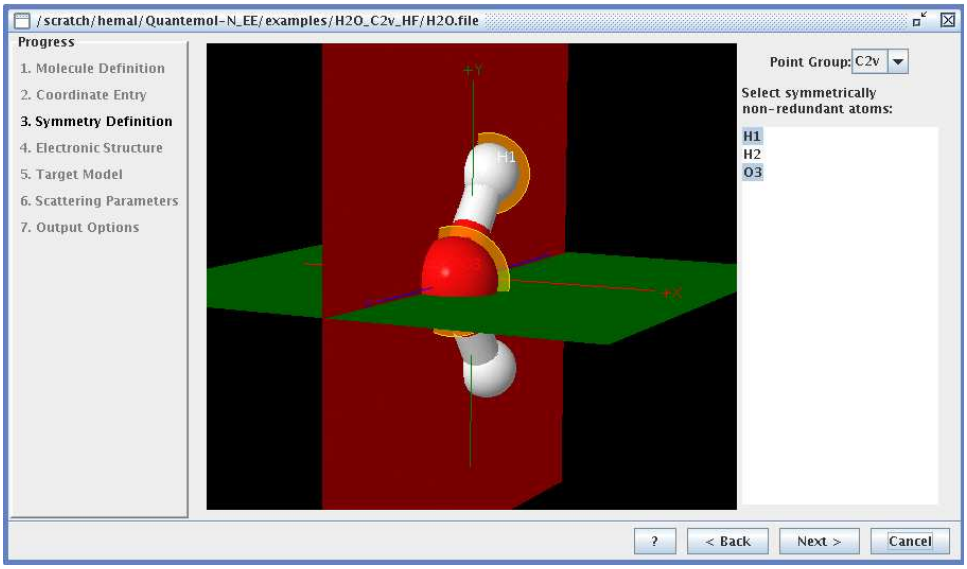

Figure 4.3: Wizard panel 3: molecular symmetry (point group and symmetrically equivalent atoms)

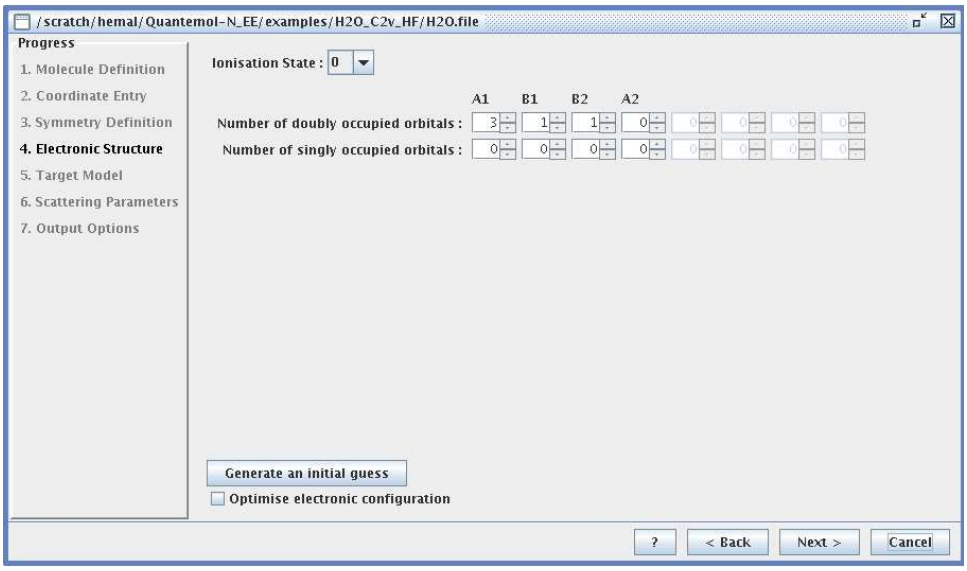

Figure 4.4: Wizard panel 4: electron configuration

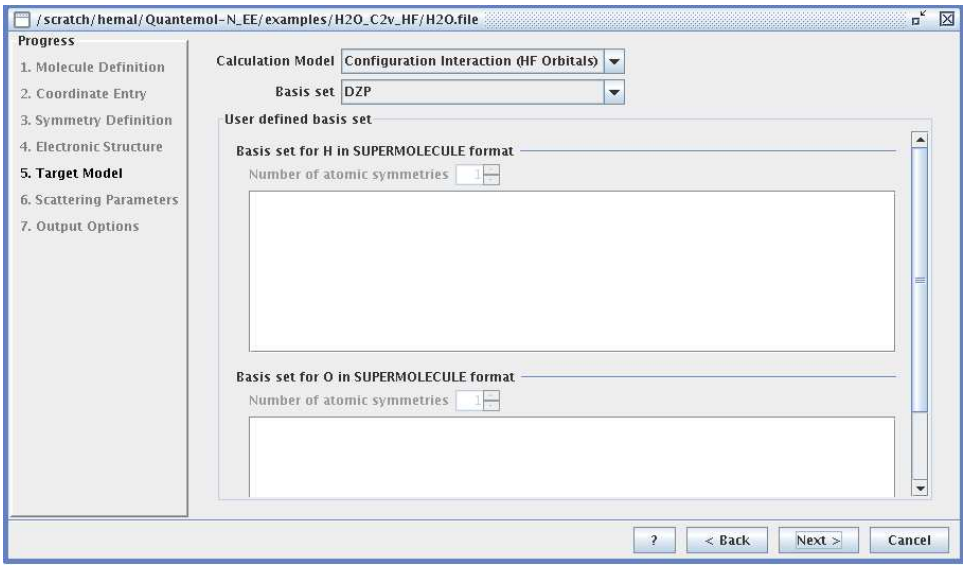

Figure 4.5: Wizard panel 5: quantum chemistry parameters

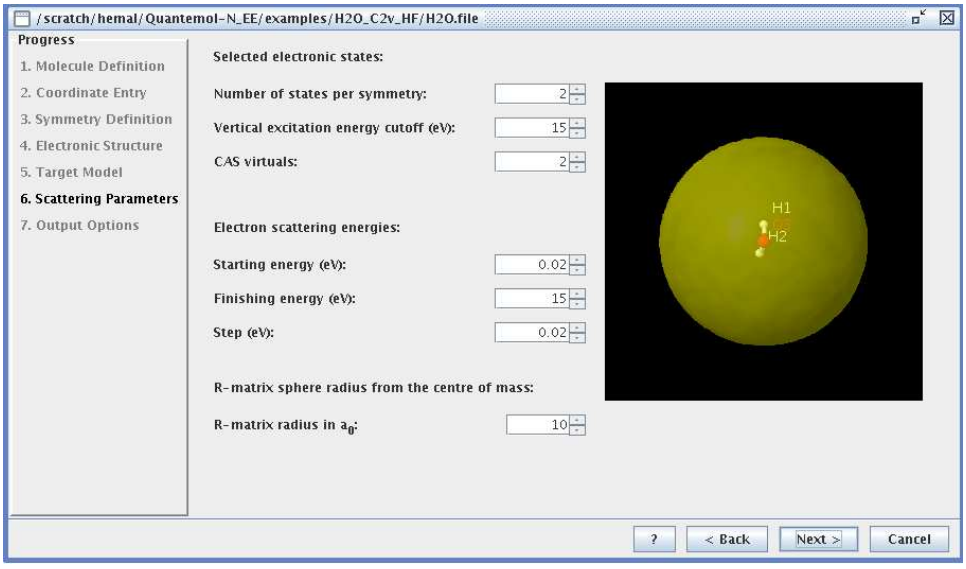

Figure 4.6: Wizard panel 6: scattering parameters

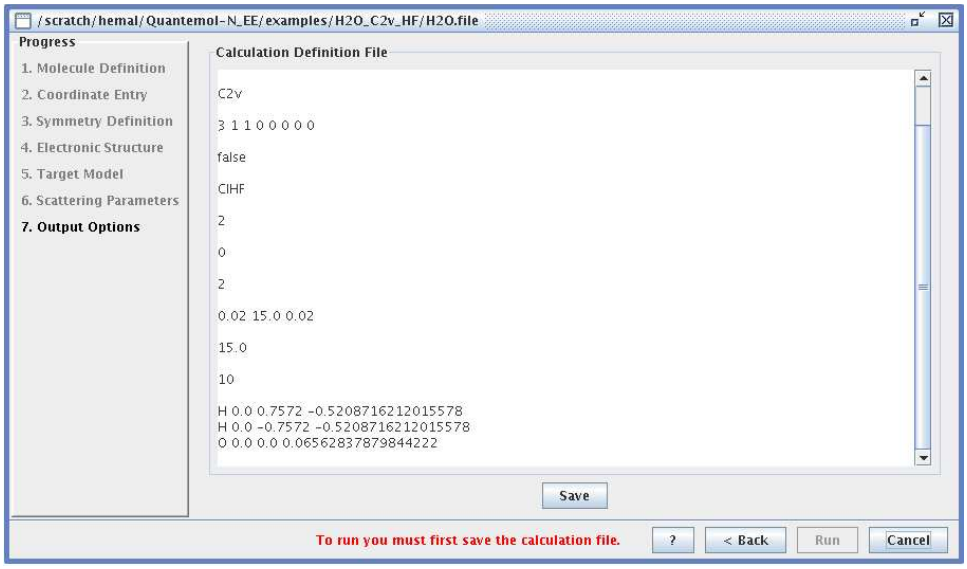

Figure 4.7: Wizard panel 7: saving the calculation definition

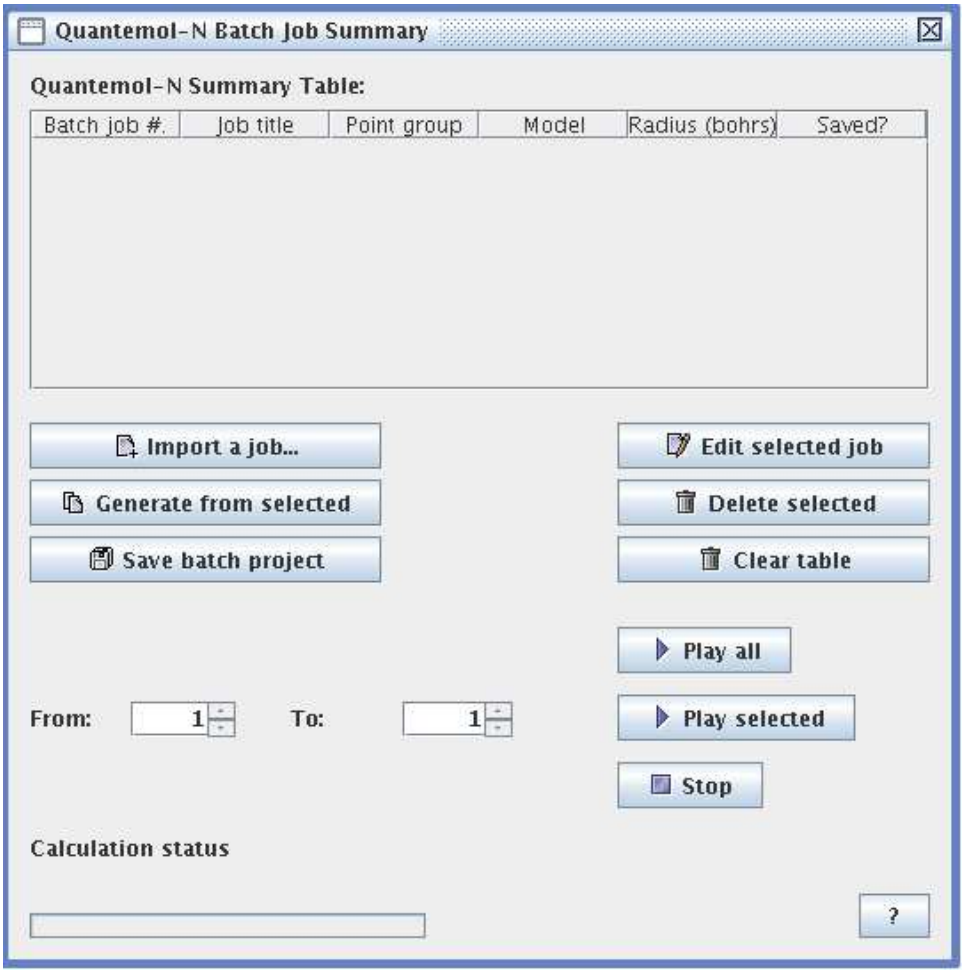

Figure 4.8: Batch job setup internal panel

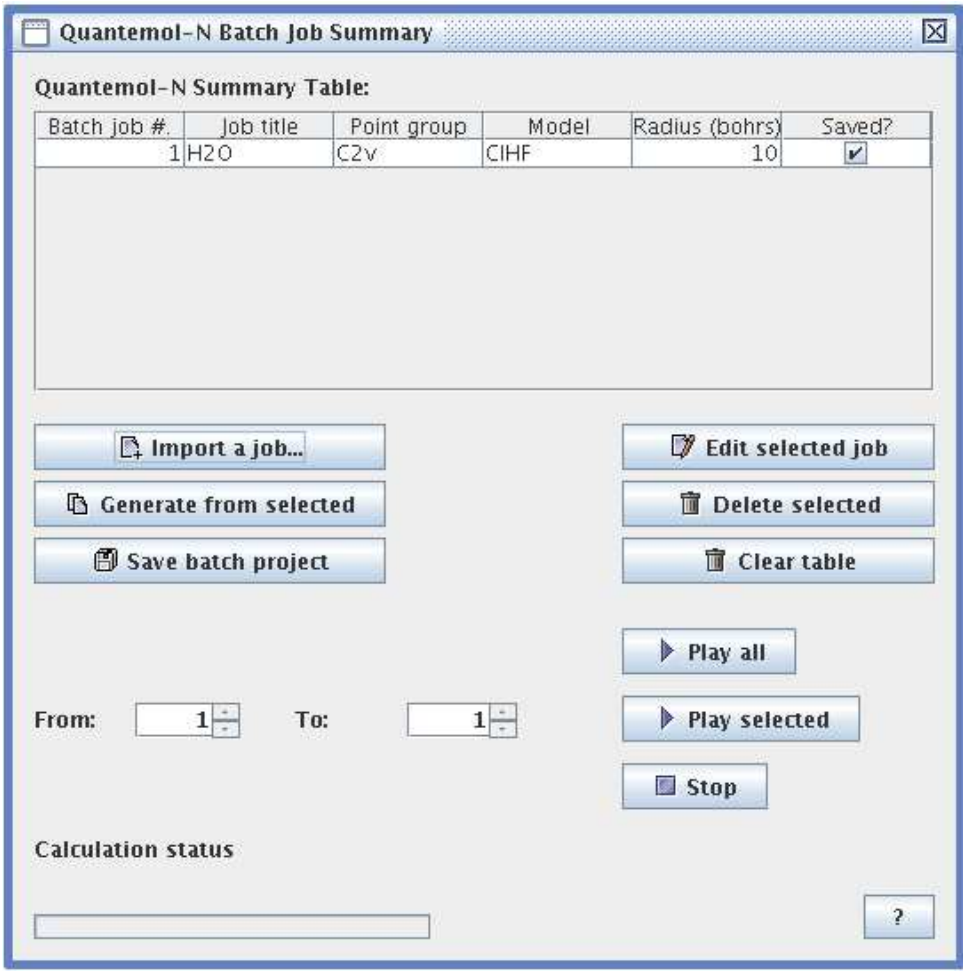

Figure 4.9: Adding a job

group option, for reasons related to ease of use, is permanently disabled in the latest version, as is the electron configuration; the other options can be changed, however. In addition one can create a copy of a selected job by pressing 'Generate from selected' button, which augments the copy to the table, a recommended procedure for running Quantemol-N calculations as a function of geometry or basis set for example. Once the parameters have been changed they must be saved by clicking on the 'Save' button on the job parameters window. Proceeding in this way a queue of R-matrix calculations can be created. At runtime each calculation is allocated a calculation directory, so no one calculation is over-written by another: the directory structure of the software is shown in figure 4.11.

The queue can be started by either pressing 'Play', which runs the entire list of jobs in the table one at a time to completion, or a subset using the JSpinner components

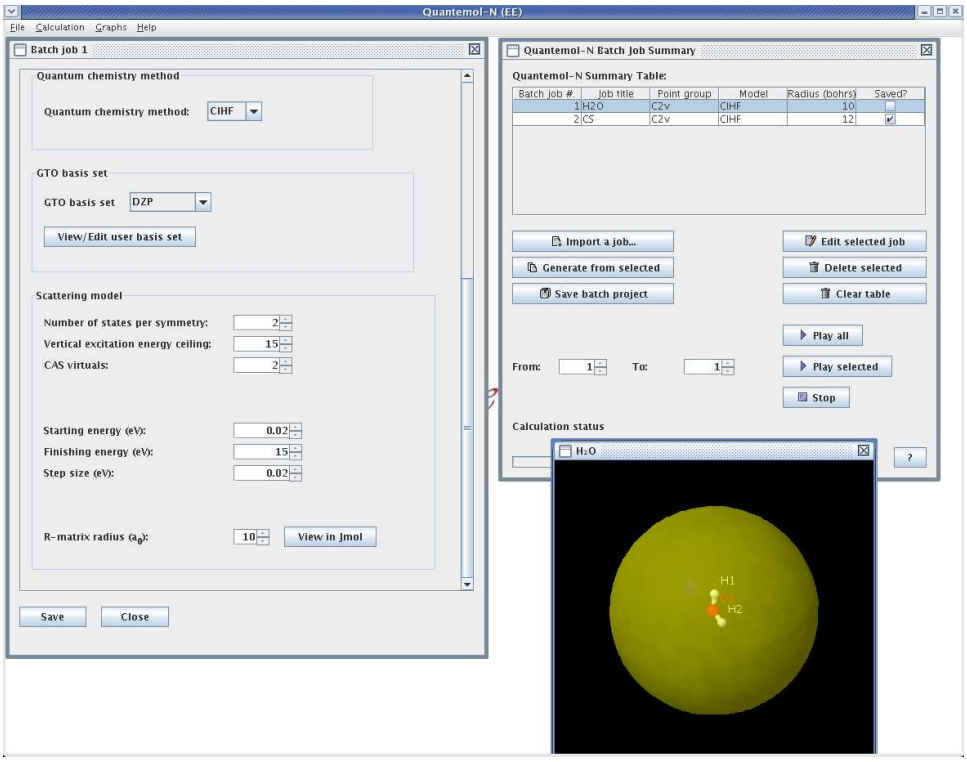

Figure 4.10: Editing a job

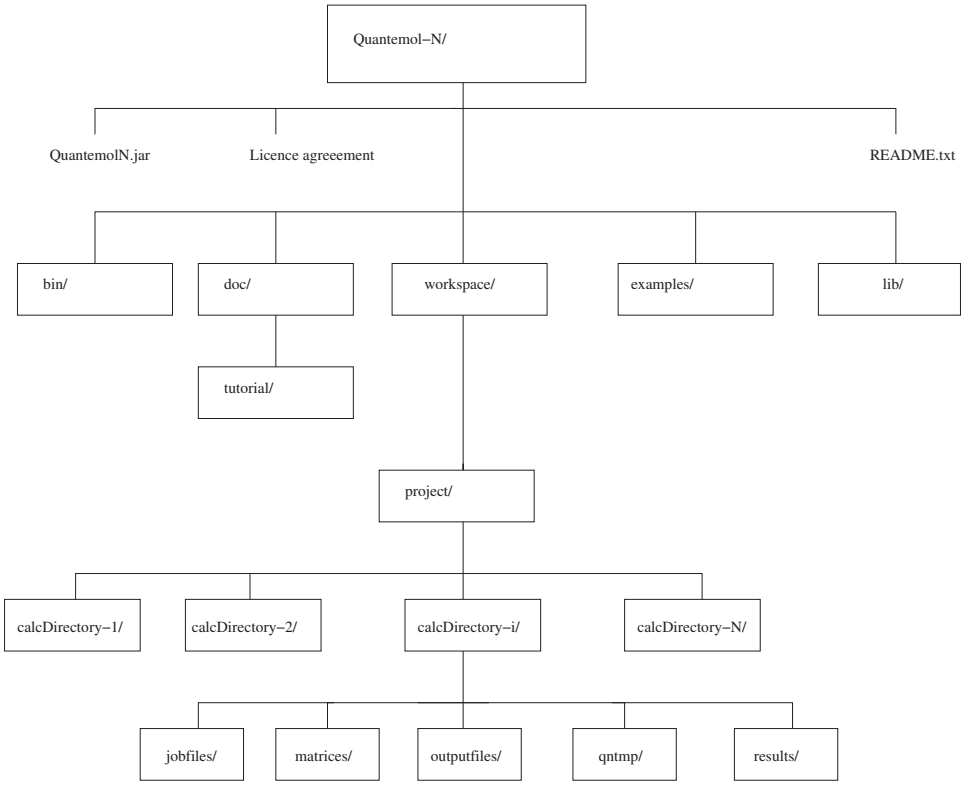

Figure 4.11: Quantemol-N directory structure

and then clicking 'Play selected'. The batch job can be stopped at any time simply by pressing 'Stop'. In both the case of setting up an ordinary calculation and batch calculation, upon successful completion, the user will be prompted to save their project to a location of their choice. If a calculation terminates with an error the software proceeds to the next one and the error is documented for purposes of troubleshooting. At the end of the batch calculation the user is informed that one of the calculations exited with an error and where the de-bugging file is housed. The file contains the calculation parameters and the error stack trace.

4.2.3 Results

Quantemol-N generates vertical excitation energies, graphs of eigenphase sums (figure 4.12), inelastic cross sections (figure 4.13), BEB ionisation cross sections (Kim et al., 1997) (figure 4.14) and rate coefficients (figure 4.15). Resonances are automatically fitted (Tennyson and Noble, 1984) to yield their parameters. The data are saved to simple text files to facilitate further analysis.

It is especially important to state precisely the model employed in one's calculation in order that the results may be re-produced later by other studies. So during the Quantemol-N calculation, the key details of a theoretical model (GTO basis set, geometry, electron configuration, CAS, R-matrix radius etc.) set up by the software are saved to a text file for the user's information. In the example for water, the software employed the DZP basis set, a ground state configuration of $1a_1^2\ 2a_1^2\ 3a_1^2\ 1b_1^2\ 1b_2^2$ and a CAS in which only two electrons were frozen and the remaining electrons allowed to move amongst the $2a_1$, $3a_1$, $4a_1$, $1b_1$, $1b_2$, $2b_2$ occupied and virtual orbitals. One virtual orbital of each of the symmetries A_1, B_1 and B_2 was augmented to the continuum orbitals for construction of the CC inner region scattering eigenket. The file confirms that we employed the close-coupling expansion in our R-matrix calculation and that in the continuum orbitals partial waves up to and including g ($l = 4$)-wave were retained in the expansion. Ten target states were included in the inner region CC expansion and for the construction of the R-matrix at the spherical boundary, with the interaction radius set to 10 a_0, and which was propagated to a distance of 100.1 a_0 for matching to the asymptotic boundary condition. Finally, in the calculation of the BEB cross section, the orbitals employed by Quantemol-N are shown in table 4.1.

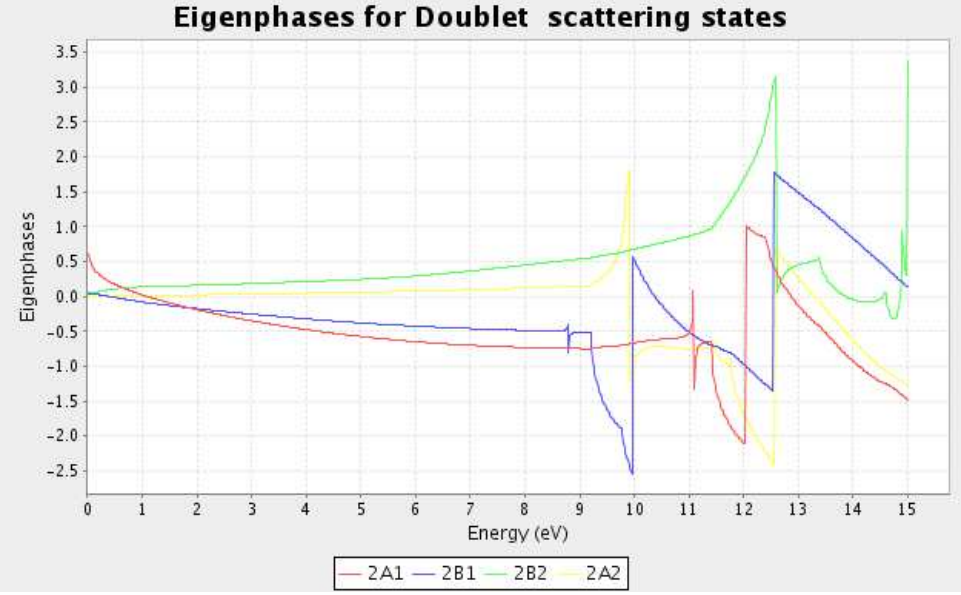

Figure 4.12: H_2O eigenphase sums for a 10-state CC calculation

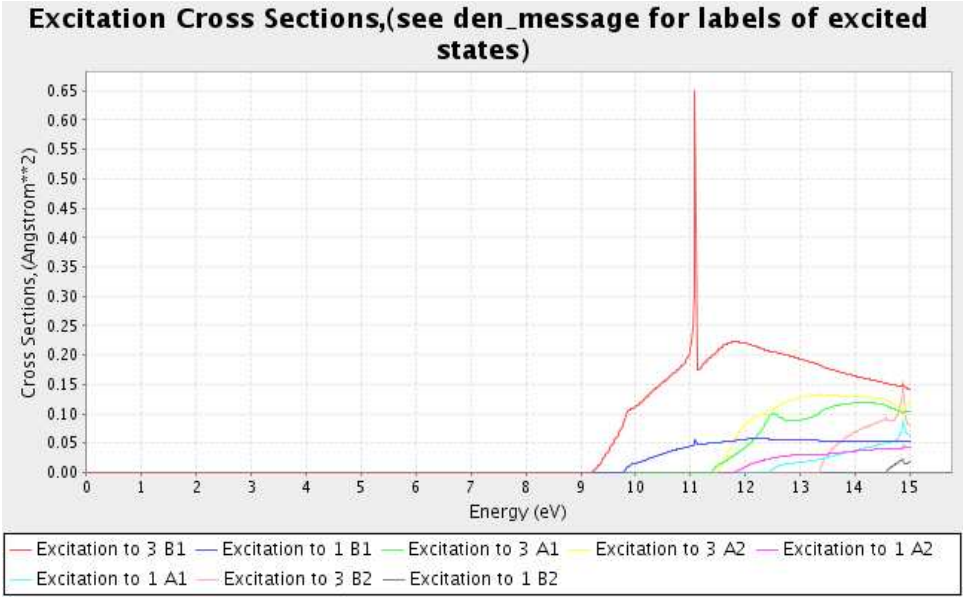

Figure 4.13: H_2O inelastic cross sections for a 10-state CC calculation

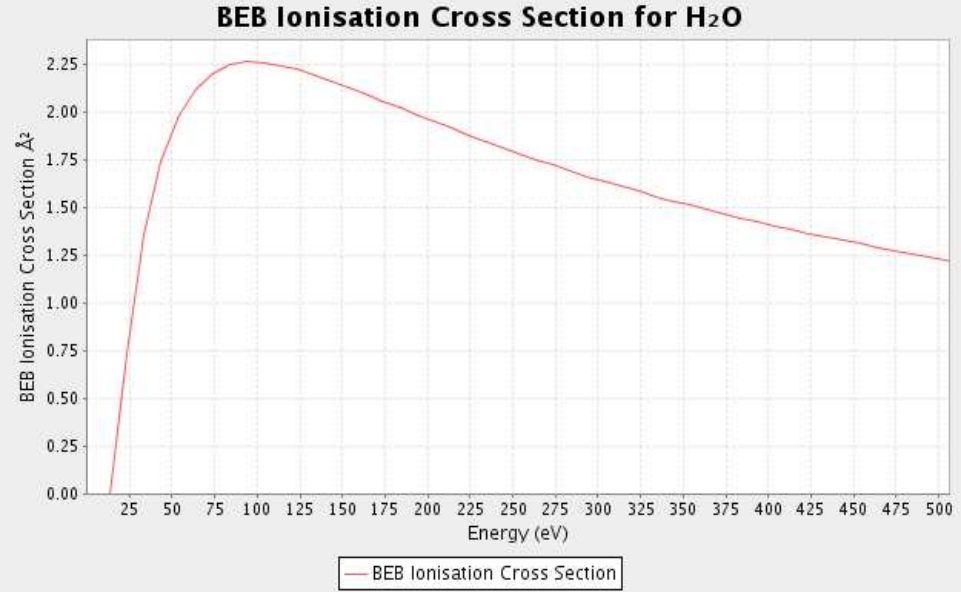

Figure 4.14: H_2O BEB ionisation cross section

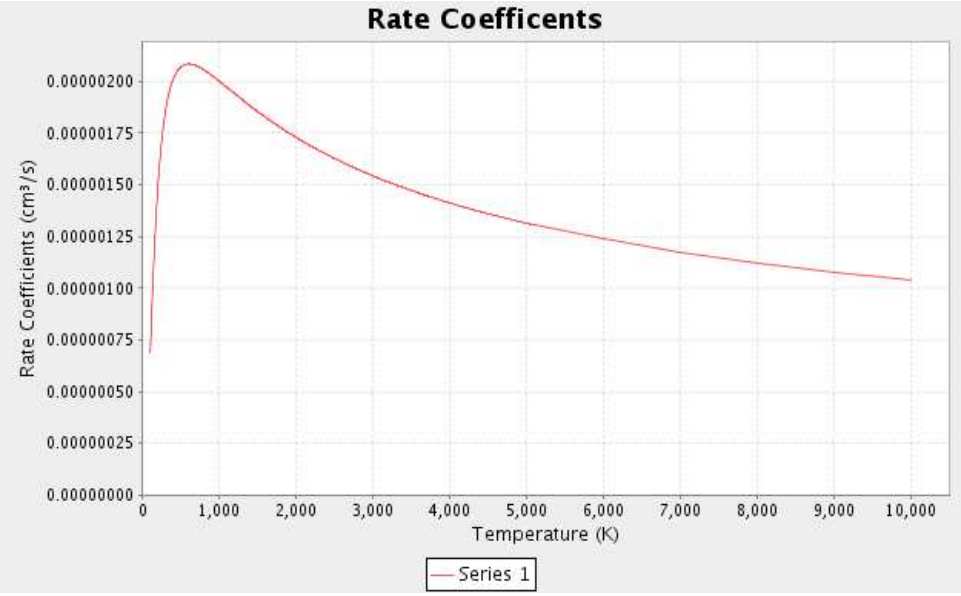

Figure 4.15: H_2O total (elastic+inelastic) rate coefficients for electron-impact scattering

Orbital	$\|B\|$	U	N
$1a_1$	559.42	+794.56	2
$2a_1$	36.61	+70.74	2
$1b_2$	19.32	+48.32	2
$3a_1$	15.66	+56.68	2
$1b_1$	13.67	+61.50	2

Table 4.1: H_2O molecular orbitals, where B is the binding energy and U is the average kinetic energy. The parameters are given in eV

4.3 The Author's Contribution

A number of additional capabilities were added to the software, including automation of some important parts of the calculations and improving and augmenting the 'help' facility. These are discussed below.

4.3.1 Tutorial facility

In order to make Quantemol-N easier to use, a tutorial system was developed, which would show the user how to prepare an ordinary R-matrix calculation, one for each panel, and where appropriate links to other tutorials or external URLs discussing the underlying theory in a simple way. The tutorial may be started either by clicking on the '?' button on the displaying panel (figure 4.1 for example) or pressing the 'F1' key. The same was developed for the calculation queuing system. The htm files, which were written by Salim Damani and Sunil Godhania, are distributed with the software. Sample screenshots are shown in figures 4.16 and 4.17.

4.3.2 R-matrix calculation queuing system

The system was originally developed at the request of T. A. Field (Queen's University Belfast) to allow a series of calculations to be carried out on one molecule as a function of bond length (see chapter 8). In the process of the development, we extended it to enable one to run a queue of different molecules, or the same molecule with different parameters. But in order to make the queuing system possible, we had to make parts of the software directory structure dynamic, especially the part which houses the useful scattering data, job files, output files and the R-, K- and T-matrices. Now at runtime a calculation directory is created each time a new calculation is started. The directory

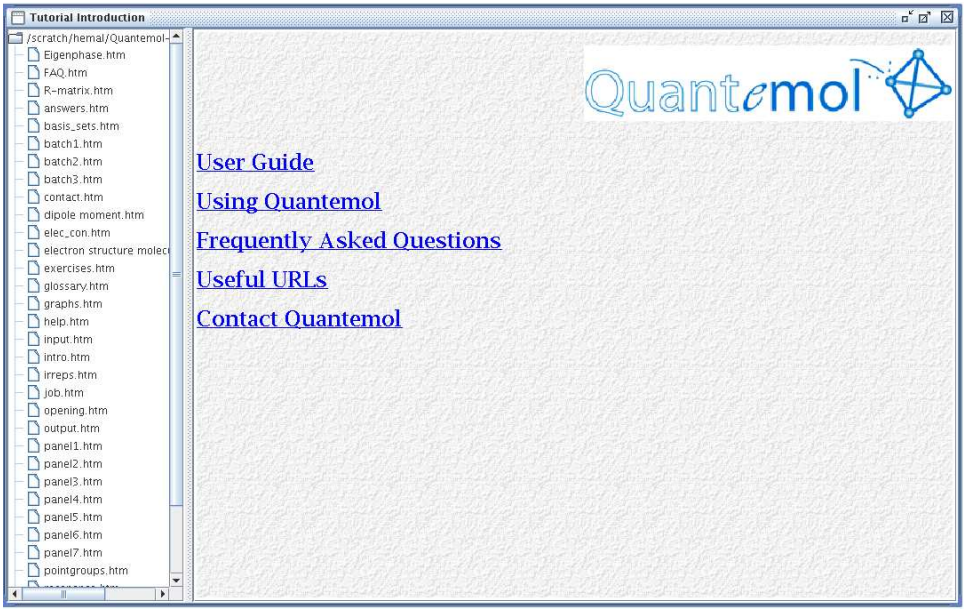

Figure 4.16: Quantemol-N tutorial facility

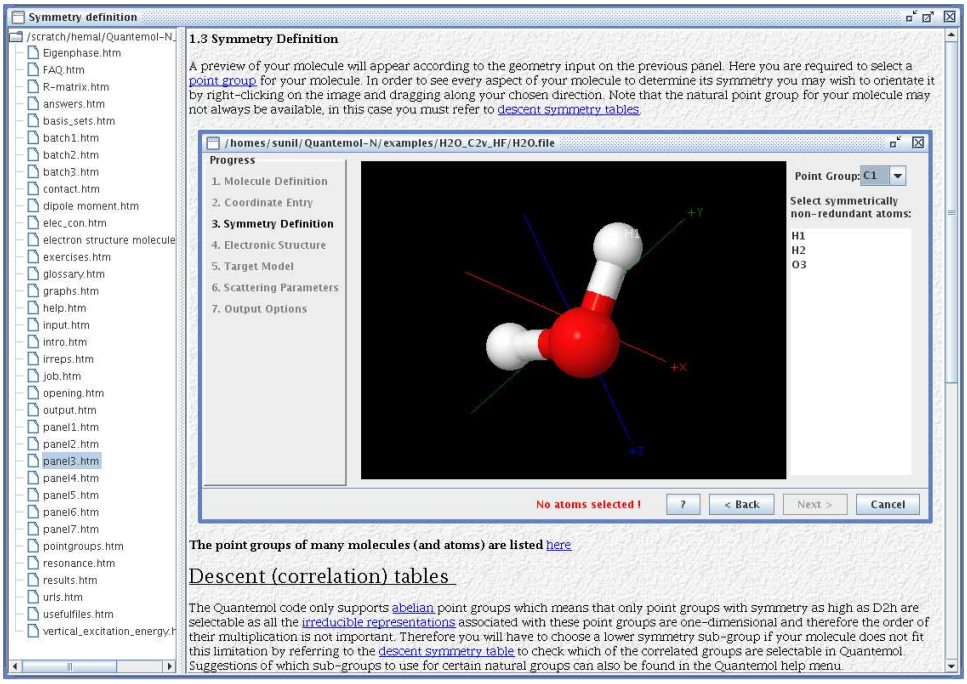

Figure 4.17: Quantemol-N tutorial facility

structure is shown in figure 4.11. Simplicity of the structure is vitally important in order that one could find the results required easily and quickly. For ordinary calculations and entirely new batch calculation projects, however, the calculation directory of any old calculation(s) is (are) deleted. Once the calculation(s) is (are) finished, the user is prompted to save.

4.3.3 Automation of the SCF optimisation

The orbitals generated by SCF are employed in the target (CI and HF) and scattering calculations. However, obtaining the correct ground state configuration (molecular orbitals) required the user to input the configuration into panel 3 (figure 4.3). Although this information is freely available from various literature and the internet (NIST, 1997), this is quite difficult for the non specialist to carry out. Hence we developed a JAVA code that would automate the entire process, from the generation of an initial guess to the determination of the ground state configuration.

Consider the simple case of a closed shell molecule. Here the initial guess distributes the core electrons across molecular orbitals of all the various symmetries, while the remaining valence electron pairs are placed into orbitals of the fully symmetric IR label (A_1, A_g, A, A$'$ etc.). For open shell molecules, the last electron is put into the orbital of B_1, B_{2u}, B or A$''$ symmetry. The initial guess is then optimised as follows. The submitted guess, from which are derived the ifock and iocc parameters, is optimised by the SWSCF code to yield a new set of occupied and virtual orbitals. The JAVA code proceeds to sort the orbitals, using the primitive bubble sort algorithm, in order of increasing energy, and the new configuration fed back into the SWSCF code. This procedure is repeated 12 times. On two separate occasions within the loop, after re-calculating the orbitals, the configuration is doubly ionised and SWSCF is re-run to confirm that this is the true ground state. Of course the SCF energy is checked and the electron configuration corresponding to the lowest SCF energy is retained. The reason for the ionisation is that some configurations fully converged to excited states (e.g. $1a_1^2$, $2a_1^2$, $3a_1^2$, $4a_1^2$, $1b_1^2$,$1b_2^2$, $2b_2^2$ for HNC; whereas it should be $1a_1^2$, $2a_1^2$, $3a_1^2$, $4a_1^2$, $5a_1^2$, $1b_1^2$, $1b_2^2$, and O_3 1–7a_1, 1b_1, 1–4b_2, the correct configuration being 1–6a_1, 1b_1, 1–4b_2, 1a_2). In the case of open-shell systems we only singly ionised the molecule. If the initial guess causes SCF divergence problems, in particular those guesses which have put electrons in a_2 orbitals, the error is captured and an electron pair is moved from an orbital of symmetry A_2, the chief source

of the divergence problems, to an orbital of A_1 symmetry and the SWSCF re-run– SiH_4 has been such a case. If the error persists a guess where 10 electrons are added to 5 a_1 orbitals is used, with surpluses or deficits corrected during sorting.

The algorithm has been successful for closed shell systems, more so than open shell ones. Interestingly for C_2 a ground state electronic structure different from that accepted in literature was found which yielded an SCF energy much lower than the accepted configuration.

Systems such as O_2, which has an even number of electrons, but is an open shell system (two singly occupied orbitals) are not treated by this code.

After the calculation has finished, the user is prompted to save the new electron configuration to file. From then on Quantemol-N uses this configuration in all future calculations.

4.3.4 Automated Generation of the Target Complete Active Space

A previously programmed algorithm for generating a target complete active space (CAS) involved comparing orbital binding energies, but often it did not freeze the correct number of electrons. For example, for SiH_4, only two electrons would be frozen, resulting in more (2377) CSFs being generated than is usually the case if ten electrons were frozen, or neopentane (2,2-dimethyl propane), where 36 electrons were frozen (all six electrons in each of the five carbon atoms and one electron in six of the 12 hydrogen atoms).

In the new algorithm, for molecules with less than 25 electrons, the number frozen per atom is equal to the number of electrons in the noble gas in the preceding period. The active space is generated as follows. Initially one puts the molecular virtual orbital energies into a set. One then iterates over the list of unoccupied virtual orbitals and map the orbital energy (key) to the orbital, or list of orbitals in cases where there is degeneracy (value). Hence the number of virtual orbitals retained in the active space is entirely determined by the number of orbital energies, and this is what is meant by 'Number of virtuals orbitals' (figure 4.6). Varying this parameter essentially decides the number of orbitals energies employed as keys, and so allows one to vary the size of the active space and control the amount of correlation included in the target. Returning to the case of SiH_4, ten electrons (the 1s, 2s and 2p electrons) would be frozen in the target wavefunction. ($1a_1$, $2a_1$, $3a_1$, $1b_2$ and $1b_1$) and the remaining eight electrons distributed in the $4a_1$, $5a_1$, $6a_1$, $2b_2$, $2b_1$, $3b_1$, $3b_2$ occupied and virtual orbitals. In the case of

electron rich molecules, those less than about 43 electrons, one is strongly advised to freeze additional electrons. Here our algorithm determines the atom(s) with the highest proton number, Z_{max} say, and freeze an additional electron pair on that (those) and any atoms with proton number $Z_{max} \pm 1$ (K. L. Baluja, private communication). This has been tested on a few molecules with 27 or more electrons successfully. The algorithm cannot, however, be applied to very electron-rich molecules, such as C_5F_8 which has 102 electrons.

4.3.5 BEB Electron-Impact Ionisation Cross Section

Electron-impact ionisation cross sections are useful in areas such as atmospheric physics as well as plasma physics, and all that is required to compute them in the BEB formalism (Kim et al., 1997) are the SCF binding energies B, average kinetic energy U, occupation number N and the dipole constant Q, which is usually taken to be unity. Two of the parameters B and N are already obtained from the SCF optimisation procedure. The orbital kinetic energies are read in by the SCATCI program. These are then employed in the standard formula to give a cross section for some incident electron energy for an occupied molecular orbital. The cross sections are then summed over all the molecular orbitals to give the ionisation cross section. The BEB formalism has been applied to calculate such cross sections for some new molecules e.g. SiO (see chapter 7).

4.3.6 Theoretical Model Documentation

It is necessary in R-matrix calculations to note the model employed to calculate the scattering quantities (eigenphase sum, R-, K- and T-matrices) and observables (cross sections, target dipole transition moments, resonance parameters). Although the information is technical, it is still necessary when the user comes to publish their results. Once the calculation(s) is (are) executed, the key information that would be required to re-produce the calculation are documented in a single text file which can form the basis for any report on the work: point group; net molecular charge; atom cartesian position vectors; basis set name when the user selects one of the basis sets distributed with the software, or exponents and contraction coefficients in the case of a basis set selected from the external web-based library; ground state electron configuration; complete active space (frozen orbitals and the active space itself); virtual molecular orbitals augmented to the continuum orbitals; scattering method (close-coupling or static-exchange); prop-

erties of the continuum orbitals (upper limit on the partial wave expansion); number of target states retained in the $N + 1$-trial wavefunction and for the construction of the R-matrix at the spherical boundary; interaction radius; radial distance to which the R-matrix is propagated (for extraction of the K-matrix); the molecule's Koopman's theorem ionisation energy; and the assumptions taken to calculate the BEB cross section, namely that $Q = 1$, and the orbital parameters used (the binding energy, B, orbital average kinetic energy, U, and occupation number N).

4.3.7 Current and Future Projects

Some new projects, following discussions with users, have been established. By far our most important project is to compute the rotationally resolved differential cross section, where possible, in the natural symmetry of the molecule. From these data we intend for Quantemol-N to compute the momentum transfer cross section, an observable with great application in plasma physics. At present we are implementing the BOUND subroutine into the outer region. Finally, it is also our intention to remove the third panel which has been the most prohibitive to new users.

4.4 Conclusion

The R-matrix method has proved to be highly successful for treating a variety of collision problems in atomic and molecular physics (Burke and Berrington, 1993). In particular the UK molecular R-matrix codes have been widely used for the treatment of low-(and now intermediate- Gorfinkiel and Tennyson (2004)) energy electron scattering. We have developed an expert system, Quantemol-N, for running these codes so that *ab initio* scattering calculations can be performed by the non-specialist. As we have demonstrated here in the case of e-H_2O the software is capable of setting up a high quality theoretical model with little more input than a knowledge of the equilibrium geometry of the target molecule.

A number of new features have been added to make Quantemol-N much more easier to use, useful and powerful. Additional projects continue to be carried out.

Future projects may include developing an algorithm to construct a feasible complete active space for molecules with more than 43 electrons. This will be important for molecules such as SF_6 and C_5F_8, which are being extensively used for plasma etching.

Chapter 5

Electron Collision with the HCN and HNC Molecules using the *ab initio* R-Matrix Theory

5.1 Introduction

Hydrogen cyanide (HCN) and its isomer hydrogen isocyanide (HNC) are examples of linear and very polar species, both well-known astrophysically. Indeed, after H_2 and CO, HCN is one of the most abundant molecules in the interstellar medium (ISM). Although HCN is the significantly more stable, HNC is also well-known in the ISM where concentrations of HNC often exceed those of HCN (Hirota et al., 1998; Hiraoka et al., 2006). Recently HNC has been identified in the spectra of cool carbon stars, where HCN is very well known (Harris et al., 2003) and in comets (Rodgers and Chamley, 1998).

Low-energy electron collisions with these two molecules are of particular interest to the astrophysical community. Their large dipole transition moments (about 3 Debye) implies that the electron collision cross sections are expected to be very large. The computed observables for electron-molecule scattering have many important applications in astrophysics, including the computation of electron densities in shocked regions of the ISM (Jimenez-Serra et al., 2006) and population analysis in comets, where electron collisions can provide a significant excitation mechanism for rotational transitions in the HCN molecule in comet Hale-Bopp (Lovell et al., 2004).

This chapter will discuss previous quantum chemistry and electron scattering studies, and the application of the *ab initio* R-matrix method to electron scattering by HCN and

HNC at the close-coupling level. This discussion includes the target quantum chemistry and scattering models we used to construct the target wavefunctions and the R-matrix respectively.

While most of the calculations reported below used the standard UK R-matrix codes, we took the opportunity to use the Quantemol-N software (Tennyson et al., 2007): it was our intention to compare the models *automatically* generated by it to those of our own. The defaults which most affect the calculations below are that the orbitals for the complete active space (CAS) and the number of target states included in the close-coupling expansion are chosen on energy grounds. Unless stated otherwise, these default values were all used in the Quantemol-N calculations.

All the calculations reported here invoked the fixed-nuclei (FN) approximation.

5.2 Previous Quantum Chemistry and Electron Scattering Studies on HCN

The first *ab initio* quantum chemistry calculation of HCN was carried out by Schwenzer et al. (1974), where they sought to reconcile, amongst other things, a discrepancy between Herzberg (1966) and the Walsh diagram in the B $^1A''$ electronic state. They specifically analysed the ground and 12 lowest-lying electronically-excited states, and the basis set employed was one of contracted Gaussian-type functions centred upon each nucleus. Schwenzer et al. (1974) calculated the CH and CN bond lengths and the HCN bond angle of each electronic state by minimising the total energy with respect to the said quantities. Their calculations yielded a ground state (X $^1\Sigma^+$) energy of -92.958 E_h. A key finding from this study was that the second electronically excited state (B $^1A''$) was not consistent with the previous study of Herzberg and Innes (1957). Instead Schwenzer et al. (1974) suggested a plausible symmetry assignment of $^1A'$.

Another study was carried out into the electronically excited states of HCN by Nayak et al. (2005), chiefly in order to assign labels to a meta-stable form of HCN (HNC or a triplet state of HCN) and other experimentally observed transitions. But they also predicted geometries for these states and compared them to previous experimental and theoretical inquiries and other spectroscopic quantities including ionisation potentials and adiabatic excitation energies. The model involved using two GTO basis sets, one for geometry optimisation and another for the computation of the spectroscopic quanti-

ties. For geometry optimisation Nayak et al. (2005) used a (4s, 1p)/[2s, 1p] contracted Dunning's basis augmented with an s- and p-function for the hydrogen atom, and a Dunning's (9s, 4p, 1d)/[3s, 2p, 1d] contraction augmented with two s-functions, two p-functions and one d-function for the C and N atoms. For the computation of transition and dissociation energies, ionisation potentials and dipole moments, a larger basis set was constructed from Dunning's (5s, 2p)/[3s, 2p] aug-cc-pVTZ contraction scheme for the H atom, and Dunning's (11s, 6p, 3d, 1f)/[5s, 4p, 3d, 1f] aug-cc-pVTZ basis was used for the C and N atoms. The method employed for their geometry optimisation study was the complete active space (CAS) SCF method; calculation of the other quantities was carried out using a coupled cluster based linear response theory.

All the quantities listed were in good agreement with previous experimental and theoretical studies. The transition energies obtained by the Nayak et al. (2005) study are compared to the present one. Experimentally measured adiabatic excitations are only available for a smaller set of target states (Herzberg, 1966; Krishnamachari and Venkatasubramanian, 1984).

An attempt to compute accurate multipole moments for HCN was carried out using the self-consistent field and coupled cluster (CCSD(T)) approximations by Maroulis and Pouchain (1996). The study used a number of very large Gaussian-type functions (although the effect of a smaller basis set upon the chemical properties was also tested) and a very weak electric field was applied in the calculation of the dipole moment. The study involved keeping the two inner most molecular orbitals frozen, while excitations to the two highest virtual orbitals were not allowed. All calculations were performed at the experimental equilibrium geometry R_{CH} =1.06549 Å and R_{CN} =1.15321 Å with the hydrogen atom placed on the positive part of the molecular axis. Their SCF electric dipole moment was higher than that of experiment, with a value of −1.3 a.u. (expt.: −1.174 a.u. (NIST, 2008)), whereas the corresponding value calculated at CCSD(T) level was −1.18 a.u., in very good agreement with the experimental dipole moment.

To date the only detailed theoretical calculations on low-energy electron scattering by HCN were carried out by Jain and Norcross (1985) and Jain and Norcross (1986) for incident electron energies 6 meV to 11.6 eV. For calculations that employed a model-exchange potential, their theoretical target model consisted of a near Hartree-Fock limit wavefunction. Orthogonality of bound and scattering orbitals was enforced as a constraint in some of their calculations, and where the exchange interaction was treated

exactly, they generated Gaussian-type orbitals (GTOs) using standard molecular structure codes. For the higher scattering symmetries, a model-exchange potential was employed. The target observables Jain and Norcross (1985) calculated were the total electronic energy, dipole and quadrupole moments and, via Koopman's theorem, the ionization energy. In modelling the correlation and polarisation interactions a parameter-free correlation-polarisation potential was employed. In addition they carried out a detailed examination of the effects of exchange and polarisation using several models of the interaction potential: static exchange (SE), static exchange-plus-polarisation (SEP), SEP-plus-orthogonalisation (SEPO), exact static exchange (ESE) and exact static exchange-plus-polarisation (ESEP). The equation of motion for the scattering electron was set up using a single centre integral equations approach to the close coupling (CC) calculation, and solved in the body-fixed co-ordinate frame. Since experimental differential cross sections are measured much more accurately than integral cross sections, they computed the rotational excitation differential cross section (DCS) using the multipole-extracted adiabatic nuclei (MEAN) approximation. Importantly, if scattering equations are solved in the FN approximation, the DCS diverges in the forward direction. Such divergence may be removed by accounting for nuclear rotational motion.

All the models discussed predicted the existence of a $^2\Pi$ shape resonance whose position and width parameters were particularly sensitive to the treatment of the polarisation interaction. The best model was the ESEP which yielded a resonance position of 2.56 eV and a width of 1.78 eV. No resonance was detected for the $^2\Sigma^+$ and $^2\Delta$ symmetries.

Jain and Norcross (1986) then considered the effect of stretching upon these target and scattering observables as obtained by the ESEP model. Specifically they computed first and second derivatives of the target observables with respect to CH and CN stretch. In the $^2\Pi$ scattering symmetry when the CN bond was stretched (with CH bond length fixed), the position and width of the shape resonance decreased; with CN bond contraction the opposite occurred. With respect to CH bond stretch (CN bond length fixed) there was no change. At the equilibrium geometry, for the $^2\Sigma^+$ scattering state no resonance was detected. Upon CH or CN bond stretch a shape resonance began to appear and a $^2\Sigma^+$ state resonance was detected at 2.3 a_0, which disappeared beyond 2.7 a_0.

Experimental works include those of Srivastava et al. (1978), Edard et al. (1990) and Burrow et al. (1992). These studies confirmed the existence of the $^2\Pi$ shape resonance. Edard et al. (1990) also obtained absolute cross sections by comparing, in the

same experimental conditions, the electron loss spectrum of the isoelectronic species N_2. However, none have considered electron impact excitation of HCN.

5.3 Previous Quantum Chemistry and Electron Scattering Studies of HNC

Schwenzer et al. (1975) provide a rare theoretical study of electronically excited HNC. They too reported adiabatic excitation energies. As their calculations used a double zeta basis set and single excitation CI, their results cannot be regarded as definitive. They compared their results to the corresponding ones for HCN. The ground state energy of HNC was predicted to lie 0.76 eV higher than HCN. In addition, although the symmetry ordering of the HNC electronic states was the same as HCN some of them were found to be lying below the corresponding states of HCN.

To our knowledge there has been no previous work, either experimental or theoretical, on electron collisions with HNC. However, HCN and HNC are each predicted to support an extremely weakly (dipole) bound anion state (Skurski et al., 2001). The only known experimental quantity is the dipole moment which has a value -1.20 a.u. (NIST, 2008).

5.4 HCN and HNC Quantum Chemistry Model

All the electronic structure calculations were carried out at the experimental equilibrium geometries (NIST, 2008). We employed two elaborate methods for these calculations– complete active space configuration interaction (CASCI) using Hartree-Fock molecular orbitals, and CASCI instead using pseudo natural orbitals. For HCN and HNC the ground state electronic configuration is $1\sigma^2\ 2\sigma^2\ 3\sigma^2\ 4\sigma^2\ 5\sigma^2\ 1\pi^4$, namely, both have a fully symmetric X $^1\Sigma^+$ electronic ground state. Since the UK R-matrix package only supports Abelian point groups (Morgan et al., 1998), all calculations discussed here were computed using the C_{2v} point group for which the ground state configuration then transforms to $1a_1^2\ 2a_1^2\ 3a_1^2\ 4a_1^2\ 5a_1^2\ 1b_1^2\ 1b_2^2$ (X $^1A_1$).

A number of Gaussian-type orbital (GTO) basis sets of double zeta quality or better were tested, including 6–31G, 6–31G* and 6–311G. In each case a Hartree-Fock self consistent field (HF-SCF) calculation was performed to obtain a set of occupied and virtual molecular orbitals. In the subsequent configuration interaction (CI) calculation, a complete active space was employed where the $1a_1$ and $2a_1$ orbitals (4 electrons) were frozen

and the remaining 10 electrons allowed to move freely among the $3a_1$, $4a_1$, $5a_1$, $6a_1$, $1b_1$, $2b_1$, $1b_2$ and $2b_2$ active space orbitals. The number of configuration state functions yielded for the ground state for such a CAS was 328 for both molecules. For calculations using Quantemol-N the basis set 6–31G was adopted. This software generates its own quantum chemistry model, subject to the analysis of molecular orbitals obtained from the SCF computation. Hence the complete active space used by Quantemol-N for the CI calculation was slightly larger than the study utilising the R-matrix package directly:

$$(1a_1 2a_1)^4 (3a_1 4a_1 5a_1 6a_1 7a_1 1b_1 2b_1 1b_2 2b_2)^{10} \tag{5.1}$$

whereas for HNC the Quantemol-N CAS and that of this work coincided.

One problem with representing the target states is the need to utilise a single set of molecular orbitals for all states. It is possible to improve the general quality of the target eigenfunction by constructing weighted pseudo natural orbitals (NOs). In all NO calculations we used the first five lowest states $^1A_1$, $^3A_1$, $^3A_2$, $^3B_1$ and $^3B_2$ to construct the wavefunctions. Each target state was represented by CI wavefunctions and all possible single and double excitations to unoccupied virtual orbitals were included. However, in order to incorporate double excitation and make the calculations feasible, it was necessary to freeze eight electrons (1s and 2s electrons of the C and N atoms). For both HNC and HCN, weighting coefficients were biased towards the ground state: 5.75, 1.5, 1.5, 1.5 and 1.5 for $^1A_1$, $^3A_1$, $^3A_2$, $^3B_1$ and $^3B_2$ respectively. Care must be taken in choosing a target model for a pseudo natural orbitals calculation because it is often the case that degeneracy between orbitals (e.g. b_1 and b_2) and hence target states can be broken. The weighting coefficients used in the present work yielded excellent degeneracy between the B_1 and B_2 (Π) and A_1 and A_2 (Δ) electronic states. For our pseudo natural orbitals study the incorporation of single and double excitations yielded about 9,000 configurations for the $^1\Sigma^+$ ground state.

The important observables obtained from this electronic structure calculation were the target Hamiltonian eigenvalues (hence the vertical excitation energies) and the dipole (and other higher order moments). For HCN these quantities are reported in table 5.1 and are compared with the adiabatic theoretical study of Nayak et al. (2005) and the experimental work of Herzberg (1966). In the present study we solved for 24 (C_{2v}) target electronic states; by default Quantemol-N only considers those states whose excitation

thresholds are below 10 eV, a typical ceiling for incident scattering electron energies. For purposes of brevity table 5.1 shows only those (eighteen) electronic states with excitation thresholds below ionisation together with the above-mentioned quantities. The dipole moments obtained in our study agree quite well with the more accurate coupled cluster study of Nayak et al. (2005). In particular, our target models using the 6–31G and 6–31G* basis, and the Quantemol-N model agree very well with the study of Maroulis and Pouchain (1996), who obtained a value of −1.18 a.u., and the experimental value of NIST (2008). There is, however, disagreement between the excitation thresholds of the present study with the data of Nayak et al. (2005) because the latter accounts for the geometric rearrangement of the nuclei post electronic excitation, and consequent reduction of the molecular symmetry to C_s. Hence we transformed the state assignments of Nayak et al. (2005) to $C_{\infty v}$ symmetry.

We compare our data to the cruder study of Schwenzer et al. (1975): table 5.2 shows that the data from Quantemol-N and the equivalent R-matrix calculation are in agreement because, as mentioned earlier the quantum chemistry models are precisely the same. The ground state dipole moments are all close to the observed value of −1.20 a.u. We also found that the HNC ground state lies 0.73 eV above that of HCN, close to the accurate value of 0.65 eV obtained by van Mourik et al. (2001).

5.5 HCN and HNC Scattering Calculation

Accurate computation of the resonance involves improved modelling of the polarisation interaction, which is achieved by inclusion of energetically closed electronic excitation channels (hence 24 states were included in the close-coupling expansion). As a result the eigenphase generally increases and the expected resonance position is lowered, reflecting the improved modelling. Scattering calculations were performed on all four C_{2v} scattering symmetries $^2A_1$, $^2B_1$, $^2B_2$ and $^2A_2$. The continuum GTOs employed were those of Faure et al. (2002) with partial wave expansion up to and including g-wave. They were Schmidt orthogonalised to the target molecular orbitals and then symmetrically (Löwden) orthogonalised among themselves. Only those continuum orbitals with eigenvalues (of the symmetric orthogonalisation overlap matrix) greater than (2×10^{-7}) were retained. One virtual orbital of each irreducible representation was chosen to augment the continuum orbital set in the inner region scattering wavefunction where orbitals were available to do so. The R-matrix sphere radius was set to 10 a_0. The scattering model

Target State	6-31G	6-311G	6-31G*	6-31G+NO	Q-N*	CC[a]	Expt.[b]
X $^1\Sigma^+$ ($^1A_1$)	-92.902	-92.911	-92.939	-92.939	-92.9109		
1 $^3\Sigma^+$ ($^3A_1$)	6.87	7.04	6.90	6.63	6.85	6.13	
1 $^3\Delta$ ($^3A_1$,$^3A_2$)	8.03	8.04	7.98	7.96	8.05	7.00	
1 $^3\Pi$ ($^3B_1$,$^3B_2$)	8.50	8.61	8.89	8.53	8.50	4.44	8.53[c]
1 $^3\Sigma^-$ ($^3A_2$)	8.72	8.72	8.67	8.97		5.47	
1 $^1\Sigma^-$ ($^1A_2$)	9.09	9.02	8.98	9.23	9.15	6.48	6.48
1 $^1\Delta$ ($^1A_1$, $^1A_2$)	9.41	9.30	9.26	9.82		6.93	6.77
1 $^1\Pi$ ($^1B_1$,$^1B_2$)	9.84	9.91	10.18	10.04	9.83	8.10	8.10
2 $^3\Pi$ ($^3B_1$,$^3B_2$)	11.87	11.69	11.7			6.81	
2 $^1\Pi$ ($^1B_1$,$^1B_2$)	12.17	11.80	11.98			8.64	8.88
2 $^3\Sigma^+$ ($^3A_1$)	12.40	12.16	12.61				
2 $^1\Sigma^+$ ($^1A_1$)	12.53	12.24	12.76			7.79	
3$^3\Pi$ ($^3B_1$,$^3B_2$)						7.47	
μ/a.u.	−1.19	−1.21	−1.17	−1.13	−1.193	−1.26[d]	−1.173[e]

Table 5.1: HCN vertical excitation energies, in eV, as calculated in this work and compared to the published adiabatic excitation energies. Also given are the absolute ground state energy of the target, in Hartree, the ground state dipole transition moment and the number of CSFs generated by the CAS CI calculation. The state designations are given in $C_{\infty v}$ (C_{2v}) point group symmetry.

* Quantemol-N

[a] Nayak et al. (2005)

[b] Herzberg (1966)

[c] Krishnamachari and Venkatasubramanian (1984)

[d] Jain and Norcross (1985)

[e] NIST (2008)

used by Quantemol-N was the same as the direct R-matrix study except that only those electronic target states with excitation thresholds below 10 eV (the ceiling set for the incident electron energies) were included in the close coupling expansion.

Convergence of the polarisation interaction remains an issue for calculations based on the close-coupled approximation (Gil et al., 1994; Gorfinkiel and Tennyson, 2004). It is for this reason that methods were used which differed in the way the target molecular virtual orbitals were employed, in addition to varying quantum chemistry parameters. Initial calculations contracted the virtual orbitals with the continuum therefore allow-

Target State	6-31G	6-311G	6-31G*	6-31G+NO	Quantemol-N	Theory[a]
X $^1\Sigma^+$ ($^1A_1$)	-92.875	-92.892	-92.909	-92.897	-92.875	
1 $^3\Pi$ ($^3B_1$,$^3B_2$)	6.16	6.40	6.48	6.20	6.16	
1 $^3\Sigma^+$ ($^3A_1$)	7.88	7.94	7.91	7.45	7.88	4.46
1 $^3\Delta$ ($^3A_1$,$^3A_2$)	8.61	8.63	8.65	8.36	8.61	4.60
1 $^3\Sigma^-$ ($^3A_2$)	8.98	8.99	9.06	8.94		5.22
1 $^1\Pi$ ($^1B_1$,$^1B_2$)	9.01	9.08	9.313	9.18	9.01	7.34
1 $^1\Sigma-$ ($^1A_2$)	9.26	9.25	9.310	9.20	9.26	4.95
1 $^1\Delta$ ($^1A_1$,$^1A_2$)	9.27	9.26	9.35	9.38		5.51
2 $^3\Sigma^+$ ($^3A_1$)	10.52	10.23	10.66	13.31		5.44
2 $^1\Sigma^+$ ($^1A_1$)	10.56	10.25	10.71	13.42		6.22
2 $^3\Pi$ ($^3B_1$,$^3B_2$)	11.85	11.46	11.67	13.83		
2 $^1\Pi$ ($^1B_1$,$^3B_2$)	12.23	11.71	12.05			8.50
2 $^3\Sigma^-$ ($^3A_2$)						5.96
2 $^1\Sigma^-$ ($^1A_2$)						8.17
$3^3\Sigma^-$ ($^3A_2$)						6.09
μ/a.u	-1.15	-1.21	-1.16	-1.146	-1.15	

Table 5.2: HNC vertical excitation energies, in eV, calculated in the present work compared to the published adiabatic excitation energy. The absolute ground state, in Hartree and the ground state dipole moment in a.u. are also given

[a] Schwenzer et al. (1975)

ing the scattering electron the occupy them, meaning that such CSFs were treated as arguments of the first summation of the coupled-states (or close-coupled) expansion. To allow for increased short range polarisation models which treat the CSFs where the scattering electron occupies the virtual MOs separately from when it occupies the continuum orbital were tested. Such CSFs are therefore uncontracted and analysed as part of the second L^2 summation of the CC expansion. The resonance parameters were obtained by fitting the eigenphase sum curve to the Breit-Wigner profile (Tennyson and Noble, 1984).

5.5.1 Eigenphase Sums and Resonance Parameters

Figure 5.1 shows the $^2\Sigma^+$ eigenphase sum curve for HCN which rises sharply as the scattering energy tends to zero, in accordance with Levinson's theorem for a system sup-

Model	E_r	Γ_r
6–31G	2.83	1.34
6–31G[a]	2.46	1.14
6–311G	2.84	1.49
6–31G*	3.14	1.59
6–31G + NO[a]	2.79	1.22
Quantemol-N	3.27	1.64
Theory[b]	2.56–2.80	1.78–2.40
Experiment[c]	2.26	

Table 5.3: HCN $^2\Pi$ shape resonance parameters, in eV, as a function of theoretical model

[a] uncontracted CSFs employed in $N + 1$-eigenket close-coupling expansion,

[b] Jain and Norcross (1985),

[c] Burrow et al. (1992)

porting a weakly bound state. The $^2\Sigma^+$ eigenphase for HNC shows a similar behaviour. Importantly, no resonance structure was observed for this scattering symmetry. Furthermore the structure of the curve at energies below the first excitation threshold (about 6.8 eV) is similar to the curve given by Jain and Norcross (1985). Figure 5.2 which presents the same data for the $^2\Pi$ scattering symmetry, shows the clear signature of a broad low-energy shape resonance. For both scattering symmetries our eigenphases show considerable threshold structure, associated with the opening of new excitation channels above 6.8 eV; this structure is not present in the eigenphases of Jain and Norcross (1985) because they employed a 1-state approximation.

Table 5.3 summarises the results we obtained for the position and width of the $^2\Pi$ resonance. These results show considerable sensitivity to the precise model used, with the position varying by more than 0.5 eV and the width by over 20% between different calculations. This behaviour is similar to that observed by Jain and Norcross (1985), for whom the results which explicitly included polarisation effects are quoted. Unsurprisingly their static exchange calculations gave resonances which are systematically higher and broader.

Our predicted resonances for HCN lie at very similar energy positions to those of Jain and Norcross (1985), the lowest being 0.2 eV higher than the most precise experimental measurement of Burrow et al. (1992). However, one should note that this experiment measures the adiabatic resonance energy, whereas the theoretical values are for the

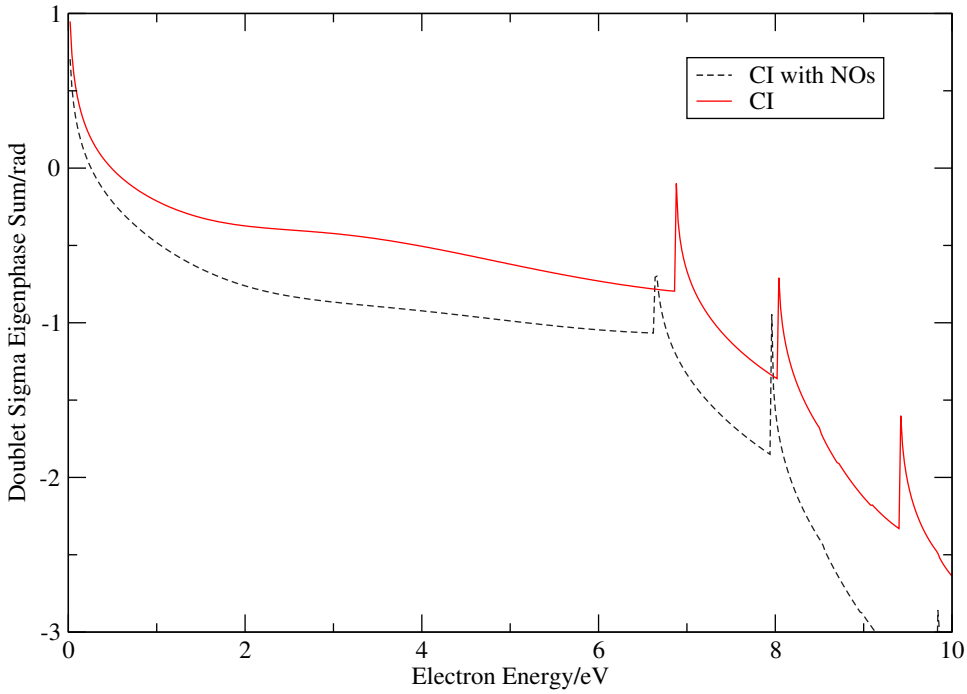

Figure 5.1: Comparison of HCN $^2\Sigma^+$ eigenphase sum curve

Model	E_r	Γ_r
6–31G	2.77	0.91
6–31G^a	2.57	0.80
6–311G	2.90	1.06
6–31G*	3.03	1.10
6–31G + NO^a	2.43	0.67
Quantemol-N	3.15	1.15

Table 5.4: HNC $^2\Pi$ shape resonance parameters, in eV, as a function of theoretical model
^{a} uncontracted CSFs employed in $N+1$-eigenket close-coupling expansion

higher vertical energies. The HCN $^2\Pi$ shape resonance as obtained by our study is quite broad and systematically lower than the two studies of Jain and Norcross (1985, 1986). Generally, a narrower resonance corresponds to an improved treatment of short-range polarisation effects. The widths obtained, which are greater than 1 eV, are consistent with the experimental findings that the resonance is too broad to support vibrational structure (Burrow et al., 1992). No Feshbach resonances were detected for HCN. Calculations predict that HNC also has a $^2\Pi$ shape resonance- this is to be expected since HNC is isoelectronic to HCN. The resonance parameters obtained are given in tables 5.4, 5.5 and 5.6.

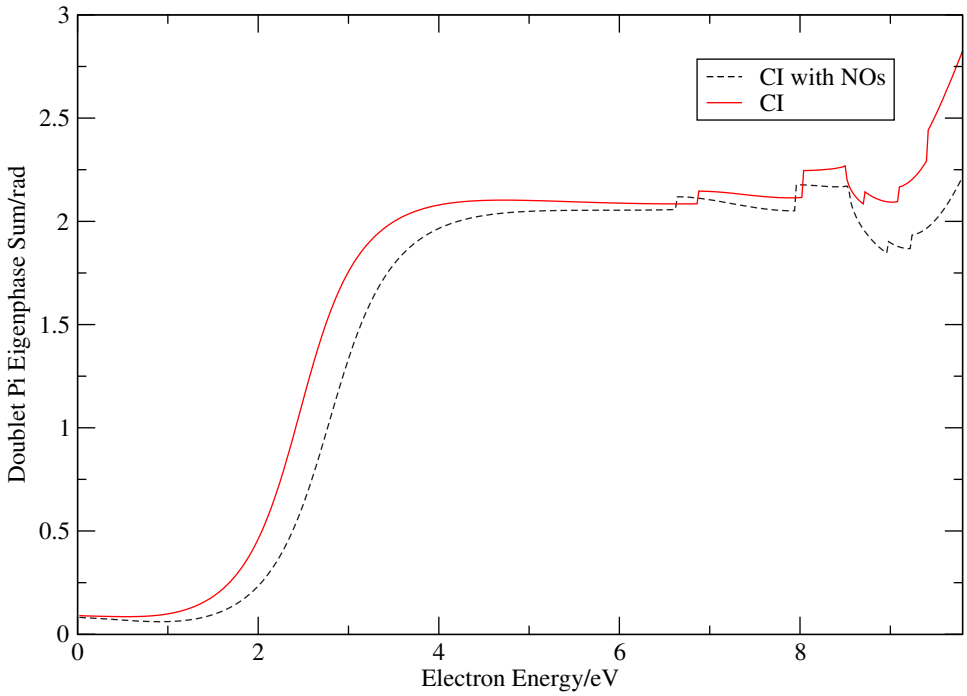

Figure 5.2: Comparison of HCN $^2\Pi$ eigenphase sum curve

Model	E_r	Γ_r
6–31G		
6–31G^a	7.82	$2.2\times\ 10^{-3}$
6–311G	7.85	$3.0\times\ 10^{-3}$
6–31G*		
6–31G + NO^a	7.43	$1.2\times\ 10^{-3}$
Quantemol-N	7.84	$9.6\times\ 10^{-4}$

Table 5.5: HNC $^2\Sigma^+$ Feshbach resonance parameters, in eV, as a function of theoretical model
^{a} uncontracted CSFs employed in $N+1$-scattering eigenket close-coupling expansion

The calculations predict the position of the $^2\Pi$ shape resonance to be similar to the corresponding HCN resonance, but narrower with a width of about 60 % of that computed for HCN.

The chief distinction between electron scattering by HCN and HNC is that the latter yields a number of narrow resonances which, unlike the shape resonances obtained for both isomers, appear only in those calculations with an enhanced treatment of polarisation. Such behaviour is thus characteristic for Feshbach resonances which are absent in scattering calculations which do not treat polarisation effects adequately.

Tables 5.5 and 5.6 gives parameters for the $^2\Sigma^+$ and $^2\Delta$ Feshbach resonances respec-

Model	E_r	Γ_r
6–31G		
6–31G[a]	8.57	4.0×10^{-4}
6–311G		
6–31G*	8.61	5.5×10^{-4}
6–31G + NO[a]	8.34	3.5×10^{-4}
Quantemol-N	8.58	3.4×10^{-4}

Table 5.6: HNC $^2\Delta$ Feshbach resonance parameters, in eV, as a function of theoretical model [a] uncontracted CSFs employed in $N+1$-scattering eigenket close-coupling expansion

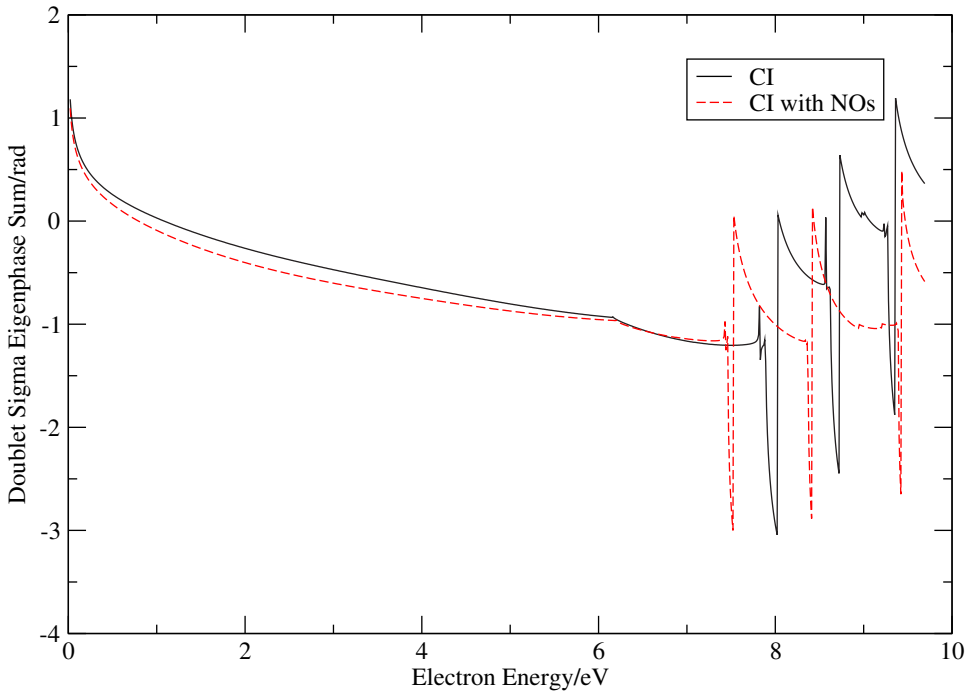

Figure 5.3: Comparison of HNC $^2\Sigma^+$ eigenphase sum curve

tively. Observables absent from the tables correspond to models that did not detect a resonance. The resonance positions in the tables appear to vary by almost 0.5 eV. This is not actually a property of the scattering calculation but of the underlying representation of the electronic target states. With reference to table 5.2, it appears that the $^2\Sigma^+$ and $^2\Delta$ resonances appear to be associated with the first excited $^3\Sigma^+$ and $^3\Delta$ states of HNC respectively. In all cases our calculations found that the resonance appears less than 0.1 eV below their respective channel thresholds. Sensitivity of the resonance position is therefore directly associated with differences in the target excitation thresholds. The correlation between which models (those employing uncontracted CSFs to model short-

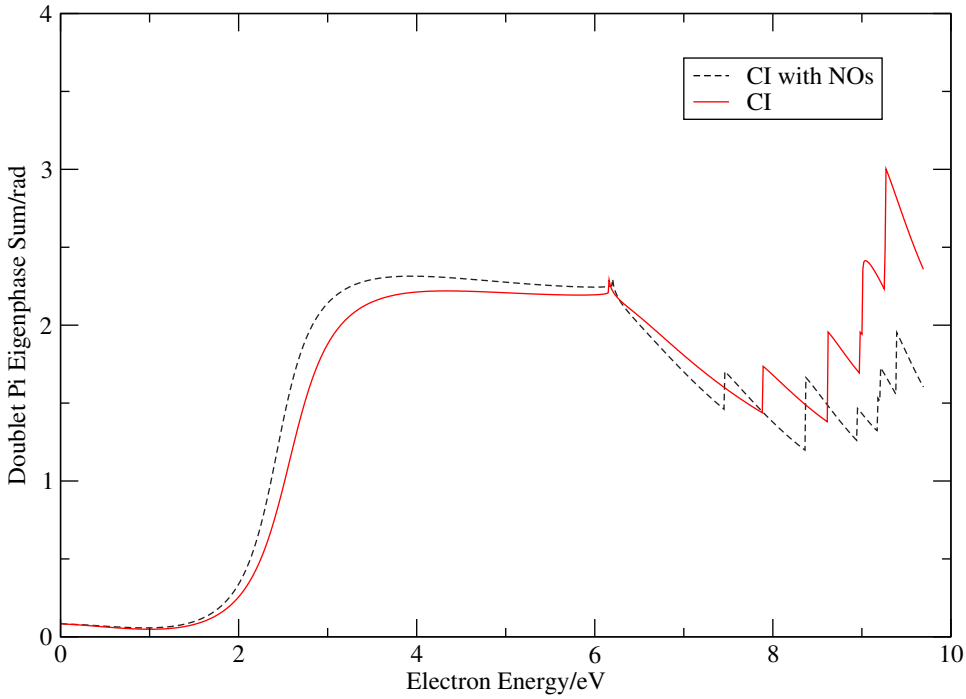

Figure 5.4: Comparison of HNC $^2\Pi$ eigenphase sum curve

range polarisation) predict Fechbach resonances of $^2\Sigma$ and $^2\Delta$ symmetry is not surprising given that both resonances arise from the addition of a σ electron to target states with the same configuration ($1\sigma^2\ 2\sigma^2\ 3\sigma^2\ 4\sigma^2\ 5\sigma^2\ 1\pi^3\ 2\pi^1$); these resonances probably have the same configuration: $1\sigma^2\ 2\sigma^2\ 3\sigma^2\ 4\sigma^2\ 5\sigma^2\ 1\pi^3\ 2\pi^1\ 6\sigma^1$. Figures 5.3 and 5.4 show the $^2\Sigma^+$ and $^2\Pi$ eigenphases. Below the channel excitation thresholds both are similar to those of HCN as the two species are isoelectronic. Above the thresholds the eigenphases display considerable structure owing to the opening of new scattering channels.

5.5.2 Electronic Excitation

Electron-impact electronic excitation of either HCN or HNC does not appear to have been considered previously. Figures 5.5–5.8 give electron-impact excitation cross sections for excitation to the two lowest electronic states of HCN and HNC respectively. These observables were calculated using a 6–31G GTO basis set and uncontracted CSFs. The main variation between theoretical models in the magnitude of the excitation cross-sections in the near threshold region is due to the location of the excitation threshold. Hence the resonance energy position is determined by the quality of the quantum chemistry model rather than the parameters of the scattering models. Given the absence of previous studies it is not possible to make any sort of comparison.

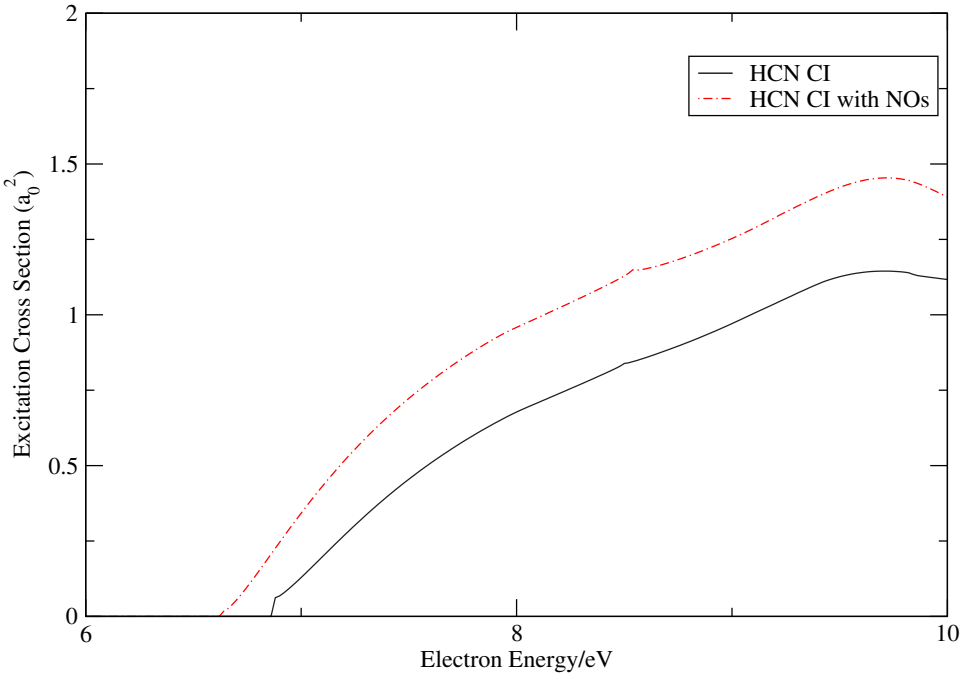

Figure 5.5: Comparison of HCN $X\ ^1\Sigma^+ \rightarrow\ ^3\Sigma^+$ electronic excitation cross-sections

5.6 Conclusion

The *ab initio* R-matrix method has been applied to electron scattering by HCN and HNC. The present work represents the first study to have been carried out upon electron scattering by HNC. 24 target states were retained in the inner region (close-coupled scattering wavefunction) and in the outer region so as to attain an improved model of the polarisation interaction. They were represented by configuration interaction (CI) wavefunctions in which four electrons were frozen in all configurations and ten electrons allowed to move amongst the 3σ, 4σ, 5σ, 6σ, 1π and 2π target virtual orbitals. Of the 24 electronic states 16 were closed channels in the incident scattering energies considered here. In the best model the target eigenkets were subsequently improved by the use of pseudo natural orbitals incorporating all the possible single and double excitations to unoccupied virtual orbitals. For HCN a shape resonance of $^2\Pi$ symmetry was detected in all the models that were tested. This has been confirmed experimentally (Burrow et al., 1992; Srivastava et al., 1978) and theoretically (Jain and Norcross, 1985, 1986), the results of which are in good agreement with the corresponding observables of this inquiry. Although the width has not been determined experimentally, the present scattering calculations suggest that the width is narrower than that predicted by Jain and Norcross (1985). Generally, resonances tend to narrow with the improved treatment of

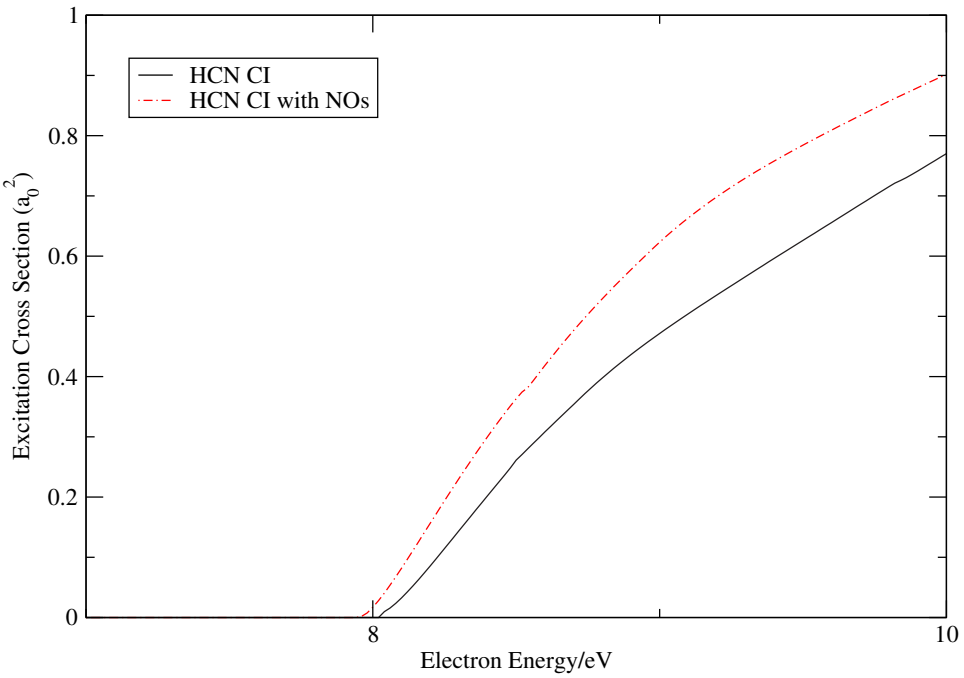

Figure 5.6: Comparison of HCN $X\ ^1\Sigma^+ \rightarrow\ ^3\Delta$ electronic excitation cross-sections

polarisation, hence the narrowest width (1.14 eV) may be the upper bound on the true width.

Electron scattering by the HNC isomer also yields a $^2\Pi$ shape resonance at a similar energy to its HCN^- counterpart, but with a smaller width. However, unlike HCN, HNC supports a number of Feshbach resonances. Particularly, the superior calculations found narrow resonances of $^2\Sigma^+$ and $^2\Delta$ symmetry lying less than 0.1 eV below their electronically excited parent states respectively. These probably arise from the same configuration:

$$1\sigma^2 2\sigma^2 3\sigma^2 4\sigma^2 5\sigma^2 1\pi^3 2\pi^1 6\sigma^1 \tag{5.2}$$

Coupled state electron scattering calculations such as those of the present work contain a wealth of information on various scattering processes. Results on electron impact excitation have been presented for both isomers. The T-matrices and dipole moment obtained from the best model for HCN and HNC were employed in the study of electron impact rotational excitation and de-excitation rate coefficients (chapter 10) which are of particular importance in astrophysics (Lovell et al., 2004).

Finally, the opportunity was taken to compare the results with those obtained by the new Quantemol-N expert system. This application yielded similar results to those

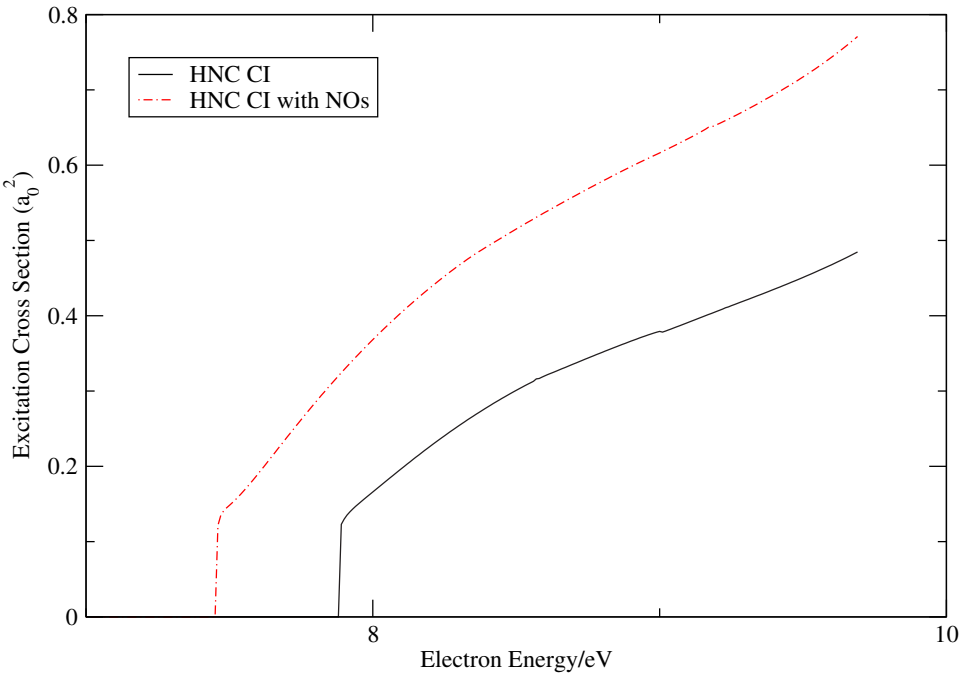

Figure 5.7: Comparison of HNC $X\ ^1\Sigma^+ \rightarrow\ ^3\Sigma^+$ electronic excitation cross-sections

obtained using the R-matrix package directly. The most important difference, which gave rise to higher positions in the shape resonances, is the reduced number of target states that were used in the inner and outer region in its default model.

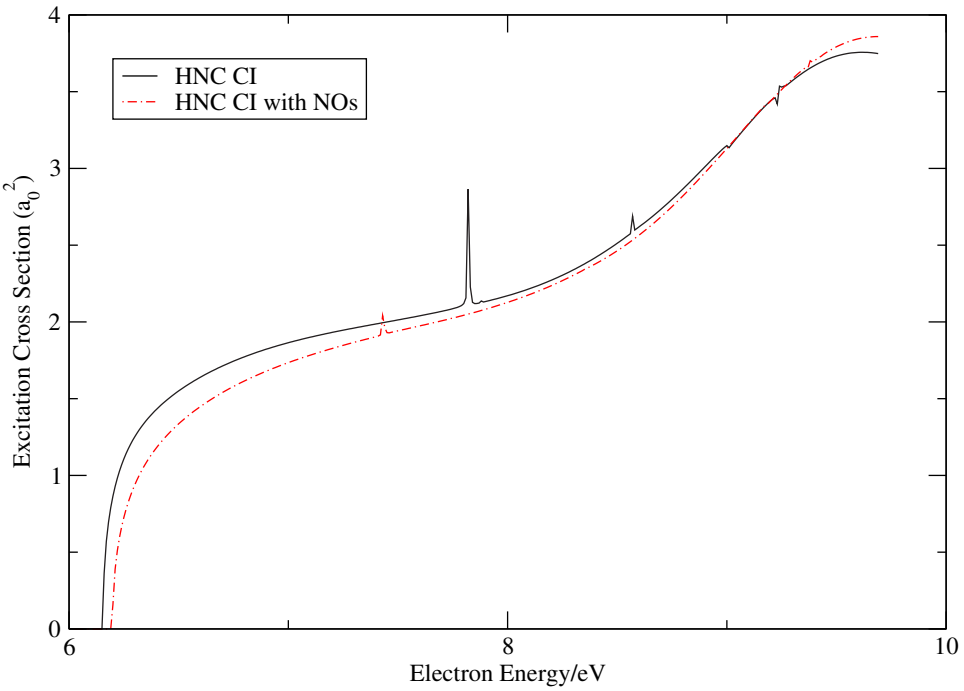

Figure 5.8: Comparison of HNC $X\ ^1\Sigma^+ \rightarrow\ ^3\Pi$ electronic excitation cross-sections

Chapter 6

Electron Collision with the CO Molecule

6.1 Introduction

The species CO is the most abundant molecule in the interstellar medium after H_2. It has been detected in the ISM and, for the first time, in Uranus' atmosphere using infrared spectroscopy (Encrenaz et al., 2009) and its bands have been confirmed in M dwarfs (Pavlenko and Jones, 2002). Consequently, detailed infra-red observations of the CO 2–0 bands in the 2.297–2.310 μm region of M dwarfs have been made by Jones et al. (2005). Sensitive measurements of CO and its isotopomers ^{13}CO, $C^{18}O$ and $C^{17}O$ have been presented by Harrison et al. (1999) in the rotational lines $J = 1 \rightarrow 0$, $2 \rightarrow 1$ and $3 \rightarrow 2$. Other astrophysical studies of CO and its isotopologues include Wada and Tomisaka (2005), Bayet et al. (2006), Paglione et al. (2001), Williams and Blitz (1998) and Crovisier et al. (1995). It has also been observed in comets (Jewitt et al., 1996)

The high abundance of CO in the interstellar medium has been the motivation for a number of collision studies, particularly those with atoms: the study of Pestellini et al. (2002), for example, applied the full close-coupling (CC) method to ^4He scattering by CO. Using the infinite sudden order (IOS) approximation calculations were carried out of cross sections for energy transfer between vibrational levels of CO. Pestellini et al. (2002) made two key findings: that vibrational energy transfer was dominated by the transition $\Delta\nu = 0$ and, interestingly, at low energies the scattering was dominated by a shape resonance.

Electron collisions have also been shown to be important interactions in the interstellar medium. The calculations of DiSanti et al. (2001) in particular strongly suggested that rotational populations in comets could in fact be controlled by collisions with elec-

trons rather than radiative cooling.

Unlike HCN and HNC, CO has a very small dipole moment with an experimental value of −0.043 a.u. (Muenter, 1975) therefore making it comparatively more difficult to model in terms of quantum chemistry, and an interesting theoretical property of CO is that the dipole moment direction yielded by its Hartree-Fock wavefunction has the opposite sign of the one observed experimentally. This is corrected using a complete active space configuration interaction (CASCI or CI) wavefunction (Harrison (2006) and references therein). It is because of the abundance of CO in the ISM and the fact that CO remains stable after the electron has collided with it that the present study is carried out.

This chapter will discuss previous quantum chemistry and electron scattering calculations. It presents a new application of the *ab initio* R-matrix method to electron scattering by CO. Rotationally summed differential cross sections for a selected range of incident electron energies (1 eV, 1.91 eV, 3 eV and 5 eV) were also calculated using the Born closure approach of Itikawa (2000) to confirm the accuracy of the models set up. The Binary Encounter Bethe (BEB) electron impact ionisation cross sections (Hwang et al., 1996; Kim and Rudd, 1994) were computed using Quantemol-N (Tennyson et al., 2007).

All calculations carried out during the present study employed the fixed nuclei approximation. The positive direction of the dipole moment μ was assigned to the polarity C^+O^-. As shall be seen below, a negative sign implies the opposite polarity C^-O^+.

6.2 Previous Quantum Chemistry and Electron Scattering Studies

There has been major concern about the disparity between the sign yielded by the *ab initio* theoretical value and experimental measurement of the CO dipole moment. An experimental determination was carried out by Muenter (1975) who obtained a value of −0.043 a.u. The theoretical calculation of Huo (1965) obtained the opposite polarity to that observed in microwave experiments (Rosenblum et al., 1958; Burrus, 1958); Billingsley and Krauss (1974) carried out a multi-configurational self-consistent field computation (MCSCF) of the dipole function for CO and obtained a dipole moment −0.0657 a.u. (−0.167 D).

The work of Harrison (2006) was devoted to the effect of correlations on the direction of the CO dipole moment as a function of internuclear distance using the aug-cc-pV5Z basis set and the complete active space self consistent field (CASSCF) and multi-reference configuration interaction (MRCI) methods. They also corrected the sign of the dipole moment using these methods. Their study yielded equilibrium dipole moments of -0.137 a.u. and -0.073 a.u. respectively, a little higher than measured experimentally. According to Harrison, the sign of the dipole moment changes because there is a distance R such that the charge contribution $q(O)R$ is negative ($q(O) = -0.0733e$), and the sum of the induced atomic dipoles is positive, and they cancel.

Kirby-Docken and Liu (1977) performed detailed electronic structure calculations of CO. Using CASCI wavefunctions they computed the potential energy curve and dipole moment function for the ground state X $^1\Sigma^+$. Kirby-Docken and Liu (1977) focused on three types of CI calculations and determined the occupied and virtual molecular orbitals using the multi-configuration self-consistent field (MCSCF) calculation as a function of internuclear distance. The core 1s electrons of the C and O atoms were frozen in all configurations. Their first CI wavefunction included all 176 CSFs of $^1\Sigma^+$ symmetry assignment generated by distributing the 10 valence electrons into the space (3σ, 4σ, 5σ, 6σ, 1π, 2π); their second CI calculation was a first order configuration interaction (FOCI) calculation; and the third CI calculation involved incorporating all possible single and double excitations (CISD). All these calculations exhibited a sign change at 2.4 a_0 ($R_{CO,eq} = 2.132$ a_0 NIST (2008)) and at the equilibrium geometry all three calculations yielded values of the dipole moment that were higher than experiment (-0.043 a.u. Muenter (1975)). In addition they also analysed the dipole moment derivatives.

There are a wealth of electron scattering calculations carried out on CO at various levels of approximations. Particularly, two fixed nuclei R-matrix calculations have been carried out by Salvini et al. (1984) at the 1-state static exchange (SE) and static exchange-plus-polarisation (SEP) approximation. Salvini et al. (1984) used the UK diatomic R-matrix package and their calculations were carried out on the $^2\Sigma^+$, $^2\Pi$ and $^2\Delta$ scattering symmetries using the SCF target wavefunctions of Nesbet (1964) augmented by a δ Slater type orbital. The basis set consisted of 7 σ and 3 π Slater-type orbitals centred on each nucleus. Salvini et al. (1984) carried out additional work using the more accurate target function of McLean and Yoshimine (1968). These two

wavefunctions yielded ground state eigenvalues of -112.758 E_h and -112.789 E_h and dipole moments $+0.156$ a.u. and $+0.105$ a.u. respectively at the equilibrium geometry compared to -0.043 a.u (Muenter, 1975). The continuum basis set consisted of a partial wave expansion up to and including $l = 6$ in order to obtain converged solutions for all the scattering symmetries considered. In the setup of their SE calculations two or three square integrable (L^2) functions were retained, where the scattering electron was allowed to occupy the 6σ, 7σ or 8σ, the 2π, 3π or 4π and the 1δ or 2δ virtual molecular orbitals for the $^2\Sigma^+$, $^2\Pi$ and $^2\Delta$ scattering symmetries respectively. In their SEP calculations 2-particle,1-hole correlation functions were also included, where one electron was excited out of the 4σ, 5σ or 1π occupied molecular orbitals into the 6σ, 7σ, 8σ, 2π, 3π and 4π virtual orbitals. Virtual excitations to the 1δ and 2δ virtual orbitals were also included for the final converged calculations using the Nesbet target wavefunctions. Their $^2\Pi$ eigenphase sum curve was found to be in good agreement with the previous static exchange studies of Levin et al. (1980) and Collins et al. (1980), and confirmed the existence of the low-energy $^2\Pi$ shape resonance. The SEP calculation resulted in the position of the resonance being shifted to lower energies, in good agreement with the corresponding experimental values. The best SEP calculation gave a position E_r=1.72 eV and a width Γ_r=0.76 eV compared to E_r=1.8 eV and Γ_r=1.0 eV measured by Tronc et al. (1980). Salvini et al. (1984) also explored the variation of the resonance parameters with respect to bond contraction and stretching at both the SE and SEP approximations. The trend they observed was that with bond contraction the resonance position shifted to higher energies and broadened, while with bond stretch the resonance narrowed. Salvini et al. (1984) recommended that further study be carried out on e-CO scattering using post-Hartree-Fock methods and include nuclear motion.

Other theoretical studies include the R-matrix calculation of Morgan (1991), which included vibrational excitation channels by non-adiabatic means using the method proposed by LeDourneuf et al. (1979). The occupied and virtual molecular orbitals were computed by Morgan (1991) using SCF (self-consistent field) optimisation using STO (Slater-type) atomic basis sets. The CASCI model adopted by Morgan (1991) froze the 8 core electrons (1s and 2s electrons of the C atom and O atom) and the remaining 6 electrons allowed to move among the orbitals 5σ, 6σ, 1π and 2π occupied and virtual molecular orbitals, which is smaller than the CAS that would normally be used. Nevertheless the model resulted in a dipole moment (-0.049 a.u.) in excellent agreement

with experiment (Muenter, 1975). The scattering calculations were carried out at the SE, SEP and close-coupled (CC) levels of approximation and, like Salvini et al. (1984), a continuum basis set with partial wave expansion up to $l = 6$ was used as well. The study analysed scattering for the bond lengths 1.8, 1.9, 2.0, 2.132, 2.25, 2.35, 2.5, 2.65, 2.8 and 3.0 a_0. Morgan (1991) observed that the resonance parameters where very sensitive to the precise scattering model employed- in tandem with Salvini et al. (1984) the retention of δ orbitals had a significant effect upon the parameters. The best model yielded a position and width of 1.68 eV and 0.95 eV respectively.

Using the R-matrix diatomic code a later *ab initio* R-matrix study was carried out by Morgan and Tennyson (1993) at the many-state close-coupling approximation, where the target electronic states were represented by CASCI eigenfunctions. For the continuum orbitals partial wave expansion was again up to and including $l = 6$ partial waves. In the set up of the target wavefunctions Morgan and Tennyson (1993) employed an STO (Slater-type orbitals) basis set that yielded 12 σ, 8 π, 6 δ and 2 ϕ occupied and virtual molecular orbitals. The target wavefunctions were constructed using an active space consisting of the 5σ, 6σ, 1π and 2π molecular orbitals. Fixed-nuclei calculations were carried out on the same grid of 10 bond lengths as Morgan (1991). The CC expansion retained those electronically excited states whose vertical excitation energies were below 12 eV and an R-matrix radius of 10 a_0 was used; although a number of sphere radii were tested, all the scattering observables were found to be insensitive to variation of radius. Morgan and Tennyson (1993) carried out their calculations for incident electron energies 6–18 eV and the total scattering symmetries $^2\Sigma^+$, $^2\Pi$, $^2\Delta$ and $^2\Phi$. 6 resonances were detected in total: 3 of $^2\Pi$ symmetry and one for each of the symmetries $^2\Sigma^+$, $^2\Delta$ and $^2\Phi$. At the larger bond lengths the $^2\Pi$ shape resonance was observed to become a bound state, in keeping with the findings of Salvini et al. (1984).

The study of Jain and Norcross (1992) employed an exact-exchange plus parameter free polarisation model, also in the fixed nuclei approximation, and considered an incident electron energy range of 5 meV to 10.0 eV. The scattering observables computed were the rotationally resolved elastic, inelastic, and averaged differential, integral and momentum transfer cross-sections. In order to overcome poor convergence of the total and differential cross sections they employed the multipole-extracted adiabatic nuclei (MEAN) approximation (Norcross and Padial, 1982). Their quantum chemistry model involved using a near-Hartree-Fock limit wavefunction, and the Gaussian-type orbital

basis set for the X $^1\Sigma^+$ ground state was generated using standard molecular structure codes. The wavefunctions were hence used to obtain the ground state target Hamiltonian eigenvalue ($-112.7708\ E_h$), and the dipole, quadrupole and octupole moments: the dipole moment (+0.0993 a.u.) was about twice the accepted experimental value of -0.043 a.u. (Muenter, 1975). Jain and Norcross (1992) solved a set of integral equations for the radial part of the continuum for a particular scattering symmetry with the exchange interaction neglected for the higher scattering symmetries. The effects of polarisation were modelled free of adjustable parameters via a correlation-polarisation model. The experimental values of the spherical and non-spherical polarisabilities at the equilibrium geometries (α_0=13.34 a_0^3 and α_2=2.39 a_0^3) were substituted into the correlation-polarisation model. Jain and Norcross (1992) confirmed the conclusions of the previous studies that low-energy electron collisions with CO are dominated by a low-energy $^2\Pi$ shape resonance, whose parameters they predicted to be 3.30 eV and 1.91 eV in the case of exact static exchange (ESE) and 1.85 eV and 0.95 eV in the case of exact static-exchange-plus-polarisation (ESEP), in good agreement with previous theoretical and experimental studies. Their resonances were obtained by fitting to the Breit-Wigner profile. Jain and Norcross (1992) also observed that the $^2\Pi$ resonance was sensitive to treatment of exchange and polarisation effects. Their use of Hartree-Fock wavefunctions meant they over-estimated forward scattering at very low-energies.

The work of Zetner et al. (1998) measured the differential and integral cross sections for electron impact excitation of the a $^3\Pi$, a$'$ $^3\Sigma^+$, d $^3\Delta$ and A $^1\Pi$ electronic target states of CO at energies very close to the ionisation threshold (10, 12.5 and 15.0 eV) to complete the missing data occurring between the data of Zobel et al. (1996) and Middleton et al. (1993).

With respect to the experimental electron scattering studies carried out on CO, work has been carried out by Tronc et al. (1980) and Buckman and Lohmann (1986), the latter of which focused on the region around the $^2\Pi$ shape resonance (0.5–5 eV) using a time-of-flight spectrometer. Their total cross-section data, computed using the Beer-Lambert law, predicted the existence of a resonance at about 1.95 eV. In addition there are the low-energy studies of Kwan et al. (1983) and Zubek and Szmytkowski (1979); finally there are also the works of Jung et al. (1982) and Furlong and Newell (1993) measured the rotational-vibrational differential cross section in the energy range 0.5 eV to 6 eV for ΔJ=0,+1,+2,+3 and +4. Experimental cross sections at the high end of the incident

energy spectrum have been measured by Hudson et al. (2004), Freund et al. (1990) and Orient and Srivastava (1987).

The results of the present study are compared to the works discussed above.

6.3 Quantum Chemistry Model of CO

The quantum chemistry calculations were carried out in the equilibrium geometry of the CO diatomic (R_{CO}=1.1283Å) in the abelian C_{2v} point group (natural point group $C_{\infty v}$) using the polyatomic R-matrix package (Morgan et al., 1998).

In carrying out this part of the study, care was taken to try and correct the sign of the dipole moment yielded by the Hartree-Fock (HF) wavefunction using the configuration interaction (CI) target wavefunction, and ensure that the magnitude of the dipole moment for the CI calculation was as close as possible to the experimental value for later use in the differential cross section calculation discussed below. To this end a number of models were tested which varied the GTO (Gaussian-type orbital) atomic basis sets and the complete active space (CAS) used to construct the target wavefunction. The trial calculations used 6–311G, 6-311G with d-polarisation (6–311G*) and DZP basis sets and the active spaces

$(3a_1,4a_1,5a_1,6a_1,1b_1,2b_1,1b_2,2b_2)^{10}$ (CAS-0);

$(3a_1,4a_1,...,7a_1,1b_1,2b_1,1b_2,2b_2)^{10}$ (CAS-1);

$(3a_1,4a_1,...,8a_1,1b_1,2b_1,1b_2,2b_2)^{10}$ (CAS-2);

$(3a_1,4a_1,5a_1,6a_1,1b_1,2b_1,3b_1,1b_2,2b_2,3b_2)^{10}$ (CAS-3);

$(3a_1,4a_1,...,7a_1,1b_1,2b_1,3b_1,\ 1b_2,2b_2,3b_2)^{10}$ (CAS-4)

In all of the above configurations the $1a_1$ and $2a_1$ molecular orbitals were frozen. The HF and CI calculations using CAS-0 were carried out using Quantemol-N (Tennyson et al., 2007) for its ability to set up and perform these calculations with great speed. In all, six eigenvalues per target state (48 target state eigenfunctions in total) were computed. For all the dipole moments listed in table 6.1 the positive direction of the dipole moment vector was taken to be from the carbon atom to the oxygen atom.

The table 6.1 shows the dipole moments obtained using the models listed above. No change in the dipole moment sign was observed when basis set 6–311G was used. In contrast, DZP and 6–311G* yielded the required dipole moment sign change. The model CAS-1 using basis set DZP (hereafter defined by the triple (DZP, CAS-1, 48) where DZP is the basis set, CAS-1 is the complete active space and 48 is the total

Model	μ a.u.		
	6–311G	DZP	6–311G*
HF	+0.19624	+0.0935	+0.10615
CAS-0		−0.0234	−0.0123
CAS-1	+0.0421	−0.0332	−0.0267
CAS-2	+0.0459	−0.0312	−0.0295
CAS-3	+0.05001		
CAS-4	+0.01555		

Table 6.1: Table of CO permanent dipole moments

number of target wavefunctions) was chosen as the best target model for the scattering study discussed below as it gave a value of the dipole moment that was also closest to the absolute experimental value. This model gave the value of the ground state energy as −112.81096 E_h. The vertical excitation thresholds yielded by target model (DZP, CAS-1, 48) are given in table 6.2: only those target states with vertical excitation energies less than the ionisation threshold (for the DZP basis set, 15.01 eV– see table 6.4) are shown.

It is clear from table 6.2 that the thresholds are systematically higher than experiment and the study of Morgan and Tennyson (1993) where the latter employed a smaller complete active space and a different (Slater-type) basis set. Also given in table 6.2 is the spherical polarisability, computed using second-order perturbation theory, which has a value of just over a half of the accepted experimental value. This observable gives an indication of how well the polarisation will be modelled in the outer region. For the present study it is clearly underestimated, but this has been the case historically (Gil et al., 1994).

6.4 Scattering Model for CO

In the discussion of the scattering model below the present study employed target model (DZP, CAS-1, 48). The (GTO) continuum orbitals employed by the present study were those of Faure et al. (2002). These continuum orbitals were then augmented with one virtual molecular orbital of each symmetry where such orbitals were available to do so. The partial wave expansion of these continuum orbitals was up to and including $l = 4$, or g-partial wave, which was more than sufficient for series convergence given that CO

Electronic state (C_{2v})	T_e (eV)	Theory[a]	Experiment[b]
X $^1\Sigma^+$ ($^1A_1$)	0.0	0.0	
1 $^3\Pi$ ($^3B_1$,$^3B_2$)	7.18	6.43	6.32
1 $^1\Pi$ ($^1B_1$,$^1B_2$)	9.51	10.03	8.50
1 $^3\Sigma^+$ ($^3A_1$)	9.56	9.12	8.58
1 $^3\Delta$ ($^3A_1$,$^3A_2$)	10.18	9.74	9.34
1 $^3\Sigma^-$,($^3A_2$)	10.5	10.19	9.86
1 $^1\Delta$ ($^1A_1$,$^1A_2$)	10.71	10.37	10.12
1 $^1\Sigma^-$ ($^1A_2$)	10.73	10.31	10.01
2 $^3\Pi$ ($^3B_1$,$^3B_2$)	13.68		
2 $^3\Sigma^+$ ($^3A_1$)	14.29		
2 $^1\Pi$ ($^1B_1$,$^1B_2$)	14.82		
2 $^1\Sigma^+$ ($^1A_1$)	14.92		
μ (a.u.)	-0.0332	-0.096	-0.043[c]
α_0 (a_0^3)	7.87		13.18[d]

Table 6.2: CO vertical excitation energies for model (DZP, CAS-1, 48). Also given are the dipole moment and spherical polarisability in atomic units

[a] Morgan and Tennyson (1993)

[b] Tilford and Simmonds (1972)

[c] Muenter (1975)

[d] NIST (2008)

is a weakly polar molecule. These orbitals were Schmidt orthogonalised to the target molecular orbitals and then symmetrically (Löwdin) orthogonalised among themselves. Only those continuum orbitals with overlap matrix eigenvalues greater than (2×10^{-7}) were retained.

In order to model the polarisation interaction well, the scattering model employed in the present study retained all 48 target states in the inner region close-coupling expansion and all 300 of the generated channels for the outer region scattering calculation. Initially an R-matrix sphere radius of 10 a_0 was employed. It was observed however, that there was some significant orbital amplitude on the sphere surface hence the radius was increased to 12 a_0. As a result the boundary amplitude decreased from order 10^{-4} to order 10^{-6}.

Finally, calculations were carried out on the $^2A_1$, $^2B_1$, $^2B_2$ and $^2A_2$ scattering sym-

Model	E_r eV	Γ_r eV
Present work	2.04	1.27
Morgan (1991) SE using SCF target	3.49	1.91
Morgan (1991) SE using CI target	3.38	1.91
Salvini et al. (1984) SEP 3 partial waves, no δ virtuals	2.15	1.16
Salvini et al. (1984) SEP 6 partial waves, no δ virtuals	2.08	0.91
Salvini et al. (1984) SEP 6 partial waves, δ virtuals	1.72	0.75
Morgan (1991) SEP with 13 virtuals	1.68	0.95
Morgan (1991) SEP with 13 virtuals plus 6 δ virtuals	1.29	0.74
Jain and Norcross (1992) ESEP	1.85	0.95
Morgan and Tennyson (1993) CC	1.8	N/A
Tronc et al. (1980)	1.8	1.0
Kwan et al. (1983)	1.9	N/A

Table 6.3: Comparison of the CO $^2\Pi$ resonance parameters calculated by the present work to the theoretical models of Salvini et al. (1984), Morgan (1991) and Morgan and Tennyson (1993) and the experiments of Tronc et al. (1980) and Kwan et al. (1983)

metries and for the incident energy range 0.02 eV to 10 eV. The R-matrices obtained at $a = 12\ a_0$ for each of the above symmetries were propagated to a radial distance of 100.1 a_0 (Baluja et al., 1982) for matching to the asymptotic form of the reduced radial wavefunction and the extraction of the fixed-nuclei (FN) K-matrices, T-matrices, integral elastic and inelastic cross sections.

6.5 Scattering Observables

6.5.1 Eigenphase Sums and Resonances

Given that CO is isoelectronic to HCN one expects their eigenphase sums to be very similar and this has indeed been confirmed in the present study. The model yielded the $^2\Pi$ shape resonance predicted by the previous theoretical and experimental works. Table 6.3 lists the parameters of this shape resonance. No other resonances were detected, in contrast to the study of Morgan and Tennyson (1993) which predicted two additional resonances of $^2\Pi$ symmetry and one each of symmetry $^2\Sigma^+$, $^2\Delta$ and $^2\Phi$.

Figure 6.1 shows the corresponding eigenphase sum curve. Clearly, the eigenphase

sum of Salvini et al. (1984) is systematically higher than that of the present work, resulting in lower resonance parameters.

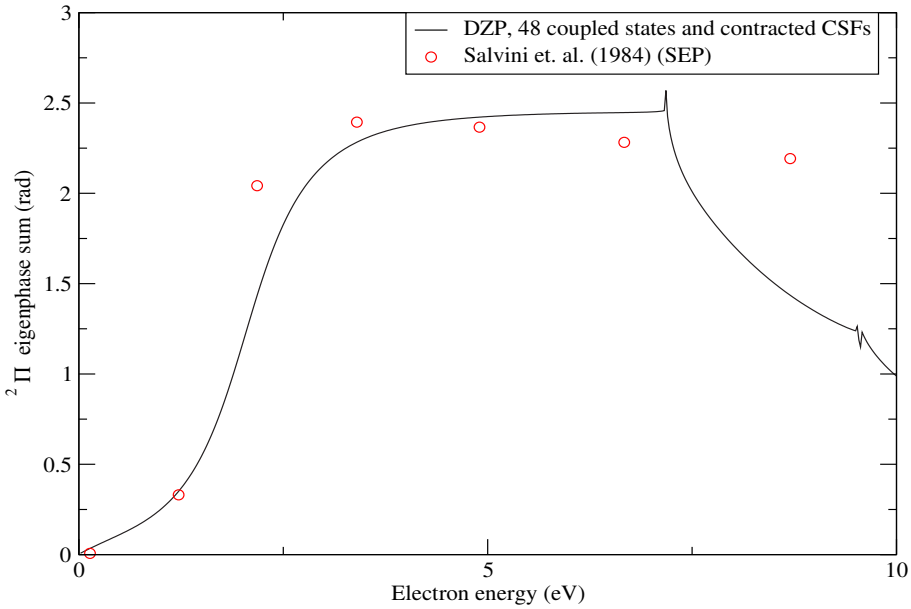

Figure 6.1: Comparison of CO $^2\Pi$ eigenphase sum curve for the 48 state close coupling model

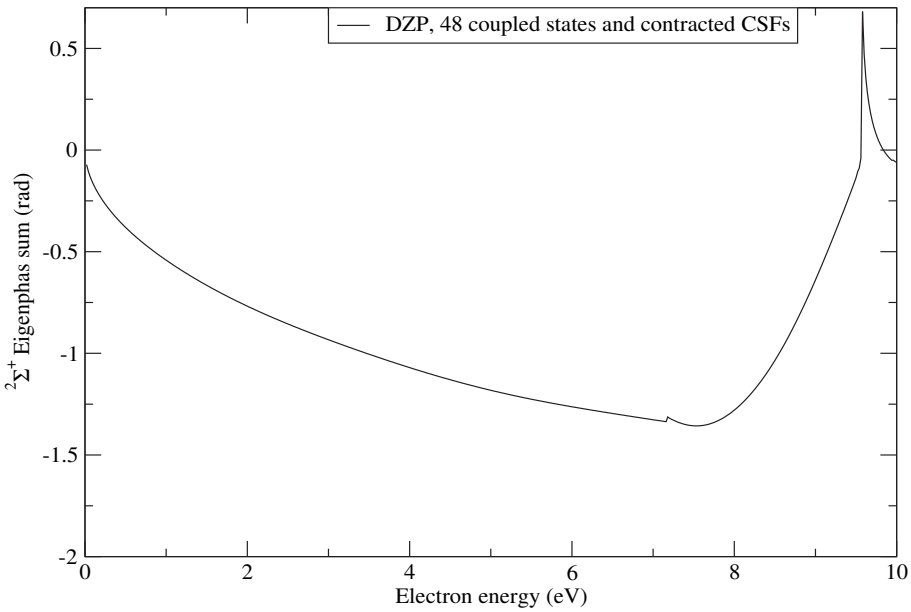

Figure 6.2: CO $^2\Sigma^+$ eigenphase sum curve for the 48 close coupling model

Figure 6.2 is quite unlike the corresponding eigenphase sum for HCN and HNC in that it does not have a sharp upturn at very low incident electron energies. This is due to its very small dipole moment (-0.0332 a.u.), whereas the dipole moments for HCN and HNC are large enough to support dipole bound states, as predicted by Levison's

theorem.

Salvini et al. (1984) found that the parameters of the $^2\Pi$ shape resonance were very sensitive to the target model employed and to the number of partial waves retained in the continuum orbitals used to represent the scattering electron, and particularly sensitive to the inclusion of δ orbitals in the 2-particle 1-hole term (table 6.3). Indeed at the static exchange (SE) approximation, using the McLean and Yoshimine (1968) target wavefunction, three partial waves gave rise to a $^2\Pi$ resonance with position and width of 3.47 eV and 2.0 eV respectively, which was lowered to 3.02 eV and 1.61 eV when six partial waves were retained and the Nesbet (1964) target wavefunction was used instead (a reduction of about 13 %). In the case of their static exchange-plus-polarisation (SEP) calculation, which used the Nesbet (1964) target wavefunction, the lowering of the resonance parameters was much more pronounced: retaining three partial waves and not including virtual orbitals in the 2-particle 1-hole configuration markedly lowered the resonance parameters to 2.15 eV and 1.16 eV; doubling the number of partial waves alone reduced the position and width further to 2.08 eV and 0.91 eV respectively. Finally, inclusion of the virtual orbitals resulted in a decrease to 1.72 eV and 0.75 eV, in agreement with experimental observations. Morgan (1991) also conducted tests to determine, at the SEP level, the influence of augmenting an increasing number of virtuals to the continuum orbitals on the $^2\Pi$ shape resonance. A consistent trend was observed where the position of the resonance reduced and the width narrowed: Morgan (1991) retained 5, 6, 7,. . .,13 virtuals of each symmetry and the resonance parameters rapidly converged to 1.68 eV and 0.95 eV (see table 1 of Morgan (1991)). Finally, augmentation of 6 δ virtuals to the 2-particle 1-hole configurations reduced the position to 1.29 eV and width to 0.74 eV. Such tests were not conducted in the present study. Instead the lowering of the parameters was attempted by the retention of all 48 target states in the inner region CC expansion and all 300 channels for the construction of the R-matrix.

6.5.2 Electron-Impact Excitation and Ionisation

Figure 6.3 shows the inelastic cross section for the excitation from the ground state to the $^3\Pi$ state. Most previous studies were only carried out at the static exchange or static exchange-plus-polarisation level; the only previous study to have carried out a detailed study of electron-impact excitation was that of Morgan and Tennyson (1993). Particular features include the observation that the $^2\Delta$ resonance produces a peak in

the excitation cross section for the $^3\Pi$; the present model however, did not produce this $^2\Delta$ resonance although it does confirm the existence of a peak in the X $^1\Sigma^+ \rightarrow ^3\Pi$ inelastic cross section (see figure 6.3) at almost exactly the same incident electron energy (9.52 eV). The inelastic cross section retains the same general shape as the R-matrix study of Morgan and Tennyson (1993) but is shifted to the right due to the location of the first inelastic channel threshold being higher.

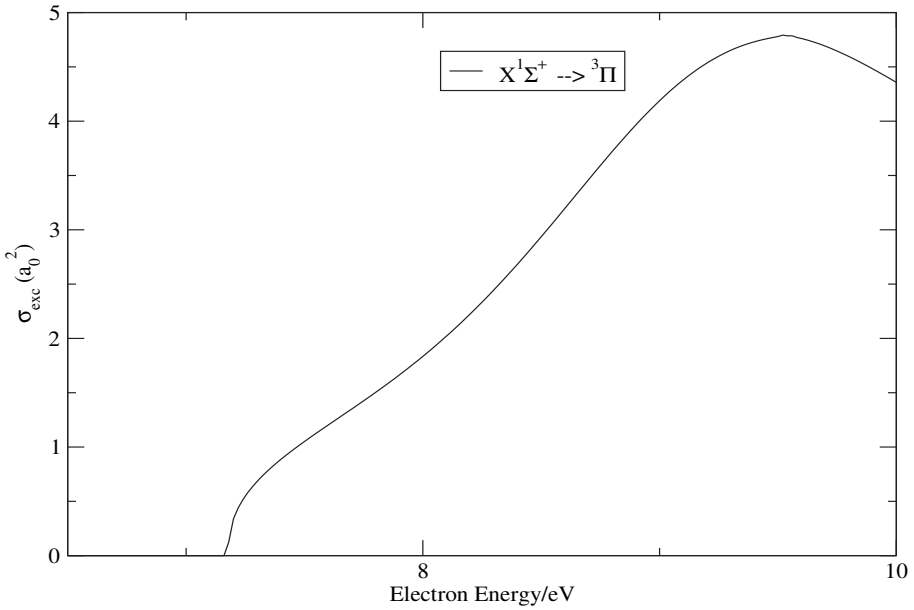

Figure 6.3: Inelastic cross section for excitation to the $^3\Pi$ electronic state (48 state close coupling model)

The present study employed Quantemol-N (Tennyson et al., 2007) to compute the electron-impact ionisation cross section using the BEB (Binary Encounter Bethe) formalism (Hwang et al., 1996; Kim and Rudd, 1994). The SCF occupied molecular orbitals calculated and used by Quantemol-N are listed in table 6.4. The same values were obtained using the R-matrix codes directly.

For all the orbitals Quantemol-N set the dipole constant Q to unity. The software computed the ionisation cross section for the i^{th} C_{2v} orbital and then summed over all occupied orbitals to yield a cross section for each energy in the range 15.01 eV to 5 keV. The cross section is shown in figure 6.5 alongside the experimental measurements of Hudson et al. (2004) and Orient and Srivastava (1987), the BEB calculations of Hwang et al. (1996) and the formulation of Joshipura and Patel (1996). The BEB calculations obtained by the present study are in very good agreement with both of the previous studies. It is to be noted that the ionisation cross section is sensitive to the ionisation energy and

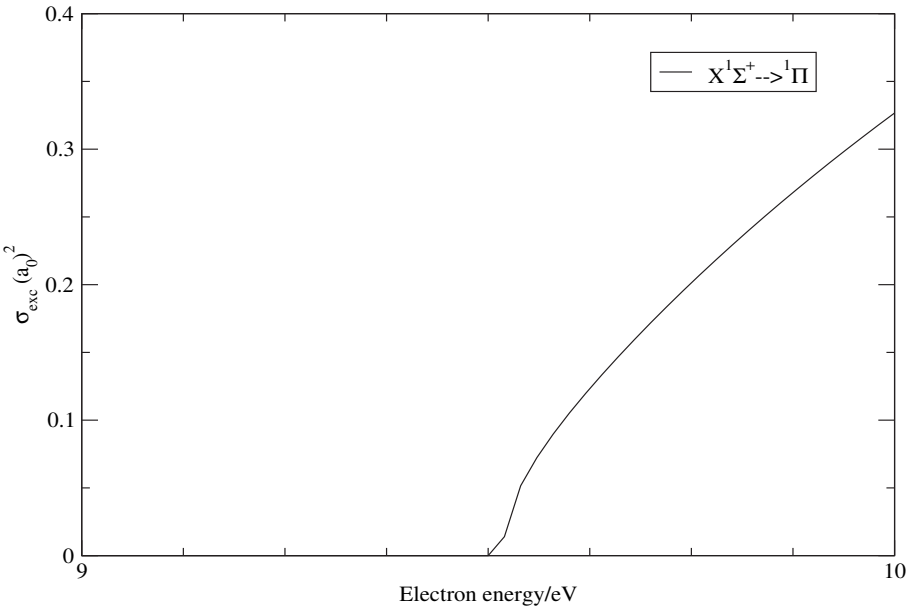

Figure 6.4: Inelastic cross section for excitation to the $^1\Pi$ electronic state (48 state close coupling model)

Orbital	$\|B\|$ (eV)	U (eV)	N
1σ $(1a_1)$	562.48	+794.60	2
2σ $(2a_1)$	309.53	+436.44	2
3σ $(3a_1)$	41.44	+78.14	2
4σ $(4a_1)$	21.82	+71.54	2
1π $(1b_1,1b_2)$	17.38	+54.18	4
5σ $(5a_1)$	15.01	+42.49	2

Table 6.4: CO molecular orbital binding (B) and average kinetic energies (U) and occupation numbers (N) for GTO basis set DZP obtained by the present study

the present study is in good agreement with the experimental value of 14.01 eV (NIST, 2008). Studies employing the BEB formalism employ this experimental value in order to attain improved agreement with experimental measurements. This was the approach used, and recommended by, Hwang et al. (1996) hence the slight difference between the data of the present study and Hwang et al. (1996).

6.5.3 Differential Cross Sections

The C_{2v} fixed-nuclei T-matrices computed in the outer region were employed in the computation of rotationally summed differential cross sections for incident scattering

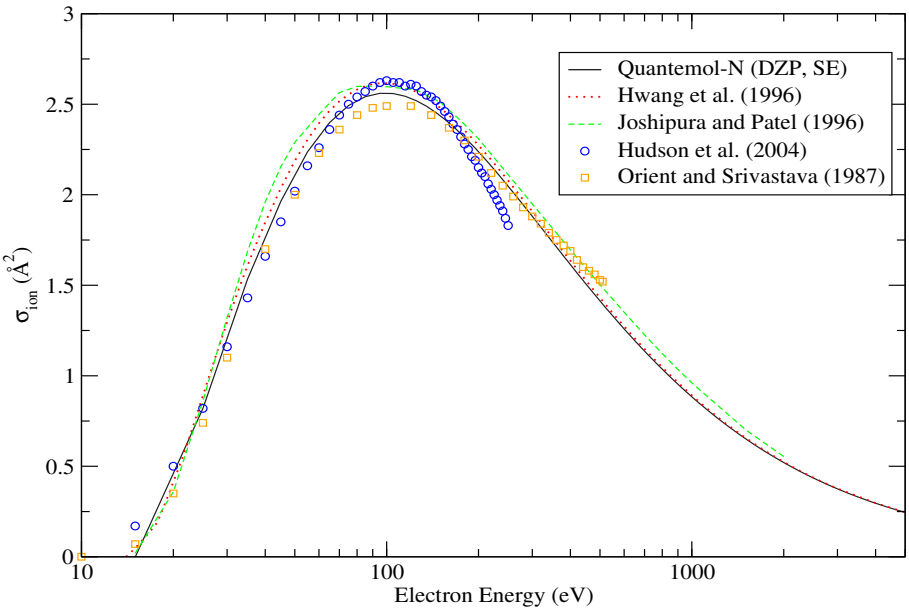

Figure 6.5: Comparison of the CO electron impact ionisation cross section

energies 1 eV, 1.91 eV, 3 eV and 5 eV, these being the selected energies of previous theoretical studies, as a means of testing the electron-molecule collision model because, experimentally, differential cross sections are much more reliably measured. An important reason for calculating an accurate value of the dipole moment is that differential cross sections are very sensitive to it, and therefore a great influence in attaining good agreement with available experimental data. The present study employed the Born-closure method on the scattering amplitude (Itikawa, 2000) to compute this observable. Comparison is made to the experimental study of Gibson et al. (1996) for all of the above energies and the theoretical study of Jain and Norcross (1992) for the energies 3 eV and 5 eV.

Initially the T-matrices were transformed to those of the natural symmetry $C_{\infty v}$ by extracting only those channel (defined here by the target symmetry Λ_i, the projectile partial wave l_i and its z-component m_{l_i} for the i^{th} channel) T-matrix elements that corresponded to the mapping $m_{l_i} = 0 \rightarrow \Sigma^+$, $m_{l_i} = 1 \rightarrow \Pi$, $m_{l_i} = 2 \rightarrow \Delta$, $m_{l_i} = 3 \rightarrow \Phi$ and $m_{l_i} = 4 \rightarrow \Gamma$ for a $^1\Sigma^+$ molecule.

The set of rotationally summed differential cross sections computed for the above incident electron energies are shown in figures 6.6–6.9.

The agreement with the Gibson et al. (1996) data at 1 eV is very good and at 1.91 eV, 3 eV and 5 eV for scattering angles between 85^o and 125^o agreement is fair. Outside this range however, agreement is poorer, especially at the forward angles. An

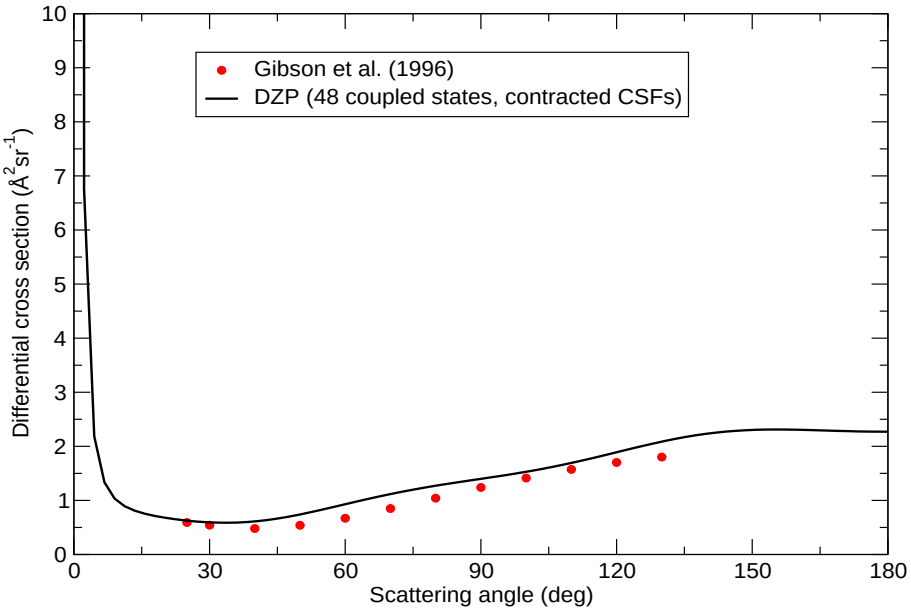

Figure 6.6: Comparison of the CO Rotationally summed differential cross section for incident energy 1 eV

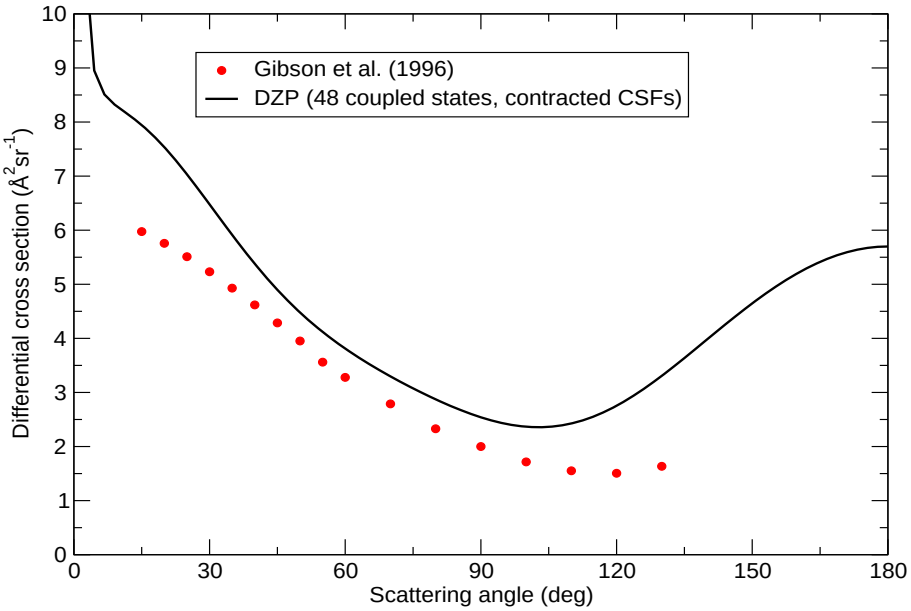

Figure 6.7: Comparison of the CO Rotationally summed differential cross section for incident energy 1.91 eV

important thing to mention in this matter is that experimentally it is difficult to measure differential cross sections at the forward angle and the experimentalist extrapolates the DCS data they measure, inaccurately, to the forward angle. Interestingly, the forward angle data of Gibson et al. (1996) appears to show behaviour that is typical of non-polar systems, even though CO has a small non-zero dipole moment. The data of the present

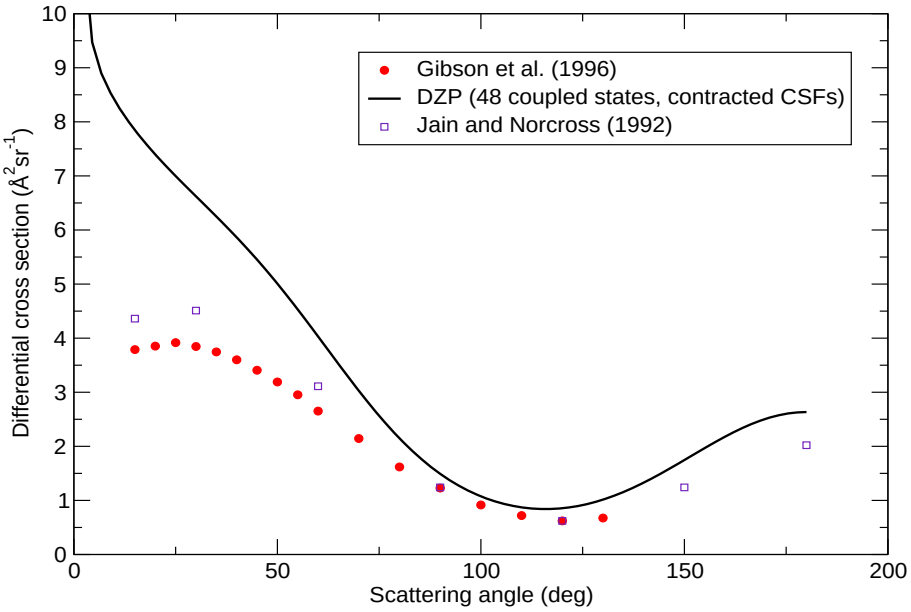

Figure 6.8: Comparison of the CO Rotationally summed differential cross section for incident energy 3 eV

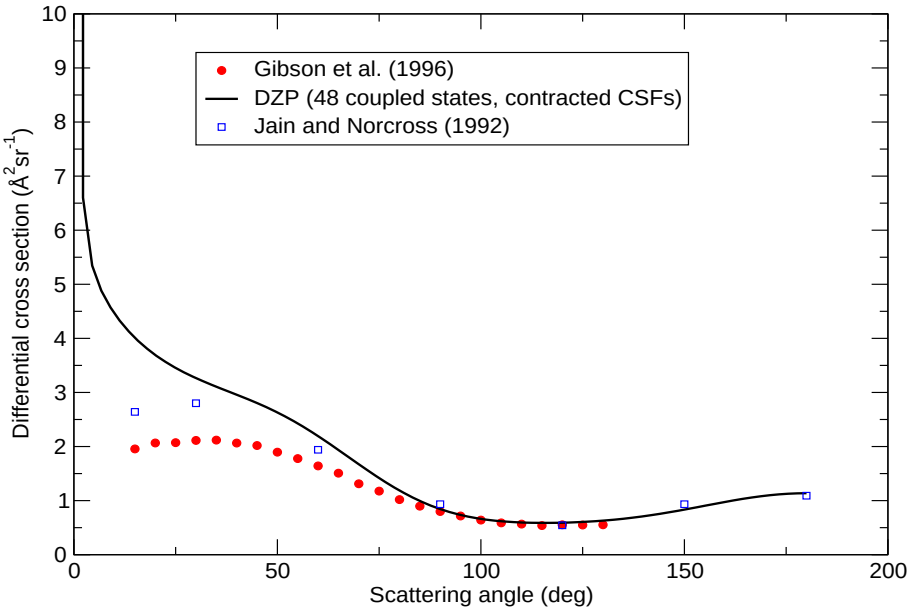

Figure 6.9: Comparison of the CO Rotationally summed differential cross section for incident energy 5 eV

study certainly seems to agree well with Jain and Norcross (1992) for angles above 90^o, but below this angle the calculation of Jain and Norcross (1992) exhibits the same trend as Gibson et al. (1996).

6.6 Conclusion

The present study has considered electron collisions with the diatomic CO at the close-coupling approximation, with the CO target being represented by CI (configuration interaction) wavefunctions. In all the complete active spaces employed to construct the target wavefunction, four electrons (two 1s electrons in the C and O atoms) were frozen in all configurations. Particular care was taken to re-produce the small magnitude of the dipole moment (-0.043 a.u. Muenter (1975)) and the correct sign of the dipole moment observed by experiments. Of the thirteen models tested two of them re-produced the required sign, but only the model employing the DZP Gaussian basis set and an active space consisting of the occupied and virtual molecular orbitals $3a_1$, $4a_1$, $5a_1$, $6a_1$, $7a_1$, $1b_1$, $2b_1$, $1b_2$, and $2b_2$, or (DZP, CAS-1, 48) yielded a dipole moment in good agreement with experiment (see table 6.1), hence this model was used to set up the scattering model. The disadvantage of model (DZP, CAS-1, 48) was that the channel thresholds were systematically higher than the experiment of Tilford and Simmonds (1972) and the theoretical study of Morgan and Tennyson (1993). This could be due to the present model employing a CAS which did not incorporate the 3π ($3b_1$ and $3b_2$) virtual orbital, which lies lower than the 7σ ($7a_1$) virtual orbital therefore omitting some short range electron-electron correlation. Morgan and Tennyson (1993) also employed a CAS that froze more than four electrons, thereby reducing the amount of electron-electron correlation in the target model. This is indicated by the fact their model had fewer CSFs. The advantage was that model (DZP, CAS-1, 48) ensured that the $N+1$-Hamiltonian eigenvalue problem was computationally feasible.

The R-matrix studies of Salvini et al. (1984) and Morgan (1991) showed the sensitivity of the resonance parameters to the augmentation of a large number of virtual molecular orbitals. Such a test was not carried out by the present study. Instead, in order to accurately model the polarisation interaction, the scattering model retained all 48 excited target states for the inner region trial scattering wavefunction and all 300 open and closed channels in the outer region scattering calculations. This model re-produced the low-energy $^2\Pi$ shape resonance observed experimentally and whose parameters were in good agreement with previous studies (table 6.3).

In the computation of the rotational differential cross sections, initially the C_{2v} T-matrices obtained by the outer region calculation were transformed to the natural symmetry $C_{\infty v}$ to yield a new set of T-matrices for the $^2\Sigma^+$, $^2\Pi$, $^2\Delta$, $^2\Phi$ and $^2\Gamma$ scattering

symmetries. This new set was employed to compute rotationally summed differential cross sections using the scattering amplitude Born closure method (Itikawa, 2000), and compared to the work of Gibson et al. (1996). Fair agreement was obtained for the incident energies 1.91 eV, 3 eV and 5 eV, but the data for 1 eV was remarkably well re-produced. The disagreement in the behaviour of the DCSs at the forward angles will certainly require additional study. Comparison with the work of Jain and Norcross (1992) showed good agreement beyond 90^o but disagreement below, with their data confirming the trend of Gibson et al. (1996). Normally one would expect that given CO does have a small non-zero dipole moment, that the low angle behaviour would be similar to that exhibited by this the present study; instead both experiment and theory show low angle behaviour typical of non-polar systems.

A future study using the observables computed in this study would be in the computation of rotational rate coefficients, which are of great importance in astrophysics (Tennyson and Faure, private communication). This study is being carried out at present. Jain and Norcross (1992) also stated that the nuclear vibrational motion plays an important role in the region of the resonance. The discrepancy between theoretical and experimental scattering results may be resolved, according to Jain and Norcross (1992), by considering a vibrational close-coupling calculation. Accounting for the vibrationally-averaged nature of the dipole moment may also be considered in the future for the rotational differential cross sections and rotational excitation problems.

Chapter 7

Electron Collision with the Silicon Monoxide (SiO) Molecule

7.1 Introduction

Astrophysicists have had a long-standing interest in SiO and this is reflected by the great number of studies carried out on this molecule confirming its presence in the interstellar medium (ISM), e.g. Turner et al. (1992), Pintado et al. (1997), Codella et al. (2002) and Nisini et al. (2007). Wilson et al. (1971) first reported on the discovery of silicon monoxide in Sagittarius B2 from line emission spectra and recently Lo et al. (2007) detected the $J = 2 - 1$ SiO transition from the massive cold dense core G333.125-0.562 and hypothesised that the SiO emission may arise from shocks associated with an outflow in the cold core. There have also been studies of SiO masers, sources of which have been detected in the Sagittarius B2 molecular cloud (Shiki and Deguchi, 1997) and galactic centres (Izumiura et al., 1998). Hence the astrophysical motivation for studying SiO has produced a number of *ab initio* quantum chemistry calculations including Cornet and Dubois (1972), Field et al. (1976), Peterson and Woods (1990), Langhoff and Bauschlicher (1993) and Muniz and Jorge (2006). Peterson and Woods (1990) carried out a configuration interaction study on SiO using diffuse basis sets, with the aim of computing accurate dipole moments and potential energies. Their study employed a CI-SD (all possible single and double electron excitations) level of theory, which yielded a dipole moment of +1.2572 a.u., in good agreement with the available experimental value of +1.219 a.u. (NIST, 2008). Chattopadhyaya et al. (2003) also performed extensive *ab initio* calculations which are discussed below.

This interest has also resulted in collisional studies being carried out on SiO to calculate rotational excitation rate coefficients, which are widely applied in astrophysical modelling. So far, the majority of research has been focused on atom-SiO collisions: recently Dayou and Balanca (2006) calculated the rotational excitation rate coefficients of SiO collisions with the helium atom for all transitions up to $J = 26$ and kinetic temperatures between 10–300 K. Their *ab initio* model involved using the coupled-cluster method at the RCCSD(T) level using a very diffuse (aug-pccVQZ) basis set for the Si, O and He atoms to obtain an accurate interaction potential for the He-SiO system. The potential was used to calculate the close coupled (CC) rotational cross sections and the (de)excitation rate coefficients. The data from their He-SiO study was then employed to predict rotational de-excitation rate coefficients for impact by para-H_2. Similarly Palov et al. (2006) calculated rate coefficients for rotationally-vibrationally inelastic scattering of the hydrogen atom by SiO to specifically model the circumstellar SiO maser. Their method involved using an approximate quantum scattering calculation (vibrational close-coupling rotational infinite order sudden (VCC-IOS) method) of the vibrationally-rotationally inelastic scattering cross sections over a relatively large range of scattering energies. Additional work on atom-SiO collision calculations has been carried out by Dickinson and Gottlieb (1970), Bieniek and Green (1981), Bieniek and Green (1983), Sisak and Secrest (1992) and Gusdorf et al. (2008). However, to date there has been very little work carried out on electron scattering by SiO in the low to medium energy range. This is despite the importance of such interactions in C-type shocks (Jimenez-Serra et al., 2006) and despite sometimes being the most dominant mechanism of molecular rotational excitation in comets for example (Lovell et al., 2004); the only electron impact study to have been carried out on SiO was a recent high-energy study by Joshipura, Vaishnav and Gangopadhyay (2007) using a complex potential formalism for the energy range 10–3000 eV. They were unable to benchmark their work in anyway precisely because of the lack of electron impact studies.

The present study reports on the application of the *ab initio* R-matrix method to low-energy scattering by SiO at the fixed nuclei approximation. In addition to the scattering quantities normally yielded by the R-matrix method, the rotationally resolved differential cross sections and the inelastic rotational integral cross sections as a function of electron energy have been calculated. These integral cross sections were then employed to calculate the rotational (de)excitation rate coefficients as a function of temperature

Molecular orbital	$\|B\|$ (eV)	U (eV)	N
1σ $(1a_1)$	1872.68	+2509.7517	2
2σ $(2a_1)$	558.58	+794.7226	2
3σ $(3a_1)$	167.87	+360.8542	2
1π $(1b_1,1b_2)$	116.17	+331.3933	4 (2,2)
4σ $(4a_1)$	116.16	+331.8232	2
5σ $(5a_1)$	34.32	+78.1625	2
6σ $(6a_1)$	16.53	+62.1116	2
2π $(2b_1, 2b_2)$	12.78	+52.1095	4 (2,2)
7σ $(7a_1)$	11.85	+44.1967	2

Table 7.1: SiO molecular orbital binding and average kinetic energies for DZP basis set and equilibrium geometry. The C_{2v} orbitals are given in the parentheses

and their rate fitting coefficients for later use in astrophysical modelling. This is the first low-energy electron collision study to have been carried out on SiO.

7.2 Quantum Chemistry Model

The present study was carried out using the C_{2v} point group- the highest Abelian subgroup of the natural point group $C_{\infty v}$ and a GTO double zeta-plus-polarisation (DZP) basis set for the Si and O atoms. The use of more diffuse basis sets is generally discouraged as the occupied molecular orbitals so obtained would have significant amplitude on the R-matrix sphere surface (typical radius 10 a_0). The experimental equilibrium geometry ($r_e = 1.5097$ Å) of the SiO diatomic was employed (NIST, 2008). The present study carried out a self-consistent field (SCF) calculation using the above-mentioned basis set and geometry to yield the ground state electronic configuration $1a_1^2\ 2a_1^2\ 3a_1^2\ 1b_1^2\ 1b_2^2\ 4a_1^2\ 5a_1^2\ 6a_1^2\ 2b_1^2\ 2b_2^2\ 7a_1^2$ (X $^1A_1$) or $1\sigma^2\ 2\sigma^2\ 3\sigma^2\ 1\pi^4\ 4\sigma^2\ 5\sigma^2\ 6\sigma^2\ 2\pi^4\ 7\sigma^2$ (X $^1\Sigma^+$) in the natural point group: the binding energy B, average kinetic energy U and occupation number N of the occupied molecular orbitals obtained by the present study are listed in table 7.1. By Koopman's theorem the first ionisation energy is 11.85 eV which is in reasonable agreement with the experimental value of 11.49 eV (NIST, 2008).

The occupied and virtual molecular orbitals obtained using HF-SCF optimisation were then used to set up the SiO electronic target states. The study specifically computed complete active space configuration interaction (CASCI) electronic target wavefunctions,

as a means of modelling the correlation interaction between the target electrons. The complete active space employed by Quantemol-N was automatically generated: ($1a_1$, $2a_1$, $3a_1$, $1b_1$, $1b_2$, $4a_1$)^{12} ($5a_1$, $6a_1$, $2b_1$, $2b_2$, $7a_1$, $3b_1$, $3b_2$, $8a_1$, $9a_1$)^{10}, namely, twelve electrons (1s, 2s and 2p electrons in the Si atom and the 1s electrons in the O atom) were frozen in all configurations and ten electrons were free to move in the 5–$9a_1$, 2–$3b_1$ and 2–$3b_2$ orbitals. This active space yielded 1,436 configurations for the $^1A_1$ ($^1\Sigma^+$) ground state. Two target models were analysed: one computed $m = 6$ target Hamiltonian eigenvalues per state and the second involved computing $m = 3$ eigenvalues per state; where m is the number of eigenvalues per electronic symmetry.

The excitation energies of the present study are compared to those obtained by Chattopadhyaya et al. (2003) who reported an extensive configuration interaction study of the low-lying electronic states of SiO which used *ab initio* based multireference singles and doubles configuration interaction calculations including the core potentials of the Si and O atoms. They also computed the T_e, r_e and ω_e spectroscopic constants of the bound $\Lambda - S$ states of the molecule, and dipole moment μ of the X $^1\Sigma^+$, a $^3\Sigma^+$, b $^3\Pi$, A $^1\Pi$ and E $^1\Sigma^+$ target states. Chattopadhyaya et al. (2003) used the same complete active space as the present study with 10 electrons in the active space. The HF-SCF molecular orbitals set used in their study were computed as a function of bond length using a very diffuse basis set. Table 7.2 shows the vertical excitation data calculated by the present study compared to the adiabatic and vertical excitation energy data of Chattopadhyaya et al. (2003) and the experimental work summarised by Herzberg and Huber (1979). It can be seen that the vertical excitation energies of the present work are systematically higher than the adiabatic data of the two previous studies, as expected, but are in better agreement with the vertical excitation energy data of the previous theoretical study of Chattopadhyaya et al. (2003). There are some notable differences between the present and the two previous studies: the low-lying $^1\Delta$ state predicted by Chattopadhyaya et al. (2003) and reported by Herzberg and Huber (1979) does not appear in this study; conversely, states such as the 2 $^1\Sigma^-$ predicted by the present study are not predicted by the two previous studies. Considering graph (a) in fig. 1 of Chattopadhyaya et al. (2003) it is interesting to observe that the lowest C $^1\Sigma^-$ and D $^1\Delta$ potential energy curves almost lie on top of each other. At the equilibrium geometry they are indistinguishable. Given this, it might be the case that the present study has not included a sufficient number of $^1A_2$ and $^1A_1$ states for the $^1\Delta$ state to appear, or that the $^1\Sigma^-$ may in fact be the

Target State	Present work	Experiment[b]	Theory[c]	
			Adiabatic	Vertical
X $^1\Sigma^+$	−363.8534			
1 $^3\Pi$ ($^3B_1$,$^3B_2$)	4.64	4.20	4.26	4.29
1 $^3\Sigma^+$ ($^3A_1$)	5.11	4.18	4.17	4.74
1 $^3\Delta$ ($^3A_1$,$^3A_2$)	5.43	4.53	4.58	5.31
1 $^3\Sigma^-$ ($^3A_2$)	5.61	4.76	4.70	5.76
1 $^1\Sigma^-$ ($^1A_2$)	5.81	4.80	4.71	5.98
1 $^1\Delta$ ($^1A_1$,$^1A_2$)		4.82	4.84	5.98
2 $^1\Sigma^+$ ($^1A_1$)	6.13	6.57	6.58	8.02
1 $^1\Pi$ ($^1B_1$,$^1B_2$)	6.15	5.32	5.45	5.98
2 $^1\Sigma^-$ ($^1A_2$)	7.30			
2 $^3\Pi$ ($^3B_1$, $^3B_2$)	8.03		7.11	7.62
3 $^1\Sigma^+$ ($^1A_1$)	8.48			
2 $^3\Sigma^+$ ($^3A_1$)	8.54	7.15	7.02	7.17
3 $^3\Pi$ ($^3B_1$,$^3B_2$)	8.93			
2 $^1\Pi$ ($^1B_1$,$^1B_2$)	9.06		7.91	9.15
3 $^1\Pi$ ($^1B_1$,$^1B_2$)	10.0			
2 $^3\Sigma^-$ ($^3A_2$)	10.1			
4 $^3\Pi$ ($^3B_1$,$^3B_2$)	10.3			
4 $^1\Sigma^+$ ($^1A_1$)	10.9			
5 $^3\Pi$ ($^3B_1$,$^3B_2$)	11.5			
3 $^3\Sigma^+$ ($^3A_1$)	11.7	8.45	8.33	
4 $^1\Pi$ ($^1B_1$,$^1B_2$)	11.8			
μ/D	2.97	3.1[a]	3.03	

Table 7.2: SiO vertical excitation energies in eV for all states below the ionisation threshold. The target states are designated in $C_{\infty v}$ (C_{2v}) symmetry The electronic states 4 $^3\Pi$ onwards do not appear in the $m = 3$ target model. Also shown are the target absolute ground state energy of the present study in E_h and the dipole moment (1 D : 0.3937 a_0).

[a] NIST (2008),

[b] Herzberg and Huber (1979),

[c] Chattopadhyaya et al. (2003),

$^1\Delta$ but for the absence of the required degenerate $^1A_1$ electronic state. Chattopadhyaya et al. (2003) and Herzberg and Huber (1979) only considered states below 9.15 eV, so it is not possible to confirm the accuracy of those target states computed by the present study that are above this ceiling, although the general trend observed for states below 9.15 eV suggests that the excitation energies of the present study above this will be upper bounds on the true values.

The present study has also calculated states at and above the ionisation threshold (not shown in table 7.2). Such states are useful for representing polarisation effects; they are better represented using pseudo continuum orbitals (Gorfinkiel and Tennyson, 2004; Tarana and Tennyson, 2008), which was not attempted here. These high-lying states do not have any physical significance but were nevertheless included in the present scattering model as discussed below.

The ground state dipole moment of the present work is in very good agreement with the experimental value (NIST, 2008) and the theoretical values of Chattopadhyaya et al. (2003) (3.03 D) and Maroulis et al. (2000) (3.01 D). A Hartree-Fock SiO wavefunction was also computed, resulting in a much larger dipole moment of 3.7 D.

The polarisability tensor gives a good indication of how well the polarisation interaction will be modelled in the outer region. In the present work, the diagonal components α_{xx}, α_{yy} and α_{zz} were computed using second-order perturbation theory. From this the mean spherical polarisability, α_0, was found to be 18.5 a_0^3 for the $m = 6$ target model. The highest value of the polarisability calculated by Maroulis et al. (2000) was 29.67 a_0^3, using the highly accurate coupled cluster CCSD(T) method. There does not appear to be any experimental value of the mean polarisability to which one might be able to compare.

7.3 Scattering Model

All scattering models employed the GTO continuum basis set of Faure et al. (2002) to model the scattering electron and a partial wave expansion up to and including g-partial wave ($l \leq 4$). These continuum orbitals were orthogonalised to the target molecular orbitals using a mixture of Schmidt and Löwdin symmetric orthogonalisation methods, and those continuum orbitals with an overlap matrix eigenvalue of less than 2×10^{-7} were removed. Since SiO is a very polar diatomic, the convergence of the continuum orbital partial wave expansion is very slow so in the present study the higher partial

waves that are excluded from the continuum orbitals were accounted for using the Born correction (Kaur et al., 2008).

By virtue of the two target models investigated, two scattering models were also studied which varied the number of target states included in the close-coupling expansion and retained for the construction of the R-matrix at the surface of the sphere. A static-exchange (SE) calculation was also carried out to determine the nature of any resonances, whether they were shape resonances or Feshbach ones. For all the studies carried out, some of the low-lying virtual molecular orbitals calculated from the SCF calculation were used to augment the continuum basis set. These orbitals allow for high partial waves in the region of the nuclear singularity; however as they do not extend in the outer region they do not assist with the slow convergence of the partial wave expansion due to the effects of the long-range dipole potential.

Initial calculations used a sphere radius of 10 a_0. However, it was found that there was significant amplitude on the spherical boundary (arising from the occupied molecular orbitals) so this radius was increased to 12 a_0 , which reduced the most significant orbital amplitude from order 10^{-4} to 10^{-6}.

In order to preserve the balance between the amount of correlation incorporated in the target wavefunction and in the scattering calculation, 11 electrons (10 target electrons and 1 scattering electron) were allowed to move freely amongst the $5a_1$, $6a_1$, $2b_1$, $2b_2$, $7a_1$, $3b_1$, $3b_2$, $8a_1$ and $9a_1$ target occupied and virtual orbitals.

Test calculations were carried out which included 24 states (150 channels) in the close-coupling expansion and retention of the same in the outer region for construction of the R-matrix on the sphere boundary. In addition calculations were carried out using 48 target states (300 channels). The reason for including so many states was so as to improve the modelling of the polarisation interaction, which, *ab initio* , is modelled by the retention of a large number of closed electronic excitation channels. So far as computational efficiency is concerned, the computation time for the outer region becomes longer due to the increased size of the large open-closed portion of the R-matrix. The computer time for the calculation of the $N + 1$-trial scattering wavefunction however, remains unaffected by the inclusion of more target states (Tennyson, 1996*b*).

Finally all calculations were carried out on the $^2A_1$, $^2A_2$, $^2B_1$ and $^2B_2$ scattering symmetries and for the incident electron energy range 0.02 eV to 10.0 eV. For matching to the asymptotic form of the reduced radial wavefunction of the scattered electron,

and hence the computation of the K-matrix, the R-matrix was propagated to a radial distance of 100.1 a_0.

7.4 Results

The present study computed the multichannel eigenphase sum, the inelastic cross section, total cross section, rotationally resolved differential cross sections (DCSs) for incident energies 1 eV, 2 eV, 3 eV and 4 eV, rotationally inelastic integral cross sections and rotational rate coefficients for all transitions up to $J = 40$. Here the best model was taken to be the 48-state CC model, and the results for these are discussed below. Quantemol-N also computed the Binary-Encounter-Bethe (BEB) ionisation cross section using the molecular orbitals listed in table 7.1 and a dipole constant, Q, set to unity for each orbital. A number of interesting phenomena were observed in the low-energy scattering data which are discussed below. The scattering model employed in the present study has no influence upon the BEB ionisation cross section calculated by Quantemol-N except the GTO basis set employed to construct the occupied and virtual molecular orbitals.

7.4.1 Eigenphase Sums, Resonances and Bound States

For both the static exchange calculation and the N-state close-coupling (CC) calculations, the $^2A_1$ eigenphase sums of the present study in figure 7.1 show a very sharp upturn as the electron energy tends to zero. This is a characteristic typical of dipole bound states and is predicted by Levison's theorem. Some of the structures shown in the close coupling eigenphase sum curves are absent from the static exchange and this is because these features represent the opening up of new excitation channels (table 7.2). Resonances manifest themselves in plots of eigenphase sums as a rapid increase of π in the eigenphase; given that the eigenphase is arbitrary modulo π, resonances, particularly when narrow, often actually appear as seeming discontinuities in these plots. Figure 7.1 also appears to show a narrow resonance feature at approximately 4.5–4.7 eV which is also absent from the static exchange eigenphase, indicating that this may be a Feshbach. The $^2A_2$ eigenphase sum curve (not shown) also shows a similar resonance feature at the same position, meaning that this Feshbach resonance has $^2\Delta$ symmetry. It is also to be noted that as more states are included in the CC expansion and retained in the outer region calculation, the eigenphase sum increases — this is a clear indication of the improved modelling of the polarisation interaction.

Symmetry	N=48		N=24	
	E_r	Γ_r	E_r	Γ_r
$^2\Pi$	5.09	0.0029		
$^2\Pi$	5.53	0.0586		
$^2\Pi$	5.96	0.343	5.72	0.357
$^2\Delta$	4.69	0.250	4.82	0.593
$^2\Sigma^-$	8.16	0.411		

Table 7.3: Resonances for the 48-state and 24-state SiO close-coupling model. The parameters are given in eV

The $^2B_1$ eigenphase sums presented in figure 7.2 are also notable in terms of structure: the SE calculation shows a resonance feature below 1 eV which disappears when one employs the CC expansion. This behaviour is typical of a weakly bound state. In addition the R-matrix poles E_{N+1} were calculated for each scattering symmetry and the $^2\Pi$ R-matrix pole was found to be -363.8601 E_h, slightly lower than the target ground state (-363.8534 E_h) and so also corresponds to a bound state of $^2\Pi$ symmetry. This and the disappearance of the $^2\Pi$ SE shape resonance very neatly confirms the density functional study of Alikhani et al. (1997). The 48-state CC model predicts that this bound state lies at position -0.12 eV compared to -0.16 eV by Alikhani et al. (1997). The present study also predicts the existence of very narrow $^2\Pi$ Feshbach resonances between 5 and 6 eV. The position E_r and width Γ_r parameters of the Feshbach resonances yielded by the close-coupled calculations are given in table 7.3. These parameters were obtained by fitting to the Breit-Wigner profile (Tennyson and Noble, 1984). The parameters of a Feshbach resonance are very sensitive to the treatment of the polarisation interaction. Table 7.3 confirms the effect of the improved modelling of the polarisation interaction, namely the lowering of the position and the narrowing of the width: in the case of the $^2\Delta$ Feshbach resonance, the width is more than halved by the retention of 24 additional states and the position is lowered by about 3 %. It is interesting to note that the 48-state CC model predicts the existence of three $^2\Pi$ and one $^2\Sigma^-$ Feshbach resonances (the latter arising from the $^2A_2$ eigenphase curve) whereas the 24-state model predicts only one $^2\Pi$ and does not predict a $^2\Sigma^-$ resonance at all. This may be another effect of improved modelling, but since no further studies retaining more than 48 states have been conducted this is difficult to confirm.

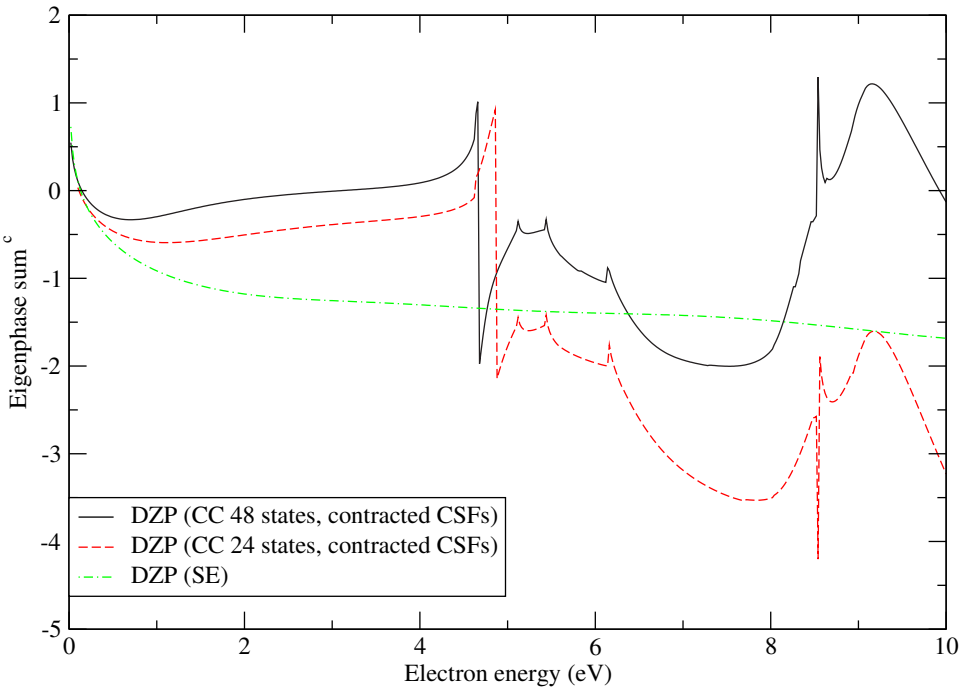

Figure 7.1: Comparison of the SiO $^2A_1$ (predominantly $^2\Sigma^+$) eigenphase sums

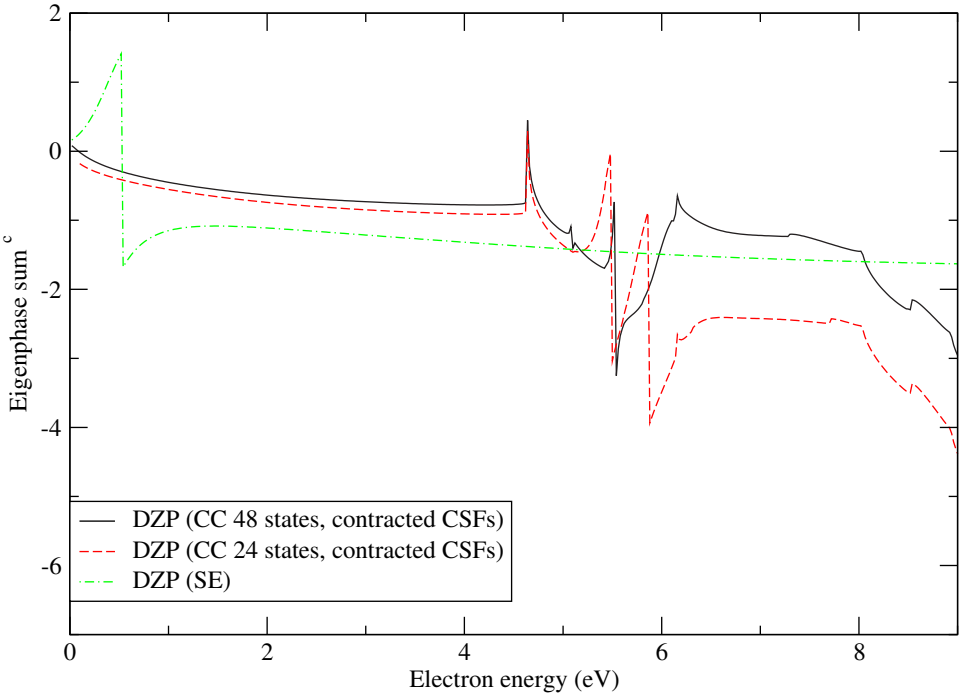

Figure 7.2: Comparison of the SiO $^2B_1$ (predominantly $^2\Pi$) eigenphase sums

7.4.2 Inelastic and Ionisation Cross Sections

The electronic excitation cross sections show some interesting peak structure. Figure 7.3 shows the inelastic cross sections for electronic excitation to the first four low-lying states $^3\Pi$, $^3\Sigma^+$, $^3\Delta$ and $^3\Sigma^-$ (table 7.2) for the 48-state CC calculation. The X $^1\Sigma^+ \rightarrow$ $^3\Pi$ excitation cross section shows a pronounced double peak structure below 5 eV. Analysis of the partial cross sections suggests that lower peak is caused by the $^2\Delta$ Feshbach resonance shown in table 7.3 whereas the second peak is simply caused by the rapid rise in the $^2\Sigma^+$ cross section often found near threshold for spin changing excitations. There is also a sharp narrow peak at around 5.5 eV in the X $^1\Sigma^+ \rightarrow$ $^3\Delta$ excitation cross section which might correspond to the second of the three $^2\Pi$ Feshbach resonances in table 7.3. A smaller and wider peak appears at about 6 eV in the X $^1\Sigma^+ \rightarrow^3 \Sigma^-$ cross section which could well correspond to the third of the three $^2\Pi$ resonances. Finally it is interesting to note the presence of a broad peak in the X $^1\Sigma^+ \rightarrow$ $^3\Delta$ cross section at about 8.2 eV which coincides with the position of the $^2\Sigma^-$ resonance.

Figure 7.4 shows the electron impact ionisation cross section of SiO computed by the present study alongside the complex potential formalism calculations of Joshipura, Vaishnav and Gangopadhyay (2007). Quantemol-N computed the ionisation cross section for the i^{th} C_{2v} molecular orbital (table 7.1) using the standard formula (Kim and Rudd, 1994) and then by summing over these occupied orbitals. It can be seen from figure 7.4 that the data of Joshipura, Vaishnav and Gangopadhyay (2007) is systematically higher than the BEB data computed by the present study over the entire energy range considered. Given the absence of other high-energy electron collision theoretical or experimental data, it is difficult to draw any sort of conclusion. It is true to say that the BEB formalism has consistently yielded cross sections that are in very good agreement with experiment (see http://physics.nist.gov/PhysRefData/Ionization/molTable.html for example). The BEB cross section is sensitive to the precise value of the ionisation energy employed and in nearly all calculations the experimental value has been adopted so as to attain agreement with experiment. This strategy was tested in the present study and since the ionisation energy of the present study (11.85 eV) is in good agreement with experiment (11.49 eV NIST (2008)), little difference in the ionisation cross section was found.

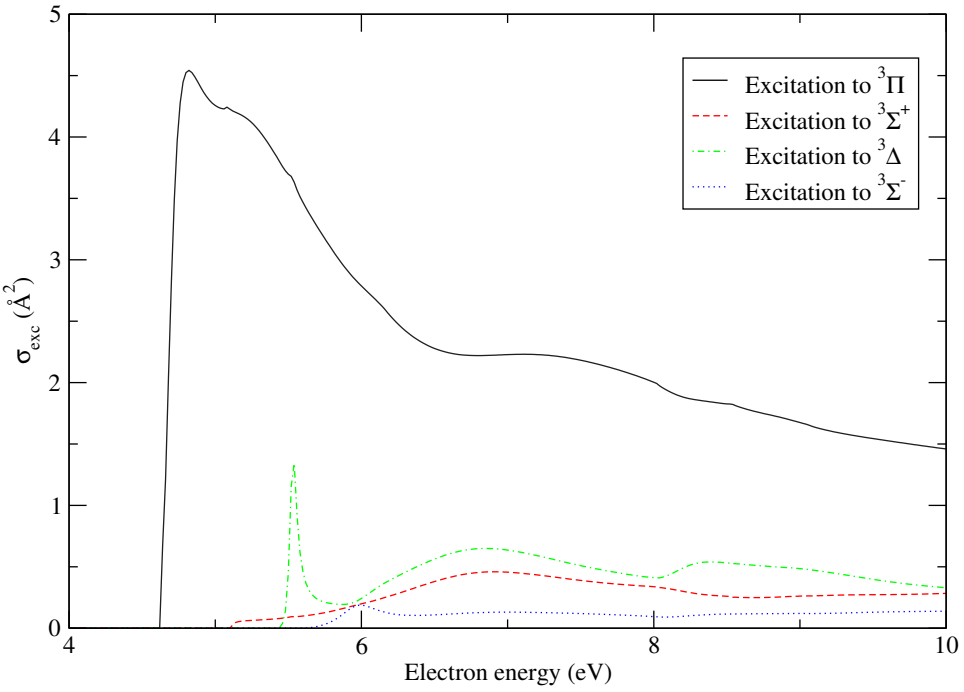

Figure 7.3: SiO electronic excitation cross sections to the first four lowest lying electronic excitation channels for the 48-state close coupling model

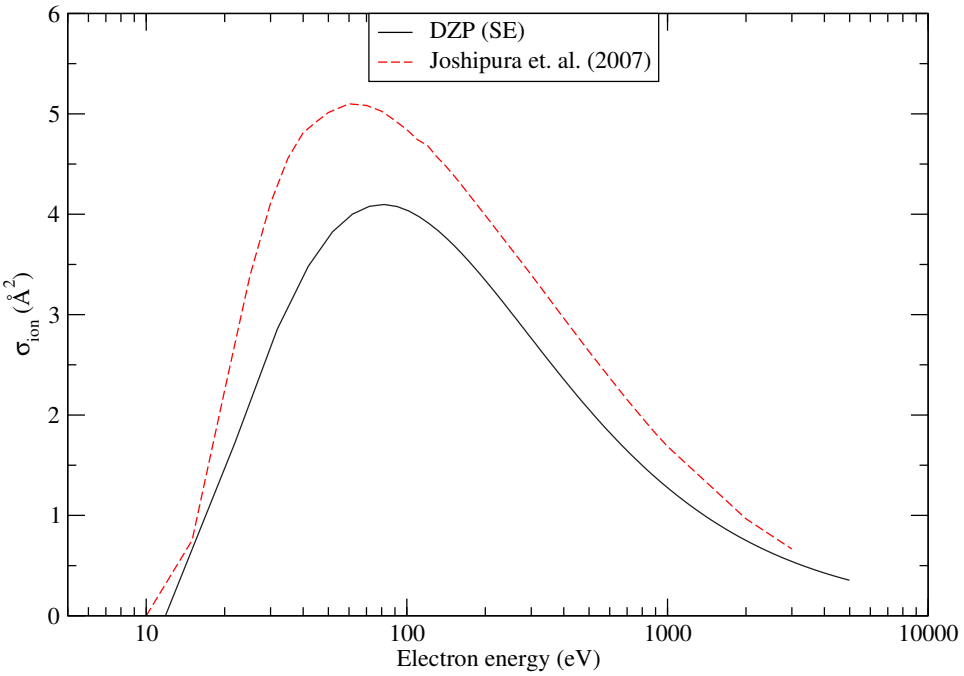

Figure 7.4: Comparison of the Quantemol-N SiO BEB ionisation cross section to the calculation of Joshipura, Vaishnav and Gangopadhyay (2007)

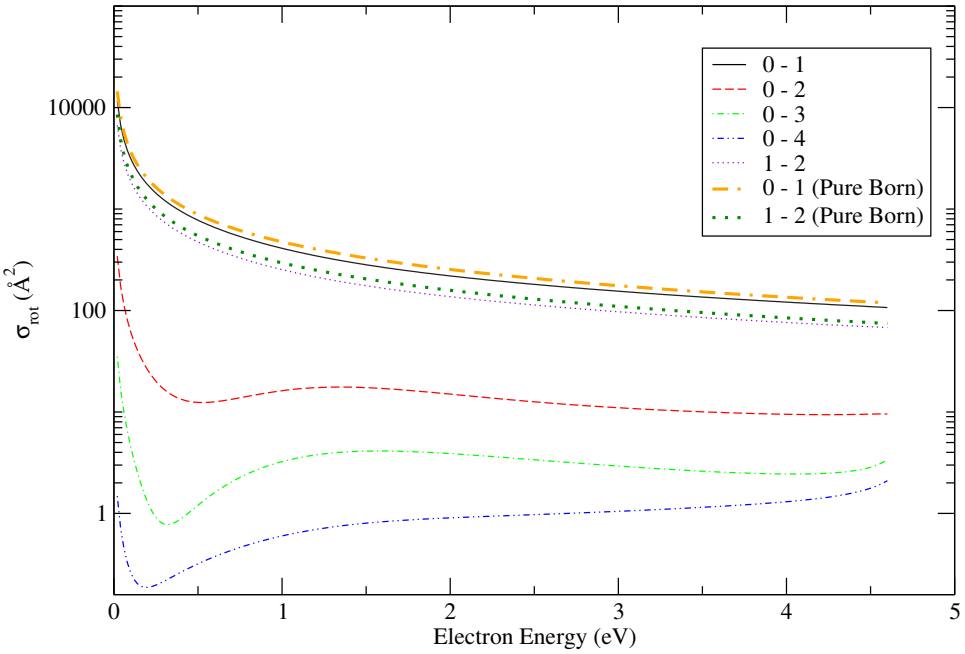

Figure 7.5: SiO rotationally inelastic cross sections for incident electron energies below 4.6 eV

7.4.3 Rotational Differential Cross Section and Integral Cross Sections

For all the figures shown in this section the 48-state CC T-matrices were employed in their calculation.

Initially the T-matrices were transformed from their C_{2v} representation to that of the natural point group $C_{\infty v}$ to yield a new set of linear T-matrices for the $^2\Sigma^+$, $^2\Pi$, $^2\Delta$, $^2\Phi$ and $^2\Gamma$ scattering symmetries, using the mappings $m_{l_i} = 0 \rightarrow \Sigma^+$, $m_{l_i} = 1 \rightarrow \Pi$, $m_{l_i} = 2 \rightarrow \Delta$, $m_{l_i} = 3 \rightarrow \Phi$ and $m_{l_i} = 4 \rightarrow \Gamma$ for a $^1\Sigma^+$ ground state molecule. Here m_{l_i} is the z-projection of the scattering electron partial wave l_i for the i^{th} channel. This new set was then employed in the calculation discussed below.

In this approach the cross section is written as a sum over partial waves within the ANR (adiabatic nuclei rotation) approximation, which assumes that the rotational excitation channels are degenerate. For low partial waves (here defined as $l \leq 4$) T-matrices computed from the R-matrix calculations are employed to compute the cross section. In the case of dipole-forbidden excitations ($\Delta J \neq 1$) the convergence of the cross section partial wave expansion is expected to be rapid hence it may be evaluated using the FN T-matrices alone; in the case of the dipole-allowed excitations ($\Delta J = 1$) the partial wave expansion converges slowly owing to the long-range nature of the dipole interaction. In order to account for the higher partial waves not included in the FN

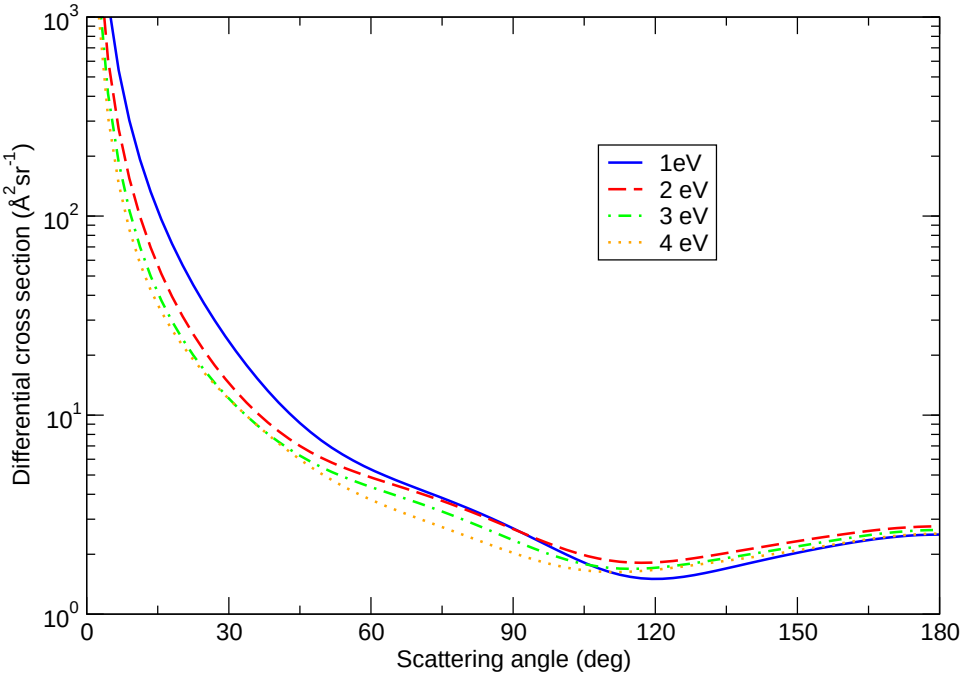

Figure 7.6: SiO rotationally summed differential cross sections for incident energies 1 eV, 2 eV, 3 eV and 4 eV

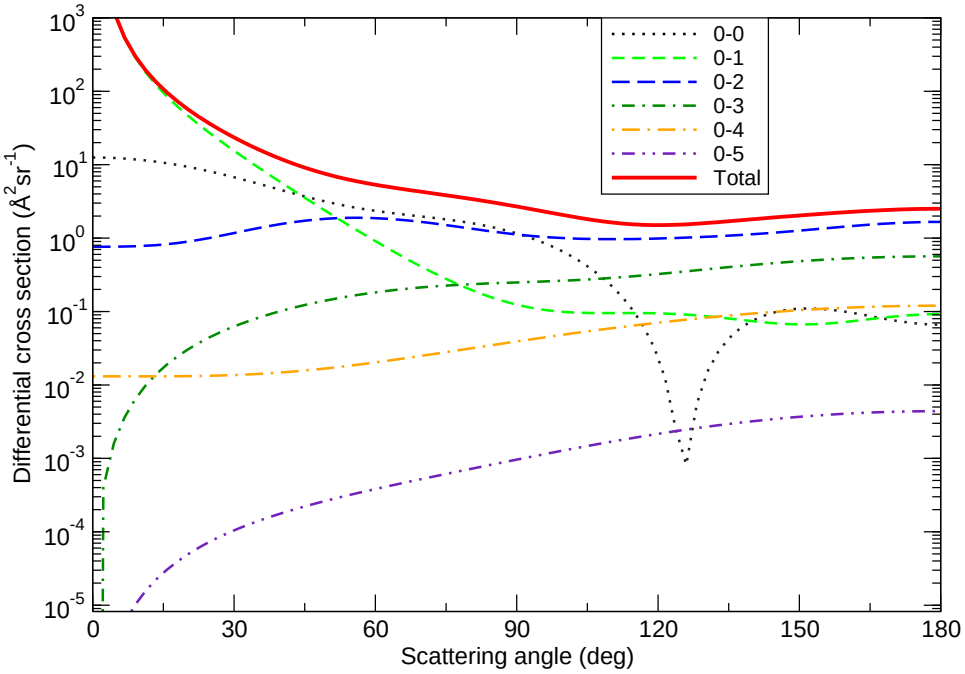

Figure 7.7: SiO rotationally resolved and summed differential cross sections for incident energy 1 eV

T-matrices, the Born correction was applied. Hence the low partial wave contribution is included via the R-matrix calculation and the Born correction. The low partial waves contribution arising from the Born contribution is therefore subtracted in order that the final rotational cross section set only contains those low partial waves due to the R-matrix calculation. It was found in chapter 10 that quadrupole and induced dipole Born completion was negligible so it was not included in the present study either. The restriction of the ANR approximation is that it is only reliable at collision energies where the collision time becomes appreciable compared to the time period of nuclear rotational motion (Feldt and Morrison, 1982). SiO has its first inelastic threshold at 4.63 eV so the computation of the inelastic rotational cross section was restricted to the range 0.02–4.6 eV. Excitation cross sections were extrapolated at very low energy, down to threshold as in chapter 10.

For strongly dipolar systems, the differential cross sections (DCSs) are more accurately measured than integral cross sections (Faure et al., 2004*b*). As a test of the accuracy of a theoretical model one would usually compare calculated differential cross sections to those of experiment. The present study cannot carry out this benchmark test as no such experimental data exist. To confirm the validity of the present treatment, the ANR integral rotational cross sections obtained using the FN T-matrices were compared to the cross sections obtained by the angular integration of the DCSs obtained using the Born closure approach (Itikawa, 2000) and both coincided to within 1 %.

Figure 7.5 shows the rotational integral cross sections as a function of energy and it may be noticed that the dipole allowed cross sections 0–1 and 1–2 dominate over the dipole forbidden 0–2 by almost two orders of magnitude, a reflection of the large dipole moment of SiO. Similar results were observed for HCN (chapter 10). As shown in fig. 7.5, these $\Delta J = 1$ cross sections are close to but slightly overestimated by the pure dipole Born calculations.

Figure 7.6 shows the rotationally summed DCSs for incident energies 1 eV, 2 eV, 3 eV and 4 eV. It is interesting to observe the appearance of two shoulder features at about 60^o and 120^o which would seem to indicate that for these energies scattering is chiefly s-, p- and d-wave in nature. The 1 eV DCS in particular is studied in more detail in figure 7.7 which shows the summed and the J-resolved differential cross sections for this energy, and a general trend can be inferred. The divergence at the forward angle is confirmed as being due to the dipole-allowed transition 0–1 dominating the scattering.

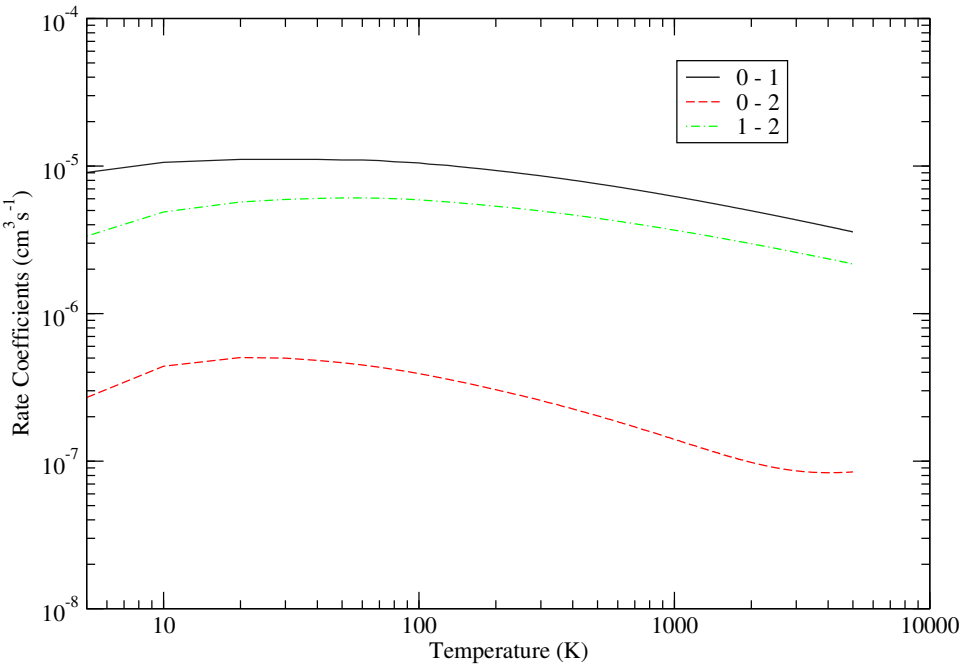

Figure 7.8: SiO rotational rate coefficients obtained for the 48-state calculation

This begins to decline in importance beyond about 50^o. The slight shoulder feature at around 60^o appears to be due to the temporarily dominant 0–0 elastic DCS and the maximum in the 0–2 DCSs between 60^o and 70^o dominating over the 0–1 DCS. The shoulder feature at 120^o seems to arise due to the slight upturn in the 0–2 differential cross section and the increased contribution of the 0–3 transition. At the backward angles the dipole forbidden 0–2 and 0–3 transitions are now dominant, especially 0–2. The elastic 0–0 differential cross section also exhibits a pronounced dip at around 130^o. Such dips were also observed by Allan and Dickinson (1981) for the polar diatomic CsCl, where a semiclassical approach was employed. They attributed their minima to an interference effect between two equally weighted classical paths. We seem to observe the same phenomenon here.

7.5 Rotational Rate Coefficients

Rotational rate coefficients were obtained for the temperature range 5–5000 K for all rotational transitions up to and including $J = 40$ using a Maxwellian velocity distribution for the electron. For use in astrophysical modelling, the temperature dependence of the downward transition rate coefficients $k(T)$ (units $\mathrm{cm^3 s^{-1}}$) was fitted to the analytic form:

transition	$E_{up}(K)$	a_0	a_1	a_2	a_3	a_4
$(1-0)$	2.1	−7.731	11.928	−22.532	18.395	−5.200
$(2-0)$	6.3	−10.395	14.975	−23.728	16.558	−3.819
$(2-1)$	6.3	−7.656	11.869	−23.242	20.127	−6.326
$(3-0)$	12.5	−11.600	11.999	−6.300	−14.916	14.215
$(3-1)$	12.5	−10.178	14.027	−20.606	11.987	−1.533
$(3-2)$	12.5	−7.603	11.605	−22.991	20.254	−6.547
$(4-0)$	20.8	−0.013	−91.311	293.200	−391.836	187.661
$(4-1)$	20.8	−11.386	11.195	−3.625	−18.944	16.301
$(4-2)$	20.8	−10.127	13.935	−20.098	10.828	−0.807
$(4-3)$	20.8	−7.596	11.643	−23.568	21.388	−7.218
$(5-0)$	31.3	0.278	−101.271	306.022	−391.605	181.361
$(5-1)$	31.3	0.227	−92.165	295.804	−395.563	189.546
$(5-2)$	31.3	−11.255	10.466	−1.111	−22.809	18.348
$(5-3)$	31.3	−10.067	13.584	−18.811	8.690	0.371
$(5-4)$	31.3	−7.581	11.584	−23.815	22.083	−7.682
$(6-0)$	43.8	−1.067	−101.243	292.697	−362.114	163.215
$(6-1)$	43.8	0.412	−101.110	305.389	−391.001	181.190
$(6-2)$	43.8	0.421	−93.236	298.996	−399.926	191.696
$(6-3)$	43.8	−11.182	10.104	0.015	−24.476	19.196
$(6-4)$	43.8	−10.036	13.439	−18.270	7.709	0.932
$(6-5)$	43.8	−7.583	11.646	−24.360	23.082	−8.256
$(7-0)$	58.3	11.481	−239.733	742.962	−980.050	467.243
$(7-1)$	58.3	−0.977	−100.479	289.822	−358.180	161.327
$(7-2)$	58.3	0.444	−100.663	303.710	−388.754	180.127
$(7-3)$	58.3	0.555	−93.980	301.082	−402.672	193.010
$(7-4)$	58.3	−11.069	9.271	2.732	−28.409	21.210
$(7-5)$	58.3	−10.010	13.327	−17.931	7.135	1.242
$(7-6)$	58.3	−7.561	11.498	−24.229	23.190	−8.410
$(8-0)$	75.0	−11.286	−8.395	−54.348	142.094	−90.529
$(8-1)$	75.0	11.916	−242.005	749.537	−988.557	471.274
$(8-2)$	75.0	−1.069	−98.999	285.134	−352.177	158.564
$(8-3)$	75.0	0.464	−100.350	302.442	−387.001	179.279
$(8-4)$	75.0	0.665	−94.637	302.945	−405.165	194.232
$(8-5)$	75.0	−10.985	8.646	4.744	−31.332	22.724
$(8-6)$	75.0	−10.000	13.293	−17.720	6.551	1.661
$(8-7)$	75.0	−7.579	11.687	−25.112	24.596	−9.162

Table 7.4: SiO rotational rate fitting coefficients obtained for the 48-coupled states calculation. Coefficients for $J > 8$ can be obtained upon request from the authors. The energies E_{up} are from the CDMS catalogue as given in http://www.strw.leidenuniv.nl/∼moldata/datafiles/sio.dat

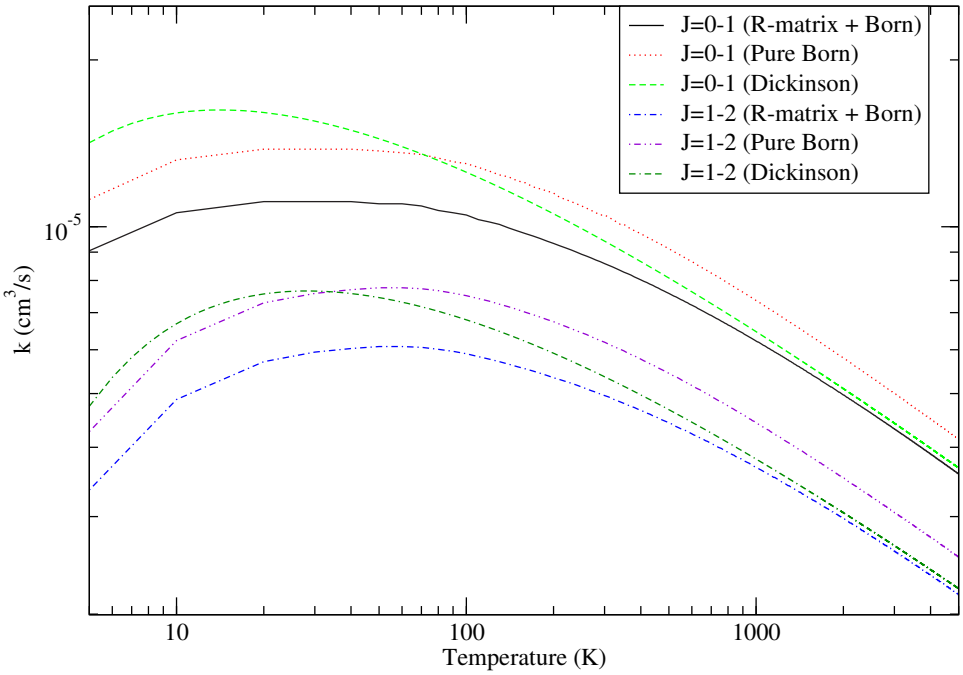

Figure 7.9: Comparison of rate coefficients obtained by the best R-matrix model to the analytical formula of Dickinson et al. (1977) and the rate coefficients using the Born approximation cross sections

$$\log_{10} k(T) = \sum_{r=0}^{N} a_r x^r \tag{7.1}$$

where $x = (T/\mathrm{K})^{-1/6}$ and $N = 4$. These de-excitation rotational rate coefficients were obtained using the principle of detailed balance:

$$k_{j_f \to j_i}(T) = \frac{2j_i + 1}{2j_f + 1} k_{j_i \to j_f}(T) \exp\left(\frac{\Delta E_{j_f \leftarrow j_i}}{k_B T}\right) \tag{7.2}$$

where j_i and j_f are the initial and final rotational quantum numbers and the rotational energy level spacing is

$$\Delta E_{j_f \leftarrow j_i} = B[j_f(j_f + 1) - j_i(j_i + 1)] \tag{7.3}$$

The fitting coefficients are listed in table 7.4 and the graph of the excitation rate coefficients for the dipole-allowed transitions $J = 0 - 1$ and $J = 1 - 2$ and the dipole forbidden $J = 0 - 2$ is given in figure 7.8. The global fitting error for the fitting coefficients in table 7.4 was found to be about 50 %. Following from our experience with CS (appendix C), we considered a new temperature range 5–3000 K which was split into

two sub-ranges 5–490 K and 490–3000 K, thus yielding two sets of fitting coefficients and new lower global fitting errors of 18 % and 2 % respectively. The new sets are given in tables 7.5 and 7.6.

Although there has been no other study carried out on electron impact rotational excitation of SiO, the excitation rate coefficients of the present study are compared to those obtained using the analytic formula of Dickinson et al. (1977) (equation (1) of that paper), the rate coefficients obtained using only the Born cross sections and the atom-SiO data of Dayou and Balanca (2006) and Palov et al. (2006). The rate coefficients obtained for collisions with electrons are typically six orders of magnitude higher than the He-SiO rate coefficients of Dayou and Balanca (2006), and four to six orders of magnitude higher than the H-SiO rate coefficients of Palov et al. (2006). One can conclude from this observation that electron collisions can compete with, if not dominate over, atom collisions as the chief rotational excitation mechanism of SiO in astrophysical regions where the ionization degree exceeds $\sim 10^{-5}$ (e.g. diffuse interstellar clouds, C-type shocks, etc.). Similar conclusions were reached in chapter 10 for HCN. We note that our rate coefficients compare favourably with both the Dickinson coefficients at the higher temperatures, but are smaller at the low temperatures. But it is worth noting though that Dickinson et al. (1977) checked their analytical formula against the CN close-coupling calculations of Allison and Dalgarno (1971). They suggested, from this and other checks, that the error was no more than 20% at 100K.

7.6 Conclusion

The present study has applied the *ab initio* R-matrix method to low-energy electron impact excitation of SiO, with the aim of calculating quantities of astrophysical interest. This is the first low-energy electron impact study to have been carried out on SiO. This study employed the configuration interaction and Hartree-Fock methods to represent the target for use in close-coupling and static exchange scattering calculations respectively. Two N-state close coupling calculations were carried out. The first one retained 24 target states (150 channels) and the second retained 48 target states, or 300 channels in the said expansion and for the construction of the R-matrix evaluated at the surface of the sphere, the radius of which was taken to be 12 a_0 so as to fully contain the target molecular electron charge cloud.

The scattering quantities computed were the eigenphase sum, the electronic exci-

Transition	E(K)	a_0	a_1	a_2	a_3	a_4
$(1-0)$	2.1	−8.130	15.049	−31.456	29.466	−10.228
$(2-0)$	6.3	−10.911	19.507	−38.042	35.874	−13.233
$(2-1)$	6.3	−7.824	13.131	−26.734	24.329	−8.182
$(3-0)$	12.5	−14.058	33.041	−71.496	71.731	−27.501
$(3-1)$	12.5	−10.711	18.718	−35.467	32.087	−11.344
$(3-2)$	12.5	−7.577	11.333	−22.033	18.864	−5.834
$(4-0)$	20.8	−12.986	14.732	−22.763	14.568	−2.782
$(4-1)$	20.8	−14.001	33.487	−72.478	72.332	−27.555
$(4-2)$	20.8	−10.713	19.033	−36.120	32.364	−11.269
$(4-3)$	20.8	−7.479	10.622	−20.378	17.127	−5.160
$(5-0)$	31.3	−9.753	−20.607	69.148	−90.760	41.901
$(5-1)$	31.3	−12.664	13.204	−18.144	8.238	0.329
$(5-2)$	31.3	−13.845	32.572	−69.452	67.853	−25.237
$(5-3)$	31.3	−10.598	18.248	−33.559	28.610	−9.344
$(5-4)$	31.3	−7.353	9.682	−18.057	14.584	−4.134
$(6-0)$	43.8	−7.649	−48.759	139.737	−169.138	74.274
$(6-1)$	43.8	−9.396	−22.290	74.073	−97.376	45.141
$(6-2)$	43.8	−12.421	11.759	−13.893	2.571	3.067
$(6-3)$	43.8	−13.853	32.866	−70.253	68.634	−25.524
$(6-4)$	43.8	−10.589	18.263	−33.448	28.129	−8.996
$(6-5)$	43.8	−7.138	8.026	−13.622	9.329	−1.835
$(7-0)$	58.3	−19.005	12.624	−17.153	6.645	1.324
$(7-1)$	58.3	−7.130	−51.411	146.798	−177.717	78.144
$(7-2)$	58.3	−9.033	−24.496	80.142	−104.921	48.598
$(7-3)$	58.3	−12.197	10.257	−9.498	−3.192	5.812
$(7-4)$	58.3	−13.616	31.063	−64.763	61.267	−21.954
$(7-5)$	58.3	−10.601	18.460	−34.025	28.732	−9.236
$(7-6)$	58.3	−7.111	7.832	−13.353	9.259	−1.906
$(8-0)$	75.0	1.186	−106.413	227.555	−209.377	69.795
$(8-1)$	75.0	−18.464	9.478	−7.941	−5.294	6.981
$(8-2)$	75.0	−6.795	−53.318	151.949	−184.089	81.069
$(8-3)$	75.0	−8.657	−27.061	87.372	−114.011	52.795
$(8-4)$	75.0	−11.845	7.657	−1.947	−12.894	10.370
$(8-5)$	75.0	−13.484	30.071	−61.717	57.080	−19.873
$(8-6)$	75.0	−10.598	18.472	−33.932	28.276	−8.868
$(8-7)$	75.0	−6.904	6.275	−9.282	4.558	0.100

Table 7.5: SiO rotational rate fitting coefficients obtained for the 48-coupled states calculation and the temperature range 5–490 K. Coefficients for $J > 8$ can be obtained upon request from the authors. The energies E_{up} are from the CDMS catalogue as given in http://www.strw.leidenuniv.nl/∼moldata/datafiles/sio.dat

Transition	E(K)	a_0	a_1	a_2	a_3	a_4
$(1-0)$	2.1	−8.660	23.827	−79.521	139.417	−101.369
$(2-0)$	6.3	29.659	−471.752	2190.351	−4453.020	3375.533
$(2-1)$	6.3	−6.798	0.061	37.017	−115.277	106.815
$(3-0)$	12.5	97.811	−1302.189	5900.014	−11789.932	8803.382
$(3-1)$	12.5	30.089	−474.648	2199.400	−4463.571	3377.818
$(3-2)$	12.5	−7.898	14.595	−33.938	37.083	−15.378
$(4-0)$	20.8	−23.057	278.654	−1796.677	4635.959	−4209.866
$(4-1)$	20.8	98.939	−1314.124	5953.516	−11897.176	8884.145
$(4-2)$	20.8	29.911	−472.217	2189.749	−4447.316	3368.057
$(4-3)$	20.8	−9.406	34.575	−132.667	252.318	−190.650
$(5-0)$	31.3	−11.268	57.985	−496.898	1369.237	−1240.138
$(5-1)$	31.3	−20.395	245.377	−1632.659	4277.922	−3918.518
$(5-2)$	31.3	99.968	−1326.187	6009.634	−12013.665	8974.893
$(5-3)$	31.3	31.354	−490.609	2278.959	−4639.070	3521.941
$(5-4)$	31.3	−8.582	23.157	−73.756	117.418	−75.558
$(6-0)$	43.8	−8.244	−9.198	−143.373	542.975	−531.643
$(6-1)$	43.8	−9.020	30.168	−359.758	1070.600	−998.306
$(6-2)$	43.8	−22.526	272.599	−1758.055	4532.138	−4110.454
$(6-3)$	43.8	101.081	−1339.692	6073.058	−12146.421	9079.051
$(6-4)$	43.8	30.350	−477.051	2211.740	−4491.732	3401.238
$(6-5)$	43.8	−6.076	−9.506	85.206	−225.782	201.342
$(7-0)$	58.3	−349.365	4561.218	−23000.356	50783.394	−41531.563
$(7-1)$	58.3	−6.786	−26.289	−59.298	359.585	−382.814
$(7-2)$	58.3	−7.285	7.765	−247.468	822.161	−794.049
$(7-3)$	58.3	−23.589	286.203	−1820.237	4656.906	−4203.645
$(7-4)$	58.3	99.217	−1314.320	5946.150	−11866.794	8849.594
$(7-5)$	58.3	30.587	−480.190	2228.043	−4529.249	3433.252
$(7-6)$	58.3	−8.571	23.374	−76.942	128.019	−87.305
$(8-0)$	75.0	9.308	−257.364	1067.575	−2091.695	1568.068
$(8-1)$	75.0	−348.735	4551.321	−22933.765	50599.832	−41352.479
$(8-2)$	75.0	−7.467	−16.467	−107.969	467.883	−474.106
$(8-3)$	75.0	−7.890	16.122	−288.080	910.410	−866.833
$(8-4)$	75.0	−24.986	304.574	−1908.683	4845.266	−4353.940
$(8-5)$	75.0	97.014	−1284.746	5799.357	−11545.433	8587.349
$(8-6)$	75.0	30.011	−472.087	2186.350	−4434.775	3353.455
$(8-7)$	75.0	−7.728	12.147	−21.256	5.255	13.816

Table 7.6: SiO rotational rate fitting coefficients obtained for the 48-coupled states calculation and the temperature range 490–3000 K. Coefficients for $J > 8$ can be obtained upon request from the authors. The energies E_{up} are from the CDMS catalogue as given in http://www.strw.leidenuniv.nl/∼moldata/datafiles/sio.dat

tation cross section and the Binary-Encounter-Bethe ionisation cross section using the HF-SCF occupied molecular orbitals. The T-matrices obtained from the R-matrix calculation were initially transformed to the natural symmetry $C_{\infty v}$ to yield a new set of T-matrices for the scattering symmetries $^2\Sigma^+$, $^2\Pi$, $^2\Delta$, $^2\Phi$ and $^2\Gamma$. These were then employed in the computation of the inelastic rotational cross sections, the rotationally resolved differential cross sections and rate coefficients and their fitting coefficients for all transitions up to $J = 40$, some or all of which may be useful in later astrophysical modelling.

The present study was able to detect some interesting features of the scattering calculation, particularly the independent confirmation of a $^2\Pi$ SiO^- bound state at -0.12 eV which was predicted by the density functional work of Alikhani et al. (1997). The present work also predicts the existence of low-lying narrow $^2\Pi$ and $^2\Delta$ Feshbach resonances at 5–6 eV and a $^2\Sigma^-$ Feshbach resonance at 8.16 eV. Due to the lack of other low-energy e-SiO scattering studies this work cannot be benchmarked at present. However, it may aid in the detailed investigation of electron density enhancements expected during the first stages of a C-type shock evolution (Jimenez-Serra et al., 2006), or indeed other astrophysical environments.

Chapter 8

Electron Scattering by the Carbon Monosulphide (CS) Molecule

8.1 Introduction

CS, an unstable radical, has been the subject of great study in astrophysics and in plasma physics: Moltzen et al. (1988) presented a comprehensive review of the molecule's role in interstellar chemistry and the importance of its etching properties in plasma physics. CS has been identified in the interstellar medium (ISM): in carbon rich circumstellar envelopes (Woods et al., 2003), it has been used to measure isotopic sulphur ratios $^{32}S/^{34}S$ in the NGC 253 galaxy (Martin et al., 2005) and has been detected in comets such as C/1995 O1 (Hale-Bopp) by Biver et al. (1997) and Snyder et al. (2001). Additional detection studies have been carried out by Scappini et al. (2007), Penzias et al. (1971), Linke and Goldsmith (1980) and Zuckerman et al. (1972).

Atom-CS collisions are very important in astrophysical modelling, particularly those with H_2 and He. Aimed at the modelling observed spectra, following high spatial and spectral resolution studies at infrared and submillimeter wavelengths by the Alma and Herschel missions, Lique et al. (2006) calculated rotational excitation rate coefficients for He-CS collisions for up to $J = 31$ for kinetic temperatures 10 K–300 K. They used a new 2D *ab initio* potential energy surface for the He-CS compound system (here the CS interatomic bond length was fixed to its equilibrium value), calculated using a supermolecular approach based on the single and double excitation coupled cluster method (CCSD) (Hampel et al., 1992) and perturbative contributions from connected triple excitations computed as defined by Watts et al. (1993). The atoms were represented by

GTO basis sets of quadruple zeta quality (cc-pVQZ), augmented with the diffuse functions of *s, p, d, f* and *g* symmetries by Kendell et al. (1992) (aug-cc-pVQZ). This basis set was further augmented by the optimized functions of Cybulski and Toczylowski (1999). The scattering calculation of Lique et al. (2006) was carried out using the close-coupling (CC) approach, and then the thermally averaged rate coefficients were calculated for kinetic temperatures 10 K to 300 K. The later study of Lique and Spielfiedel (2007) also considered ro-vibrational excitation of CS by the He atom where they employed a 3D potential energy surface which was calculated by Lique et al. (2006) but which took dependence on the CS interatomic distance explicitly into account. The dynamic calculations were carried out using the vibrational close coupling-infinite order sudden (VCC-IOS) method (Goldflam, Green and Kouri, 1977; Goldflam, Kouri and Green, 1977). Cross sections among the 38 first rotational levels of $\nu = 0$, $\nu = 1$ and $\nu = 2$ for energies up to 10,000 cm^{-1} (1.24 eV) were calculated, which after thermal averaging yielded rate coefficients for temperatures up to 1500 K. Other He-CS calculations were discussed by Lique et al. (2007).

Green and Chapman (1978) considered H_2-CS collisional excitation rate coefficients in their study. They employed an interaction potential for the H_2-CS system adopted from the electron gas model for He-CS adopted by Gordon and Kim (1972). The final cross section set was obtained from two types of calculation- a close-coupled and coupled states calculation. Finally, integration over a Boltzmann distribution of collision energies yielded rate coefficients for 10–100 K.

Electron-molecule interactions are also important in interstellar physics, as shown, for example, by the work of Jimenez-Serra et al. (2006) and Jimenez-Serra et al. (2005) who showed the importance of such collisions in C-type shocks. In diffuse interstellar clouds Drdla et al. (1989) concluded that the large dipole moment of CS aids the detection of the molecule in diffuse clouds since the dominant excitation mechanism is collisions with electrons: they obtained rate coefficients for $J + 1 \rightarrow J$ of $3{\times}10^{-6}$ cm^3s^{-1} at 10 K, five orders of magnitude higher compared to typical rate coefficients of (2–3)$\times10^{-11}$ cm^3s^{-1} for H_2-CS. Such collisions favour the dipole-allowed $\Delta J = 1$ transitions so observations of the lowest transitions may be the most useful.

There have been only a few electron collision studies carried out: the two most recent studies were a low-energy calculation (up to 10 eV) carried out by Carelli et al. (2008) and the work of Sobrinho and Lee (2005) which considered a wider incident energy

spectrum, from 1–500 eV. Both are discussed in detail below. In experiment a detailed study of dissociative electron attachment to CS was carried out recently by Graupner et al. (2006), a detailed discussion of which is also given below.

This chapter presents electron-impact excitation of CS as a function of bond stretch and contraction using the *ab initio* R-matrix method for a grid of 17 bond lengths: 1.1, 1.2, 1.3, 1.4, 1.45, 1.5, 1.52, 1.5349 (equilibrium NIST (2008)), 1.55, 1.6, 1.7, 1.8, 1.9, 2.0, 2.15, 2.3, 2.5 and 2.7 Å. For each geometry the fixed-nuclei (FN) approximation was employed. All calculations were carried out using the application Quantemol-N (Tennyson et al., 2007). The purpose of the work was to study the dissociative electron attachment (DEA) to CS in greater theoretical detail. Results obtained for the equilibrium geometry of the $^1\Sigma^+$ target ground state are also presented. To date no other electron scattering calculation at the close-coupling approximation has been carried out.

8.2 Previous Quantum Chemistry and Electron Scattering Studies

To date quantum chemistry studies have focused on the (large) dipole moment of CS. The first experimental determination of the dipole moment was carried out by Winnewisser and Cook (1968) using a parallel plate Stark modulated spectrometer, and obtained a value of +0.77 a.u.. It is also interesting to observe that the electronegativity difference has a different sign depending on the scheme. For example the Pauling difference is +0.03, the Allen electronegativity difference is +0.045 and the Mulliken difference is −0.02 (see Pauling (1932), Allen (1989) and Mulliken (1934)).

In addition to CO and SiO, Harrison (2006) analysed the dipole moment of CS at the CASSCF and MRCI levels of theory, obtaining +0.814 a.u. and +0.796 a.u. respectively, in good agreement with the experimental value of +0.77 a.u.. Harrison (2006) commented that CS stood out because it has such a large dipole moment for a diatomic whose constituent atoms had essentially the same electronegativities. In that study the dipole moment was written as a sum of a charge and induced atom dipole contribution and the distance dependence interpreted in terms of these components:

$$\mu = q(S)R + \mu(C) + \mu(S) \tag{8.1}$$

where $q(S)$ is the charge on the S atom (0.119 e for MRCI), R is the position of the S

atom (C was fixed at the origin) and $\mu(C)$ and $\mu(S)$ are the induced atomic dipoles of the C and S atoms respectively. Harrison (2006) stated that the large dipole moment was due to the two components of the dipole moments having the same sign at equilibrium and reinforcing one another (see table 4 of their paper for example). Harrison assigned a dipole moment positive sign to polarity $C^{-}S^{+}$. We adopted the same convention. Like the present study Harrison (2006) also computed the dipole moment function.

The *ab initio* study of Botschwina and Sebald (1985) used the SCF (self-consistent field), CISD (configuration interaction including all possible single and double electron excitation) and CEPA (coupled electron pair approximation-version 1) (Meyer, 1973) methods. The SCF (expectation) value for the dipole (0.6336 a.u.) was lower than experiment, the CI-SD expectation value (0.7755 a.u.) was in excellent agreement with experiment and the CEPA method yielded a much higher value (0.88 a.u.).

No studies, theoretical or experimental, have been done on the excited states of CS.

The electron scattering calculations of Carelli et al. (2008) used a 1-state single centre expansion, with the specific aim of locating and characterising the evolution of the $^{2}\Pi$ shape resonance with respect to CS bond contraction and bond stretch. Results for the equilibrium bond length of the $^{1}\Sigma^{+}$ ground state showed the position of this shape resonance to be between 0.6–0.9 eV. The major finding of their study was that with bond length contraction the $^{2}\Pi$ shape resonance widened and its position E_r increased, whereas with bond stretch the resonance position decreased and its width narrowed until beyond about 1.63 $\mathring{A}$, where the resonance became a anionic species bound state. The earlier experiment of Burnett et al. (1982) found that a stable beam of CS^{-} anions corresponded to a stretched bond length of 1.627 Å. Carelli et al. (2008) did not consider the electron-impact excitation of CS hence were unable to locate any Feshbach resonances.

Sobrinho and Lee (2005) employed a complex optical potential incorporating static, exchange, correlation-polarisation and absorption contributions to describe the electron-molecule interaction dynamics. The Schwinger variational iterative approach and the distortion approximation were applied to calculate the scattering amplitude, differential, total integral, momentum transfer and absorption cross section. Sobrinho and Lee (2005) analysed 2 target models– HF and CI with all possible singles and doubles (SDCI). The latter model yielded a dipole moment of 0.7596 a.u., in good agreement with the experimental value of 0.779 a.u. (NIST, 2008), and a target energy of -435.72419 E_h. They predicted the existence of $^{2}\Pi$ and $^{2}\Delta$ shape resonances. They too did not report

on the existence of any Feshbach resonances.

Electron-impact ionisation of CS has also been studied experimentally by Freund et al. (1990) and theoretically by Kim et al. (1997) using the BEB (Binary-Encounter-Bethe) method (Hwang et al., 1996; Kim and Rudd, 1994).

Graupner et al. (2006) carried out a detailed experimental study of the dissociative electron attachment (DEA) to CS:

$$CS(^1\Sigma^+) + e^- \rightarrow (CS^-)^* \rightarrow S^-(^2P) + C(^3P)\ (5.43\ eV) \tag{8.2}$$

$$\rightarrow S^-(^2P) + C(^1D)\ (6.70\ eV) \tag{8.3}$$

$$\rightarrow C^-(^4S) + S(^3P)\ (6.40\ eV) \tag{8.4}$$

Which the exception of channel 8.3, the fragments were all observed to be in their respective ground states. Graupner et al. (2006) observed that the DEA to CS was remarkably similar to DEA to the valence isoelectronic CO, however, they were unable to determine the identity of the attachment resonances responsible for dissociative electron attachment. They commented that computation of the CS potential energy curves and core excited (Feshbach) resonance curves would be immensely useful in improving the understanding of the molecular dynamics. It is the purpose of the chapter to address this issue.

The results obtained by the present study are compared to the previous ones discussed above.

8.3 Quantum Chemistry Model

The present study was carried out in the C_{2v} symmetry, the highest Abelian subgroup of the natural symmetry of CS $C_{\infty v}$. The equilibrium geometry was employed (R_{CS}=1.5349 Å NIST (2008)– initially with the S atom at the origin and C lying on the positive z-axis), and the Gaussian-Type orbital double zeta-plus-polarisation (DZP) basis set to carry out a Hartree-Fock self-consistent field (HF-SCF) calculation, which yielded a ground-state electron configuration of $1a_1^2\ 2a_1^2\ 3a_1^2\ 4a_1^2\ 1b_1^2\ 1b_2^2\ 5a_1^2\ 6a_1^2\ 7a_1^2\ 2b_1^2\ 2b_2^2$ (X $^1A_1$), or $1\sigma^2\ 2\sigma^2\ 3\sigma^2\ 4\sigma^2\ 1\pi^4\ 5\sigma^2\ 6\sigma^2\ 7\sigma^2\ 2\pi^4$ (X $^1\Sigma^+$) in the natural symmetry. The orbital energies are listed in table 8.1. By Koopman's theorem the ionisation energy of CS is 12.59 eV, much higher than the experimental value of 11.33 eV (NIST, 2008).

The occupied and virtual molecular orbitals obtained by the HF-SCF optimisation were then employed to set up complete active space configuration interaction (CASCI)

Orbital	$\|B\|$ (eV)	N
1σ $(1a_1)$	2503.58	2
2σ $(2a_1)$	309.03	2
3σ $(3a_1)$	245.20	2
4σ $(4a_1)$	182.06	2
1π $(1b_1, 1b_2)$	182.00	4 (2,2)
5σ $(5a_1)$	30.14	2
6σ $(6a_1)$	18.82	2
7σ $(7a_1)$	12.78	2
2π $(2b_1, 2b_2)$	12.59	4 (2,2)

Table 8.1: CS SCF occupied molecular orbitals for the DZP basis set and equilibrium geometry. The C_{2v} orbitals are given in parentheses

target electronic wavefunctions. The complete active space was generated automatically by Quantemol-N: $(1a_1, 2a_1, 3a_1, 4a_1, 1b_1, 1b_2)^{12}$ $(5a_1, 6a_1, 7a_1, 2b_1, 2b_2, 3b_1, 3b_2, 8a_1)^{10}$, namely 12 electrons (the 1s, 2s and 2p electrons of the S atom and the 1s electrons of the C atom) were frozen in all configurations and ten electrons were allowed to move freely amongst the 5–$8a_1$, 2–$3b_1$ and 2–$3b_2$ occupied and virtual molecular orbitals. The complete active space employed generated 328 CSFs (configuration state functions) for the $^1A_1$ ground state. The vertical excitation energies obtained by the present study are given in table 8.2.

The present study computed six target Hamiltonian eigenvalues per target state, a total of 48 target states. This model was employed for all the geometries listed previously. Target states at and above the ionisation threshold were computed, but are not shown in table 8.2. Such states are useful in the representation of polarisation effects in close-coupled scattering studies and are themselves better represented by the use of pseudo continuum orbitals (PCOs) (Gorfinkiel and Tennyson, 2004; Tarana and Tennyson, 2008): these PCOs were not employed by the present study. Although these high-lying states do not have any physical significance, they were nevertheless included in the scattering model discussed below. The target ground state energy is higher than the corresponding eigenvalue obtained by Sobrinho and Lee (2005) who employed the elaborate CISD method.

There are no other data to which the present study might be able to compare so it is very difficult to draw any conclusion. Historically the vertical excitation energies

Target state	Present work	Theory	Experiment
X $^1\Sigma^+$ (X $^1A_1$)	−435.3683		
1 $^3\Pi$ ($^3B_1$,$^3B_1$)	3.90		
1 $^3\Sigma^+$ ($^3A_1$)	5.03		
1 $^1\Pi$ ($^1B_1$,$^1B_2$)	5.53		
1 $^3\Delta$ ($^3A_1$,$^3A_2$)	5.73		
1 $^3\Sigma^-$ ($^3A_2$)	6.06		
1 $^1\Sigma^-$ ($^1A_2$)	6.34		
1 $^1\Delta$ ($^1A_1$, $^1A_2$)	6.37		
2 $^3\Pi$ ($^3B_1$, $^3B_2$)	8.98		
3 $^3\Pi$ ($^3B_1$, $^3B_2$)	9.95		
2 $^1\Pi$ ($^1B_1$, $^1B_2$)	10.03		
2 $^1\Sigma^+$ ($^1A_1$)	10.14		
4 $^3\Pi$ ($^3B_1$, $^3B_2$)	10.15		
2 $^3\Sigma^-$ ($^3A_2$)	10.68		
2 $^3\Sigma^+$ ($^3A_1$)	10.71		
3 $^1\Pi$ ($^1B_1$, $^1B_1$)	10.80		
5 $^3\Pi$ ($^3B_1$, $^3B_2$)	10.95		
6 $^3\Pi$ ($^3B_1$, $^3B_2$)	11.26		
2 $^1\Delta$ ($^1A_1$, $^1A_2$)	11.49		
4 $^1\Pi$ ($^1B_1$, $^1B_2$)	11.63		
3 $^1\Sigma^+$ ($^1A_1$)	11.92		
4 $^1\Sigma^+$ ($^1A_1$)	12.42		
5 $^1\Pi$ ($^1B_1$, $^1B_2$)	12.51		
μ	0.7021	0.7755[a]	0.77[b]
α_0	9.48	28.87[c]	

Table 8.2: CS ($R_{CS} = 1.5349\mathring{A}$) vertical excitation energies of all the electronic states below the ionisation threshold. The C_{2v} target states are given in parenthesis. All results are given in eV. Also shown are the target ground state in E_h, the dipole moment and spherical polarisability in a.u.

[a] Botschwina and Sebald (1985)

[b] Winnewisser and Cook (1968)

[c] Maroulis et al. (2000)

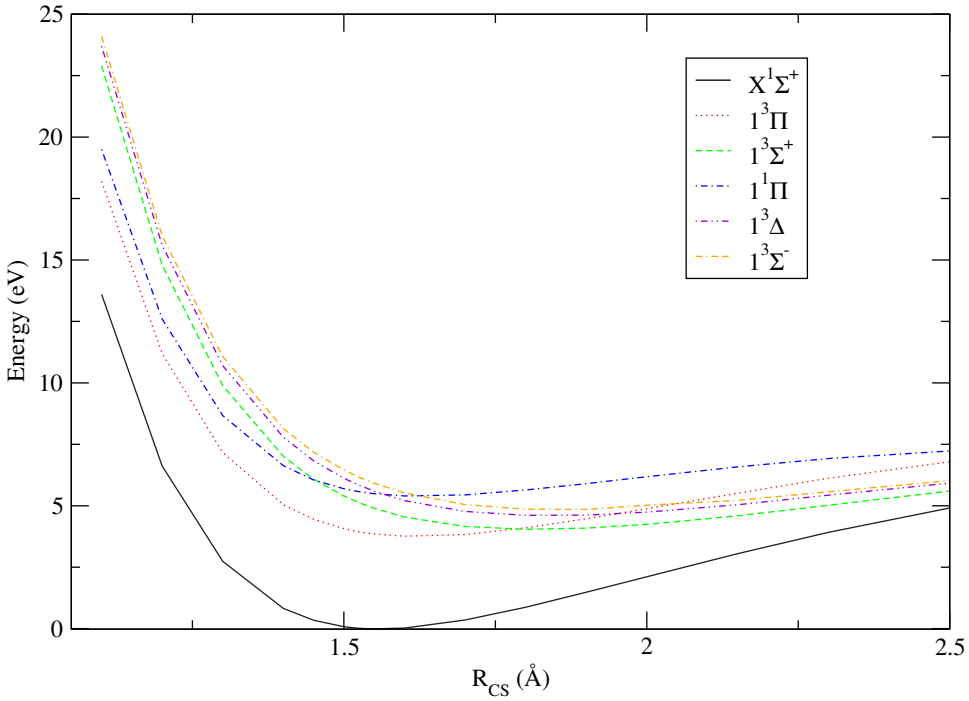

Figure 8.1: CS potential energy curves

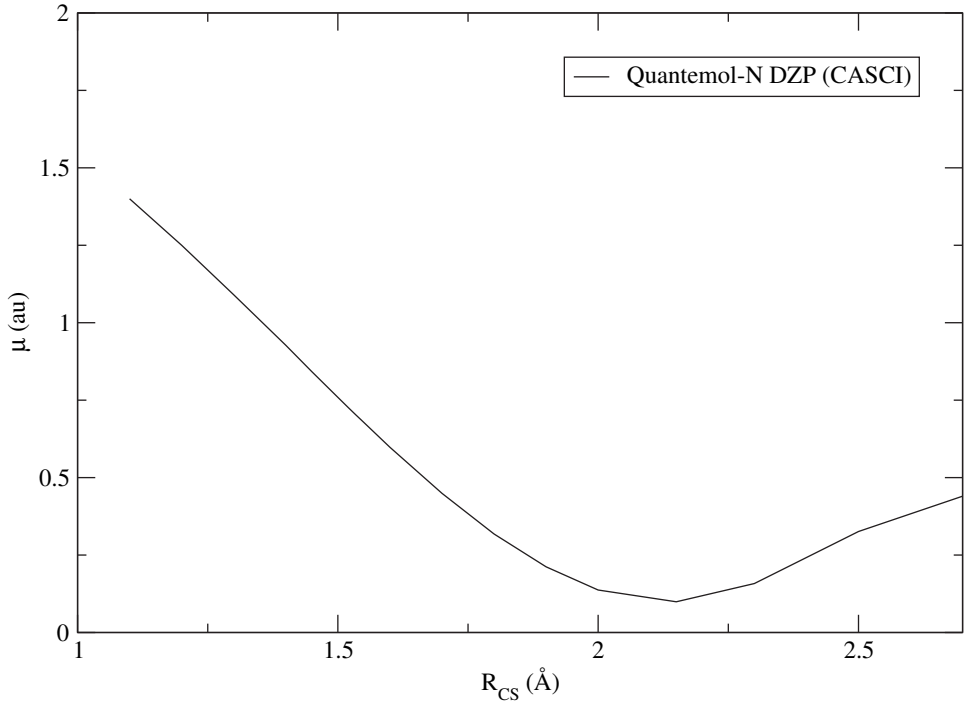

Figure 8.2: CS ground state dipole moment as a function of geometry

obtained by studies like the present one have tended to be in good agreement with previous experimental and quantum chemistry studies. The dipole transition moment however, appears to be in good agreement with the previous *ab initio* study of Botschwina and Sebald (1985) and the experiment of Winnewisser and Cook (1968). The dipole moment of the present study corresponds to the one obtained when the sulphur atom is at the origin and carbon atom lying on the positive z-axis. The dipole moment function of CS is shown in figure 8.2 and it follows a similar trend to, but lies lower in magnitude than, the CASSCF dipole moment function of Harrison (2006) which, like the present study, found that the dipole also exhibits a minimum at about 2–2.8 Å. The dipole moment of Harrison (2006) is in excellent agreement with experiment. This ought to be expected given that Harrison (2006) employed a very diffuse basis set (aug-cc-pV5Z) and the elaborate CASSCF and MRCI methods.

The vertical excitation energy data obtained by the present study are certainly very sensitive to the precise quantum chemistry model employed. Generally larger, or diffuse basis sets and use of more sophisticated methods such as MRCI, coupled-cluster approaches, CASCI incorporating all possible single and double excitations and pseudo-natural orbitals have been used previously (particularly the latter) to improve the representation of the target molecule, and lower the target ground state and excited-state Hamiltonian eigenvalues, which is important in FN R-matrix calculations, as demonstrated by the delicate case of CO. This study used Quantemol-N, which at present does not incorporate any of these methods. Very diffuse basis sets like those employed by Harrison (2006) are not used as this would yield significant target orbital amplitudes at the R-matrix boundary.

The potential energy curves are also shown in figure 8.1. The discussion above suggests that these potential energy curves are probably upper bounds on the true values.

The present study also computed the spherical polarisability using second-order perturbation theory. In this case, the present study expects this polarisability to underestimate the true value, but this has been the case historically (Gil et al., 1994). From table 8.2 it can be seen that our value of the polarisability is only about 30% of the coupled cluster (CCSD(T)) value obtained by Maroulis et al. (2000). Better agreement has been attained for other molecules with the use of the pseudo continuum orbitals (see Gorfinkiel and Tennyson (2004) for example). Again this was not attempted by the present study.

A criticism of the present target model is that the active space is rather small, including only three (two) C_{2v} ($C_{\infty v}$) virtual orbitals. This would result in less correlation being included in the target wavefunction than would otherwise be the case had a larger active space been employed. Inclusion of more target electron-electron correlation may improve on the accuracy of the vertical excitation energies. Additional studies, experimental and theoretical, need to be carried out in order to benchmark the accuracy of the quantum chemistry observables obtained by this study.

8.4 Scattering Model

The scattering calculation employed the target model discussed above, namely the DZP basis set, the CAS $(1a_1, 2a_1, 3a_1, 4a_1, 1b_1, 1b_2)^{12}(5a_1, 6a_1, 7a_1, 2b_1, 2b_2, 3b_1, 3b_2, 8a_1)^{10}$ and six eigenvalues per electronic state (all 48 target states). A series of fixed-nuclei R-matrix calculations were carried out on the bond lengths 1.1, 1.2, 1.3, 1.4, 1.45, 1.5, 1.52, 1.5349 (equilibrium), 1.55, 1.6, 1.7, 1.8, 1.9, 2.0, 2.15, 2.3, 2.5 and 2.7 Å.

The scattering model adopted by the present study employed the GTO continuum basis set of Faure et al. (2002), with a partial wave expansion up to and including g-partial wave ($l = 4$), to model the scattering electron. These continuum basis sets were orthogonalised to the target molecular orbitals using a mixture of Schmidt and Löwdin orthogonalisation techniques. Those continuum orbitals with overlap matrix eigenvalues less than 2×10^{-7} were removed. Since CS is a polar diatomic, the continuum orbital partial wave expansion is expected to converge slowly hence the Born correction was applied to account for the higher partial wave contribution (Kaur et al., 2008). Some of the low-lying SCF virtual orbitals obtained by the present study were used to augment the continuum orbital. These orbitals allow for high partial waves in the region of the nuclear singularity; however, as these virtual orbitals do not extend into the outer region they do not assist with the slow convergence of the partial wave expansion due to the effects of the long-range dipole potential.

Initially, for the equilibrium geometry, the present study used a sphere radius of 10 a_0, but there was significant amplitude on the boundary arising from the occupied molecular orbitals so a radius of 12 a_0 was adopted which reduced the surface orbital amplitude to order 10^{-6}. This radius was then adopted for all the bond lengths listed above.

In order to preserve the balance between the amount of correlation incorporated in

the target electronic wavefunction and the scattering wavefunction, the present study allowed 11 electrons (ten electrons + 1 scattering electron) to move freely amongst the 5–8a_1, 2–3b_1 and 2–3b_2 occupied and virtual molecular orbitals.

The calculations were carried out at the close-coupling (CC) approximation, where all 48 states (300 channels) were included in the CC expansion and for the construction of the R-matrix at the sphere surface as, *ab initio*, the modelling of the polarisation interaction is improved by the retention of a large number of closed channels.

Finally for each geometry, scattering calculations were carried out on the $^2A_1$, $^2B_1$, $^2B_2$ and $^2A_2$ symmetries for the incident energies 0.02–10.0 eV.

The results obtained are discussed below. Scattering quantities and observables obtained for the equilibrium geometry of the ground state are also presented.

8.5 Results

8.5.1 Eigenphase Sums, Resonances and Bound States

The $^2\Pi$ eigenphase sums for the equilibrium geometry static exchange (SE) and 48-state CC model are shown in figure 8.3. It shows a number of important features. The low-lying resonance feature seen in the SE eigenphase sum also appears in the CC eigenphase sum, but at a markedly lower position. This is a clear indication of a shape resonance, and the fact that the resonance reappears at a much lower position in the CC eigenphase sum curve confirms the improved modelling of the polarisation interaction discussed earlier. The 48-state CC calculation also shows the existence of three additional narrow resonances that are absent from the SE eigenphase curve, which is an indication that these resonances are Feshbach. The opening up of new excitation channels results in structures in the close-coupling eigenphase sum curves that are absent from the 1-state static exchange curves. The parameters for these resonances are listed in table 8.3 and were obtained by fitting to the Breit-Wigner profile (Tennyson and Noble, 1984). Some of the resonances were re-fitted using a smaller energy-spacing grid of 0.002 eV by application of R-matrix outer regions codes directly, using the R-matrix surface amplitudes and channel files obtained by Quantemol-N.

The present study confirmed the findings of Carelli et al. (2008) that a feature of e-CS scattering is the existence of a low-lying $^2\Pi$ shape resonance. The parameters for the shape resonance obtained by the present study are much lower (by about one-

Symmetry	Type	E_r	Γ_r
$^2\Pi$	Shape	0.311	0.0131
$^2\Pi$	Feshbach	5.58	0.0678
$^2\Pi$	Feshbach	6.29	0.0596
$^2\Pi$	Feshbach	6.91	0.188
$^2\Delta$	Feshbach	4.93	0.237
$^2\Sigma^-$	Feshbach	9.37	0.120

Table 8.3: CS equilibrium geometry resonance parameters for 48-state CC model. The parameters are given in eV

third) than those obtained by Carelli et al. (2008). The present work has identified Feshbach resonances for $^2\Pi$, $^2\Delta$ and $^2\Sigma^-$ scattering symmetries. It is difficult to make comparisons since no other close-coupling studies have been carried out to date. The experimental study of Graupner et al. (2006) however, stated that the appearance of three DEA channels at distinct appearance potentials suggests the occurrence of a number of Feshbach-type core-excited resonances during attachment.

So far as the quality of the observables is concerned, the inclusion of a large number of closed channels in the CC expansion may have converged the Feshbach resonance parameters, since they are very particularly sensitive to the precise treatment of the polarisation interaction in the outer region. The study therefore anticipates that the shape and Feshbach resonance parameters will be in good agreement with, but will be a little higher than, experiment. This is usually expected in *ab initio* scattering studies such as the present one. Furthermore, it is true to say that the parameters obtained by the present study will be sensitive to the precise location of the thresholds of their parent excited states, but no other excitation threshold data exist either. Experimental determination of these may help to determine the accuracy of the Feshbach resonance parameters obtained here. A test target state calculation was carried out which solved for seven Hamiltonian eigenvalues per electronic state, namely 56 states. This model yielded a spherical polarisability of 11.9 a_0^3 for the equilibrium geometry of the X $^1\Sigma^+$ ground state, an indication that the present study has not yet attained a converged treatment of the polarisation interaction.

Figure 8.4 shows the CS potential energy curves for the first six low-lying electronic states and the curves for the resonances that the present study could fit with confidence. Considering first the PES for the ground state of the anion, the shape resonance curve

lies above that of its parent state, the target $^1\Sigma^+$ ground state. The present study confirms that the $^2\Pi$ shape resonance starts to become lower and narrower in width as the CS bond is progressively stretched, until beyond 1.6 Å when the resonance becomes an anionic bound state. One means of detecting the bound state is by comparing the R-matrix pole E_{N+1} to the target ground state Hamiltonian eigenvalue. The present study computed the R-matrix poles for all the scattering symmetries and geometries. The $^2\Pi$ ($^2B_1$ and $^2B_2$) R-matrix pole for bond length 1.7 Å ($-435.3647\ E_h$) was found to be lower than the corresponding target X $^1\Sigma^+$ ground state energy for that bond length ($-435.3554\ E_h$); the ground state energy for 1.6 Å was lower than the corresponding R-matrix pole ($-435.3673\ E_h$ and $-435.3642\ E_h$ respectively), so one may conclude that the bond length at which the $^2\Pi$ shape resonance becomes bound lies somewhere between 1.6 Å and 1.7 Å, in agreement with Carelli et al. (2008). Given no additional calculations were carried out between these two bond lengths it is difficult to ascertain precisely this bound state CS bond length. No attempt was made to locate the S-matrix pole corresponding to the $^2\Pi$ bound state.

Similarly for the excited states the Feshbach resonances also become lower and narrower, beginning to become bound states beyond about 2 Å (see also figure 8.6); the $^2\Sigma^-$ Feshbach width however, increased with increasing bond length. From figure 8.4 the Feshbach resonance curves exhibit much parent swapping, which occurs when a resonance tracks a new target state potential energy curve, thus acquiring a new parent state, as the interatomic bond is stretched– for example between 1.75 Å and about 2 Å, the highest $^2\Pi$ Feshbach resonance (north-pointing triangles in figure 8.4) has parent state $^1\Pi$ and beyond 2.1 Å the parent state is the $^3\Pi$ target state. The parent swapping phenomenon is well-known and was studied by Stibbe and Tennyson (1997) in the case of e-H_2 scattering.

Figure 8.6 shows the position and width of the lowest $^2\Pi$ Feshbach resonance as a function of bond length. It is quite interesting to observe that the widths Γ_r do not vary smoothly as a function of bond length unlike the $^2\Pi$ shape resonance width parameter in figure 8.5. This may be due to the widths being sensitive to the precise details of the fit, in particular the energy grid spacing, for which the present study employed 0.02 eV. Also, it is well-known for resonance curves to cross the potential energy curves. Under these circumstances the resonance width can and does change (Halmova et al., 2006). Crossings between resonance and target potential energy curves are certainly seen in

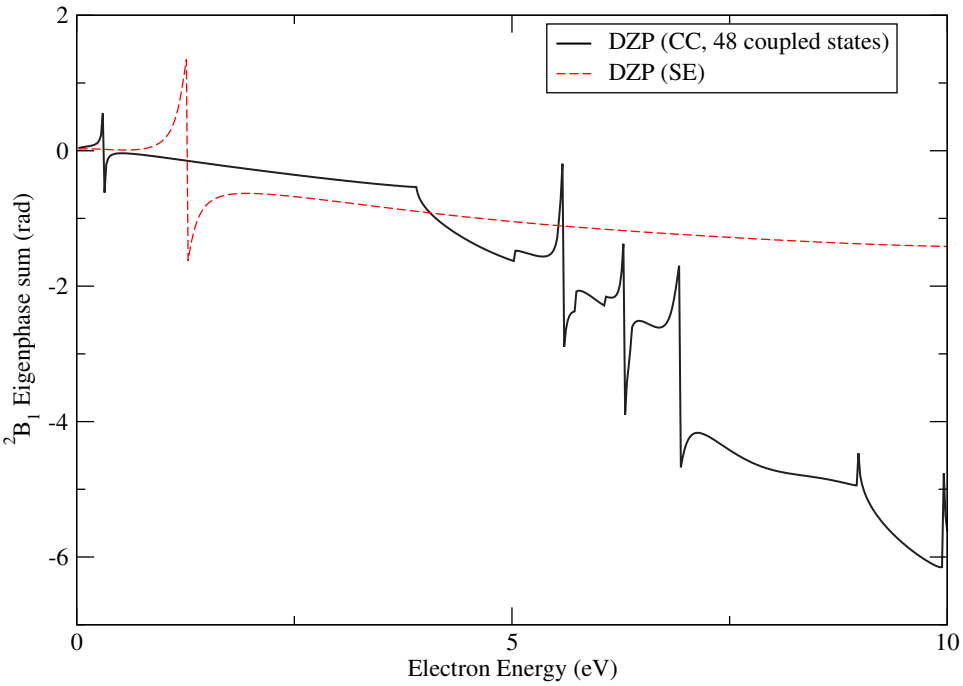

Figure 8.3: CS $^2B_1$ (predominantly $^2\Pi$) eigenphase sum for the equilibrium geometry

the present work: at about 1.55 Å the resonance curve corresponding to the lowest $^2\Pi$ Feshbach resonance curve crosses the 1 $^1\Pi$ potential energy curve, and one can see a slight discontinuity in the width curve shown in figure 8.6. Another crossing takes place at 1.8 Å, where the lowest $^2\Pi$ Feshbach resonance curve intersects the $^3\Pi$ potential energy curve.

8.5.2 Electronic Excitation Cross Sections

The electronic excitation cross sections in figure 8.7 show some interesting structures which are related to the Feshbach resonances discussed earlier. The peak in the X $^1\Sigma^+ \rightarrow$ 1 $^3\Pi$ excitation cross section is located at about 4.93 eV which coincides with the $^2\Delta$ resonance (table 8.3). Interestingly, there are two prominent peaks in the X $^1\Sigma^+ \rightarrow 1\ ^3\Sigma^+$ and X $^1\Sigma^+ \rightarrow$ 1 $^1\Pi$ cross sections at about 5.58 eV which correspond to the lowest $^2\Pi$ Feshbach resonance (see figure 8.3). A narrow peak at about 6.29 eV and a slightly wider and smaller peak at 6.9 eV were also found in the X $^1\Sigma^+ \rightarrow 1\ ^3\Delta$ excitation cross section, which correspond to the two higher $^2\Pi$ Feshbach resonances.

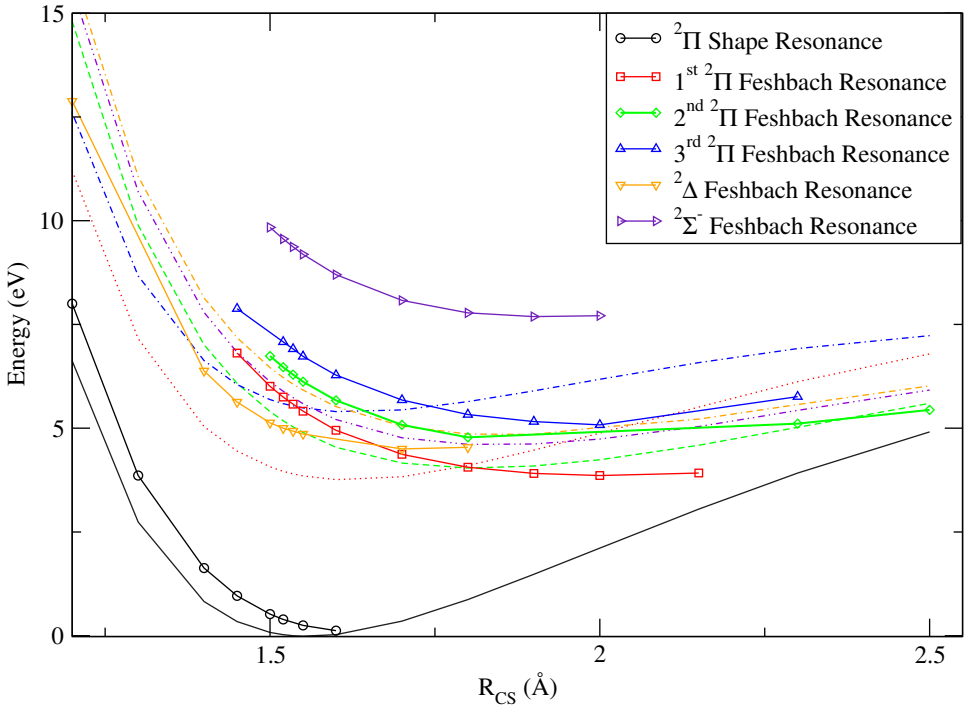

Figure 8.4: CS potential energy and resonance curves. The legends for the potential energy curves are as in figure 8.1

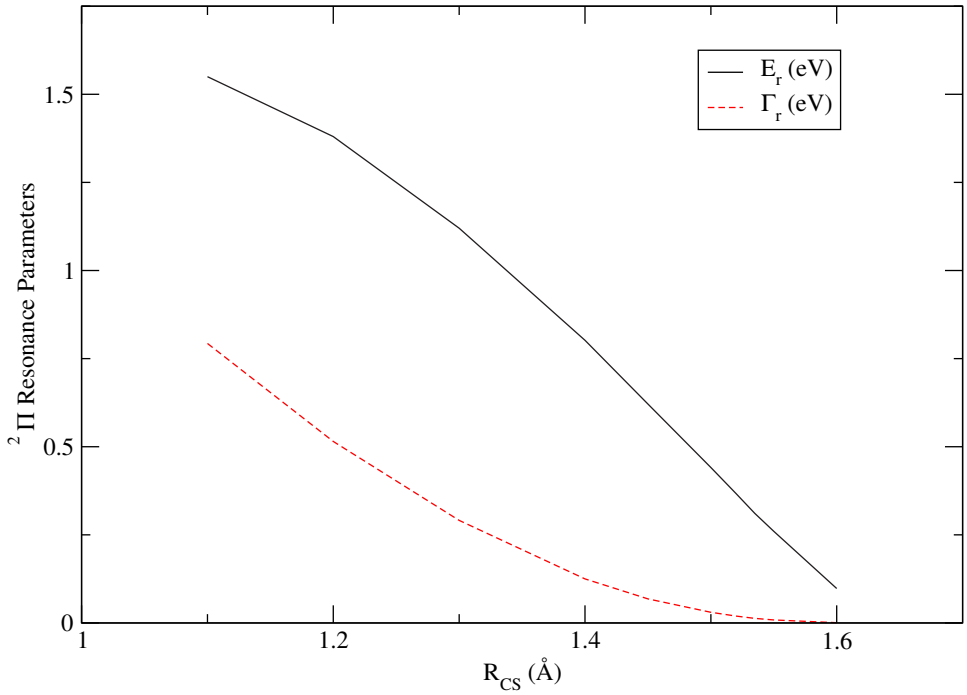

Figure 8.5: CS $^2\Pi$ shape resonance curve

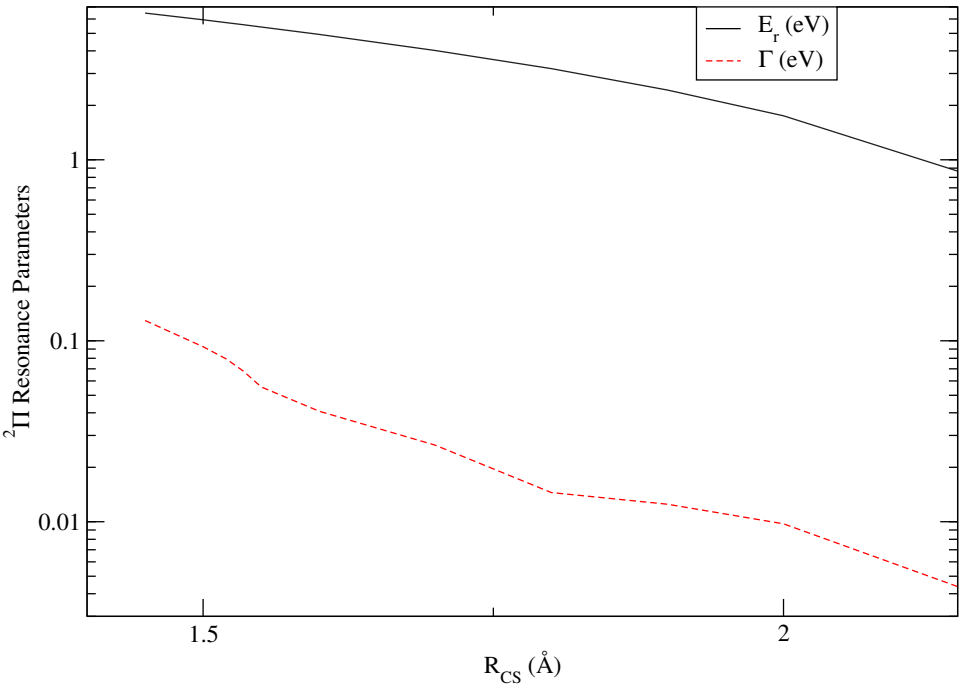

Figure 8.6: CS lowest $^2\Pi$ Feshbach resonance curve

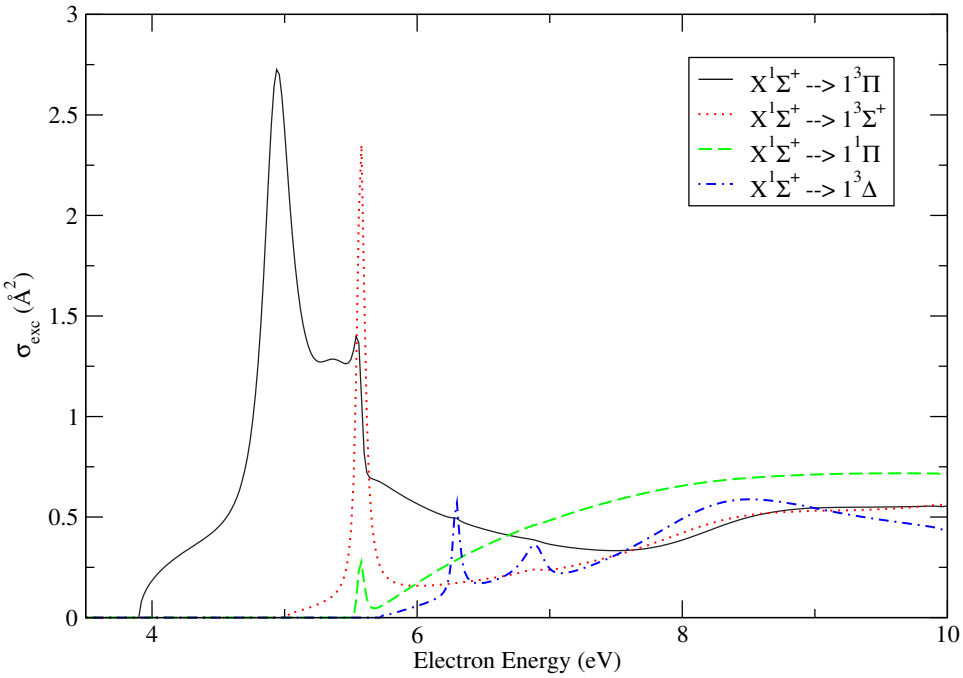

Figure 8.7: CS equilibrium excitation cross section curves for the first four lowest-lying excitation channels

Symmetry	Type	E_r	Γ_r
$^2\Pi$	Shape	0.260	0.00849
$^2\Delta$	Feshbach	4.87	0.241
$^2\Pi$	Feshbach	5.42	0.0556
$^2\Sigma^-$	Feshbach	5.60	0.00312
$^2\Pi$	Feshbach	6.14	0.0528
$^2\Pi$	Feshbach	6.75	0.178
$^2\Sigma^-$	Feshbach	9.20	0.123

Table 8.4: CS Resonances for $R_{CS} = 1.55$ Å. The parameters are given in eV.

Asymptote	Resonance Symmetry	E_r (eV)
S^-+C (6.70 eV)	$^2\Sigma^-$	9.37
	$^2\Pi$	6.75
C^-+S (6.40 eV)	$^2\Pi$	6.14
S^-+C (5.43 eV)	$^2\Sigma^-$	5.60
	$^2\Pi$	5.42
	$^2\Delta$	4.87
	$^2\Pi$	0.260

Table 8.5: CS correlation diagram. The energies in brackets are the appearance potentials obtained by Graupner et al. (2006)

8.5.3 Dissociative Electron Attachment (DEA)

The study of Graupner et al. (2006) identified three distinct appearance potentials for the DEA at 5.43 eV, 6.40 eV and 6.70 eV. With reference to table 8.4 which lists the resonance parameters for the stretching bond length 1.55 Å, the three Feshbach resonances lie very close to the appearance potentials measured by Graupner et al. (2006) which would suggest that these Feshbach resonances indeed enable dissociative electron attachment. The correlation table mapping the peaks identified by their study to the resonances listed in table 8.4 is given in table 8.5 (T. A. Field, private communication)

A more formal treatment of *ab initio* R-matrix theory including nuclear motion has been described by Burke and Tennyson (2005), which would enable a proper treatment of dissociative electron attachment; the present study did not adopt their approach.

8.6 Conclusion

The present study analysed electron scattering by CS using the *ab initio* R-matrix method at the close-coupling approximation. 17 bond-lengths between 1.1 Å and 2.7 Å were analysed each at the fixed-nuclei approximation. This is the first such many-state study to have been carried out.

The CS molecule was represented using CASCI target wavefunctions: the CAS employed froze 12 electrons in the $1a_1$, $2a_1$, $3a_1$, $4a_1$, $1b_1$ and $1b_2$ bound molecular orbitals and ten electrons were allowed to move freely amongst the $5a_1$, $6a_1$, $7a_1$, $2b_1$, $2b_2$, $3b_1$, $3b_2$ and $8a_1$ occupied and virtual molecular orbitals. The present study solved the Born-Oppenheimer problem for the 17 bond lengths to yield a potential energy curve (figure 8.1). The ground state potential energy curve remained the lowest energy one for the range of bond lengths considered so use of the equilibrium geometry ground state electron configuration for all geometries was fully justified. For basis set DZP and the equilibrium geometry, the target model yielded a dipole moment (+0.7021 a.u.), in good agreement with available experimental data (+0.77 a.u. Winnewisser and Cook (1968)). It is interesting to observe such a large dipole moment for a diatomic that has a very small electronegativity difference ($\chi = +0.02$ according to the Pauling scale (Pauling, 1932)). 48 target targets were computed for all the geometries considered. The dipole spherical polarisability at equilibrium is not known experimentally, however the value obtained by this study is expected to underestimate the true value: we have certainly confirmed this to be the case theoretically when one compares to more elaborate techniques such as that used by Maroulis et al. (2000) (see table 8.2).

The absence of any other vertical excitation data means that the target quantum chemistry model cannot be benchmarked in any way. The major criticism of the model is that perhaps there may be an insufficient amount of electron-electron correlation included in the CASCI target wavefunction owing to the small active space. This could be remedied by increasing the size of the active space to say 5–9a_1, 2–3b_1 and 2–3b_1, which was used for the isoelectronic SiO.

In developing the scattering model, the present study sought to ensure that the polarisation interaction was modelled as accurately as possible so the strategy adopted was to retain all 48 target states (300 electronic excitation channels) in the inner-region close-coupling expansion and retention of the same for construction of the R-matrix at the sphere surface, the radius of which was taken to be 12 a_0 so as to fully contain the

electronic charge distribution within the sphere.

The present study confirmed a number of findings made by the 1-state study of Carelli et al. (2008). A very low-lying $^2\Pi$ resonance was detected at 0.311 eV with a narrow width Γ_r of 0.0131 eV, much lower than Carelli et al. (2008). As in their study, this shape resonance was observed to become a bound state beyond 1.6 Å (figures 8.4 and 8.5). Analysis of the $^2\Pi$ R-matrix pole indicated that this CS^- bound state lies somewhere between 1.6 Å and 1.7 Å. The present study did not detect any $^2\Delta$ shape resonances predicted by Sobrinho and Lee (2005).

An entirely new finding made by the present study was that CS supports a number of Feshbach resonances of $^2\Pi$, $^2\Delta$ and $^2\Sigma^-$ symmetry (tables 8.3 and 8.4). As to the parentage of some of these Feshbach resonances the lowest $^2\Pi$ Feshbach resonance curve, which lies underneath the $^3\Delta$ potential energy curve, could arise from the configuration $2\pi^{-1}\ 3\pi^2$. The $^2\Delta$ Feshbach resonance curve lies below the $^1\Pi$ potential energy curve, suggesting that this target state might be the parent of the $^2\Delta$ resonance. The resonance could arise from a configuration $7\sigma^{-1}\ 3\pi^2$. However, assigning parents to Feshbach resonances is quite complicated (Stibbe and Tennyson, 1997). These Feshbach resonances may be responsible for the dissociative electron attachment asymptotes detected by Graupner et al. (2006). The correlation table predicting which resonances may be responsible for which DEA asymptotes is given in table 8.5.

So far as the evolution with respect to bond length stretching or contraction is concerned, the $^2\Pi$ and $^2\Delta$ Feshbach resonances follow a similar trajectory to the $^2\Pi$ shape resonance in that their positions become lower and their widths narrower as the CS bond is progressively stretched, as shown in figure 8.6. As the present study retained all 300 (open and closed) channels in the outer region for computation of the R-matrix at the sphere surface, the resonance position and width should be well converged with respect to the CC expansion. The resonance parameters are expected to be in good agreement with, but possibly a little higher than experiment.

In future work the R-matrices obtained for the equilibrium bond length will be employed for the computation of rotationally resolved differential cross sections, rotationally inelastic cross sections and the rotational excitation rate coefficients, which will be important in astrophysical modelling (Drdla et al., 1989). From similar studies (e.g. HCN and SiO) one may predict that the rotational excitation rate coefficients for e-CS collisions will be several orders of magnitude higher that those of H_2-CS and He-CS collisions

owing to the long-range nature of electric dipole moment of CS.

Another candidate for a similar study is CO: Graupner et al. (2006) have proposed such a study to determine why C^- is observed so weakly from CO but more strongly from CS.

Chapter 9

Electron collisions with CH_4

9.1 Introduction

The non-polar, tetrahedral methane molecule (natural point group T_d) is a well-known green-house gas but it was recently identified in the atmosphere of an extrasolar planet (Swain et al., 2008). Interstellar methane was discovered by Lacy et al. (1991) who reported the observation of solid and gaseous methane absorption toward young stars in molecular clouds. Other observational studies include Boogert et al. (2004) and Boogert et al. (1996).

Industrial applications of CH_4 include chemical vapour deposition for the manufacture of diamonds (Celii et al., 1988) and the development of carbon nanotubes and nanocrystalline diamond films (Matsushita et al., 2004). The fragmentation channels of CH_4 are important for such applications and electron-impact studies provide an insight into the underlying chemistry. Hence electron-impact dissociation of CH_4 has also been the subject of much investigation and the previous experimental studies of Makochekanwa et al. (2006) and Nakano et al. (1991) have focused on the dominant CH_3 and CH_2 fragmentation channels. Makochekanwa et al. (2006) located the $^3T_2$ threshold at about 7.5 eV, attributing it to the formation of the neutral CH_3 fragment, whereas previous studies attributed it to the CH_2 radical.

The major motivation for studying electron scattering by CH_4 has been that this molecule in particular is regarded by theorists as a benchmark system. From a theoretical standpoint the high symmetry and the heavy central C atom makes it an excellent system for collision methods based on single centre expansions and especially because of the difficulty *ab initio* potential-free methods have in reproducing polarisation effects

in this molecule fully (Gil et al., 1994; Lengsfield et al., 1991; Lima et al., 1990). This has resulted in extensive theoretical (and experimental) electron collision studies being carried out. Electron scattering by methane is known to exhibit some interesting features.

Previous electron collision studies have focused on one important feature, the Ramsauer-Townsend (R-T) minimum at about 0.4 eV. Theoretically the presence of this minimum can only be reproduced by the inclusion of the polarisation (it is absent from static exchange calculations). A pure s-wave low-energy phenomenon, the precise location in energy results from the balance of the attractive polarisation interaction and repulsive exchange. As a result the ^{2}A$_1$ eigenphase sum passes through 0^c and the electron propagates as a free particle at that energy. Gianturco et al. (1995) devoted their entire study to re-producing this effect. Their GTO multicentre wavefunction was given by a triple-zeta expansion plus d-type polarisation function on the C atom and p-type polarisation on the H atoms. The CH bond length was fixed to 2.063 a.u. and single centre expansion calculations were carried out on the A$_1$, T$_2$ and E T$_d$ scattering symmetries. Convergence tests on partial-wave expansions were carried out in all the symmetries and Gianturco et al. (1995) found $l_{max} = 7$ to produce fully converged K-matrix elements for each symmetry. They introduced the polarisation interaction with two different parameter-free models: short-range dynamical correlation was treated using density functional modelling (Gianturco and Rodriguez-Ruiz, 1993); short-range correlation was also treated using a simpler free-electron gas (FEG) model (Padial and Norcross (1984) for example). Needless to say both of these models accurately re-produced the R-T minimum in their integral cross sections (they also tested the free-electron gas model using Slater-Type orbitals). The FEG models were especially able to locate the minimum in the correct position and were in excellent agreement with the electron scattering experiment of Ferch et al. (1985).

Nestmann et al. (1994) applied the R-matrix method to elastic electron scattering by methane at the fixed-nuclei (FN) approximation using the C–H bond length 1.08583 Å and the orientation (a, a, a), ($-a$, $-a$, a), (a, $-a$, $-a$), ($-a$, a, a) for the H atoms. The T$_d$ scattering symmetries $^2A_1$, $^2T_2$ and ^2E were analysed. To represent the target states Nestmann et al. (1994) employed the accurate multireference single-double (MRD) CI approach (Buenker and Peyerimhoff, 1974, 1975*b*). As their MRD-CI code employs only Abelian point groups the D$_2$ sub-group of T$_d$ was used in their calcula-

tions. As in the present study GTO continuum basis sets were used to represented the projectile electron with only the s, p and d angular momenta retained in the partial wave expansion. Nestmann et al. (1994) carried out calculations at the 1-state static-exchange (SE) and static exchange-plus-polarisation (SEP) approximations. For the construction of the R-matrix, the sphere radius was taken to be 10 a.u. and in determining the reduced radial wavefunction for the scattered electron in the outer region, a spherical polarisability α_0 of 17.5 a_0^3 was assumed. Nestmann et al. (1994) commented that their model yielded integral cross sections in remarkably good agreement with the theory of Lengsfield et al. (1991) and the measurements of Lohmann and Buckman (1986), Sohn et al. (1986) and Ferch et al. (1985). The position of the R-T minimum and the broad structure of the maximum at 8 eV due to the $^2T_2$ symmetry were well reproduced. Interestingly, they (Nestmann et al. (1994)) were able to demonstrate sensitivity of the Ramsauer-Townsend minimum to the position of the energetically lowest $^2A_1$ R-matrix pole. Nestmann et al. (1994) also computed the differential cross section (DCS) with the dipole polarisability fixed at 17.5 a_0^3. Although they attained good agreement with the experiment of Sohn et al. (1986) and the calculation of Lengsfield et al. (1991), they observed a systematic shift of the DCS structures to lower angles.

So far as close-coupling (CC) calculations are concerned, the work of Gil et al. (1994) carried out 16-channel CC expansion studies invoking the Kohn variational principle. The main concern that arose out of their study was the validity of such large studies containing closely spaced Rydberg states, which are very diffuse and accumulate below the ionisation threshold. They argued that in order to obtain accurate cross sections for such transitions, one cannot simply include more states– this does not guarantee successful convergence: for example, they found the inelastic cross sections to the lowest-lying excited state of the same symmetry as the ground state to be very difficult to converge and not reliably predicted by close-coupling studies.

Other theoretical studies include the complex Kohn variational calculations of Lengsfield et al. (1991) and McCurdy and Resigno (1989), the multichannel Schwinger approach carried out by Lima et al. (1990), the model potential approach of Jain (1986) which specifically focused on the R-T minimum and the exact exchange study of McNaughten and Thompson (1988).

A number of experimental studies were also conducted which sought to reproduce the R-T minimum: Lohmann and Buckman (1986), whose time-of-flight spectrometer study

measured total integral cross sections for incident energies 0.1–20 eV, reproduced the R-T minimum at 0.36 eV and a cross section maximum (25.31 $Å^2$) at 8.0 eV; the time-of-flight spectrometer measurements of Ferch et al. (1985) analysed electron-methane scattering for the smaller incident energy range of 0.085–12 eV. They located the R-T minimum at 0.4 eV, in good agreement with the later work of Lohmann and Buckman (1986). A cross section maximum of 24.7 $Å^2$ was also observed at 8.0 eV.

Other experimental low-energy electron-methane scattering studies include Sueoka and Mori (1986) and Tanaka et al. (1982).

Studies have not been restricted to low-energies. There have been numerous electron scattering studies which have considered energies at and beyond the ionisation threshold, for example the calculations of Vinodkumar et al. (2006), Jain and Baluja (1992) and Hwang et al. (1996) and the electron-molecule crossed beam measurements Stano et al. (2003).

Jain and Baluja (1992) computed the elastic and inelastic cross section for the scattering of intermediate- and high-energy electrons from a variety of molecules, including CH_4, by computing complex potentials from their target wavefunctions. Its spherical component was used to yield the cross sections under the phase-shift analysis. For the non-spherical part of the complex potential Jain and Baluja (1992) employed the first-order Born approximation and added this contribution incoherently to the spherical part. For energies at and above 100 eV their computations agreed well with available data.

The recent study of Vinodkumar et al. (2006) found their inelastic cross sections to peak at 45 eV while the ionisation cross section peaked at about 70 eV. The latter cross sections agreed well with previous experimental data and their total (complete) cross section were in good agreement with Jain and Baluja (1992).

Experimental high-energy collision studies have been carried out by Duric et al. (1991) and Orient and Srivastava (1987). A BEB formalism calculation was carried out by Kim et al. (1997). These are discussed in more detail below.

This chapter presents the results obtained from a series of fixed-nuclei (FN) R-matrix close-coupling (CC) calculations for electron-scattering by CH_4 using the Quantemol-N expert system (Tennyson et al., 2007). The GTO target basis set and the number of states retained in the CC expansion and the number of channels retained in the inner region for the construction of the R-matrix at the sphere surface were varied. The aim was to converge the integral cross sections as well as possible with respect to the CC

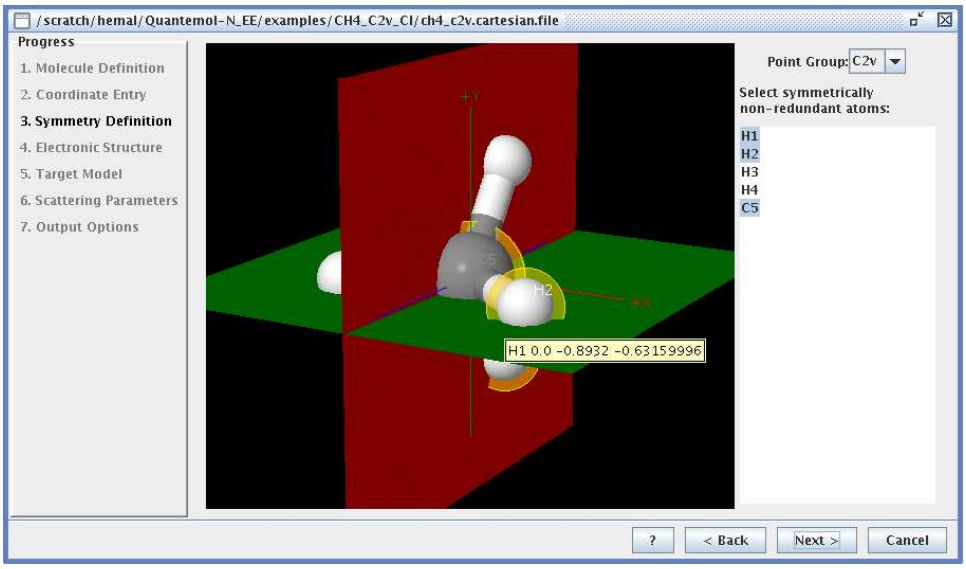

Figure 9.1: CH_4 in the orientation necessary for a C_{2v} R-matrix calculation

expansion and reproduce the R-T minimum and the broad maximum. Convergence with respect to partial wave expansion and other aspects of the present calculation were thoroughly tested by comparing rotationally summed differential cross sections. These were calculated by the POLYDCS package of Sanna and Gianturco (1998) using as input the C_{2v} K-matrices obtained by Quantemol-N. Finally, the electron-impact dissociation cross section and the BEB (Binary-Encounter-Bethe) cross section from ionisation threshold to 5000 eV were also computed and compared to the dissociation cross section measurements of Makochekanwa et al. (2006), the ionisation cross section experiments of Duric et al. (1991), Orient and Srivastava (1987) and the BEB calculations of Kim et al. (1997).

9.2 Quantum Chemistry Model

In order to optimise the present target (and scattering) calculation we employed the highest Abelian sub-group of the natural T_d point group, C_{2v}. Initially, the four hydrogen atoms were rotated in such a way that they were lying on the σ_{xz} and σ_{yz} mirror planes (figure 9.1). The C–H bond length 1.0940 Å (NIST, 2008) was adopted.

The ground state electron configuration is well-known, $1a_1^2\ 2a_1^2\ 3a_1^2\ 1b_1^2\ 1b_2^2$, or $1a_1^2\ 2a_1^2\ 1t_2^6$ in the natural symmetry ($X\ ^1A_1$). A Hartree-Fock self-consistent field (HF-SCF) calculation was carried out using the above configuration to yield a set of

Electronic state (T_d)	Present work			Theory[1]	Theory[2]	Theory[3]
	6–31G	DZP	6–31G*			
X $^1A_1$	0.0	0.0	0.0	0.0	0.0	0.0
1 $^3T_2$	12.1	13.6	12.2	12.3	9.97	10.86
1 $^3A_1$	12.6	14.4	12.7	13.0	11.09	
1 $^1T_2$	13.7		13.8	13.5	10.24	11.24
2 $^3T_2$	14.2	14.6	14.3	13.5	11.59	
1 ^3E	14.7		14.8	13.2	11.59	

Table 9.1: CH_4 Vertical excitation energies in eV for various basis sets, compared to previous theoretical works

[1] Gil et al. (1994),

[2] Williams and Poppinger (1975),

[3] Winstead et al. (1993)

bound and virtual molecular orbitals which were then employed to construct complete active space configuration interaction (CASCI) target wavefunctions. The complete active space was automatically generated by the Quantemol-N software:
$(1a_1)^2(2a_1, 3a_1, 3a_1, 4a_1, 5a_1, 1b_1, 1b_2, 2b_1, 2b_2)^8$, namely, two electrons were frozen in all configurations with the remaining eight electrons being allowed to move amongst the 2–$5a_1$, 1–$2b_1$ and 1–$2b_2$ occupied and virtual orbitals. This CAS generated 492 configuration state functions (CSFs) for the X $^1A_1$ ground state. The CASCI method yields a number of excited target states. The lowest-lying of these are known to have Rydberg character (Pauzat et al., 1972) and studies include the accurate coupled cluster linear response approach of Velasco et al. (2006) using atomic natural orbitals (ANOs) augmented with a series of 6*s* 6*p* 6*d* Rydberg functions allocated on the carbon atom; we did not include the Rydberg character of the excited states in the course of this study. Vertical excitation energies for the lowest of these states (up to the ionisation threshold of 14.75 eV) are shown in table 9.1 for the GTO basis sets DZP, 6–31G and 6–31G*. Use of the DZP basis set shifted the energies systematically upwards and the ^3E excitation threshold became higher than ionisation, hence its absence from table 9.1, and the $^1T_2$ state was found instead at 14.93 eV. But Williams and Poppinger (1975) did comment that the CI method is known to be sensitive to the basis set used.

The present vertical excitation energies are shown to be in reasonable agreement with Gil et al. (1994) but are systematically higher than the *ab initio* equations of motion

(EOM) calculations of Williams and Poppinger (1975) and the Schwinger multichannel (SMC) calculation carried out by Winstead et al. (1993).

Because the excited states of CH_4 are Rydberg-like, the target model of Williams and Poppinger (1975) employed a basis set including diffuse s and p atomic functions hence the basis on the carbon atom was modified as $1s$, $2s$, $2p$, $3s$ and $3p$, where each atomic orbital was expanded in terms of three Gaussian functions STO–3G and where the $3s$ and $3p$ functions were diffuse Rydberg-like with an optimised exponent of 0.6. For the H atom a single $1s$ function was expanded in terms of three Gaussians. They carried out additional calculations at the CI approximation. In analysing their results, Williams and Poppinger (1975) commented that their (1p-1h+2p-2h) EOM model was in much better agreement with experiment than their CI one because the former included more correlation, so it could be that the active space used during the present study is too small, resulting in less electron-electron correlation being incorporated in the target wavefunction. Our neglect of the Rydberg character of the low-lying target states may be a second reason for this work overestimating the excitation thresholds.

Winstead et al. (1993) employed an improved virtual orbitals (IVO) method to calculate the electronically excited states of CH_4 and the SCF (self-consistent field) calculation to compute the ground state. Their study only carried out two-, three- and seven-channel scattering calculations. Gil et al. (1994) also used the IVO approach for the representation of the excited states but yielded channel thresholds higher than the earlier study of Winstead et al. (1993).

Finally, it is interesting to observe that the $^3A_1$, 1 $^1T_2$ and 2 $^3T_2$ states predicted here are absent from the previous calculation of Winstead et al. (1993) which may be because the present study solved for more eigenvalues per target state.

The spherical polarisability α_0 was calculated using second-order perturbation theory as a summation over electronically excited states included in the close-coupling (CC) expansion. The values obtained from the various calculations we performed are shown in table 9.2.

Following the correction of a computer bug related to like-like transition moments in DENPROP, which resulted in the α_{zz} (diagonalised) tensor component being smaller than it should have been, the calculation which yielded the best spherical polarisability (basis set 6–31G) was re-run using a later version of Quantemol-N (version 3.5.2). The polarisability was much improved (with a 50% increase for both 6–31G and DZP) and

Basis set	N	α_0 (a_0^3)
6–31G	32	7.59
6–31G	48	7.62
6–31G*	48	7.43
DZP	48	6.22
DZP (v3.5.2)	48	9.34
6–31G (v3.5.2)	48	11.41
Experiment		16.52

Table 9.2: CH_4 spherical polarisabilities obtained by the present work compared to NIST (2008)

better agreement was attained with the experimental value of NIST (2008). Despite this, it is still lower than experiment, indicating that the polarisation interaction is underestimated (Gil et al., 1994).

Tong et al. (1991) carried out *ab initio* polarisability calculations for CH_4 at the SCF, singles and doubles CI (SDCI) and averaged coupled pair functional (ACPF) methods. Their study sought to compute first and second derivatives in order to calculate the scattering cross sections for selected overtone and combination bands. The best model (D&S basis set and the ACPF method) yielded a polarisability of 16.36 a_0^3 and 16.23 a_0^3 when SDCI was used, in very good agreement with experiment (table 9.2) and higher than our best value of the same.

Lengsfield et al. (1991) also devoted part of their scattering study to the computation of the polarisability using polarised orbitals and a full virtual space. Both of these methods yielded values in accord with experiment. For example, basis B (Core [C: $1p$ $3d$]) of their model using polarised orbitals gave rise to a polarisability of 17.49 a_0^3. This would certainly suggest that the polarisation is being modelled better by Lengsfield et al. (1991). As mentioned in the introduction, improved modelling of the polarisation interaction is crucial to reproducing the R-T minimum close to the experimentally observed position.

The target electronic states lying well above the ionisation threshold are useful in the representation of polarisation in close-coupling studies such as the present work. These high-lying states are themselves better represented using pseudo continuum orbitals (Gorfinkiel and Tennyson, 2004; Tarana and Tennyson, 2008), but these were not used in the present study. Despite having no particular physical significance these electronically excited states were nevertheless retained for later use in the scattering model

and their impact was found to be important as shall be discussed below.

9.3 Scattering Model

The present work tested all the target models discussed earlier, using a CAS $(1a_1)^2(2a_1, 3a_1, 4a_1, 5a_1, 1b_1, 1b_1, 2b_1, 2b_2)^8$ and GTO basis sets DZP, 6–31G and 6–31G*.

The scattering electron was modelled using the GTO continuum orbitals of Faure et al. (2002) which retained up to $l = 4$ (g-) partial waves. Since methane is a non-polar system the continuum wave expansion was expected to converge rapidly and no Born perturbative correction was necessary. The continuum orbitals were augmented with one low-lying virtual molecular orbital of each irreducible representation and then orthogonalised to the target molecular orbitals using a mixture of Schmidt and Löwdin orthogonalisation techniques.

The radius of the spherical boundary separating the inner and outer region was set to 10 a_0 and for matching to the asymptotic boundary condition, the R-matrix was propagated to a radial distance of 100.1 a_0, which proved to be adequate for all the models considered here.

In order to preserve the balance between the amount of correlation included in the target wavefunction and the scattering wavefunction, nine electrons (eight target electrons + 1 scattering electron) were allowed to be distributed among the $2a_1$, $3a_1$, $4a_1$, $5a_1$, $1b_1$, $2b_1$, $1b_2$ and $2b_2$ occupied and virtual orbitals.

Test calculations were carried out which varied the number of target states retained in the inner region CC expansion and for construction of the R-matrix at the surface of the partitioning sphere. These tests included 20, 32, 40 and 48 states in the inner and outer region and an SE calculation was also carried out as an additional test. The best model was considered to be the 48-state target model using the GTO 6–31G basis set. The C_{2v} K-matrices obtained from this model were then used to compute the rotationally summed DCSs and dissociation cross section and the bound molecular orbitals used to calculate the BEB electron-impact ionisation cross section.

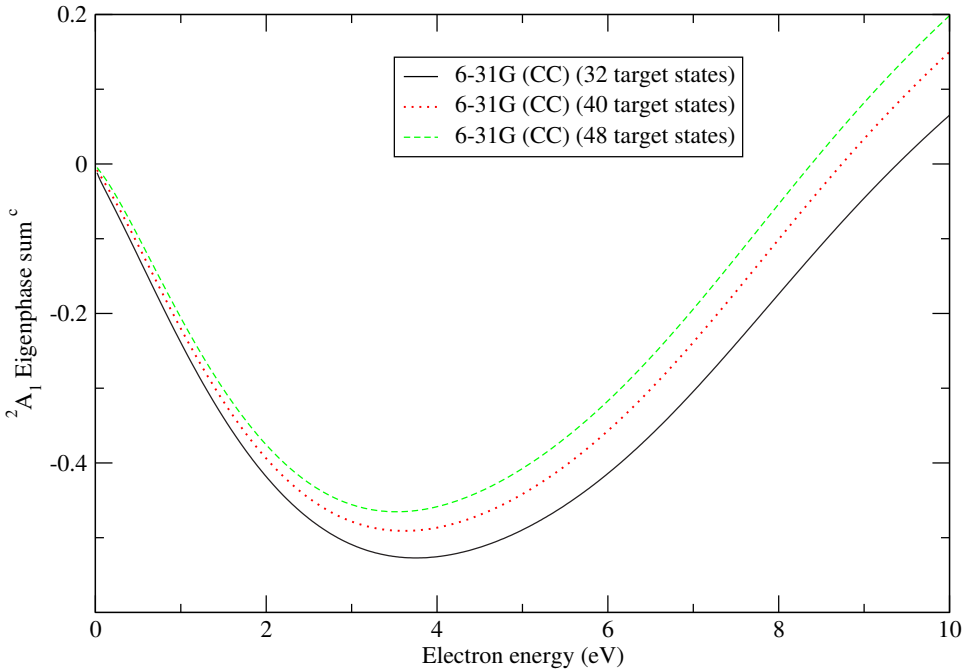

Figure 9.2: CH_4 $^2A_1$ Eigenphase Sum Curves

9.4 Results

9.4.1 Eigenphase Sums, Integral Cross Sections, The Ramsauer-Townsend Minimum and Resonances

Figure 9.2 shows the $^2A_1$ eigenphase sum for the various models described above. Unlike the molecules of previous chapters, the eigenphases exhibit no structure due to the opening up of previously closed electronic excitation channels. Given that the first channel threshold (table 9.1) is outside of the energy range considered, this is not surprising. As shown in figure 9.2, the retention of an increasing number of states used for the construction of the R-matrix increases the eigenphase sum over the entire energy range shown. This is due to the improved modelling of the (attractive) polarisation interaction.

Whereas previous collision studies have confirmed the appearance of a Ramsauer-Townsend minimum at about 0.4 eV (e.g. Nestmann et al. (1994), McCorkle et al. (1978) and Lohmann and Buckman (1986)), it is clear from figure 9.2 that the model using contracted CSFs in the inner region CC expansion cannot reproduce the R-T minimum, despite increasing the number of target states included to build the R-matrix. The $^2A_1$ eigenphase sum obtained using uncontracted CSFs is compared to that obtained using contracted CSFs in figure 9.3. Not only did the adoption of uncontracted CSFs lead to

the corresponding eigenphases lying higher than those calculated using contracted CSFs, implying that the model had improved the representation of the polarisation interaction further, it also caused the eigenphase sum to pass through 0^c, namely, this technique was able to reproduce the R-T minimum at about 0.44 eV, confirming the experiments of Lohmann and Buckman (1986) (0.36 eV) and Ferch et al. (1985) (0.40 eV) and the Kohn variational study of Lengsfield et al. (1991) (0.40 eV). The SMC SEP calculation of Lima et al. (1989) however, produced an R-T minimum at much too low a position: 0.1 eV. The calculation using the later version of Quantemol-N also located a Ramsauer minimum at 0.1 eV, otherwise it reproduced the contracted CSFs calculation exactly.

In spite of this disagreement, one can make some inferences. Most importantly, the correction to the like-like transition moments in turn corrected the polarisability, the key difference between the previous models using version 3.2 and the models set up by 3.5.2. In the R-matrix method polarisation is modelled via the transition moments of the CH_4 target, and therefore the representation of the polarisation interaction in the outer region will have been much improved as well. Particularly, the 48-state CC scattering model using Quantemol-N version 3.5.2 and the compact 6–31G basis resulted in this interaction ($\alpha_0 = 11.41$ a_0^3) being improved to such an extent that at least the Ramsauer-Townsend minimum was reproduced, albeit at a lower position. Clearly, further improvement to our scattering model would be needed in order to reproduce this feature at the observed position. This certainly confirms the observations of previous theoretical studies, namely the sensitivity of the R-T minimum to the representation of the polarisation interaction.

A narrow Feshbach resonance feature appears at about 12.1 eV in both eigenphase sum curves in figure 9.3. For the calculation involving contracted CSFs the position and width parameters, fitted using RESON (Tennyson and Noble, 1984), are 12 eV and 0.008 eV respectively and the resonance was assigned $^2T_2$ symmetry. The uncontracted CSFs calculation yielded the resonance at a lower position of 11.86 eV and with a width of 0.008 eV.

Figures 9.4 and 9.5 show the total integral cross section for electron-methane scattering for all the scattering models tested in this work. The SE calculation, as expected does not give very good results at all, but the CC calculations show systematic improvement as more target states are retained in the expansion. Indeed one can observe the R-T minimum feature in the cross section for uncontracted CSFs, whereas the feature is absent from the calculations employing contracted CSFs, as stated earlier. With refer-

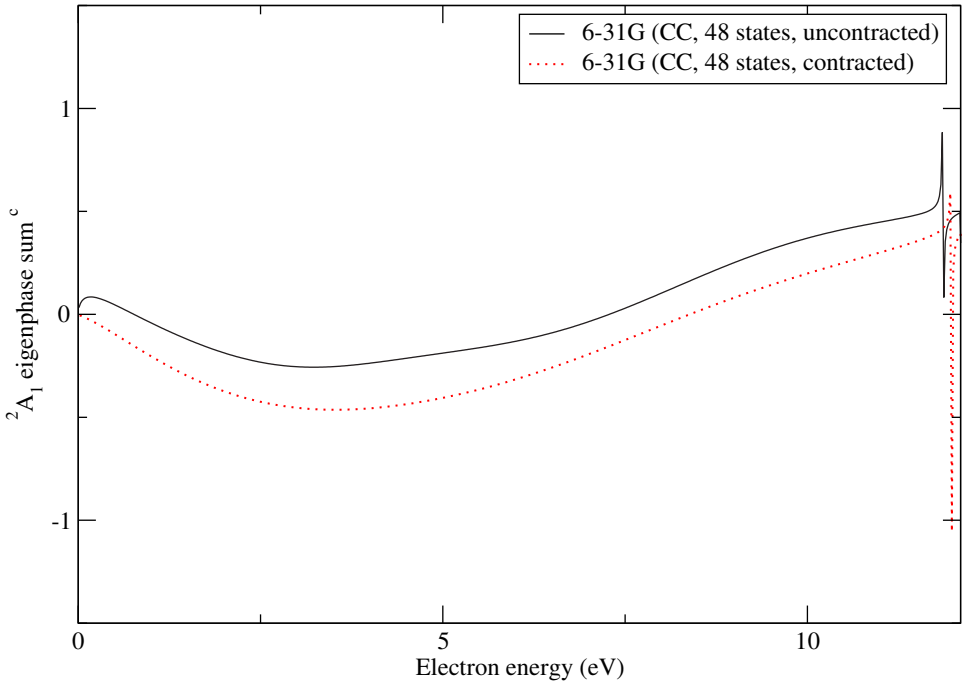

Figure 9.3: Comparison of CH_4 $^2A_1$ eigenphase sum curves

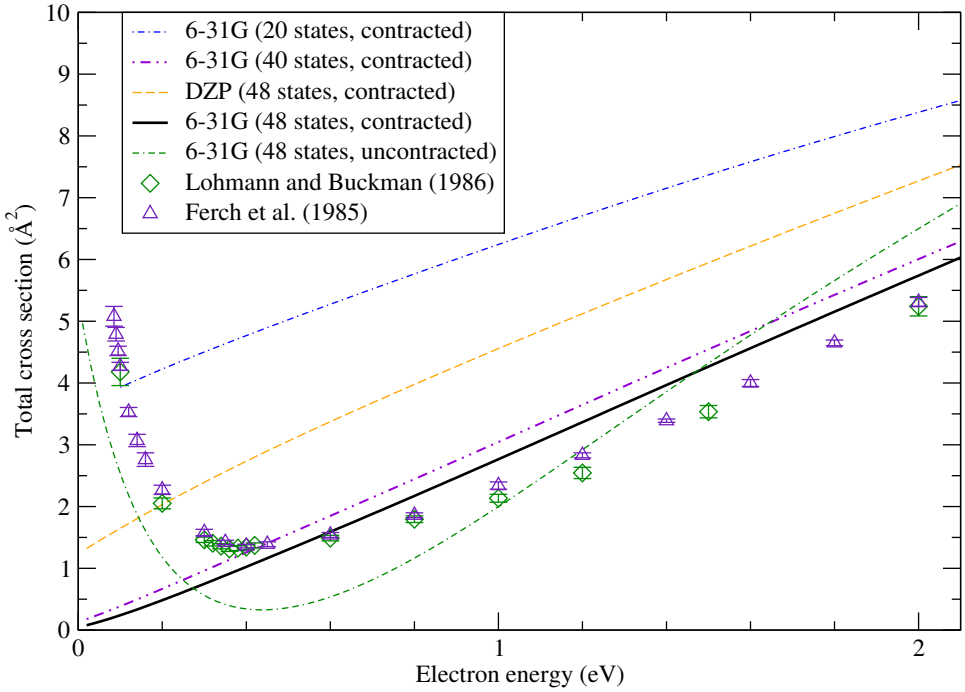

Figure 9.4: Comparison of CH_4 integral elastic cross sections in the region of the Ramsauer-Townsend minimum

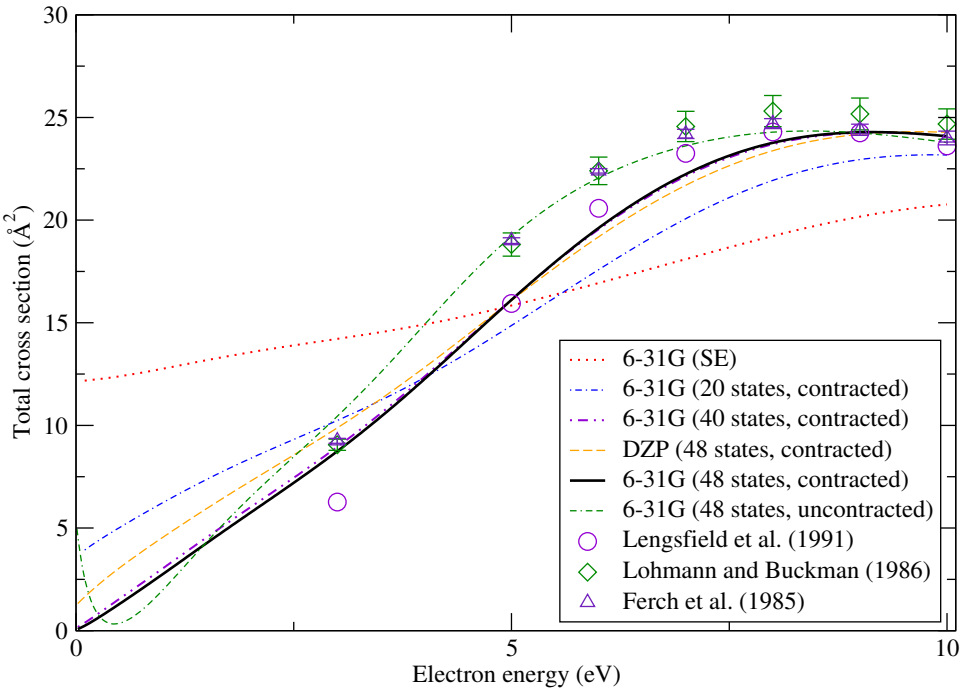

Figure 9.5: Comparison of CH_4 integral elastic cross sections

ence to figure 9.4 the integral cross sections obtained using the uncontracted CSFs are lower than those obtained by Ferch et al. (1985) and Lohmann and Buckman (1986) for energies below about 1.2 eV, but higher beyond this point. The uncontracted CSFs cross sections were found to be in very good agreement with these two previous experiments for 5 eV and beyond, passing through most of the points of Ferch et al. (1985).

Previous studies also noted the appearance of a broad maximum at around 8 eV: for example Lengsfield et al. (1991) and Lohmann and Buckman (1986) both yielded their maxima at 8 eV with cross sections of about 25 Å^2. We also reproduced this broad maximum, at 8.41 eV in the case of uncontracted CSFs, in good agreement with the previous theoretical and experimental studies, but at a higher incident energy 9.14 eV for contracted CSFs. The cross section maxima agreed with Lengsfield et al. (1991).

9.4.2 Differential Cross Sections

Differential cross sections (DCS) enable a more sensitive test of the theoretical model than integral cross sections since they are often more accurately measured experimentally and are sensitive to effects which can be averaged out in the total cross sections. Hence we computed the rotationally summed DCSs for incident energies 3 eV and 5 eV using the POLYDCS package (Sanna and Gianturco, 1998) with the C_{2v} K-matrices obtained

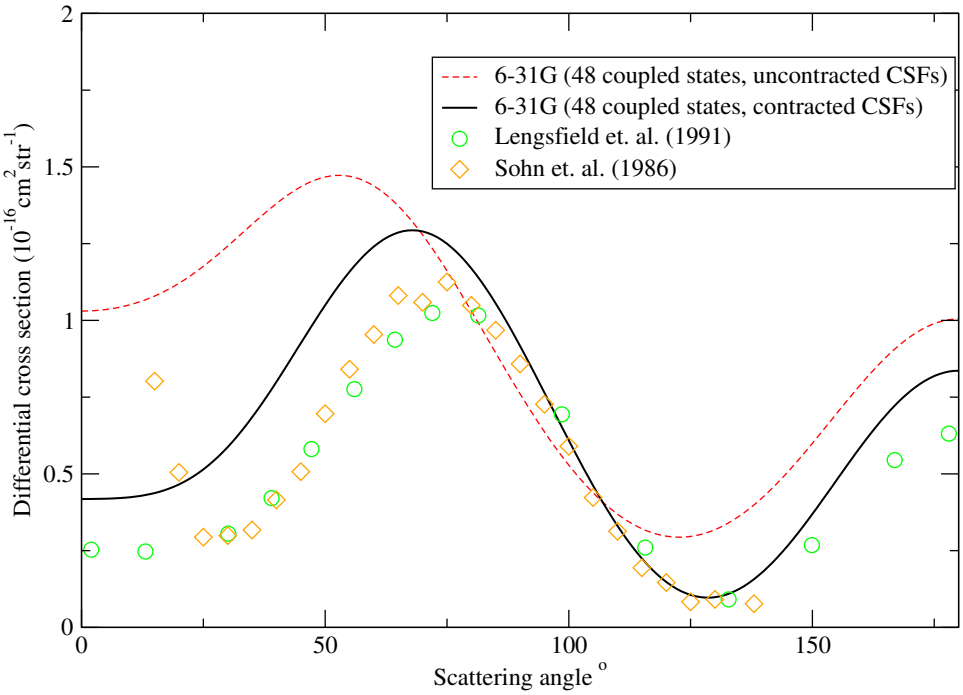

Figure 9.6: Rotationally Summed Differential Cross Sections for e-CH_4 scattering at incident energy 3 eV

by the best model as input.

Our DCSs are compared to the complex Kohn data of Lengsfield et al. (1991) and the experiment of Sohn et al. (1986). Using contracted CSFs the present study agrees well with these previous studies at the high angles in particular. The difference at the forward angles could be due to the incomplete treatment of polarisation, though it is not exactly clear what the forward angle behaviour is. Clearly agreement is not as good when uncontracted CSFs are employed, despite the very good agreement obtained in the case of the integral cross section.

9.4.3 Ionisation Cross Section

The 6–31G SCF orbital parameters computed here are listed in table 9.3 and were employed in the computation of the BEB ionisation cross section appealing to the formalism of Kim et al. (1997). Our data are compared to Kim et al. (1997), whose molecular orbital binding and kinetic energies were obtained using the restricted Hartree-Fock (RHF) method and the GTO basis set 6–311G, and to the experiments carried out by Orient and Srivastava (1987) and Duric et al. (1991) in figure 9.8. They are certainly in good agreement with the later theoretical and experimental works. It is important to note that

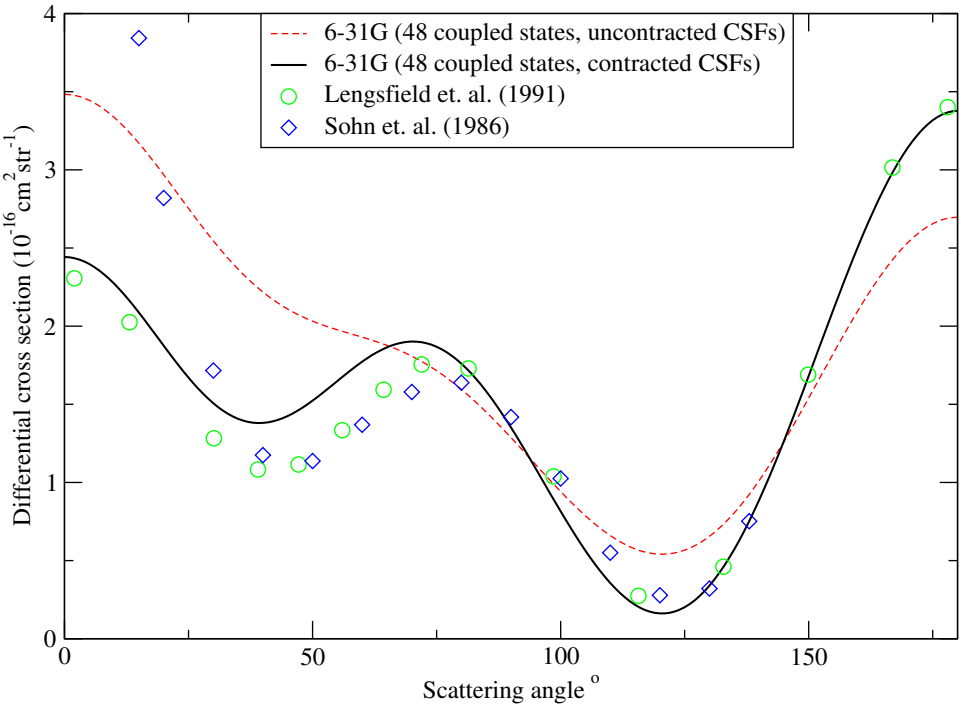

Figure 9.7: Rotationally summed differential cross sections for e-CH_4 scattering at incident energy 5 eV

Orbital	$\|B\|$		U		N
	This work	Theory[1]	This work	Theory[1]	
$1a_1$ ($1a_1$)	305.03	290.70	+435.89	+436.07	2
$2a_1$ ($2a_1$)	25.69	25.73	+33.85	+33.05	2
$1t_2$ ($3a_1$, $1b_1$ $1b_2$)	14.75	14.25	+25.68	+25.96	6

Table 9.3: T_d (C_{2v}) occupied molecular orbital parameters. The orbital binding B and kinetic energies U are given in eV

[1] Kim et al. (1997)

the BEB formalism is very sensitive to the ionisation energy employed to compute the ionisation cross section: Kim et al. (1997) and Hwang et al. (1996) strongly recommend using the experimental value of the ionisation energy in order to attain good agreement with experiment. The former used the experimental vertical ionisation potential and a different basis set which explains the difference between our data and theirs. We used the ionisation energy obtained by invoking Koopman's theorem (14.75 eV) which is higher than observed experimentally (12.61 eV NIST (2008)).

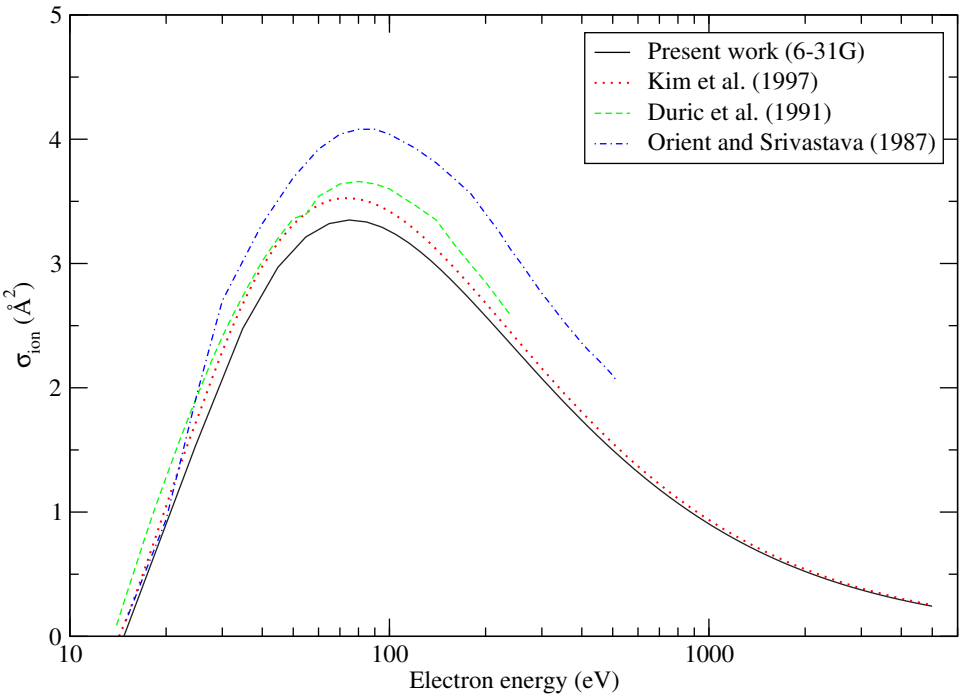

Figure 9.8: CH_4 BEB ionisation cross sections

9.4.4 Electron-Impact Dissociation Cross Sections

The electron-impact dissociation cross sections obtained using contracted CSFs are compared to the recent study of Makochekanwa et al. (2006). Our data are shifted to higher energies. This shift is attributed to the channel thresholds lying much higher than observed previously (table 9.1). The cross sections are also systematically lower than those measured by Makochekanwa et al. (2006), but they do exhibit a similar trend, with both data producing a narrow peak structure at 11.5 eV, which Makochekanwa et al. (2006) assigned to the lowest 4s Rydberg state, and 14.0 eV for this work.

9.5 Conclusion

We applied the *ab initio* fixed nuclei R-matrix method to elastic electron scattering by the non-polar CH_4 molecule at the CC approximation.

The CH_4 target was represented using CASCI wavefunctions to generate the ground and electronically excited wavefunctions. For the complete active space the two 1s electrons of the carbon atom were frozen in all configurations. The remaining electrons were allowed to move in the $3a_1$, $4a_1$, $5a_1$, $1b_1$, $2b_1$, $1b_2$, $2b_2$ bound and virtual molecular orbitals. Target models were tested which varied the number of eigenvalues per target

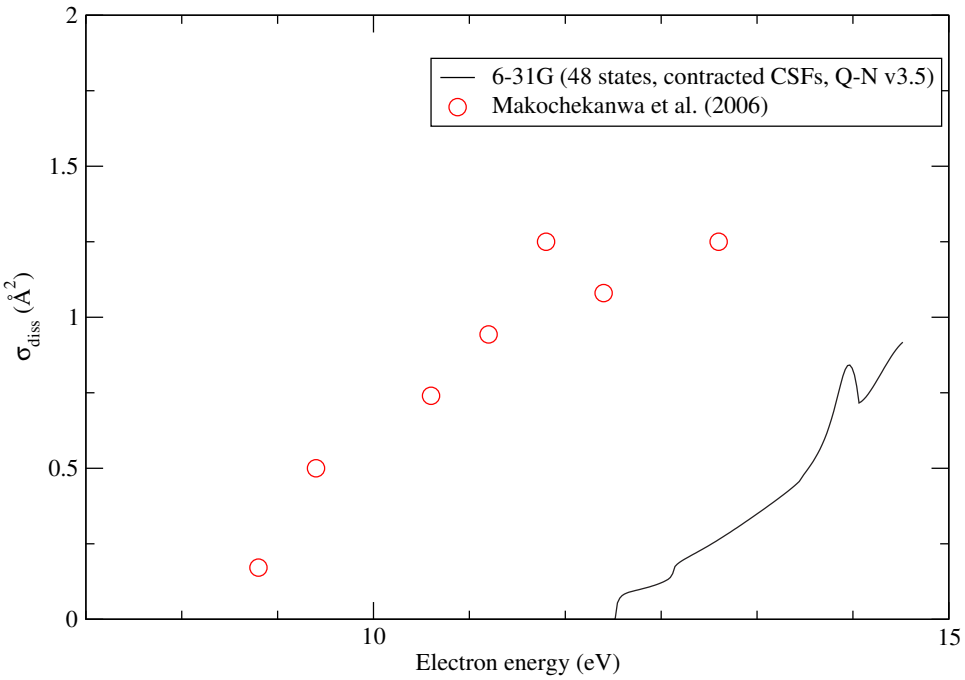

Figure 9.9: CH_4 dissociation cross sections

state that were solved for and the GTO basis sets used to present the SCF molecular orbitals (6–31G, 6–31G* and DZP). The best model was one using the 6–31G basis set and computing for six eigenvalues per target state, or 48 target states in total. This model yielded a spherical polarisability of 7.59 a_0^3 using version 3.2 of Quantemol-N and 11.4 a_0^3 using the later version 3.5.2.

An R-matrix sphere of radius 10 a_0 was sufficient to fully contain the electron charge cloud.

Previous studies have discussed the importance of accurately modelling the polarisation interaction in order to accurately re-produce the Ramsauer-Townsend minimum. *Ab initio* this interaction was modelled by retaining many strongly closed channels in the inner region close-coupling expansion and for construction of the R-matrix at the surface of the sphere. The scattering calculations tested retained 1 (a static exchange calculation) 20, 32, 40 and 48 target states. This study has demonstrated that increasing the number of coupled states in the CC expansion converges the total cross sections to values in good agreement with previous theoretical and experimental studies. However although there is convergence with respect to the CC expansion, this need not imply that one has achieved a complete converged treatment of the polarisation or the long range polarisability. Therefore an uncontracted CSFs model, which increases the po-

larisation effects, was used to enable an improved treatment: it was able to reproduce the Ramsauer-Townsend minimum at 0.44 eV, in good agreement with the experimental values of 0.40 eV (Ferch et al., 1985) and 0.36 eV (Lohmann and Buckman, 1986) and the theoretical value of Nestmann et al. (1994). The cross section maximum observed by these studies was reproduced at a higher incident energy.

The rotationally summed differential cross sections for incident energies 3 eV and 5 eV computed for CH_4 were in good agreement with previous theoretical and experimental data, especially for angles greater than 75^o when contracted CSFs were employed. The agreement was not as good when the uncontracted CSFs were used, this despite the integral cross sections being in excellent agreement across the incident energy range considered.

We have shown CH_4 to support a narrow $^2T_2$ Feshbach-type resonance at about 12 eV. In addition to being sensitive to the treatment of the polarisation, the Feshbach resonance parameters are also sensitive to the precise location of the excitation threshold of its parent target state. The energies predicted here are considered to be upper bounds on the true values as the channel thresholds are systematically too high.

The Binary-Encounter-Bethe formalism was applied to compute the electron-impact ionisation cross section from the ionisation threshold to 5000 eV. The threshold was much higher than measured experimentally (12.61 eV NIST (2008)) and resulted in the present work being lower than previous measurements and being shifted very slightly to higher incident electron energies relative to the previous studies. Kim et al. (1997) carried out a similar study using the basis set 6–311G and the experimental vertical ionisation potential (14.25 eV) which resulted in slight disagreement with the present calculation.

The dissociation cross section was not in agreement with the previous study of Makochekanwa et al. (2006), with our data being much lower and shifted by about 3 eV towards higher energies relative to their measurements. However, the present cross sections followed closely the trend observed by Makochekanwa et al. (2006), both producing noticeable peaks in the dissociation cross section.

A criticism of the present quantum chemistry model is that the Rydberg character of the excited states was completely neglected. In addition our complete active space is smaller than it could have been, producing only 492 CSFs for the X $^1A_1$ target wavefunction and lacking correlation. Williams and Poppinger (1975) reached similar

conclusions, even in the case of their CI calculations incorporating all possible single excitations. Such deficiencies may explain why the channel thresholds were significantly higher than previous *ab initio* quantum chemistry studies and, consequently, why our electron-impact dissociation cross sections were shifted to higher incident energies. We computed the cross sections by summing all the inelastic cross sections that were open within the 0.02–15 eV incident energy range. Hence another reason for the general disagreement in the dissociation cross sections with Makochekanwa et al. (2006) may be that some of the inelastic cross sections could not be included because their corresponding channel thresholds were overestimated and outside this energy range thereby producing lower dissociation cross sections.

We also computed target and scattering observables for C_2H_6 (ethane) and C_3H_8 (propane), but these proved much more difficult: in these cases a large number of coupled states were included in the close-coupling expansion (64 and 72 respectively). Still the agreement with previous theoretical and experimental studies was very poor (hence the work is not presented in this thesis at all). Our CASCI target models yielded very low polarisabilities (5.89 a_0^3 and 3.72 a_0^3 for ethane and propane respectively compared to 28.52 a_0^3 and 39.26 a_0^3 obtained experimentally (NIST, 2008)). Clearly such a large number of states is still insufficient to attain a converged treatment of the polarisation interaction.

In conclusion this study has demonstrated the need for accurate target wavefunctions so as to obtain accurate scattering quantities and observables. Therefore a future study will be to investigate the influence of more accurate *ab initio* quantum chemistry methods, perhaps pseudo natural orbitals incorporating all possible singles and doubles excitations and accounting for the Rydberg nature of the low-lying excited states, and examine their influence upon the vertical excitation energies and the dissociation cross sections. R-matrix calculations including Rydberg states have been performed before (Rozum et al., 2003).

Chapter 10

Electron-impact Rotation and Hyperfine Excitation of HCN, DCN, HNC and HNC

10.1 Introduction

Hydrogen cyanide, HCN, and its isomer HNC (hydrogen isocyanide) are amongst the most abundant organic molecules in space, from star-forming regions to circumstellar envelopes and comets. They also belong to the small class of molecules detected in high-redshift galaxies, along with CO and HCO^+ (Guelin et al. (2007) and references therein). In addition to thermal emission from various rotational transitions within different vibrational states at (sub)millimetre and far-infrared wavelengths (e.g. Cernicharo et al. (1996)), a few masering lines have been detected towards several stars (Lucas and Cernicharo, 1989). Several isotopologues have also been identified, particularly the deuterated species DCN and DNC (Leurini et al., 2006).

An interesting observation concerning the rotational spectra of HCN is that of the hyperfine anomalies (Walmsley et al., 1982). At high resolution it is possible to resolve the hyperfine components arising from the nitrogen ^{14}N nuclear spin from transitions arising from the low-lying rotational levels. The hyperfine lines have been found in a number of cases (Izumiura et al., 1995; Park et al., 1999; Ahrens et al., 2002) not to be in thermal equilibrium with each other. These anomalies have been shown to depend upon the degree of thermal overlap, on the opacity and on the collisional rates (Guilloteau and Baudry, 1981).

Thirty years ago it had already been suggested that when the electron fraction exceeds about 10^{-5}, electron impact excitation of polar molecules may be significant in

Figure 10.1: Comet C/1995 O1 (Hale-Bopp) where electron collisions play an important role in the rotational excitation of HCN. Taken on 4th April 1997 (Credit: E. Kolmhofer, H. Raab; Johannes-Kepler-Observatory, Linz, Austria (http://www.sternwarte.at))

addition to collisions with neutrals (Dickinson et al., 1977). Such conditions may be found in interstellar clouds and photon dominated regions, where $n(e)/n(\mathrm{H})$ can reach a few 10^{-4}. Recently Lovell et al. (2004) devoted their study to the effect of electron collisions in the rotational excitation of cometary HCN: they showed that electron collisions are the dominant excitation mechanism in the comets Hale-Bopp (figure 10.1) and Hyakutake (figure 10.2) where the electron fraction $n(e)/n(H_2O)$ lies in the range 10^{-5} to 1. The authors stated that accounting for electron collisions may thus alleviate the need for large HCN-H_2O cross sections in models that neglect effects due to electrons. Similar conclusions were reached in the case of water by Faure et al. (2004*a*).

Recently, Jimenez-Serra et al. (2006) used rotational emissions of SiO, HCO^+, HCN and HNC in order to probe electron densities in C-type shocks. In particular, they ascribed differences in the ambient and precursor components to electron density en-

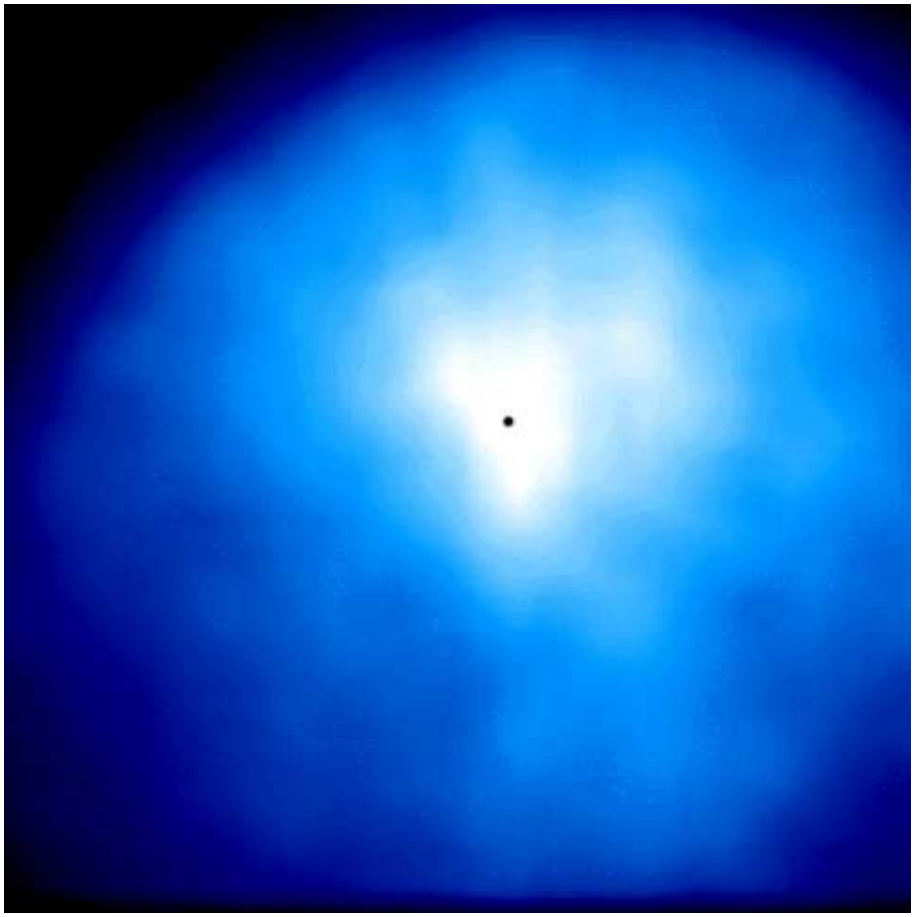

Figure 10.2: Ultraviolet Radiation From Hydrogen Atoms in Coma of Comet Hyakutake (C/1996 B2)) (Credit: M. Combi (University of Michigan); Image URL: http://hubblesite.org/newscenter/archive/releases/1998/13/image/a)

hancements during the first stages of the C-type shock evolution. The dipolar HCO^+ was found to be a sensitive tracer to this effect.

A theoretical determination of rotational cross-sections and rate coefficients for e-HCN scattering was carried out by Saha et al. (1981) for the inelastic transitions $J = 0 \rightarrow 1$, $J = 1 \rightarrow 2$ and $J = 0 \rightarrow 2$ using the rotational close coupling method. Their rate coefficients were obtained in the temperature range 5–100 K. Additional scattering studies include that of Jain and Norcross (1985), where the adiabatic nuclei rotation (ANR) approximation was combined with model potentials, and He-HCN scattering by Green and Thaddeus (1974), Green (1974) and Monteiro and Stustzki (1986). The latter also computed hyperfine rate coefficients for 0–4 and $T = 10 - 30$ K.

Here we considered the electron-impact rotational and hyperfine excitation of HCN and HNC and their isotopologues DCN and DNC respectively. The *ab initio* R-matrix

method combined with the adiabatic nuclei rotation (ANR) approximation was applied to calculate the rotationally resolved and summed differential cross sections, rotationally resolved integral cross sections, rotational and hyperfine excitation rate coefficients for all levels up to $J = 8$ and electron temperature range 5–6000 K.

This chapter opens with a brief discussion of the particulars of the R-matrix model that was used to obtain the required scattering wavefunctions and quantities, especially the fixed nuclei (FN) T-matrices.

10.2 R-matrix Calculations

The R-matrix calculation was carried out using the highest Abelian sub-group of HCN and HNC C_{2v} (natural point group is $C_{\infty v}$), at the fixed equilibrium geometry of these triatomics. An R-matrix sphere of radius 10 a_0 was sufficient to contain the electron charge clouds. The calculation was performed using the UK polyatomic R-matrix package (Morgan et al., 1998).

HCN and HNC (hence DCN and DNC) were represented using the 6–31G GTO basis set. The target wavefunctions were calculated using the CASCI method. These were subsequently improved by use of pseudo natural orbitals which were calculated using the five lowest-lying C_{2v} electronically excited $^1A_1$, $^3A_1$, $^3A_2$, $^3B_1$ and $^3B_2$ with all possible single and double excitations to virtual orbitals included. However in order to include the double excitations, it was necessary to freeze eight electrons (the $1s$ and $2s$ electrons of the C and N atoms). For both HCN and HNC the weighting coefficients for the density matrix averaging procedure were 5.75, 1.5, 1.5, 1.5 and 1.5 for $^1A_1$, $^3A_1$, $^3A_2$, $^3B_1$ and $^3B_2$ respectively. Concerning the quantum chemistry properties, the dipole moments -2.87 D and -2.91 D were obtained for HCN and HNC respectively compared to -2.985 D (Ebenstein and Muenter, 1984) and -3.05 D (Blackman et al., 1976) determined experimentally.

The scattering wavefunctions were determined using a close-coupling (CC) expansion that retained 24 target states, many of which were strongly closed so as to improve the modelling of the polarisation interaction, a standard *ab initio* technique. This was to ensure that the parameters of the expected $^2\Pi$ shape resonance were kept as low as possible. Calculations were carried out on the $^2A_1$, $^2B_1$, $^2B_2$ and $^2A_2$ scattering symmetries.

The scattering electron was represented by the GTO basis set of Faure et al. (2002)

with a partial wave expansion up to and including g-wave ($l = 4$). The continuum orbitals where augmented with one virtual molecular orbital of each symmetry, where such orbitals were available to do so. In order to improve the modelling of the polarisation further, we employed uncontracted CSFs to construct the inner region CC expansion and thereby reduce the resonance parameters yielded by this model further. Discussion on the problem of convergence of this interaction in CC methods may also be found in Gil et al. (1994) and Gorfinkiel and Tennyson (2004). The resulting fixed nuclei (FN), body fixed ($C_{\infty v}$) T-matrices were used to calculate the pure rotational excitation cross sections in the energy range 0.01–6.2 eV. The positions of the $^2\Pi$ shape resonances for HCN and HNC are inside this interval.

In the fixed geometry approximation the DCN and DNC wavefunctions are identical to those of HCN and HNC respectively. The chief distinction between the isotopologues arises, in our treatment, from the different rotational excitation thresholds.

10.3 Results

10.3.1 Differential Cross Sections

Experimental differential cross sections are measured reliably and used to test a theoretical scattering model. In the case of polar molecules integral cross sections deduced from experiments are dependent upon the extrapolation procedure applied to estimate the small angle scattering that cannot be detected in experiment (Faure et al., 2004*b*).

Figure 10.3 shows our rotationally resolved and summed differential cross sections compared to the experiment of Srivastava et al. (1978). Whereas the present calculations reproduce their results qualitatively, quantitatively our results are larger by a factor of 2 at angles below 100^o. As anticipated the dipole-allowed $0 \rightarrow 1$ transition dominates over all the other transitions. Sharp dips are also observed at about 20^o, 70^o and 120^o, and they are not entirely suppressed by the contributions of the other transitions in the summed curve. We note that Allan and Dickinson (1981) also observed similar dips in electron scattering by the polar diatomic CsCl using the semiclassical approach. As stated in chapter 7, these dips were attributed to an interference effect between two equally weighted classical paths. Clearly, more experimental study is necessary to interpret the differences observed between theory and experiment, as suggested by Jain and Norcross (1985).

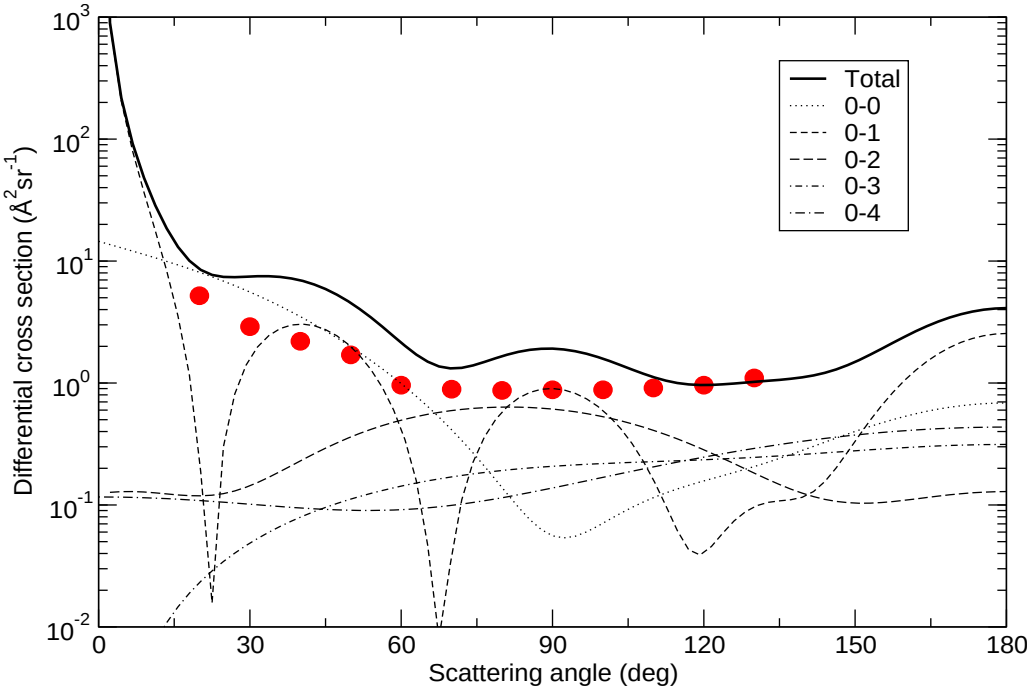

Figure 10.3: Differential cross sections for vibrationally elastic scattering (rotationally summed) of electrons by HCN at 5 eV. The present calculation is given by the thick solid line and the experimental data (full red circles) are from Srivastava et al. (1978). Other lines denote rotationally resolved differential cross sections

As expected for very polar species, the Born completion was found to be crucial in the case of the dipole interaction. The dipole-allowed transitions ($\Delta J = 1$) were found to be dominated by the higher partial waves ($l > 4$), with a small contribution from the FN T-matrices. Born completion for the quadrupole and induced dipole interactions was found to be negligible, with high partial waves only increasing $\Delta J = 0, 2$ by less than 2%. This clearly shows that cross sections for the dipole forbidden transitions converge more rapidly with respect to partial wave expansion. Therefore only the Born closure approximation for the dipole interaction was applied in the computation of the rotational integral cross section.

In figure 10.4 we compare our integral rotational cross sections with those of Jain and Norcross (1985) and Saha et al. (1981). Excellent agreement is attained down to 0.01 eV. At lower energy, the extrapolation formula of Rabádan et al. (1998) (equation 1 of their paper) was adopted and which was calibrated using the rotational CC results of Saha et al. (1981). This procedure introduced uncertainties in the computation of the rate coefficients below about 100 K, in addition to closed channel effects that were ignored in the present calculation. Consequently those coefficients below 100 K are expected to

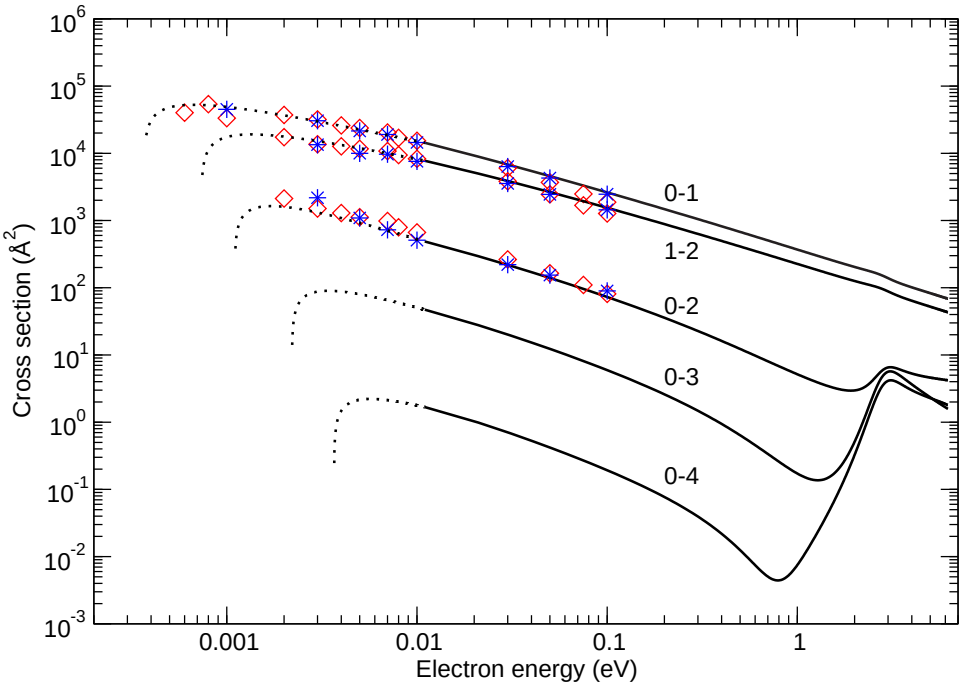

Figure 10.4: Integral cross sections for rotationally inelastic scattering (rotationally summed) of electrons by HCN. Lozenges and stars denote the results of Saha et al. (1981) and Jain and Norcross (1985) respectively. The present calculations are given by the thick solid lines

be less accurate than those at higher temperatures.

Figure 10.4 also exhibits a large shape resonance at about 2.8 eV. It is especially pronounced in the cross sections for transitions $\Delta J > 2$. This $^2\Pi$ resonance has been confirmed experimentally (Burrow et al., 1992) and discussed previously in chapter 5. For HNC it appears at a slightly lower position of 2.5 eV. The dipole-allowed transitions are much larger than the others owing to the dominance of the long-range dipole interaction typical of polar molecules.

Finally, to our knowledge there is no data, theoretical or experimental, on the rotational excitation of DCN, HNC and DNC available in literature.

10.3.2 Rotational Excitation Rate Coefficients

HCN and HNC (hence DCN and DNC) have their first inelastic thresholds at 6.63 and 6.20 eV respectively so the rotational cross sections were computed in the range 0.01–6.2 eV and extrapolated to rotational thresholds, as discussed earlier. The electron velocity distribution was assumed to be Maxwellian and the rate coefficients were obtained for temperatures in the range 5–6000 K for transitions among all the levels up to $J = 8$. The de-excitation rate coefficients were extracted using the detailed balance

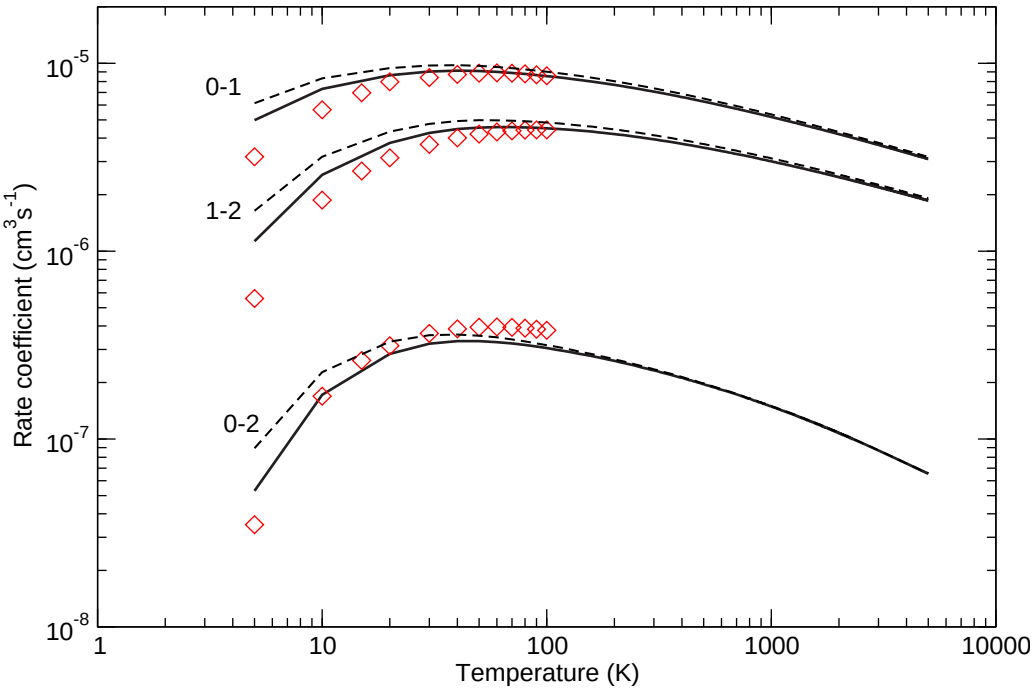

Figure 10.5: Rotational excitation rate coefficients of HCN and DCN by electron-impact. Lozenges denote the HCN results of Saha et al. (1981). The present calculations are given by the thick solid lines for HCN and dashed lines for DCN

relation. For use in modelling the temperature dependence of the de-excitation rate coefficients $k(T)$, with units of $\mathrm{cm^3 s^{-1}}$, was fitted to the analytic form:

$$\log k(T) = \sum_{i=0}^{N} a_i x^i \tag{10.1}$$

where $x = (T/\mathrm{K})^{-\frac{1}{6}}$, $N = 4$ and T was restricted to the range 5–2000 K. The coefficients a_i, listed in tables 10.1– 10.4, are such that the unit of k is $\mathrm{cm^3 s^{-1}}$.

Excitation rate coefficients for HCN and DCN are presented in figure 10.5. The small differences with the results of Saha et al. (1981) reflect the sensitivity of low-temperature rate coefficients to the near-threshold cross sections. One can also note that the smaller rotational thresholds of DCN, with respect to HCN, lead to a significant but moderate increase in rate coefficients below 100 K. Consequently, rate coefficients for other isotopologues such as $\mathrm{H^{13}CN}$ and $\mathrm{H^{15}NC}$ are expected to be similar to those of HCN and HNC respectively since the rotational thresholds are only slightly different.

In figure 10.6 electron-impact rate coefficients for HCN and HNC are presented alongside the rate coefficients for excitation of HCN by He atoms. It is quite clear from the figure that HCN and HNC have similar rate coefficients, with typical differences less than 50% for the plotted transitions. The $J = 0 \rightarrow 1$ curves are almost superposed in

Transition	E_{up} (K)	a_0	a_1	a_2	a_3	a_4
$(1-0)$	4.3	−7.543	10.018	−17.974	14.328	−4.169
$(2-0)$	12.8	−10.923	22.212	−52.611	60.265	−26.660
$(2-1)$	12.8	−7.552	10.772	−21.515	19.858	−7.067
$(3-0)$	25.5	−13.297	30.136	−71.602	79.988	−34.340
$(3-1)$	25.5	−10.830	22.286	−52.461	59.201	−25.830
$(3-2)$	25.5	−7.589	11.377	−24.257	24.067	−9.239
$(4-0)$	42.5	−15.647	35.452	−84.761	94.380	−40.338
$(4-1)$	42.5	−13.222	30.599	−73.095	81.660	−35.036
$(4-2)$	42.5	−10.827	22.664	−53.590	60.351	−26.259
$(4-3)$	42.5	−7.633	11.910	−26.550	27.495	−10.976
$(5-0)$	63.8	−17.755	36.842	−88.707	99.539	−42.965
$(5-1)$	63.8	−15.718	37.455	−91.762	104.331	−45.407
$(5-2)$	63.8	−13.277	31.655	−76.702	86.569	−37.456
$(5-3)$	63.8	−10.815	22.782	−53.882	60.382	−26.134
$(5-4)$	63.8	−7.677	12.402	−28.613	30.532	−12.492
$(6-0)$	89.3	−17.947	22.002	−49.290	54.613	−24.371
$(6-1)$	89.3	−18.379	44.219	−114.389	136.990	−62.411
$(6-2)$	89.3	−16.049	41.262	−105.105	123.812	−55.550
$(6-3)$	89.3	−13.426	33.410	−82.796	95.273	−41.916
$(6-4)$	89.3	−10.888	23.601	−56.532	63.817	−27.757
$(6-5)$	89.3	−7.737	13.016	−31.039	34.097	−14.297
$(7-0)$	119.1	−17.477	2.037	2.640	−10.257	8.971
$(7-1)$	119.1	−19.755	39.818	−106.846	130.991	−59.153
$(7-2)$	119.1	−20.167	61.606	−172.992	219.967	−103.973
$(7-3)$	119.1	−17.003	50.704	−137.567	170.812	−79.770
$(7-4)$	119.1	−13.717	36.432	−93.345	110.640	−49.901
$(7-5)$	119.1	−10.947	24.277	−58.843	66.970	−29.308
$(7-6)$	119.1	−7.791	13.571	−33.249	37.364	−15.963
$(8-0)$	153.1	−9.087	−41.736	42.984	14.247	−28.504
$(8-1)$	153.1	−14.491	−23.527	84.511	−119.423	58.957
$(8-2)$	153.1	−16.613	11.279	−11.836	−2.489	6.619
$(8-3)$	153.1	−17.542	36.928	−88.046	95.525	−39.360
$(8-4)$	153.1	−18.534	64.949	−184.148	234.228	−109.912
$(8-5)$	153.1	−14.334	42.448	−114.006	140.539	−65.328
$(8-6)$	153.1	−11.068	25.526	−63.164	73.166	−32.507
$(8-7)$	153.1	−7.823	13.903	−34.635	39.376	−16.952

Table 10.1: Coefficients a_i of the polynomial fit to the HCN de-excitation rate coefficients. These coefficients are only valid in the temperature range 5–2000 K. E_{up} are the upper energy levels

Transition	E_{up} (K)	a_0	a_1	a_2	a_3	a_4
$(1-0)$	3.5	−7.513	9.737	−16.754	12.437	−3.174
$(2-0)$	10.4	−10.931	22.292	−52.959	60.944	−27.038
$(2-1)$	10.4	−7.527	10.532	−20.385	18.095	−6.144
$(3-0)$	20.9	−13.275	29.938	−71.022	79.434	−34.150
$(3-1)$	20.9	−10.799	22.009	−51.638	58.299	−25.449
$(3-2)$	20.9	−7.561	11.088	−22.909	21.979	−8.157
$(4-0)$	34.8	−15.559	34.612	−81.872	90.381	−38.336
$(4-1)$	34.8	−13.189	30.289	−72.067	80.410	−34.476
$(4-2)$	34.8	−10.794	22.357	−52.623	59.213	−25.753
$(4-3)$	34.8	−7.592	11.502	−24.778	24.819	−9.611
$(5-0)$	52.1	−17.594	35.278	−83.187	91.562	−38.855
$(5-1)$	52.1	−15.554	35.865	−86.214	96.384	−41.332
$(5-2)$	52.1	−13.199	30.907	−74.137	83.071	−35.733
$(5-3)$	52.1	−10.807	22.701	−53.656	60.318	−26.194
$(5-4)$	52.1	−7.643	12.076	−27.155	28.395	−11.451
$(6-0)$	73.0	−17.202	14.785	−24.098	17.750	−5.212
$(6-1)$	73.0	−17.737	38.047	−92.971	105.803	−46.244
$(6-2)$	73.0	−15.705	37.912	−93.299	106.476	−46.487
$(6-3)$	73.0	−13.236	31.583	−76.490	86.276	−37.307
$(6-4)$	73.0	−10.843	23.178	−55.163	62.141	−27.005
$(6-5)$	73.0	−7.677	12.439	−28.711	30.698	−12.601
$(7-0)$	97.3	−16.289	−7.875	30.337	−38.294	15.702
$(7-1)$	97.3	−18.107	24.976	−59.631	69.686	−32.154
$(7-2)$	97.3	−18.405	45.121	−117.556	141.673	−64.869
$(7-3)$	97.3	−16.011	41.257	−105.090	123.775	−55.517
$(7-4)$	97.3	−13.372	33.096	−81.743	93.795	−41.171
$(7-5)$	97.3	−10.838	23.256	−55.432	62.368	−27.064
$(7-6)$	97.3	−7.728	12.953	−30.725	33.628	−14.069
$(8-0)$	125.1	−9.469	−41.064	53.519	−24.563	5.360
$(8-1)$	125.1	−17.037	−1.195	15.814	−33.284	23.214
$(8-2)$	125.1	−19.699	39.962	−107.384	131.888	−59.701
$(8-3)$	125.1	−19.905	59.603	−166.518	211.269	−99.909
$(8-4)$	125.1	−16.738	48.424	−129.770	159.575	−74.013
$(8-5)$	125.1	−13.600	35.446	−89.911	105.637	−47.303
$(8-6)$	125.1	−10.913	24.049	−58.131	66.107	−28.940
$(8-7)$	125.1	−7.765	13.337	−32.316	36.014	−15.296

Table 10.2: Coefficients a_i of the polynomial fit to the DCN de-excitation rate coefficients. These coefficients are only valid in the temperature range 5–2000 K. E_{up} are the upper energy levels

Transition	E_{up} (K)	a_0	a_1	a_2	a_3	a_4
$(1-0)$	4.4	−7.403	8.926	−14.801	10.563	−2.590
$(2-0)$	13.1	−9.639	14.074	−35.391	44.128	−21.007
$(2-1)$	13.1	−7.423	9.788	−18.744	16.659	−5.761
$(3-0)$	26.1	−12.814	28.897	−74.598	89.274	−40.332
$(3-1)$	26.1	−9.592	14.548	−36.465	44.710	−21.001
$(3-2)$	26.1	−7.455	10.360	−21.423	20.817	−7.926
$(4-0)$	43.5	−15.927	39.571	−100.775	117.735	−52.025
$(4-1)$	43.5	−12.763	29.537	−76.487	91.297	−41.134
$(4-2)$	43.5	−9.578	14.777	−36.902	44.619	−20.689
$(4-3)$	43.5	−7.521	11.100	−24.432	25.262	−10.173
$(5-0)$	65.3	−15.764	21.053	−41.693	38.333	−13.813
$(5-1)$	65.3	−16.129	42.754	−111.610	133.075	−59.844
$(5-2)$	65.3	−12.209	24.827	−61.026	71.672	−32.590
$(5-3)$	65.3	−9.621	15.387	−38.753	46.790	−21.638
$(5-4)$	65.3	−7.583	11.785	−27.233	29.445	−12.313
$(6-0)$	91.4	−15.158	1.477	7.836	−15.293	7.402
$(6-1)$	91.4	−16.923	33.431	−84.174	99.707	−45.347
$(6-2)$	91.4	−16.830	49.989	−136.387	168.824	−78.263
$(6-3)$	91.4	−13.108	33.596	−90.122	110.323	−50.739
$(6-4)$	91.4	−9.107	10.635	−23.005	26.473	−12.585
$(6-5)$	91.4	−7.668	12.643	−30.602	34.339	−14.756
$(7-0)$	121.8	−9.723	−58.673	181.107	−236.439	111.453
$(7-1)$	121.8	−12.497	−22.208	88.515	−132.742	68.301
$(7-2)$	121.8	−17.644	39.253	−96.958	104.695	−39.340
$(7-3)$	121.8	−18.318	64.133	−183.445	234.541	−110.659
$(7-4)$	121.8	−13.698	39.371	−109.796	138.629	−65.302
$(7-5)$	121.8	−9.814	17.433	−45.443	55.767	−26.026
$(7-6)$	121.8	−7.686	12.855	−31.518	35.688	−15.428
$(8-0)$	156.6	−12.532	−8.671	−48.477	123.185	−76.018
$(8-1)$	156.6	−9.784	−56.529	173.568	−225.735	106.060
$(8-2)$	156.6	−12.407	−22.181	87.726	−131.074	67.259
$(8-3)$	156.6	−14.860	14.808	−20.242	5.667	3.941
$(8-4)$	156.6	−17.161	50.763	−126.624	131.935	−45.525
$(8-5)$	156.6	−14.757	49.398	−143.428	186.181	−89.164
$(8-6)$	156.6	−10.025	19.503	−52.460	65.752	−31.138
$(8-7)$	156.6	−7.546	2.952	7.712	−20.936	12.334

Table 10.3: Coefficients a_i of the polynomial fit to the HNC de-excitation rate coefficients. These coefficients are only valid in the temperature range 5–2000 K. E_{up} are the upper energy levels

Transition	E_{up} (K)	a_0	a_1	a_2	a_3	a_4
$(1-0)$	3.7	−7.384	8.764	−13.998	9.270	−1.898
$(2-0)$	11.0	−9.621	13.929	−35.013	43.803	−20.891
$(2-1)$	11.0	−7.388	9.471	−17.374	14.561	−4.671
$(3-0)$	22.0	−12.764	28.480	−73.414	87.992	−39.825
$(3-1)$	22.0	−9.554	14.223	−35.527	43.683	−20.576
$(3-2)$	22.0	−7.415	9.987	−19.843	18.427	−6.694
$(4-0)$	36.6	−15.858	38.929	−98.621	114.823	−50.591
$(4-1)$	36.6	−12.724	29.182	−75.374	89.958	−40.533
$(4-2)$	36.6	−9.556	14.614	−36.544	44.501	−20.775
$(4-3)$	36.6	−7.475	10.691	−22.757	22.803	−8.942
$(5-0)$	54.9	−15.543	18.882	−34.000	27.004	−7.873
$(5-1)$	54.9	−15.904	40.627	−104.370	122.762	−54.559
$(5-2)$	54.9	−12.752	29.932	−77.731	92.857	−41.854
$(5-3)$	54.9	−9.558	14.818	−36.983	44.601	−20.644
$(5-4)$	54.9	−7.533	11.316	−25.280	26.537	−10.839
$(6-0)$	76.9	−13.939	−10.066	47.036	−71.217	35.657
$(6-1)$	76.9	−15.950	24.200	−52.614	54.255	−22.087
$(6-2)$	76.9	−16.211	44.121	−116.306	139.844	−63.333
$(6-3)$	76.9	−12.874	31.372	−82.537	99.488	−45.176
$(6-4)$	76.9	−9.596	15.308	−38.466	46.324	−21.378
$(6-5)$	76.9	−7.577	11.788	−27.254	29.476	−12.326
$(7-0)$	102.5	−12.645	−31.579	91.009	−110.232	49.377
$(7-1)$	102.5	−15.491	5.896	−6.381	3.094	−0.486
$(7-2)$	102.5	−17.326	37.781	−98.624	119.852	−55.263
$(7-3)$	102.5	−16.959	51.549	−141.660	176.358	−82.102
$(7-4)$	102.5	−13.109	33.807	−90.846	111.375	−51.288
$(7-5)$	102.5	−9.671	16.091	−40.984	49.613	−22.945
$(7-6)$	102.5	−7.628	12.320	−29.380	32.606	−13.908
$(8-0)$	131.8	−13.106	−2.647	−70.842	157.263	−94.056
$(8-1)$	131.8	−9.600	−58.397	180.148	−235.148	110.842
$(8-2)$	131.8	−12.423	−22.254	88.666	−132.965	68.413
$(8-3)$	131.8	−17.403	37.141	−88.825	91.193	−31.327
$(8-4)$	131.8	−18.257	63.816	−182.467	233.321	−110.159
$(8-5)$	131.8	−13.595	38.537	−106.951	134.530	−63.196
$(8-6)$	131.8	−9.779	17.182	−44.598	54.590	−25.434
$(8-7)$	131.8	−7.665	12.717	−31.059	35.143	−15.217

Table 10.4: Coefficients a_i of the polynomial fit to the DNC de-excitation rate coefficients. These coefficients are only valid in the temperature range 5–2000 K. E_{up} are the upper energy levels

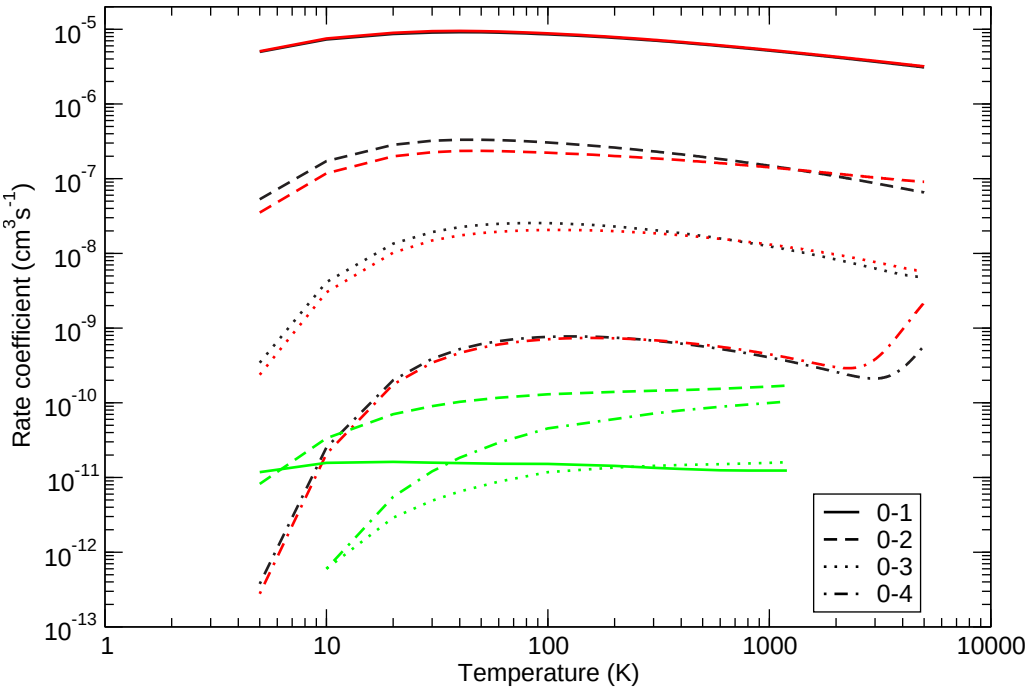

Figure 10.6: Rotational excitation rate coefficients of HCN and HNC as a function of temperature. The black and red lines denote the present results for electron-impact excitation of HCN and HNC respectively. The green lines give the results of Green and Thaddeus (1974) and Green (unpublished data) for the rotational excitation of HCN by He atoms

the entire temperature range, reflecting the dominance of the long-range dipole interaction. Differences larger than a factor of two were found, however, for the smallest rate coefficients ($\Delta J > 2$). The He-HCN rate coefficients are much smaller than the electron-impact rate coefficients. In particular the $J = 0 \rightarrow 1$ rate coefficient is about six orders of magnitude smaller than the electron one. The propensity rules are very different, with even ΔJ favoured strongly over odd ΔJ in the case of He collisions, which reflects an interference effect related to the even anisotropy of the He-HCN potential energy surface (McCurdy and Miller, 1977). As a result, the difference between e-HCN and He-HCN rate coefficients is much larger for dipole-allowed transitions than for others: as an example, the $J = 0 \rightarrow 4$ transition at 1000 K is only a factor of four smaller than the corresponding electron-impact rate.

These large differences between the He-HCN and e-HCN rotational rate coefficients, in terms of magnitude and propensity rules, suggest that the modelling of HCN (and HNC) in astrophysical environments must be sensitive to the relative abundance of electrons and neutrals.

10.3.3 Hyperfine Rate Coefficients

We computed the hyperfine rate coefficients from the pure rotational ones in accordance with the formalism of Neufeld and Green (1994) and only considered the hyperfine effects due to the N nucleus (angular momentum $I = 1$). Tables 10.6, 10.7, 10.8 and 10.9 show the hyperfine transition rate coefficients for HCN, DCN, HNC and DNC respectively. Table 10.5 shows the relative propensities predicted by our calculations at 20 K for a few hyperfine transitions induced by electron impact. It may be seen that the present implementation of the method, based upon the downward fundamental rate coefficients, yields reasonable agreement with the CC results of Monteiro and Stustzki (1986) for He-HCN collisions. Errors on the rate coefficient values were thus found to be between 10 % and 50 %, implying that the IOS approximation provides a good description of hyperfine transition rates. Secondly, it clear that the well-known $\Delta J = \Delta F$ propensity rule is much stronger for e-HCN scattering than for He-HCN. This propensity rule was derived by Alexander and Dagdigian (1985) who stated that this propensity rule is independent of the scattering dynamics and follows the properties of the Wigner $6j$ symbols. It is thus expected to become strong as J and J' increase, as can be observed in tables 10.6–10.9. The fact that it is stronger for electrons than for He atoms is simply due to the smallness of the $\Delta J > 2$ electron-impact rate coefficients.

It may also be noted that in tables 10.6–10.9 transitions of the type $(J, F = J) \rightarrow (J' = 1, F' = 0)$ are strictly forbidden in accordance with the Wigner-$6j$ symbols. Monteiro and Stustzki (1986) demonstrated that this selection rule only becomes a propensity one at the close coupling level.

Table 10.6: Hyperfine de-excitation rate coefficients in cm^3s^{-1} for HCN. Where necessary powers of 10 are given in parentheses

J	F	J'	F'	10 K	100 K	1000 K
1	0	0	1	0.373(-5)	0.297(-5)	0.173(-5)
1	1	0	1	0.373(-5)	0.297(-5)	0.173(-5)
1	1	1	0	0.0	0.0	0.0
1	2	0	1	0.373(-5)	0.297(-5)	0.173(-5)
1	2	1	0	0.492(-7)	0.277(-7)	0.121(-7)
1	2	1	1	0.111(-6)	0.624(-7)	0.272(-7)
2	1	0	1	0.123(-6)	0.693(-7)	0.302(-7)
2	1	1	0	0.199(-5)	0.164(-5)	0.101(-5)

Continued on to next page

J	F	J'	F'	10 K	100 K	1000 K
2	1	1	1	0.149(-5)	0.123(-5)	0.757(-6)
2	1	1	2	0.110(-6)	0.887(-7)	0.533(-7)
2	2	0	1	0.123(-6)	0.693(-7)	0.302(-7)
2	2	1	0	0.0	0.0	0.0
2	2	1	1	0.269(-5)	0.221(-5)	0.136(-5)
2	2	1	2	0.902(-6)	0.740(-6)	0.456(-6)
2	2	2	1	0.615(-7)	0.346(-7)	0.151(-7)
2	3	0	1	0.123(-6)	0.693(-7)	0.302(-7)
2	3	1	0	0.259(-8)	0.165(-8)	0.683(-9)
2	3	1	1	0.518(-8)	0.331(-8)	0.137(-8)
2	3	1	2	0.358(-5)	0.295(-5)	0.182(-5)
2	3	2	1	0.524(-8)	0.297(-8)	0.128(-8)
2	3	2	2	0.504(-7)	0.284(-7)	0.124(-7)
3	2	0	1	0.756(-8)	0.467(-8)	0.182(-8)
3	2	1	0	0.652(-7)	0.398(-7)	0.179(-7)
3	2	1	1	0.652(-7)	0.398(-7)	0.179(-7)
3	2	1	2	0.961(-8)	0.591(-8)	0.264(-8)
3	2	2	1	0.277(-5)	0.232(-5)	0.150(-5)
3	2	2	2	0.516(-6)	0.433(-6)	0.279(-6)
3	2	2	3	0.157(-7)	0.130(-7)	0.826(-8)
3	3	0	1	0.756(-8)	0.467(-8)	0.182(-8)
3	3	1	0	0.0	0.0	0.0
3	3	1	1	0.932(-7)	0.570(-7)	0.256(-7)
3	3	1	2	0.468(-7)	0.286(-7)	0.129(-7)
3	3	2	1	0.260(-8)	0.169(-8)	0.732(-9)
3	3	2	2	0.293(-5)	0.246(-5)	0.159(-5)
3	3	2	3	0.369(-6)	0.310(-6)	0.200(-6)
3	3	3	2	0.353(-7)	0.199(-7)	0.866(-8)
3	4	0	1	0.756(-8)	0.467(-8)	0.182(-8)
3	4	1	0	0.777(-10)	0.554(-10)	0.207(-10)
3	4	1	1	0.146(-9)	0.104(-9)	0.388(-10)
3	4	1	2	0.140(-6)	0.854(-7)	0.384(-7)
3	4	2	1	0.288(-9)	0.188(-9)	0.813(-10)
3	4	2	2	0.240(-8)	0.157(-8)	0.677(-9)
3	4	2	3	0.330(-5)	0.277(-5)	0.179(-5)
3	4	3	2	0.134(-8)	0.759(-9)	0.329(-9)
3	4	3	3	0.286(-7)	0.161(-7)	0.702(-8)

J	F	J'	F'	Present	He (CC)	He (IOS)
1	1	2	1	24.9	21.4	19.2
		2	2	74.9	59.7	65.4
		2	3	0.2	18.9	15.4
1	1	3	2	33.3	30.0	26.3
		3	3	66.6	61.3	60.5
		3	4	0.1	8.8	13.2
2	2	3	2	11.2	17.0	16.6
		3	3	88.7	69.8	75.8
		3	4	0.1	13.3	7.7

Table 10.5: Relative propensities for hyperfine collisional rate coefficients as a percentage of the total rates for $T = 20$ K. Present=rates calculated here; He (CC)=close-coupling He−HCN results of Monteiro and Stustzki (1986); He (IOS)=IOS scaling for He−HCN.

Table 10.7: Hyperfine de-excitation rate coefficients in cm^3s^{-1} for DCN. Where necessary powers of 10 are given in parentheses

J	F	J'	F'	10 K	100 K	1000 K
1	0	0	1	0.392(-5)	0.311(-5)	0.179(-5)
1	1	0	1	0.392(-5)	0.311(-5)	0.179(-5)
1	1	1	0	0.0	0.0	0.0
1	2	0	1	0.392(-5)	0.311(-5)	0.179(-5)
1	2	1	0	0.516(-7)	0.281(-7)	0.121(-7)
1	2	1	1	0.116(-6)	0.632(-7)	0.273(-7)
2	1	0	1	0.129(-6)	0.702(-7)	0.303(-7)
2	1	1	0	0.212(-5)	0.172(-5)	0.105(-5)
2	1	1	1	0.159(-5)	0.129(-5)	0.786(-6)
2	1	1	2	0.117(-6)	0.933(-7)	0.553(-7)
2	2	0	1	0.129(-6)	0.702(-7)	0.303(-7)
2	2	1	0	0.0	0.0	0.0
2	2	1	1	0.286(-5)	0.233(-5)	0.142(-5)
2	2	1	2	0.960(-6)	0.780(-6)	0.474(-6)
2	2	2	1	0.645(-7)	0.351(-7)	0.152(-7)
2	3	0	1	0.129(-6)	0.702(-7)	0.303(-7)
2	3	1	0	0.277(-8)	0.170(-8)	0.689(-9)
2	3	1	1	0.554(-8)	0.341(-8)	0.138(-8)
2	3	1	2	0.381(-5)	0.310(-5)	0.189(-5)
2	3	2	1	0.550(-8)	0.301(-8)	0.129(-8)
2	3	2	2	0.529(-7)	0.288(-7)	0.124(-7)

Continued on to next page

J	F	J'	F'	10 K	100 K	1000 K
3	2	0	1	0.798(-8)	0.478(-8)	0.183(-8)
3	2	1	0	0.685(-7)	0.406(-7)	0.180(-7)
3	2	1	1	0.685(-7)	0.406(-7)	0.180(-7)
3	2	1	2	0.101(-7)	0.602(-8)	0.266(-8)
3	2	2	1	0.298(-5)	0.247(-5)	0.156(-5)
3	2	2	2	0.556(-6)	0.459(-6)	0.290(-6)
3	2	2	3	0.169(-7)	0.138(-7)	0.857(-8)
3	3	0	1	0.798(-8)	0.478(-8)	0.183(-8)
3	3	1	0	0.0	0.0	0.0
3	3	1	1	0.979(-7)	0.581(-7)	0.258(-7)
3	3	1	2	0.491(-7)	0.291(-7)	0.129(-7)
3	3	2	1	0.280(-8)	0.175(-8)	0.739(-9)
3	3	2	2	0.315(-5)	0.261(-5)	0.165(-5)
3	3	2	3	0.397(-6)	0.328(-6)	0.207(-6)
3	3	3	2	0.370(-7)	0.202(-7)	0.869(-8)
3	4	0	1	0.798(-8)	0.478(-8)	0.183(-8)
3	4	1	0	0.825(-10)	0.574(-10)	0.209(-10)
3	4	1	1	0.155(-9)	0.108(-9)	0.392(-10)
3	4	1	2	0.147(-6)	0.870(-7)	0.386(-7)
3	4	2	1	0.312(-9)	0.195(-9)	0.821(-10)
3	4	2	2	0.260(-8)	0.162(-8)	0.684(-9)
3	4	2	3	0.355(-5)	0.294(-5)	0.186(-5)
3	4	3	2	0.141(-8)	0.769(-9)	0.330(-9)
3	4	3	3	0.300(-7)	0.163(-7)	0.705(-8)

Table 10.8: Hyperfine de-excitation rate coefficients in cm^3s^{-1} for HNC. Where necessary powers of 10 are given in parentheses

J	F	J'	F'	10 K	100 K	1000 K
1	0	0	1	0.388(-5)	0.307(-5)	0.177(-5)
1	1	0	1	0.388(-5)	0.307(-5)	0.177(-5)
1	1	1	0	0.0	0.0	0.0
1	2	0	1	0.388(-5)	0.307(-5)	0.177(-5)
1	2	1	0	0.347(-7)	0.203(-7)	0.115(-7)
1	2	1	1	0.780(-7)	0.456(-7)	0.259(-7)
2	1	0	1	0.867(-7)	0.507(-7)	0.288(-7)
2	1	1	0	0.205(-5)	0.167(-5)	0.103(-5)
2	1	1	1	0.154(-5)	0.126(-5)	0.770(-6)
2	1	1	2	0.111(-6)	0.893(-7)	0.543(-7)

Continued on to next page

J	F	J'	F'	10 K	100 K	1000 K
2	2	0	1	0.867(-7)	0.507(-7)	0.288(-7)
2	2	1	0	0.0	0.0	0.0
2	2	1	1	0.277(-5)	0.226(-5)	0.139(-5)
2	2	1	2	0.928(-6)	0.757(-6)	0.464(-6)
2	2	2	1	0.434(-7)	0.254(-7)	0.144(-7)
2	3	0	1	0.867(-7)	0.507(-7)	0.288(-7)
2	3	1	0	0.199(-8)	0.134(-8)	0.719(-9)
2	3	1	1	0.398(-8)	0.267(-8)	0.144(-8)
2	3	1	2	0.369(-5)	0.302(-5)	0.185(-5)
2	3	2	1	0.373(-8)	0.220(-8)	0.123(-8)
2	3	2	2	0.356(-7)	0.208(-7)	0.118(-7)
3	2	0	1	0.586(-8)	0.381(-8)	0.193(-8)
3	2	1	0	0.459(-7)	0.293(-7)	0.172(-7)
3	2	1	1	0.459(-7)	0.293(-7)	0.172(-7)
3	2	1	2	0.683(-8)	0.438(-8)	0.254(-8)
3	2	2	1	0.284(-5)	0.237(-5)	0.152(-5)
3	2	2	2	0.528(-6)	0.440(-6)	0.282(-6)
3	2	2	3	0.158(-7)	0.131(-7)	0.836(-8)
3	3	0	1	0.586(-8)	0.381(-8)	0.193(-8)
3	3	1	0	0.0	0.0	0.0
3	3	1	1	0.657(-7)	0.419(-7)	0.246(-7)
3	3	1	2	0.330(-7)	0.210(-7)	0.123(-7)
3	3	2	1	0.198(-8)	0.136(-8)	0.767(-9)
3	3	2	2	0.300(-5)	0.250(-5)	0.161(-5)
3	3	2	3	0.378(-6)	0.315(-6)	0.202(-6)
3	3	3	2	0.249(-7)	0.146(-7)	0.827(-8)
3	4	0	1	0.586(-8)	0.381(-8)	0.193(-8)
3	4	1	0	0.699(-10)	0.522(-10)	0.229(-10)
3	4	1	1	0.131(-9)	0.978(-10)	0.429(-10)
3	4	1	2	0.985(-7)	0.628(-7)	0.368(-7)
3	4	2	1	0.220(-9)	0.151(-9)	0.852(-10)
3	4	2	2	0.184(-8)	0.126(-8)	0.710(-9)
3	4	2	3	0.338(-5)	0.282(-5)	0.181(-5)
3	4	3	2	0.952(-9)	0.560(-9)	0.315(-9)
3	4	3	3	0.202(-7)	0.118(-7)	0.670(-8)

Table 10.9: Hyperfine de-excitation rate coefficients in cm^3s^{-1} for DNC. Where necessary powers of 10 are given in parentheses

J	F	J'	F'	10 K	100 K	1000 K
1	0	0	1	0.408(-5)	0.321(-5)	0.183(-5)
1	1	0	1	0.408(-5)	0.321(-5)	0.183(-5)
1	1	1	0	0.0	0.0	0.0
1	2	0	1	0.408(-5)	0.321(-5)	0.183(-5)
1	2	1	0	0.360(-7)	0.205(-7)	0.115(-7)
1	2	1	1	0.811(-7)	0.462(-7)	0.259(-7)
2	1	0	1	0.901(-7)	0.513(-7)	0.288(-7)
2	1	1	0	0.218(-5)	0.176(-5)	0.106(-5)
2	1	1	1	0.163(-5)	0.132(-5)	0.799(-6)
2	1	1	2	0.118(-6)	0.939(-7)	0.563(-7)
2	2	0	1	0.901(-7)	0.513(-7)	0.288(-7)
2	2	1	0	0.0	0.0	0.0
2	2	1	1	0.294(-5)	0.238(-5)	0.144(-5)
2	2	1	2	0.986(-6)	0.797(-6)	0.481(-6)
2	2	2	1	0.450(-7)	0.256(-7)	0.144(-7)
2	3	0	1	0.901(-7)	0.513(-7)	0.288(-7)
2	3	1	0	0.211(-8)	0.137(-8)	0.726(-9)
2	3	1	1	0.421(-8)	0.274(-8)	0.145(-8)
2	3	1	2	0.392(-5)	0.318(-5)	0.192(-5)
2	3	2	1	0.388(-8)	0.223(-8)	0.123(-8)
2	3	2	2	0.370(-7)	0.211(-7)	0.118(-7)
3	2	0	1	0.614(-8)	0.388(-8)	0.194(-8)
3	2	1	0	0.479(-7)	0.297(-7)	0.172(-7)
3	2	1	1	0.479(-7)	0.297(-7)	0.172(-7)
3	2	1	2	0.713(-8)	0.445(-8)	0.254(-8)
3	2	2	1	0.304(-5)	0.251(-5)	0.158(-5)
3	2	2	2	0.566(-6)	0.467(-6)	0.293(-6)
3	2	2	3	0.170(-7)	0.139(-7)	0.868(-8)
3	3	0	1	0.614(-8)	0.388(-8)	0.194(-8)
3	3	1	0	0.0	0.0	0.0
3	3	1	1	0.686(-7)	0.425(-7)	0.246(-7)
3	3	1	2	0.344(-7)	0.213(-7)	0.123(-7)
3	3	2	1	0.212(-8)	0.140(-8)	0.774(-9)
3	3	2	2	0.321(-5)	0.265(-5)	0.167(-5)
3	3	2	3	0.404(-6)	0.334(-6)	0.210(-6)
3	3	3	2	0.259(-7)	0.147(-7)	0.827(-8)
3	4	0	1	0.614(-8)	0.388(-8)	0.194(-8)

Continued on to next page

J	F	J'	F'	10 K	100 K	1000 K
3	4	1	0	0.737(-10)	0.536(-10)	0.231(-10)
3	4	1	1	0.138(-9)	0.100(-9)	0.432(-10)
3	4	1	2	0.103(-6)	0.636(-7)	0.368(-7)
3	4	2	1	0.235(-9)	0.156(-9)	0.860(-10)
3	4	2	2	0.196(-8)	0.130(-8)	0.717(-9)
3	4	2	3	0.362(-5)	0.299(-5)	0.188(-5)
3	4	3	2	0.990(-9)	0.567(-9)	0.315(-9)
3	4	3	3	0.210(-7)	0.120(-7)	0.670(-8)

10.4 Conclusion

We have computed the electron-impact rotational excitation cross sections, rotationally resolved differential cross sections, rotational and hyperfine (de)-excitation rate coefficients for the HCN and HNC triatomic molecules and their isotopologues. Our calculations were based on the *ab initio* R-matrix method combined with the ANR approximation. The results hence obtained showed that the collisions are dominated by the dipolar transitions which was not surprising given the long range nature of the dipole moment (approximately 3 D). Short-range correlation effects were also found to be important and were included via the inner region scattering eigenkets as corrections to the Born approximation. Dipole forbidden transitions therefore have appreciable rate coefficients which cannot be ignored in any detailed population models of the isotopologues of HCN and HNC. We have shown that electron-impact rate coefficients are crucial for modelling environments where the electron fraction is greater 10^{-6}. Jimenez-Serra et al. (2006) suggested using rotational emissions of HCO^+, HCN and HNC to probe electron densities in C-type shocks. The present rate coefficients should help in the investigation of electron density enhancements expected during the first stages of a C-type shock evolution, and in the modelling of the observed variable HCN/HNC ratio in comets (Biver et al., 2006).

Since hyperfine structure is resolved in some astronomical spectra, we computed, using the IOS approximation, the hyperfine rate coefficients, considering only the nuclear spin of the ^{14}N atom as the effect of the H and D atoms was assumed to be negligible. Our implementation based on the downward fundamental rate coefficients yielded reasonable

agreement with the CC results of Monteiro and Stustzki (1986) for He-HCN scattering. The hyperfine excitation rate coefficients were obtained by invoking the detailed balance relation. The major finding was that the $\Delta J = \Delta F$ propensity rule was much stronger for electron collisions than for helium ones.

Chapter 11

Conclusion

The aim of this thesis was to analyse low-energy (< 10 eV) electron scattering by molecules of astrophysical interest. The focus was particularly on polar molecules including HCN, HNC (with dipole moments of about -3 D), the weakly polar CO (-0.043 D), SiO (about $+3$ D), CS ($+1.98$ D) and the non-polar alkane CH_4 using the widely applied *ab initio* R-matrix method of Wigner (1946) and Wigner and Eisenbud (1947). We calculated the K-, T- and R-matrix, the eigenphase sums, resonance parameters and electronically inelastic and BEB ionisation cross sections.

Using the T-matrix we computed: the integrated rotational cross sections using the adiabatic nuclear rotation approximation (ANR) and the rotationally resolved differential cross sections using the Born completion method on the scattering amplitude (Itikawa, 2000). From the integrated rotational cross sections, and by modelling the electron velocity distribution as Maxwellian, the rotational excitation rate coefficients were then computed, from which we calculated hyperfine transition rate coefficients using the formalism of Neufeld and Green (1994). All of these observables are intended for later use in astrophysical modelling.

This thesis has presented a number of new findings.

For the first time an electron scattering calculation was carried out on HNC (hydrogen isocyanide) at the close-coupling (CC) level of approximation, and we were able to show that electron scattering by HCN and HNC is dominated by a low-lying $^2\Pi$ shape resonance, which for the best HNC model was found to lie at 2.43 eV with a narrower width of 0.67 eV compared to HCN where the resonance was located at 2.46 eV with a width of 1.14 eV. The chief distinguishing feature of e-HNC scattering was the appearance of $^2\Sigma^+$ and $^2\Delta$ Feshbach resonances, which were entirely absent from scattering by

HCN.

The T-matrices from the best models were initially transformed to their $C_{\infty v}$ representation, and then employed in the calculation of the electron-impact rotational excitation cross sections and rate coefficients. They were also used for the calculation of the same for the isotopologues DCN and DNC.

After H_2, CO is one of the most abundant molecules in the interstellar medium. Hence using the polyatomic codes directly we carried out CC scattering calculations which retained a large number of open and closed channels (300). Our study confirmed that scattering is dominated by the appearance of a $^2\Pi$ shape resonance, which was located at 2.03 eV, in good agreement with a previous measurement of 1.9 eV by Kwan et al. (1983) for example. We did not however, detect the additional $^2\Pi$, $^2\Sigma^+$ $^2\Delta$ and $^2\Phi$ resonances obtained by Morgan and Tennyson (1993), but given that they were located at positions outside of the energy range we considered, it is not surprising. Concerning the quantum chemistry calculations, it was necessary to determine a model that would yield a dipole moment accurate in terms of magnitude and with the correct experimentally observed sign. This has been a source of contention in previous quantum chemistry studies, where the HF approximation has yielded the incorrect sign, which has to be corrected by more accurate post-HF methods which include correlation. We were able to obtain good agreement with previous studies and so using this model the rotational DCSs were computed. Although good agreement was attained with the data of Gibson et al. (1996), concerns remain as to the correct behaviour at low scattering angles which, according to the experimental data, has that associated with non-polar systems.

No scattering studies have been carried out on SiO to date. In chapter 7 we presented for the first time quantities of the eigenphase sum, electronically inelastic cross sections, rotationally resolved differential and integrated cross sections and the excitation rate coefficients.

In terms of important features of the calculation, our study was able to independently confirm the existence of a $^2\Pi$ anionic bound state at -0.12 eV. Feshbach resonances of $^2\Sigma^-$, $^2\Pi$ and $^2\Delta$ symmetries were also detected, and whose appearance was sensitive to the number of target states retained for construction of the inner region wavefunction and of the R-matrix. Due to the absence of any previous low-energy studies, this study cannot be benchmarked at present. The BEB ionisation cross section, however, was compared to the data of Joshipura, Gangopadhyay and Vaishnav (2007) and our data

were found to be lower than theirs over the entire energy range considered in the study. It is well-known that the BEB cross section (Kim et al., 1997) is sensitive to the precise value of the ionisation energy employed, and previous studies have used the experimental value. Upon adopting this strategy, we observed virtually no change in the cross sections.

Until now, the one-state calculation of Carelli et al. (2008) was the only theoretical study into electron-scattering by CS to have been carried out. They studied the evolution of a low-energy $^2\Pi$ shape resonance as a function of bond stretch and contraction. They did not study the Feshbach resonances. In chapter 8 we carried out a 300-channel CC R-matrix study for a range of bond lengths– 1.1–2.7 Å (equilibrium at 1.5349 Å, NIST (2008)) using the DZP basis set. The existence of a $^2\Pi$ bound state beyond about 1.6 Å was confirmed, in accordance with the observation of Carelli et al. (2008). A number of Feshbach resonances of $^2\Sigma^-$, $^2\Pi$ and $^2\Delta$ scattering symmetries were also detected, and a correlation table of which resonance corresponds to which dissociation channel is given in table 8.5.

Unlike SiO and CS there are a multitude of theoretical and experimental electron-impact studies on CH_4. All studies reported on the appearance of a low-energy Ramsauer-Townsend minimum and a cross section maximum at about 8 eV. We carried out a detailed study in which it was found that in order to attain good agreement with experiment, it was necessary to improve the modelling of the polarisation interaction, which was modelled by retaining a large number of closed channels. Convergence of the integral cross sections was attained when 48 states, or 300 channels, were included for the construction of the R-matrix at the interaction radius, here taken to be 10 a_0. However, this is by no means an indication of a converged treatment of the polarisation interaction and so a different structure of the trial wavefunction using 'uncontracted' configuration state functions was employed instead. Unlike the studies using the usual contracted CSFs, the uncontracted CSFs model yielded the Ramsauer-Townsend minimum at 0.4 eV, in good agreement with previous calculations and experimental observations (experimental value 0.36 eV (Lohmann and Buckman, 1986)).

Rotationally resolved DCSs for CH_4 were calculated to confirm the accuracy of the best model using POLYDCS (Sanna and Gianturco, 1998).

Despite the successes, there are criticisms of the CH_4 study, particularly the channel thresholds, which were found to be much higher than those measured experimentally. As a result, our dissociation cross sections were in disagreement with Makochekanwa et al.

(2006), although the shapes of the two cross section curves were similar, both producing noticeable peaks.

Nearly all scattering studies mentioned above employed the JAVA-based application Quantemol-N (Tennyson et al., 2007), which provides a simple, intuitive and user-friendly expert interface to the UK polyatomic R-matrix codes. The motivation for developing the software was to enable non-specialists to take full advantage of these codes. In fact it has proved to be a productive tool even for experienced users.

Additional facilities were added to make the software much more powerful, including a batch job facility to allow a user to run a queue of R-matrix calculations (T. A. Field, private communication), a tutorial capability and calculation of BEB ionisation cross sections.

The software has now branched into two versions– a standard edition (Quantemol-N (SE)) and an enterprise edition (Quantemol-N (EE)), the latter providing the said job queuing system. Further information may be found at http://www.quantemol.com.

Quantemol-N is under constant development. There are a number of tasks that are being carried out at present, including the ability to locate bound states using BOUND (Sarpal, Branchett, Tennyson and Morgan, 1991; Rabadán and Tennyson, 1996), integration with the application MOLPRO (Werner et al., 2008); calculation of the differential and momentum transfer cross sections using and extending the formalism of Itikawa (2000); calculation of the charge density for use in the SCOP method (Joshipura, Gangopadhyay and Vaishnav, 2007); and calculation of cross sections for much larger molecules: at the moment we are considering 2,2-dimethyl propane, or neopentane, which has a similar structure to the methane molecule (a tetrahedral molecule hence a member of the T_d point group) except that all the hydrogen atoms are replaced by the methyl functional group.

From the electron-impact rotational excitation studies that were performed on SiO, HCN, HNC, DCN and DNC, our work has confirmed, without doubt, the need to include electron-molecule interactions in any astrophysical modelling, such as comets, especially when the scatterers are very polar molecules as stated previously by Xie and Mumma (1992) and Lovell et al. (2004). In particular, we have been able to show that in some cases collisions with electrons can compete with, if not, easily dominate over atom-molecule collisions.

Future work includes a much more accurate quantum chemistry calculation for CH_4

following the discussion above. For example, it is certainly possible to use a much bigger complete active space than the one used in this study which generated only 492 CSFs. The high-lying Rydberg states of CH_4 were entirely neglected in our study and should be included as part of the study to determine the precise impact on the channel thresholds.

It was interesting to note the comment made by Lengsfield et al. (1991) that the Ramsauer-Townsend minimum moves to higher energies with increasing polarisability α_0. Following a bug fix, two new calculations were performed using a new version of Quantemol-N (version 3.5.2) with the same number of target states (48), but different GTO basis sets. Using the DZP basis a polarisability of 9.34 a_0^3 was obtained while the more compact 6–31G basis set yielded a higher value of 11.41 a_0^3 (expt. 16.52 a_0^3 (NIST, 2008)). The 6–31G basis set calculation did re-produce the Ramsauer minimum but at a lower energy of 0.1 eV (experimental value 0.36 eV (Lohmann and Buckman, 1986)); the same could not be said of the DZP calculation. Hence it is certainly true to say that the position is sensitive to the precise value of the polarisability. It would be interesting then to confirm the above comment of Lengsfield et al. (1991) using the R-matrix method, perhaps including pseudo-states (MRMPS) (Gorfinkiel and Tennyson, 2004).

The polarisabilites of C_2H_6 (5.89 a_0^3) and C_3H_8 (3.72 a_0^3) were very low compared to the experimentally determined ones, which indicated that the modelling of the polarisation interaction was being significantly underestimated. Consequently, our cross sections were found to be in poor agreement with experiments. It would be particularly interesting, therefore, to see whether the bug-fix in DENPROP and application of the MRMPS method make a difference to the quality of this observable and the other scattering quantities, especially the eigenphase sums.

CS is also important in astrophysics and at present we are using the model described in chapter 8 to compute the rotationally resolved integral cross sections and the corresponding excitation rate coefficients.

Graupner et al. (2006) observed dissociative electron attachment to CS to be remarkably similar to that for CO. They recommended that theoretical calculations similar to those presented in chapter 8 be carried out in order to determine why C^- is so weakly observed from CO but strongly from CS. This will be carried out in the near future (T. A. Field, private communication), in which we shall attempt to confirm the existence of the high-lying resonances discussed above.

Finally, the PYTHON Hyperfines code (chapter 3), developed to enable hyperfine

rate coefficients for molecules with half-integer nuclear spin I to be calculated as well as integer ones, is being applied to AlH at present (S. Kaur, K. L. Baluja, private communication).

Appendix A

Non-Hermiticity of the Hamiltonian: A Potential Scattering Example

Let the wavefunction of an enclosed system $\psi_i = f_i(r)Y_{l_i}^{m_i}(\theta,\phi)$. Evaluating the Hamiltonian matrix element $\langle\psi_j|\hat{H}\psi_i\rangle - \langle\hat{H}\psi_j|\psi_i\rangle$ over the interval containing the internal region yields:

$$M = -\frac{1}{2}[\langle\psi_j|\nabla^2\psi_i\rangle - \langle\nabla^2\psi_j|\psi_i\rangle] \tag{A.1}$$

(the potential matrix elements are assumed to be Hermitian and vanish). Thus the braket simplifies to a radial integral below

$$M = -\frac{1}{2}\left\{\int_0^a r^2 dr f_j^* \frac{1}{r^2}\frac{d}{dr}\left(r^2\frac{df_i}{dr}\right) - \int_0^a r^2 dr \left[\frac{1}{r^2}\frac{d}{dr}\left(r^2\frac{df_j}{dr}\right)\right]^* f_i\right\} \tag{A.2}$$

$$\tag{A.3}$$

Simplifying notation:

$$M = -\frac{1}{2}(I_1 - I_2) \tag{A.4}$$

$$I_1 = \int_0^a f_j^* \frac{d}{dr}\left(r^2\frac{df_i}{dr}\right) dr \tag{A.5}$$

$$I_2 = \int_0^a \frac{d}{dr}\left(r^2\frac{df_j^*}{dr}\right) f_i dr \tag{A.6}$$

We shall evaluate the integrals I_1 and I_2 using integration by parts where for I_1:

$$v = f_j^* \tag{A.7}$$

$$\frac{du}{dr} = \frac{d}{dr}\left(r^2\frac{df_i}{dr}\right) \tag{A.8}$$

and for I_2

$$v = f_i \tag{A.9}$$

$$\frac{du}{dr} = \frac{d}{dr}\left(r^2 \frac{df_j^*}{dr}\right) \tag{A.10}$$

Upon evaluation of these integrals, one obtains non-zero surface terms resulting in the Hamiltonian not being Hermitian.

$$M = -\frac{a^2}{2}(f_j(a)^* f_i'(a) - f_j'(a)^* f_i(a)) \neq 0 \tag{A.11}$$

Define the Bloch operator and the modified Hamiltonian:

$$\hat{L} = \frac{1}{2a}\delta(r-a)\frac{d}{dr}r \tag{A.12}$$

$$\hat{\mathcal{H}} = \hat{H} + \hat{L} \tag{A.13}$$

Computing the modified Hamiltonian matrix elements over the same interval

$$-\frac{1}{2}\langle\psi_j|\nabla^2\psi_i\rangle + \langle\psi_j|\hat{L}\psi_i\rangle - \frac{1}{2}\langle\nabla^2\psi_j|\psi_i\rangle - \langle\hat{L}\psi_j|\psi_i\rangle \tag{A.14}$$

it may be shown that evaluating those matrix elements involving the Bloch operator simplify to

$$\frac{1}{2a}\left\{a^2\left[f_j(a)^*\frac{d}{dr}[rf_i(r)]_a - \frac{d}{dr}[rf_j(r)^*]_a f_i(a)\right]\right\} \tag{A.15}$$

Finally appealing to the product rule equation (A.15) may be shown to cancel the kinetic energy surface term (A.11), and Hermicity is regained. Discussion on the above problem may be found in Lane and Robson (1966).

Appendix B

The Outer Region Coupled Differential Equations

B.1 Derivation

Considering

$$\hat{H}_{N+1}|\Psi^{\Delta}\rangle = E|\Psi^{\Delta}\rangle \tag{B.1}$$

one may decompose this Schrödinger equation to

$$-\frac{1}{2}\nabla^2_{N+1}\Psi^{\Delta} + \left\{-\sum_A \frac{Z_A}{|\mathbf{r}_{N+1}-\mathbf{r}_A|} + \sum_i \frac{1}{|\mathbf{r}_{N+1}-\mathbf{r}_i|}\right\}\Psi^{\Delta} + \hat{H}_N\Psi^{\Delta} = E\Psi^{\Delta} \tag{B.2}$$

Let

$$\hat{V}_1 = -\sum_A \frac{Z_A}{|\mathbf{r}_{N+1}-\mathbf{r}_A|} \tag{B.3}$$

$$\hat{V}_2 = \sum_i \frac{1}{|\mathbf{r}_{N+1}-\mathbf{r}_i|} \tag{B.4}$$

In the outer region one may employ the single centre expansion:

$$\Psi^{\Delta} = \sum_{\lambda} \frac{F^{\Delta}_{\lambda}}{r_{N+1}} \psi^N_{\lambda} Y^{m_\lambda}_{l_\lambda} \tag{B.5}$$

In evaluating the kinetic energy term of equation (B.2)

$$\nabla^2\Psi^{\Delta} = \sum_{\lambda}\left[F^{\Delta\prime\prime}_{\lambda} - \frac{l_\lambda(l_\lambda+1)}{r^2_{N+1}}F^{\Delta}_{\lambda}\right]\frac{\psi^N_\lambda Y^{m_\lambda}_{l_\lambda}}{r_{N+1}} \tag{B.6}$$

Further manipulation of equation (B.2) and substituting equation (B.6) the coupled differential equations become:

$$\sum_{\lambda}\left\{F_{\lambda}^{\Delta\prime\prime}-\frac{l_{\lambda}(l_{\lambda}+1)F_{\lambda}^{\Delta}}{r_{N+1}^{2}}+2(E-E_{\lambda})F_{\lambda}^{\Delta}\right\}\psi_{\lambda}^{N}Y_{l_{\lambda}}^{m_{\lambda}}=2\sum_{\lambda}\hat{V}F_{\lambda}^{\Delta}\psi_{\lambda}^{N}Y_{l_{\lambda}}^{m_{\lambda}} \tag{B.7}$$

where

$$\hat{V} = \hat{V}_1+\hat{V}_2 \tag{B.8}$$

$$\hat{V} = -\sum_{A}\frac{Z_A}{|\mathbf{r}_{N+1}-\mathbf{r}_A|}+\sum_{i}\frac{1}{|\mathbf{r}_{N+1}-\mathbf{r}_i|} \tag{B.9}$$

and projecting on to $\psi_{\lambda'}^{N}Y_{l_{\lambda'}}^{m_{\lambda'}}$

$$F_{\lambda'}^{\Delta\prime\prime}-\frac{l_{\lambda'}(l_{\lambda'}+1)F_{\lambda'}^{\Delta}}{r_{N+1}^{2}}+2(E-E_{\lambda'})F_{\lambda'}^{\Delta}=2\sum_{\lambda}V_{\lambda'\lambda}F_{\lambda}^{\Delta} \tag{B.10}$$

where

$$V_{\lambda'\lambda}=\langle\psi_{\lambda'}^{N}Y_{l_{\lambda'}}^{m_{\lambda'}}|\hat{V}|\psi_{\lambda}^{N}Y_{l_{\lambda}}^{m_{\lambda}}\rangle \tag{B.11}$$

B.2 The Channel Coupling Potential

In the outer region the position vector of the scattering electron is greater than those of the target electrons and the constituent nuclei. Therefore one may appeal to the Legendre generating function and the spherical harmonic addition theorem to show that:

$$\sum_{i}\frac{1}{|\mathbf{r}_{N+1}-\mathbf{r}_i|}=\sum_{l}\sum_{m=-l}^{l}\frac{1}{r_{N+1}^{l+1}}\sum_{i}R_{l}^{m}(\mathbf{r}_i)Y_{l}^{m}(\theta_{N+1},\phi_{N+1}) \tag{B.12}$$

where

$$R_{l}^{m}(\mathbf{r}_i)=\frac{4\pi}{2l+1}{r_i}^{l}Y_{l}^{m}(\theta_i,\phi_i) \tag{B.13}$$

Furthermore, define

$$V_{\lambda'\lambda}^{1}=\langle\psi_{\lambda'}^{N}Y_{l_{\lambda'}}^{m_{\lambda'}}|\hat{V}_1|\psi_{\lambda}^{N}Y_{l_{\lambda}}^{m_{\lambda}}\rangle \tag{B.14}$$

$$V_{\lambda'\lambda}^{2}=\langle\psi_{\lambda'}^{N}Y_{l_{\lambda'}}^{m_{\lambda'}}|\hat{V}_2|\psi_{\lambda}^{N}Y_{l_{\lambda}}^{m_{\lambda}}\rangle \tag{B.15}$$

Computing $\langle \psi^N_{\lambda'} Y^{m_{\lambda'}}_{l_{\lambda'}} | \hat{V}_2 | \psi^N_{\lambda} Y^{m_{\lambda}}_{l_{\lambda}} \rangle$ to begin with, we then obtain

$$V^2_{\lambda'\lambda} = \sum_l \sum_{m=-l}^{l} \frac{(-1)^{m_{\lambda'}}}{r^{l+1}_{N+1}} M^m_l(\lambda' \to \lambda) C(l_{\lambda'}, l, l_\lambda) \begin{pmatrix} l_{\lambda'} & l & l_\lambda \\ -m_{\lambda'} & m & m_\lambda \end{pmatrix} \begin{pmatrix} l_{\lambda'} & l & l_\lambda \\ 0 & 0 & 0 \end{pmatrix} \tag{B.16}$$

where

$$M^m_l(\lambda' \to \lambda) = \langle \psi^N_{\lambda'} Y^{m_{\lambda'}}_{l_{\lambda'}} | \sum_i R^m_l(\mathbf{r}_i) | \psi^N_{\lambda} Y^{m_{\lambda}}_{l_{\lambda}} \rangle \tag{B.17}$$

Let us define

$$b_{l,\lambda'\lambda} = \sum_{m=-l}^{l} (-1)^{m_{\lambda'}+1} \left[-M^m_l(\lambda' \to \lambda) \right] C(l_{\lambda'}, l, l_\lambda) \begin{pmatrix} l_{\lambda'} & l & l_\lambda \\ -m_{\lambda'} & m & m_\lambda \end{pmatrix} \begin{pmatrix} l_{\lambda'} & l & l_\lambda \\ 0 & 0 & 0 \end{pmatrix} \tag{B.18}$$

In a similar fashion to the above, we can show that:

$$V^1_{\lambda'\lambda} = \sum_l \sum_{m=-l}^{l} \sum_A \frac{Z_A R^m_l(\mathbf{R}_A)(-1)^{m_{\lambda'}+1}}{r^{l+1}_{N+1}} \delta_{\lambda\lambda'} C(l_{\lambda'}, l, l_\lambda) \begin{pmatrix} l_{\lambda'} & l & l_\lambda \\ -m_{\lambda'} & m & m_\lambda \end{pmatrix} \begin{pmatrix} l_{\lambda'} & l & l_\lambda \\ 0 & 0 & 0 \end{pmatrix} \tag{B.19}$$

Again we let

$$c_{l,\lambda'\lambda} = \sum_{m=-l}^{l} \sum_A Z_A R^m_l(\mathbf{R}_A)(-1)^{m_{\lambda'}+1} \delta_{\lambda\lambda'} C(l_{\lambda'}, l, l_\lambda) \begin{pmatrix} l_{\lambda'} & l & l_\lambda \\ -m_{\lambda'} & m & m_\lambda \end{pmatrix} \begin{pmatrix} l_{\lambda'} & l & l_\lambda \\ 0 & 0 & 0 \end{pmatrix} \tag{B.20}$$

Hence if we let $a_{l,\lambda'\lambda} = b_{l,\lambda'\lambda} + c_{l,\lambda'\lambda}$ then

$$\langle \psi^N_{\lambda'} Y^{m_{\lambda'}}_{l_{\lambda'}} | \hat{V} | \psi^N_{\lambda} Y^{m_{\lambda}}_{l_{\lambda}} \rangle = \sum_l \frac{a_{l,\lambda'\lambda}}{r^{l+1}_{N+1}} \tag{B.21}$$

where

$$C(l_{\lambda'}, l, l_\lambda) = \sqrt{\frac{(2l_{\lambda'}+1)(2l+1)(2l_\lambda+1)}{4\pi}} \tag{B.22}$$

$$a_{l,\lambda'\lambda} = \sum_{m=-l}^{l} \mu^m_l(\lambda' \to \lambda)(-1)^{m_{\lambda'}+1} C(l_{\lambda'}, l, l_\lambda) \begin{pmatrix} l_{\lambda'} & l & l_\lambda \\ -m_{\lambda'} & m & m_\lambda \end{pmatrix} \begin{pmatrix} l_{\lambda'} & l & l_\lambda \\ 0 & 0 & 0 \end{pmatrix} \tag{B.23}$$

and the molecular multipole moments

$$\mu_l^m(\lambda' \to \lambda) = -M_l^m(\lambda' \to \lambda) + \sum_A Z_A R_l^m(\mathbf{R}_A)\delta_{\lambda\lambda'} \tag{B.24}$$

Appendix C

Publications

Electron-impact rotational excitation of the carbon monosulphide (CS) molecule
H. N. Varambhia, A. Faure, T. A. Field, K. Graupner and J. Tennyson
MNRAS (to be published) (2009)

Electron collision with the silicon monoxide (SiO) molecule using the R-matrix method
H. N. Varambhia, M. Gupta, A. Faure, K. L. Baluja and J. Tennyson
J. Phys. B: At. Mol. Opt. Phys. 42, 095204 (2009)

Cross sections For Scattering of Electrons on BF_3
M. Radmilović-Radjenović, H. N. Varambhia, M. Vranić, J. Tennyson and Z. Lj. Petrović
Publ. Astron. Obs. Belgrade No. 84, 57 (2008)

R-matrix calculations of low-energy electron alkane collisions
H. N. Varambhia, J. J. Munro and J. Tennyson
Int. J. Mass Spectrom. 271, 1 (2008)

Quantemol-N: an expert system for performing electron molecule collision calculations using the R-matrix method
J. Tennyson, D. B. Brown, J. J. Munro, I. Rozum, H. N. Varambhia and N. Vinci
J. Phys.: Conf. Ser. 86, 012001 (2007)

Electron-impact rotational and hyperfine excitation of HCN, HNC, DCN and DNC
A. Faure, H. N. Varambhia, T. Stoecklin and J. Tennyson

Mon. Not. R. Astron. Soc. 382, 840 (2007)

Electron collision with the HCN and HNC molecules using the R-matrix method

H. N. Varambhia and J. Tennyson

J. Phys. B: At. Mol. Opt. Phys. 40, 1211 (2007)

Bibliography

Abdolsalami F, Abdolsalami M and Gomez P 1994 *Phys. Rev. A* **50**, 360–363.

Abuain T, Walker I C and Dance D F 1985 *J. Chem. Soc., Faraday Trans.* **81**, 1061–1066.

Ahrens V, Lewen F, Takano S, Winnewisser G, Urban S, Negirev A A and Koroliev A N 2002 *Z. NaturForsch* **57**, 669–681.

Alexander M H and Dagdigian P J 1985 *J. Chem. Phys.* **83**, 2191–2200.

Alikhani M E, Tremblay B and Manceron L 1997 *J. Mol. Struct. (Theochem)* **394**, 25–31.

Allan R J and Dickinson A S 1981 *J. Phys. B: At. Mol. Opt. Phys.* **14**, 1675–1694.

Allen L C 1989 *J. Am. Chem. Soc.* **111**, 9003–9014.

Allison A C and Dalgarno A 1971 *Astron. Astrophys.* **13**, 331–332.

Almlof J and Taylor P R 1984 'Advanced Theories and Computational Approaches to the Electronic Structure of Molecules'.

Altshuler S 1957 *Phys. Rev.* **107**, 114–117.

Baluja K L, Burke P G and Morgan L A 1982 *Computer Phys. Communs.* **27**, 299–307.

Baluja K L, Zhang R, Franz J and Tennyson J 2007 *J. Phys. B: At. Mol. Opt. Phys.* **40**, 3515–3524.

Bayet E, Gerin M, Phillips T G and Contursi A 2006 *Astron. Astrophys.* **460**, 467–485.

Bechtel H A, Steeves A H and Field R W 2006 *Astrophys. J.* **649**, L53–L56.

Bezzaouia S, Telmini M and Jungen C 2004 *Phys. Rev. A* **70**, 012713.

Bieniek R J and Green S 1981 *Chem. Phys. Lett.* **84**, 380–384.

Bieniek R J and Green S 1983 *Astrophys. J.* **265**, 29.

Billingsley F B and Krauss M 1974 *J. Chem. Phys.* **60**, 4130.

Biver N, Bockelee-Morvan D, Colom P, Crovisier J, Germain B, Lellouch E, Davies J K, Dent W R F, Moreno R, Paubert G, Wink J, Despois D, Lis D C, Mehringer D, Benford D, Gardner M, Philips T G, Gunnarsson M, Rickman H, Winnberg A, Bergman P, Johansson L E B and Rauer H 1997 *Earth, Moon, and Planets* **78**, 5–11.

Biver N, Bockele-Morvan D, Crovisier J, Lis D C, Moreno R, Colom P, Henry F, Herpin F, Paubert G and Womack M 2006 *Astron. Astrophys* **449**, 1255–1270.

Blackman G L, Brown R D, Godfrey P D and Gunn H I 1976 *Nature* **261**, 395–396.

Boogert A C A, Blake G A and Oeberg K 2004 *Astrophys. J* **615**, 344–353.

Boogert A C A, Schuttle W A, Tielens A G G M, Whittet D C B, Helmich F B, Ehrenfruend P, Wesselius P R, de Graauw T and Prusti T 1996 *Astron. Astrophys.* **315**, L377–L380.

Botschwina P and Sebald P 1985 *J. Mol. Spectrosc.* **110**, 1–18.

Bottcher C 1970 *Mol. Phys.* **19**, 193–198.

Bottcher C 1971 *Chem. Phys. Lett.* **9**, 57–61.

Bouchiha D, Caron L G, Gorfinkiel J D and Sanche L 2008 *J. Phys. B: At. Mol. Opt. Phys.* **41**, 045204.

Boudaïffa B, Cloutier P, Hunting D, Huels M A and Sanche L 2000 *Science* **287**, 1658–1660.

Boys S F 1950 *Proc. Roy. Soc. A* **200**, 542–544.

Breit G and Wigner E 1936 *Phys. Rev.* **49**, 519–531.

Broadfoot A L, Belton M J S, Takacs P Z, Sandel B R, Shemansky D E, Holberg J B, Ajello J M, Atreya S K, Donahue T M, Moos H W, Bertaux J L, Blamont J E, Strobel D F, McConnell J C, Dalgarno A, Goody R and McElroy M B 1979 *Science* **204**, 979–982.

Broadfoot A L, Sandel B R, Shemansky D E, Holberg J B, Smith G R, Strobel D F, McConnell J C, Kumar S, unten D M, Atreya S K, Donahue T M, Moos H W, Bertaux J L, Blamont J E, Pomphrey R B and Linick S 1981 *Science* **212**, 206–211.

Buckman S J and Lohmann B 1986 *Phys. Rev. A* **34**, 1561–1563.

Buenker R J and Peyerimhoff S D 1974 *Theor. Chim. Acta* **35**, 33–58.

Buenker R J and Peyerimhoff S D 1975*a* *Chem. Phys.* **8**, 56–67.

Buenker R J and Peyerimhoff S D 1975*b* *Theor. Chim. Acta* **39**, 217–228.

Burke P G 1973 *Computer Phys. Communs.* **6**, 288–302.

Burke P G and Berrington K A 1993 *Atomic and Molecular Processes, an R-matrix approach* IOP Publishing, Bristol.

Burke P G, Hibbert A and Robb W D 1971 *J. Phys. B: At. Mol. Opt. Phys.* **4**, 153–161.

Burke P G, Mackey I and Shimamura I 1977 *J. Phys. B: At. Mol. Opt. Phys.* **10**, 2497–2512.

Burke P G, Noble C J and Burke V M 2007 *Adv. Atom. Mol. Opt. Phys.* **54**, 237–318.

Burke P G and Seaton M J 1971 *Methods Comput. Phys.* **10**, 1–80.

Burke P G and Tennyson J 2005 *Mol. Phys.* **103**, 2537–2548.

Burnett S M, Felgerie C S, Stevens A E and Lineberger C 1982 *J. Phys. Chem.* **86**, 4486–4488.

Burrow P D, Howard A E, Johnston A R and Jordan K D 1992 *J. Phys. Chem.* **96**, 7570–7578.

Burrus C A 1958 *J. Chem. Phys.* **28**, 427–429.

Buttle P J A 1967 *Phys. Rev.* **160**, 719–729.

Caprasecca S, Gorfinkiel J D, Bouchiha D and Caron L G 2009 *J. Phys. B: At. Mol. Opt. Phys.* **42**, 095205.

Carelli F, Sebastianelli F, Baccarelli I and Gianturco F A 2008 *Int. J. Mass Spectrometry* **277**, 155–161.

Celii F G, Pehrsson P E, Wang H T and Butler J E 1988 *Appl. Phys. Lett.* **52**, 2043.

Cernicharo J, Barlow M J, Gonzalez-Alfonso E, Cox P, Nguyen P E C R Q, Omont A, Guelin M and Liu X W 1996 *Astron. Astrophys.* **315**, L201–204.

Chang E S and Fano U 1972 *Phys. Rev. A* **6**, 173–185.

Chang E S and Temkin A 1970 *J. Phys. Soc. Jpn.* **29**, 172–179.

Chattopadhyaya S, Chattopadhyay A and Das K K 2003 *J. Phys. Chem. A* **107**, 148–158.

Chistophorou L G and Olthoff J K 2004 *Fundamental Electron Interactions with Plasma Processing Gases* Kluwer Academic/Plenum Publishers.

Chu S I 1976 *Astrophys. J.* **206**, 640–651.

Chu S I and Dalgarno A 1974 *Phys. Rev. A* **10**, 788–792.

Clark C W 1977 *Phys. Rev. A* **16**, 1419–1422.

Codella C, Scappini F, Bachiller R and Benedettini M 2002 *Mon. Not. R. Astr. Soc.* **331**, 893–900.

Collins L A and Norcross D W 1978 *Phys. Rev. A* **18**, 467–498.

Collins L A, Robb W D and Morrison M A 1980 *Phys. Rev. A* **21**, 488–495.

Corey G and McCourt F R 1983 *J. Chem. Phys.* **87**, 2723–2730.

Cornet R and Dubois I 1972 *Can. J. Phys.* **50**, 630.

Coulson C A and Walmsley M 1967 *Proc. Phys. Soc.* **91**, 31–32.

Crawford O and Dalgarno A 1967 *Chem. Phys. Lett.* **1**, 23.

Crawford O H and Dalgarno A 1971 *J. Phys. B: At. Mol. Opt. Phys.* **4**, 494–502.

Crovisier J, Biver N, Bockelee-Morvan D, Colom P, Jorda L, Lellouch E, Paubert G and Despois D 1995 *Icarus* **115**, 213–216.

Cybulski S M and Toczylowski R R 1999 *J. Chem. Phys.* **111**, 10520–10528.

Danby G and Tennyson J 1988 *Phys. Rev. Lett.* **61**, 2737–2739.

Dayou F and Balanca C 2006 *Astron. Astrophys.* **459**, 297–305.

DeMaria A J 1973 *Proc. IEEE* **61**, 731–748.

Dickinson A S 1977 *J. Phys. B: At. Mol. Opt. Phys.* **10**, 967–981.

Dickinson A S, Phillips T G, Goldsmith P F, Percival I C and Richards D 1977 *Astron. Astrophys.* **54**, 645–647.

Dickinson A S and Richards D 1975 *J. Phys. B: At. Mol. Opt. Phys.* **8**, 2846–2857.

Dickinson D F and Gottlieb C A 1970 *Astrophys. Lett.* **7**, 205.

DiSanti M A, Mumma M J, Russo N D and Sauer K M 2001 *Icarus* **153**, 361–390.

Dora A, Tennyson J, Bryjko L and van Mourik T 2009 *J. Chem. Phys.* **130**, 164307.

Draine B T 1980 *Astrophys. J.* **241**, 1021–1038.

Drdla K, Knapp G R and van Dishoeck E F 1989 *Astrophys. J* **345**, 815–827.

Duric N, Cadez I and Kurepa M 1991 *Int. J. Mass Spectrom. Ion Processes* **108**, R1–R10.

Ebenstein W L and Muenter J S 1984 *J. Chem. Phys.* **80**, 3989–3991.

Edard F, Hitchcock A P and Tronc M 1990 *J. Chem. Phys.* **94**, 2768–2774.

EMSL Gaussian Basis Set Order Form 2009.
URL: *http://www.emsl.pnl.gov/forms/basisform.html*

Encrenaz T, Lellouch E, Drossart P, Orton G, Feuchtgruber H and Atreya S K 2009 First Detection of CO in Uranus. to be published.
URL: *http://www2.cnrs.fr/en/131.htm*

Fabrikant I I 1980 *Phys. Lett. A* **77**, 421–423.

Fandreyer R, Burke P G, Morgan L A and Gillan C J 1993 *J. Phys. B: At. Mol. Opt. Phys.* **26**, 3625–3637.

Fano U 1970 *Phys. Rev. A* **2**, 353–365.

Faure A, Gorfinkiel J D, Morgan L A and Tennyson J 2002 *Computer Phys. Communs.* **144**, 224–241.

Faure A, Gorfinkiel J D and Tennyson J 2004*a* *Mon. Not. R. Astr. Soc.* **347**, 323–333.

Faure A, Gorfinkiel J D and Tennyson J 2004*b* *J. Phys. B: At. Mol. Opt. Phys.* **37**, 801–807.

Faure A, Kokoouline V, Greene C H and Tennyson J 2006 *J. Phys. B: At. Mol. Opt. Phys.* **39**, 4261–4273.

Faure A and Tennyson J 2001 *Mon. Not. R. Astr. Soc.* **325**, 443–448.

Faure A and Tennyson J 2002 *J. Phys. B: At. Mol. Opt. Phys.* **35**, 1865–1873.

Feldt A N and Morrison M A 1982 *J. Phys. B: At. Mol. Opt. Phys.* **15**, 301–308.

Ferch J, Granitza B and Raith W 1985 *J. Phys. B: At. Mol. Opt. Phys.* **18**, L445–L450.

Feshbach H 1958 *Ann. Phys.* **5**, 357–390.

Feshbach H 1962 *Ann. Phys.* **19**, 287–313.

Field R W, Lagerqvist A and Renhorn I 1976 *Physica Scripta* **14**, 298–319.

Flower D R, des Forets G P, Field D and May P W 1996 *Mon. Not. R. Astr. Soc.* **280**, 447–457.

Fraser P A and Burley S K 1982 *Eur. J. Phys.* **3**, 230–238.

Freund R S, Wetzel R C and Shul R J 1990 *Phys. Rev. A* **41**, 5861–5868.

Frey M T, Huill S B, Smith K A, Dunning F B and Fabrikant I I 1995 *Phys. Rev. Lett.* **75**, 810–813.

Furlong J and Newell W R 1993 *in* B IOP, ed., 'Proc. 18th Int. Conf. on Physics of Electronic and Atomic Collisions'.

Garrett W R 1970 *Chem. Phys. Lett.* **5**, 393–397.

Garrett W R 1971 *Phys. Rev. A* **3**, 961–972.

Garrett W R 1972 *Mol. Phys.* **24**, 465–487.

Garrett W R 1975 *Phys. Rev. A* **11**, 509–515.

Gianturco F A, Rodrigues-Ruiz J A and Sanna N 1995 *J. Phys. B: At. Mol. Opt. Phys.* **28**, 1287–1300.

Gianturco F A and Rodriguez-Ruiz J A 1993 *Phys. Rev. A* **47**, 1075–1086.

Gibson J C, Morgan L A, Gulley R J, Brunger M J, Bundschu C T and Buckman S J 1996 *J. Phys. B: At. Mol. Opt. Phys.* **29**, 3197–3214.

Gil T J, Lengsfield B H, McCurdy C W and Rescigno T N 1994 *Phys. Rev. A* **49**, 2551–2560.

Goldflam R, Green S and Kouri D J 1977 *J Chem. Phys.* **67**, 4149–4161.

Goldflam R, Kouri D J and Green S 1977 *J. Chem. Phys.* **67**, 5661–5675.

Gómez-Camacho J, Pérez-Bernal F and Arias J M 1998 *Phys. Rev. A* **58**, 1174–1182.

Gordon R G and Kim Y S 1972 *J. Chem. Phys.* **56**, 3122–3133.

Gorfinkiel J D, Faure A, Taioli S, Piccarreta C, Halmová G and Tennyson J 2005 *Eur. Phys. J. D* **35**, 231–237.

Gorfinkiel J D and Tennyson J 2004 *J Phys. B: At. Mol. Opt. Phys.* **37**, L343–50.

Graupner K, Field T A and Feketeova L 2006 *New J. Phys.* **8**, 314.

Green S 1974 Hydrogen cyanide.
URL: *http://data.giss.nasa.gov/mcrates/*

Green S and Chapman S 1978 *Astrophys. J Suppl.* **37**, 169–194.

Green S and Thaddeus P 1974 *Astrophys. J* **191**, 653–658.

Guelin M, Salome P, Neri R, Garcia-Burillo S, Gracia-Carpio J, Cernicharo J, Planesas P C P, Solomon P M, Tacconi L J and Bout P V 2007 *Astron. Astrophys.* **462**, L45–L48.

Guilloteau S and Baudry A 1981 *Astron. Astrophys.* **97**, 213–217.

Gupta M and Baluja K L 2005 *J. Phys. B: At. Mol. Opt. Phys.* **38**, 4057–4073.

Gupta M and Baluja K L 2006 *Phys. Rev. A* **74**, 052713.

Gusdorf A, Cabrit S, Flower D R and des Forets G P 2008 *Astron. Astrophys.* **482**, 809–829.

Halderson D 1988 *Nucl. Phys.* **487**, 647–652.

Halmova G, Gorfinkiel J D and Tennyson J 2006 *J. Phys. B: At. Mol. Opt. Phys.* **39**, 2849–2860.

Hampel C, Peterson K A and Werner H J 1992 *Chem. Phys. Lett.* **190**, 1–12.

Harris G J, Pavlenko Y V, Jones H R A and Tennyson J 2003 *Mon. Not. R. Astron. Soc.* **344**, 1107–1118.

Harrison A, Henkel C and Russell A 1999 *Mon. Not. R. Astron. Soc.* **303**, 157–172.

Harrison J F 2006 *J. Phys. Chem. A* **110**, 10484–10857.

Harvey A G and Tennyson J 2009 *J. Phys. B: At. Mol. Opt. Phys.* **42**, 095101.

Herzberg G 1966 *Electronic Spectra and Electronic Structure of Polyatomic Molecules* Van Nostrand Reinhold, New York.

Herzberg G and Huber K P 1979 *Molecular Spectra and Molecular Structure* Vol. 4 Van Nostrand Reinhold.

Herzberg G and Innes K K 1957 *Can. J. Phys.* **35**, 842.

Hiraoka K, Mochizuki N and Wada A 2006 *in* 'AIP Conf. Proc. ASTROCHEMISTRY: From Laboratory Studies to Astronomical Observations' Vol. 855.

Hirota T, Yamamoto S, Mikami H and Ohishi M 1998 *Astrophys. J.* **503**, 717–728.

Hudson J E, Vallance C and Harland P 2004 *J. Phys. B: At. Mol. Opt. Phys.* **37**, 445–455.

Hunter L W 1975 *J. Chem. Phys.* **62**, 2855.

Huo W H 1965 *J. Chem. Phys.* **43**, 624–647.

Huo W M and Brown D 1999 *Phys. Rev. A* **60**, 295–305.

Hwang W, Kim Y K and M. E. Rudd M E 1996 *J. Chem Phys.* **104**, 2956.

Itikawa Y 1978 *Phys. Rep.* **46**, 117–164.

Itikawa Y 2000 *Theo. Chem. Acc.* **105**, 123–131.

Itikawa Y and Takayanagi K 1969 *J. Phys. Soc. Jpn.* **26**, 1254–1264.

Izmaylov A F, Adamson S O and Zaitsevskii A 2004 *J. Phys. B: At. Mol. Opt. Phys.* **37**, 2321–2329.

Izumiura H, Deguchi S and Fujii T 1998 *Astrophys. J* **494**, 89–92.

Izumiura H, Ukita N and Tsuji T 1995 *Astrophys. J.* **440**, 728.

Jain A 1986 *Phys. Rev. A* **34**, 954–958.

Jain A and Baluja K L 1992 *Phys. Rev. A* **45**, 202–218.

Jain A and Norcross D 1985 *Phys. Rev. A* **32**, 134–143.

Jain A and Norcross D 1986 *J. Chem. Phys.* **84**, 739–744.

Jain A and Norcross D W 1992 *Phys. Rev. A* **45**, 1644–1656.

Jewitt D, Senay M and Matthews H E 1996 *Science* **1996**, 1110–1113.

Jimenez-Serra I, Martin-Pintado J and Rodriguez-Franco A 2005 *Astrophys. J. Lett.* **627**, 121–124.

Jimenez-Serra I, Martin-Pintado J, Viti S, Martin S, Rodriguez-Franco A, Faure A and Tennyson J 2006 *Astrophys. J.* **650**, L135–L138.

Jmol: an open-source Java viewer for chemical structures in 3D 2009.
URL: *http://jmol.sourceforge.net/*

Jones H R A, Pavlenko Y, Viti S, Barber R J, Yakovina L A, Pinfield D and Tennyson J 2005 *Mon. Not. R. Astron. Soc.* **358**, 105–112.

Joshipura K N, Gangopadhyay S and Vaishnav B G 2007 *J. Phys. B: At. Mol. Opt. Phys.* **40**, 199–210.

Joshipura K N and Patel P M 1996 *J. Phys. B: At. Mol. Opt. Phys.* **29**, 3925–3932.

Joshipura K N, Vaishnav B G and Gangopadhyay S 2007 *Int. J. Mass Spectrometry* **261**, 146–151.

Jung K, Antoni T, Kochem R M K H and Ehrhardt H 1982 *J. Phys. B: At. Mol. Opt. Phys.* **15**, 3535–3555.

Kaur S, Baluja K L and Tennyson J 2008 *Phys. Rev. A* **77**, 032718.

Kendell R A, Dunning T H and Harrison R J 1992 *J. Chem. Phys.* **96**, 6796.

Khakoo M A, Silva H, Muse J, Lopes M C A, Winstead C and McKoy V 2008 *Phys. Rev. A* **78**, 052710.

Khakoo M A, Winstead C and McKoy V 2009 *Phys. Rev. A* **79**, 052711.

Kim Y K, Hwang W, Weinberger N M, Ali M A and Rudd M 1997 *J. Chem. Phys.* **106**, 1026–1033.

Kim Y K and Rudd M E 1994 *Phys. Rev. A* **50**, 3954–3967.

Kimura M, Itikawa Y and Bederson B 2001 *Adv. At. Mol. Opt. Phys.* **44**, 33–57.

Kirby-Docken K and Liu B 1977 *J. Chem. Phys.* **66**, 4309–4316.

Kohn W 1948 *Phys. Rev. A* **74**, 1763–1772.

Kolorenc P, Brems V and Horacek J 2005 *Phys. Rev. A* **72**, 012708.

Krishnamachari S L N G and Venkatasubramanian R 1984 *Spectrosc.Lett.* **19**, 401–407.

Kumar S 1979 *Nature* **280**, 758–760.

Kwan C K, Hsieh Y F, Kauppila W E, Stein S J and Uddin M N 1983 *Phys. Rev. A* **27**, 1328–1336.

Lacy J H, Carr J S, Evan N J, Baas F, Achtermann J M and Arens J F 1991 *Astrophys. J* **376**, 556–560.

Lane A M and Robson D 1966 *Phys. Rev.* **151**, 774–787.

Lane A M and Thomas R G 1958 *Rev. Mod. Phys.* **30**, 257–353.

Lane N F 1980 *Rev. Mod. Phys.* **52**, 29–119.

Langhoff S R and Bauschlicher C W 1993 *Chem. Phys. Lett.* **211**, 305–311.

LeDourneuf M, Schneider B I and Burke P G 1979 *J. Phys. B: At. Mol. Opt. Phys.* **12**, 369–369.

Lengsfield B H, Rescigno T N and McCurdy C W 1991 *Phys. Rev. A* **44**, 4296–4308.

Leurini S, Rolffs R, Thorwirth S, Parise B, Schilke P, Comito C, Wyrowski F, Guesten R, Bergman P, Menten K M and Nyman L A 2006 *Astron. Astrophys.* **454**, L47–L50.

Levin D A, Fliflet A W and McKoy V 1980 *Phys. Rev. A* **21**, 1202–1209.

Lévy-Leblond J M 1967 *Phys. Rev.* **153**, 1–4.

Lima M A P, Brescansin L M, da Silva A J R, Winstead C and McKoy V 1990 *Phys. Rev. A.* **41**, 327–332.

Lima M A P, Watari K and McKoy V 1989 *Phys. Rev. A* **39**, 4312–4315.

Linke R A and Goldsmith P F 1980 *Astrophys. J* **235**, 437–431.

Lique F and Spielfiedel A 2007 *Astron. Astrophys.* **462**, 1179–1185.

Lique F, Spielfiedel A and Cernicharo J 2006 *Astron. Astrophys.* **451**, 1125–1132.

Lique F, Spielfiedel A and Feautrier N 2007 *J. Phys. B: At. Mol. Opt. Phys.* **40**, 787–799.

Lo N, Cunningham M, Bains I, Burton M G and Garay G 2007 *Mon. Not. R. Astr. Soc.* **381**, L30–L34.

Lohmann B and Buckman S J 1986 *J. Phys. B: At. Mol. Opt. Phys.* **19**, 2565–2570.

Lovell A J, Kallivayalil N, Schloerb F B, Combi M R, Hansen K C and Gombosi T I 2004 *Astrophys. J.* **613**, 615–621.

Löwdin P O 1955 *Phys. Rev.* **97**, 1474–1489.

Lucas R and Cernicharo J 1989 *Astron. Astrophys.* **218**, L20.

Makochekanwa C, Oguri K, Suzuki R, Ishihara T, Hoshino M and Kimura M 2006 *Phys. Rev. A* **74**, 042704.

Maroulis G, Makris C, Xenides D and Karamanis P 2000 *Mol. Phys.* **98**, 481–491.

Maroulis G and Pouchain C 1996 *Theo. Chem. Acc.* **93**, 131–140.

Martin S, Martin-Pintando J, Mauersberger R, Henkel C and Garcia-Burillo S 2005 *Astrophys. J* **620**, 210.

Matsushita A, Nagai M, Yamakawa K, Hiramatsu M, Sakai A, Hori M, Goto T and Zaima S 2004 *Jpn. J. Appl. Phys.* **43**, 424–425.

McCorkle D L, Christophorou L G, Maxey D V and Carter J G 1978 *J. Phys. B: At. Mol. Opt. Phys.* **11**, 3067–3079.

McCurdy C W and Miller W H 1977 *J. Chem. Phys.* **67**, 463.

McCurdy C W and Resigno T N 1989 *Phys. Rev. A* **39**, 4487–4493.

McLean A D and Yoshimine M 1968 *IBM Journal of Research and Development* **12**, 206.

McNaughten P and Thompson D G 1988 *J. Phys. B: At. Mol. Opt. Phys.* **21**, L703–L707.

McWeeny R 1989 *Methods of Molecular Quantum Mechanics* Academic Press.

Meier R R 1991 *Space Sci. Reviews* **58**, 1–185.

Meyer W 1973 *J. Chem. Phys.* **58**, 1017–1035.

Middleton A G, Brunger M J and Teubner P J O 1993 *J. Phys. B: At. Mol. Opt. Phys.* **26**, 1743–1759.

Mittleman M H and Myerscough V P 1966 *Phys. Lett.* **23**, 545–546.

Mittleman M H and von Holdt R E 1965 *Phys. Rev.* **140**, 726–729.

Moltzen E K, Klabunde K J and Senning A 1988 *Chem. Rev.* **88**, 391–406.

Monteiro T S and Stustzki J 1986 *Mon. Not. R. Astr. Soc* **221**, 33–39.

Morgan L A 1984 *Computer Phys. Communs.* **31**, 419–422.

Morgan L A 1991 *J. Phys. B: At. Mol. Opt. Phys* **24**, 4649–4660.

Morgan L A, Gillan C J, Tennyson J and Chen X 1997 *J. Phys. B: At. Mol. Opt. Phys.* **30**, 4087–4096.

Morgan L A and Tennyson J 1993 *J. Phys. B: At. Mol. Opt. Phys.* **26**, 2429–2441.

Morgan L A, Tennyson J and Gillan C J 1998 *Computer Phys. Communs.* **114**, 120–128.

Morrison M A 1988 *Adv. At. Mol. Phys.* **24**, 51–156.

Mosinsky M 1953 *Phys. Rev.* **91**, 984–985.

Muenter J S 1975 *J. Mol. Spectrosc.* **55**, 490–491.

Mulliken R S 1934 *J. Chem. Phys.* **2**, 782–793.

Muniz E and Jorge F 2006 *Int. J. Quant. Chem.* **106**, 943–952.

Munjal H and Baluja K L 2006 *Phys. Rev. A* **74**, 032712.

Nakano T, Toyoda H and Sugai H 1991 *Jpn. J. Appl. Phys.* **30**, 2908–2911.

Nayak M K, Chaudhuri R K and Krishnamachari S N L G 2005 *J. Chem. Phys.* **122**, 184323.

Nesbet R K 1964 *J. Chem. Phys.* **40**, 3619.

Nestmann B M, Pfingst K and Peyerimhoff S 1994 *J. Phys. B: At. Mol. Opt. Phys.* **27**, 2297–2308.

Neufeld D A and Green S 1994 *Astrophys. J* **432**, 158.

Nisini B, Codella C, Giannini T, Garcia J S, Richer J S, Bachiller R and Tafalla M 2007 *Astron. Astrophys.* **462**, 163–172.

NIST 1997 'Electron Impact Cross Sections for Ionization and Excitation'. **URL:** *http://physics.nist.gov/PhysRefData/Ionization/Xsection.html*

NIST 2008 'Computational chemistry comparison and benchmark database'. **URL:** *http://cccbdb.nist.gov/*

Noble C J, Dorr M and Burke P G 1993 *J. Phys. B: At. Mol. Opt. Phys.* **26**, 2983–3000.

Noble C J and Nesbet R K 1984 *Computer Phys. Communs.* **33**, 399–411.

Norcross D W and Padial N T 1982 *Phys. Rev. A* **25**, 226–238.

Orient O J and Srivastava S K 1987 *J. Phys. B: At. Mol. Opt. Phys.* **20**, 3923–3936.

Padial N T and Norcross D W 1984 *Phys. Rev. A* **29**, 1742–1748.

Paglione T A D, Wall W F, Young J S, Heyer M H, Richard M, Goldstein M, Kaufman Z, Nantais J and Perry G 2001 *Astrophys. J.* **135**, 183–200.

Palov A P, Gray M D, Field D and Balint-Kurti G G 2006 *Astrophys. J.* **639**, 204–209.

Park Y S, Kim J and Minh Y C 1999 *Astrophys. J.* **520**, 223–232.

Pauling L 1932 *J. Am. Chem. Soc.* **54**, 3570–3582.

Pauzat F, Ridard F and Levy B 1972 *Mol. Phys.* **23**, 1163.

Pavlenko Y V and Jones H R A 2002 *Astron. Astrophys* **396**, 967–975.

Pearl J, Hanel R, Kunde V, Maguire W, Fox K, Gupta S, Ponnamperuma C and Raulin F 1979 *Nature* **280**, 755–758.

Penzias A A, Solomon P M, Wilson R W and Jefferts K B 1971 *Astrophys. J* **168**, 53–.

Pestellini C C, Bodo E, Balakrishnan N and Dalgarno A 2002 *Astrophys. J* **571**, 1015–1020.

Peterson K A and Woods R C 1990 *J. Chem. Phys.* **92**, 6061.

Pfingst K, Nestmann B M and Peyerimhoff S D 1994 *J. Phys. B: At. Mol. Opt. Phys.* **27**, 2283–2296.

Pintado J M, de Vicente P, Fuente A and Planesas P 1997 *Astrophys. J. Lett.* **482**, 45.

Rabádan I, Sarpal B K and Tennyson J 1998 *Mon. Not. R. Astr. Soc.* **299**, 171–175.

Rabadán I and Tennyson J 1996 *J. Phys. B: At. Mol. Opt. Phys.* **29**, 3747–3761.

Rabadán I and Tennyson J 1998 *Computer Phys. Communs.* **114**, 129–141.

Rabadán I and Tennyson J 1999 *J. Phys. B: At. Mol. Opt. Phys.* **32**, 4753–4762.

Rescigno T N 1995 *Phys. Rev. A* **52**, 329–333.

Rescigno T N, Lengsfield B H, McCurdy C W and Parker S D 1992 *Phys. Rev. A* **45**, 7800–7809.

Robb W D 1972 *Computer Phys. Communs.* **4**, 16–19.

Rodgers S D and Chamley S B 1998 *Astrophys. J* **501**, 227–230.

Rohr K and Linder F 1976 *J. Phys. B: At. Mol. Opt. Phys.* **9**, 2521–2537.

Roothan C C J 1951 *Rev. Mod. Phys.* **23**, 69–89.

Rosenblum B, Nethercot A H and Townes C H 1958 *Phys. Rev.* **109**, 400–412.

Rozum I, Mason N J and Tennyson J 2003 *J. Phys. B: At. Mol. Opt. Phys.* **36**, 2419–2432.

Rudge M R H, Trajmer S and Williams W 1976 *Phys. Rev. A* **13**, 2074–2086.

Saha S, Ray S, Bhattacharyya B and Barua A K 1981 *Phys. Rev. A* **23**, 2926–2932.

Salvini S, Burke P G and Noble C J 1984 *J. Phys B: At. Mol. Opt. Phys.* **17**, 2549–2561.

Sanna N and Gianturco F A 1998 *Computer Phys. Communs.* **114**, 142–167.

Sarpal B K, Branchett S E, Tennyson J and Morgan L A 1991 *J. Phys. B: At. Mol. Opt. Phys.* **24**, 3685–3699.

Sarpal B K, Tennyson J and Morgan L A 1991 *J. Phys. B: At. Mol. Opt. Phys.* **24**, 1851–1866.

Sarpal B K, Tennyson J and Morgan L A 1994 *J. Phys. B: At. Mol. Opt. Phys.* **27**, 5943–5953.

Scappini F, Pestellini C C, Casu S and Olberg M 2007 *Astron. Astrophys.* **466**, 243–246.

Schneider B 1975 *Chem. Phys. Lett.* **31**, 237–241.

Schneider B I and Hay P J 1976 *Phys. Rev. A* **13**, 2049–2056.

Schneider B I and Rescigno T N 1988 *Phys. Rev. A* **37**, 3749–3754.

Schneider I F, Rabadán I, Carata L, Suzor-Weiner L H A A and Tennyson J 2000 *J. Phys. B: At. Mol. Opt. Phys.* **33**, 4849–4861.

Schwenzer G M, O'Neil S V, Schaefer H F, Baskin C P and Bender C F 1974 *J. Chem. Phys.* **60**, 2787.

Schwenzer G M, Schaefer H F and Bender C F 1975 *J. Chem. Phys.* **63**, 569.

Secrest D 1975 *J. Chem. Phys.* **62**, 710.

Shiki S and Deguchi S 1997 *Astrophys. J* **478**, 206–210.

Shimamura I 1998 *Mol. Phys.* **93**, 3–17.

Shimoi M and Itikawa Y 1999 *J. Phys. B: At. Mol. Opt. Phys.* **32**, 65–79.

Sisak M and Secrest D 1992 *J. Chem. Phys.* **96**, 230.

Skurski P, Gutowski M and Simons J 2001 *J. Chem. Phys.* **114**, 7443–7449.

Slater J C 1960 *Quantum Theory of Atomic Structure* McGraw-Hill.

Snyder L E, Veal J M, Woodney L M, Wright M C H, Palmer P, A'Hearn M F, Kuan Y J, de. Pater L and Forster J R 2001 *Astron. J* **121**, 1147–1154.

Sobrinho A M C and Lee M T 2005 *Int. J. Quant. Chem* **103**, 703.

Sohn W, Kochem K H, Scheuerlein K M, Jung K and Ehrhardt H 1986 *J. Phys. B: At. Mol. Opt. Phys.* **19**, 3625–3632.

Srivastava S K, Tanaka H and Chutjian A 1978 *J. Chem. Phys.* **69**, 1493.

Stano M, Matejcik S, Skalny J D and Mirk T D 2003 *J. Phys. B: At. Mol. Opt. Phys.* **36**, 261–271.

Stibbe D T and Tennyson J 1997 *J. Phys. B: At. Mol. Opt. Phys.* **30**, L301–L307.

Stone A J 2009 'Anthony Stone's Wigner coefficient calculator'.
URL: *www-stone.ch.cam.ac.uk/wigner.html*

Strelnitskii V S 1984 *Mon. Not. R. Astr. Soc.* **207**, 339–354.

Sueoka O and Mori S 1986 *J. Phys. B: At. Mol. Opt. Phys.* **19**, 4035–4050.

Swain M R, G.Vasisht and Tinetti G 2008 *Nature* **452**, 329–331.

Szabo A and Ostlund N S 1996 *Modern Quantum Chemistry: Introduction to Advanced Electronic Structure Theory* Dover Publications.

Takatsuka K and McKoy V 1981 *Phys. Rev. A* **24**, 2473–2480.

Takatsuka K and McKoy V 1984 *Phys. Rev. A* **30**, 1734–1740.

Takekawa M and Itikawa Y 1998 *J. Phys. B: At. Mol. Opt. Phys.* **31**, 3245–3261.

Tanaka H, Okada T, Boesten L, Suzuki T, Yamamoto T and Kubo M 1982 *J. Phys. B: At. Mol. Opt. Phys.* **15**, 3305–3319.

Tarana M and Tennyson J 2008 *J. Phys. B: At. Mol. Opt. Phys.* **41**, 205204.

Taylor J R 2006 *Scattering Theory: The Quantum Theory of Nonrelativistic Collisions* Dover Publications.

Tennyson J 1986 *J. Phys. B: At. Mol. Phys.* **19**, 4255–4263.

Tennyson J 1987 *J. Phys. B: At. Mol. Opt. Phys.* **20**, L375–L378.

Tennyson J 1996*a* *J. Phys. B: At. Mol. Opt. Phys.* **29**, 1817–1828.

Tennyson J 1996*b* *J. Phys. B: At. Mol. Opt. Phys.* **29**, 6185–6201.

Tennyson J 1997 *Computer Phys. Communs.* **100**, 26–30.

Tennyson J 2010 *Phys. Rep.* (submitted).

Tennyson J, Brown D B, Munro J J, Rozum I, Varambhia H N and Vinci N 2007 *J. Phys.: Conf. Series* **86**, 012001.

Tennyson J and Noble C J 1984 *Computer Phys. Communs.* **33**, 421–424.

Tennyson J, Noble C J and Burke P G 1986 *Int. J. Quantum Chem.* **29**, 1033–1042.

Tennyson J, Noble C J and Salvini S 1984 *J. Phys. B: At. Mol. Opt. Phys.* **17**, 905–912.

Thummel H T, Nesbet R K and Peyerimhoff S D 1992 *J. Phys. B: At. Mol. Opt. Phys.* **25**, 4553–4579.

Tilford S G and Simmonds J D 1972 *J. Phys. Chem. Ref. Data* **1**, 147.

Tong A T, Bacskay G B, Hush N S and Bogaard M P 1991 *Mol. Phys.* **74**, 1037–1064.

Trevisan C S, Orel A E and Rescigno T N 2006 *Phys. Rev. A* **74**, 042716.

Tronc M, Azria R and Coat Y L 1980 *J. Phys. B: At. Mol. Opt. Phys.* **13**, 2327–2332.

Turner B E 2001 *ApJS* **136**, 579–629.

Turner B E, Chan K W, Green S and Lobowich D A 1992 *Astrophys. J.* **399**, 114.

Turner J E and Fox K 1966 *Phys. Lett.* **23**, 547–549.

van Mourik T, Harris G J, Polyanski O L, Tennyson J, Csaszar A G and Knowles P J 2001 *J. Chem. Phys.* **115**, 3706–3718.

Velasco A M, Pitarch-Ruiz J, de Meras A M J S, Marin J S and Martin I 2006 *J. Chem. Phys.* **124**, 124313.

Vinodkumar M, Joshipura K N, Limbachiya C G and Antony B K 2006 *Eur. Phys. J. D* **37**, 67–74.

Wada K and Tomisaka K 2005 *Astrophys. J.* **619**, 93–104.

Walmsley C M, Churchwell E, Nash A and Fitzpatrick E 1982 *Astrophys. J.* **258**, L75–L78.

Watts J D, Gauss J and Bartlett R J 1993 *J. Chem. Phys.* **98**, 8718–8733.

Werner H J, Knowles P J, Lindh R, Manby F R, Schütz M, Celani P, Korona T, Mitrushenkov A, Rauhut G, Adler T B, Amos R D, Bernhardsson A, Berning A, Cooper D L, Deegan M J O, Dobbyn A J, Eckert F, Goll E, Hampel C, Hetzer G, Hrenar T, Knizia G, Köppl C, Liu Y, Lloyd A W, Mata R A, May A J, McNicholas S J, Meyer W, Mura M E, Nicklass A, Palmieri P, Pflüger K, Pitzer R, Reiher M, Schumann U, Stoll H, Stone A J, Tarroni R, Thorsteinsson T, Wang M and Wolf A 2008 'MOLPRO, version 2008.3, a package of ab initio programs'.
URL: *http://www.molpro.net*

Wigner E 1946 *Phys. Rev.* **70**, 606–618.

Wigner E P and Eisenbud L 1947 *Phys. Rev.* **72**, 29–41.

Williams G R J and Poppinger D 1975 *Mol. Phys.* **30**, 1005–1013.

Williams J P and Blitz L 1998 *Astrophys. J* **494**, 657–675.

Wilson R W, Penzias A A, Jefferts K B, Kutner M and Thaddeus P 1971 *Astrophys. J.* **167**, 97.

Winnewisser G and Cook R L 1968 *J. Mol. Spectrosc.* **28**, 266–268.

Winstead C and McKoy V 2000 *Adv. Atom. Mol. Opt. Phys.* **43**, 111–145.

Winstead C and McKoy V 2006 *J. Chem. Phys.* **125**, 174304.

Winstead C and McKoy V 2007 *Phys. Rev. A* **76**, 012712.

Winstead C, Sun Q, McKoy V, Lino J L S and Lima M A P 1993 *J. Chem. Phys.* **98**, 2132–2137.

Woods P M, Schoeier F L, Nyman L A and Olofsson H 2003 *Astron. Astrophys.* **402**, 617–634.

Xie X and Mumma M J 1992 *Astrophys. J* **386**, 720–728.

Zetner P W, Kanik I and Trajmer S 1998 *J. Phys. B: At. Mol. Opt. Phys.* **31**, 2395–2413.

Zobel J, U. Mayer K Y and Ehrhardt H 1996 *J. Phys. B: At. Mol. Opt. Phys.* **29**, 813–838.

Zubek M and Szmytkowski C 1979 *Phys. Lett. A* **74**, 60–62.

Zuckerman B, Morris M, Palmer P and Turner B E 1972 *Astrophys. J* **173**, 125–129.